Universidade do Minho
Escola de Engenharia

Hugo da Silva Gaspar

Impact of novel fullerene acceptors and chemical additives on the morphology and efficiency of organic solar cells

julho de 2020

Impact of novel fullerene acceptors and chemical additives on the morphology and efficiency of organic solar cells
Hugo da Silva Gaspar
UMinho | 2020

Universidade do Minho
Escola de Engenharia

Hugo da Silva Gaspar

Impact of novel fullerene acceptors and chemical additives on the morphology and efficiency of organic solar cells

Tese de Doutoramento
Doutoramento em Ciência e Engenharia de Polímeros e Compósitos

Trabalho efetuado sob a orientação do
Doutor Júlio César Machado Viana
do
Doutor Carlos Gabriel Pires Morgado Bernardo
e do
Doutor João Paulo Costa Tomé

julho de 2020

Acknowledgements

During my PhD journey I had the opportunity to meet and interact with several people from different nationalities who helped me in different ways along the process.

First, I would like to thank the most important people in my life which are my parents, who gave me all the support and love. To my supervisor Dr. Júlio Viana for the general guidance and support and for his crucial help in funding my work. Co-supervisor Dr. Gabriel Bernardo played a key role during all PhD, he helped me in every way and he has made possible my 6 months stay as a research scholar in the department of Physics at the University of Sheffield (U.K.) – I thank him for everything he did for me. Dr. João Tomé was my co-supervisor who oriented me, as well Dr. Flávio Figueira, on the synthesis of the novel fullerenes. From the University of Sheffield, I would like to thank: Dr. David Lidzey for the opportunity to start making OPV devices on his EPMM (Electronic and Photonic Molecular Materials Group) research laboratory; my office mates (Dr. Andrew Parnell, Dr. Mike Weir and Dr. Sam Coveney) for always having a good spirit. In the ISIS neutron facilities at Rutherford Appleton Laboratory (RAL) I had the opportunity to study my samples using Small Angle Neutron Scattering (SANS) with the help of Dr. Stephen King whom I like to thank.

Due to some equipment difficulties at CENTI, Dr. Luiz Pereira at University of Aveiro was crucially important by providing me the conditions (glovebox with metal evaporator) and support to perform an important part of my work. At Faculdade de Ciências da Universidade do Porto, I perform AFM analysis with the help of Dr. Carlos Pereira and Ana. At last, I would like to thank Dr. Dzmitry Ivanou, from LEPABE/FEUP, for the help in the cyclic voltammetry measurements and analysis and FCT for the funding of my PhD scholarship.

STATEMENT OF INTEGRITY

I hereby declare having conducted this academic work with integrity. I confirm that I have not used plagiarism or any form of undue use of information or falsification of results along the process leading to its elaboration.

I further declare that I have fully acknowledged the Code of Ethical Conduct of the University of Minho.

Impact of novel fullerene acceptors and chemical additives on the morphology and efficiency of organic solar cells

Organic photovoltaics (OPVs) have experienced significant developments in power conversion efficiency (PCE), attaining recently over 16 % for small area single junction devices. Aiming to bring the OPV technology to market, much efforts are being made to further improve their efficiencies and the development of novel fullerenes and the improvement of the active layer morphology (ex: additives, annealing) are some of the strategies currently being pursued.

In this thesis, 16 novel *N*-methyl-fulleropyrrolidine acceptors, based on the fullerenes C_{60} (8) and C_{70} (8), were synthesized (Prato reaction). The functionalization of C_{70} yields a mixture of 4 regioisomers that have different HOMO/LUMO levels as determined by DFT calculations. The sixteen fullerene derivatives were tested in bulk-heterojunction (BHJ) solar cells with the low bandgap polymer PffBT4T-2OD. The different pendant groups attached to the *N*-methyl-fulleropyrrolidines consisted of phenyl groups (Chapter II) and thiophene and carbazole groups (Chapter III).

For both sets, the corresponding HOMO/LUMO energy levels were determined by cyclic voltammetry. Even though several of the synthesized fulleropyrrolidine acceptors have more favorable (higher) LUMO levels than the standard $PC_{71}BM$, when tested in PffBT4T-2OD based solar cells they originate devices with lower performances than reference devices based on $PC_{71}BM$. Additionally, devices based on C_{60}-fulleropyrrolidines show in general better photovoltaic performances than the corresponding devices based on C_{70}-fulleropyrrolidines (structural and energetic disorder introduced by the regiosomer mixture of C_{70} derivatives) .

The effect of different additives on the morphology and performance of PffBT4T-2OD:$PC_{71}BM$ based OPVs is investigated in Chapter IV. Some additives possess antagonist effects: some are shown to improve the PCE; others decrease PCE by ~30% and others eliminate any PCE. Grazing-Incidence Wide-Angle X-ray Scattering (GIWAXS) reveals a clear stepwise variation in the crystallinity of the systems when changing the additive between the two extreme-situations of maximum PCE (1-chloronaphthalene) and PCE null (hexadecane). Small Angle Neutron Scattering (SANS) reveals that the morphology of devices with PCE ~0% is composed of large phase domains with correlation lengths ~30 nm, i.e. much larger than the typical exciton diffusion length in organic semiconductors.

Keywords: Fullerenes, *N*-methyl-fulleropyrrolidine, OPVs, PCE

Impacto de novos aceitadores de fulereno e aditivos químicos na morfologia e eficiência de células solares orgânicas

A energia fotovoltaica orgânica (OPVs) tem vivenciado desenvolvimentos significativos na eficiência de conversão de energia (PCE), atingindo recentemente mais de 16% para dispositivos de junção única de área pequena. Com o objetivo de trazer a tecnologia OPV ao mercado, estão sendo feitos muitos esforços para melhorar ainda mais suas eficiências e o desenvolvimento de novos fulerenos e o aprimoramento da morfologia da camada ativa (por ex: aditivos, recozimento) são algumas das estratégias atualmente adotadas.

Nesta tese, 16 novos aceitadores de N-metil-fulleropirrolidina, com base nos fulerenos C_{60} (8) e C_{70} (8), foram sintetizados (reação de Prato). A funcionalização do C_{70} produz uma mistura de 4 regioisômeros que têm níveis diferentes de HOMO / LUMO, conforme determinado pelos cálculos de DFT. Os 16 derivados de fulereno foram testados em células solares *BHJ* com o polímero de baixo intervalo de banda PffBT4T-2OD. Os diferentes grupos pendentes ligados às N-metil-fulleropirrolidinas consistiram em grupos fenil (capítulo II) e grupos tiofeno e carbazol (capítulo III).

Para ambos os conjuntos, os níveis de energia HOMO / LUMO correspondentes foram determinados por voltametria cíclica. Embora vários dos aceitadores de fulleropyrrolidina sintetizados tenham níveis LUMO mais favoráveis (mais altos) do que o $PC_{71}BM$ padrão, quando testados em células solares baseadas em PffBT4T-2OD, eles originam dispositivos com desempenho mais baixo do que os dispositivos de referência baseados no $PC_{71}BM$. Além disso, os dispositivos baseados em C_{60}-fulleropirrolidinas apresentam, em geral, melhores desempenhos fotovoltaicos do que os dispositivos correspondentes baseados em C_{70}-fulleropyrrolidinas (desordem estrutural e energética introduzida pela mistura de regiosômeros dos derivados C_{70}).

O efeito de diferentes aditivos na morfologia e desempenho dos OPVs baseados em PffBT4T-2OD: $PC_{71}BM$ é investigado no Capítulo IV. Alguns aditivos possuem efeitos antagonistas: alguns melhoram o PCE; outros diminuem o PCE em ~ 30% e outros eliminam qualquer PCE. A dispersão de raios-X de ângulo amplo de incidência rasante (GIWAXS) revela uma clara variação gradual na cristalinidade dos sistemas ao alterar o aditivo entre as duas situações extremas de PCE máximo (1-cloronaftaleno) e PCE nulo (hexadecano). A dispersão de neutrões a baixos angulos (SANS) revela que a morfologia de dispositivos com PCE ~ 0% é composta por grandes domínios de fase com comprimentos de correlação ~ 30 nm, ou seja, muito maiores que o comprimento típico de difusão do excitão em semicondutores orgânicos.

Palavras chave: Fullerenos, *N*-methyl-fulleropirrolidina, OPVs, PCE

Table of Contents

List of Figures

AFM	Atomic Force Microscopy
AN	*p*-anisaldehyde
BHJ	Bulk-heterojunction
BDT	Benzodithiophene
CB	Chlorobenzene
CT	Charge transfer States
CLN	1-chloronaphthalene
CBA	*o*-chlorobenzaldehyde
D:A	Donor:Acceptor
DAB	Debye-Anderson-Brumberger
DB	Debye-Bueche
DIF-ful-C_{60}	Trifluoromethyl derived fulleropyrrolidine
DIO	1,8-diiodooctane
DPE	Diphenyl ether
E_g	Bandgap
EWG	Electron withdrawing group
FA	Formic acid
FF	Fill factor
GI-WAXS/GI-SAXS	Grazing Incidence Wide and Small Angle X-ray Scattering
HD	Hexadecane
HTL/EBL	Hole transport layer/electron blocking layer
HOMO	Highest occupied molecular orbital
HSP	Hansen Solubility Parameters
ICBA	1',1'',4',4''-tetrahydrodi [1,4] methanonaphthaleno[5,6]fullerene-C_{60}
ITO	Indium tin oxide
J	Current flow in the external load
J_{ph}	Photocurrent generation
J_{sc}	Short-circuit current
LUMO	Lowest unoccupied molecular orbital
L_D	Exciton diffusion length
M_n	Molecular weight
MN	1-methylnaphthalene
NF	Non-fullerene
NEXAFS	Near-Edge X-ray Absorption Fine Structure
NCBA	Dihydronaphthyl-based C_{60} bis-adduct
NMP	N-methyl-pyrrolidone
NIR	Near-infrared
ODT	1,8-octanedithiol
OPVs	Organic photovoltaics

PCE	Power conversion efficiency
$PC_{61}BM$	[6,6]-Phenyl-C_{61}-butyric acid methyl ester
$PC_{71}BM$	[6,6]-Phenyl-C_{71}-butyric acid methyl ester
PDI	Polydispersity
PEDOT:PSS	Poly(3,4-ethylenedioxythiophene)-poly(styrenesulfonate)
PEIE	Polyethylenimine ethoxylated
PffBT4T-2OD	((poly[(5,6-difluoro-2,1,3-benzothiadiazol-4,7-diyl)-alt-(3,3‴di(2-octyldodecyl)2, 2′;5′,2″;5″,2‴-quaterthiophen-5,5‴-diyl)
PFN	(Poly[(9,9-bis(3'-(N,N-dimethylamino)propyl)2,7-fluorene)-alt-2,7-(9,9-dioctylfluorene)])
PO	1-phenyloctane
PTB7	poly[[4,8-bis[(2-ethylhexyl)oxy] benzo[1,2-b:4,5-b']dithiophene-2,6-diyl][3-fluoro-2- [(2-ethylhexyl) carbonyl]thieno[3,4-b]thiophenedi-yl]]
PTB7-Th	poly[4,8-bis(5-(2-ethylhexyl)thiophen-2-yl)benzo [1,2-b;4,5-b']dithiophene-2,6-diyl-alt-(4-(2-ethylhexyl)-3-fluorothieno[3,4-b]thiophene-)-2-carboxylate-2-6-diyl)]
P3HT	Poly(3-hexylthiophene-2,5-diyl)
RSoXS	Resonant Soft X-Ray Scattering
R_s	Series resistance
R_{sh}	Shunt resistance
SANS	Small Angle Neutron Scattering
SAXS	Small-Angle X-ray Scattering
SCLC	Space-charge-limited current
SH-na	1-naphthalenethiol
SLD	Scattering length densities
TA	Transient Absorption
TEM	Transition Electron Macroscopy
TPV	Transient photovoltage
TT	Thienothiophene
V	Applied voltage
V_{ext}	External applied voltage
o-DCB	1,2-dichlorobenzene

Chapter I. Introduction

The work reported in this chapter is based in the review article "*Recent Developments in the Optimization of the Bulk Heterojunction Morphology of Polymer: Fullerene Solar Cells, Materials, 11(12):2560,* ***2018****"*.

Organic photovoltaics (OPVs) represent a promising approach to generate renewable energy. Compared with currently available technologies, OPVs can be easily manufactured over much larger areas, on lightweight plastic substrates with high flexibility, using high-throughput roll-to-roll (R2R) processing technologies [1-6]. These capabilities strongly suggest that OPVs will enable large reductions in module fabrication cost and a consequent reduction on the energy payback time. The low production costs associated with OPVs might be the key for opening solar energy to new markets such as, for example, in rural communities and developing countries with poor transmission infrastructures by allowing people to invest and generate their own electricity. On the other hand, gadget market, in a low power, low cost energy conversion and wearable structure incorporation, are perhaps the most suitable application.

Although the progress in OPVs has been slower than for example in perovskite solar cells, the efficiency of single junction polymer solar cells has been increasing steadily in the last 10-15 years, evolving from 5 % in 2005 to above 16 % in 2018[7], and tandem cells have reached an efficiency, above 17 % [8]. Criteria such as efficiency, lifetime and cost, need to be satisfied to successfully commercialize large scale organic photovoltaics, but considering the steady progress that has been happening in the field, the future of the technology looks bright.

Polymer solar cells were dominated, for over two decades, by donor: acceptor blends based on fullerene acceptors. However, due to rapid developments in non-fullerene (NF) small molecule acceptors, in recent years this new acceptors have outperformed the fullerene ones and a large number of reviews have recently addressed the application of this newer type of acceptors in OPVs [9-14]. Despite this, the research activity in the field of fullerene-based polymer solar cells remains very intense and important developments have occurred in the last few years.

In this introducing chapter, we will focus mainly on the efforts performed over the last three years to improve the bulk-heterojunction (BHJ) morphology and the efficiency of small active area (typically < 15 mm^2) polymer:fullerene solar cells based on three of the most recent and highest efficiency low bandgap polymers, namely PTB7, PTB7-Th (also known as PBDTTT-EFT) and PffBT4T-2OD.

These studies include either changing the morphology using different processing strategies (different solvents and additives; different thermal treatments; different donor: acceptor ratios; etc.) or changing the morphology using other fullerenes different from the standards $PC_{71}BM$ and $PC_{61}BM$.

Strategies to improve the morphological stability of the bulk-heterojunction are also reported. As a benchmark for high performance, when considering studies involving the standard fullerenes $PC_{71}BM$ and $PC_{61}BM$, mostly research works reporting power conversion efficiencies (PCE) of 8 % or higher are reviewed. This requirement is relaxed when considering studies involving other fullerenes.

1.1 Device architectures

OPV devices can be typically manufactured with three different architectures, as sketched in Figure 1: standard (normal); inverted and tandem.

The device architecture of a normal or standard device is shown in Figure 1.1a. In this configuration, ITO is usually coated with a hole transport layer/electron blocking layer (HTL/EBL) of poly(3,4-ethylenedioxythiophene)-poly(styrenesulfonate) (PEDOT:PSS). The BHJ layer is coated on top of the HTL and finally a low work function metal electrode (usually, calcium and aluminium) is deposited on top for collecting the electrons generated in the BHJ (cathode). Suitable improvement in the cathode can also be done by using dielectric materials like LiF that promote a remarkable decrease in the electrode work function by tunnelling process. The exposure of the acidic PEDOT:PSS to ITO has been reported as a potential stability problem, especially at high temperatures and high relative humidities.

Although the standard geometry is still the most widely used, its limited operational lifetime is a disadvantage. Compared to the standard device, the inverted OPV configuration shown in Figure 1.1b has some associated advantages. In this configuration, the ITO acts as an electron collector (cathode) and is usually coated with a transparent metal oxide layer like zinc oxide or titanium dioxide. The active BHJ layer is deposited on top of the metal oxide layer, followed by a HTL (usually PEDOT:PSS) and the device is finalized with the deposition of a high work-function metal anode. Compared to the normal structure, the inverted structure has the advantage of allowing the use, as top anode, of an ambient stable high work-function metal such as gold (Au), silver (Ag) and copper (Cu), which can be deposited under normal ambient atmosphere conditions using scalable deposition technologies such as inkjet printing [15-17]. A recent and extensive review on this particular OPV device architecture can be found elsewhere [18].

The device architecture of a tandem device is represented in Figure 1.1c. The tandem architecture integrates two or more sub-cells, integrating photoactive layers with complementary absorption spectra, stacked in series. The main advantage of the tandem architecture, compared to the single-junction architecture, is that it can maximize the proportion of the solar irradiation that is absorbed and used to generate electricity. A recent study suggests that OPVs with PCE > 17% can be obtained using highly optimized tandem architectures [8].

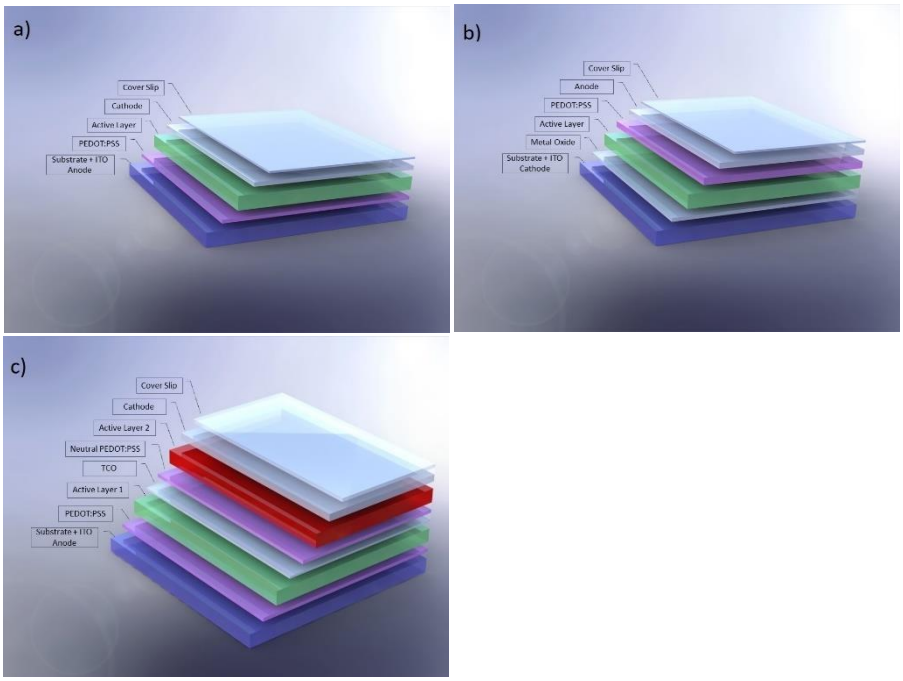

Figure 1. 1. Architectures used in the construction of OPV devices: (a) Standard (Normal); (b) Inverted and (c) Tandem.

1.2 Relationship between Nanoscopic and Macroscopic Device Physics

The first OPVs devices ever reported was in the 1980s, but their results were discouraging [19]. Improvement was achieved with the first generation of highly soluble polymers such as polythiophenes, polyphenylenevinylenes and their derivatives, but the lack of quality, reproducibility and purity lead to a poor quality of device performance. For these early OPV devices the main reason for the low efficiency became clear when a greater degree of understanding of the nature of photoexcited states in organic semiconductors was attained. Only a small fraction of these bound states separates in a simple OPV device, leading to charge generation efficiency in pristine organic semiconductors in the order 0.1% or lower. The separation of these excitons was found to be driven by the presence of defects or impurities [20]. Initial studies built on observations that coating (by evaporating fullerene on top of a spin-cast

polymer layer) the active layer increased the probability of charge separation creating a second generation with two-layer OPV (Figure 1.2).

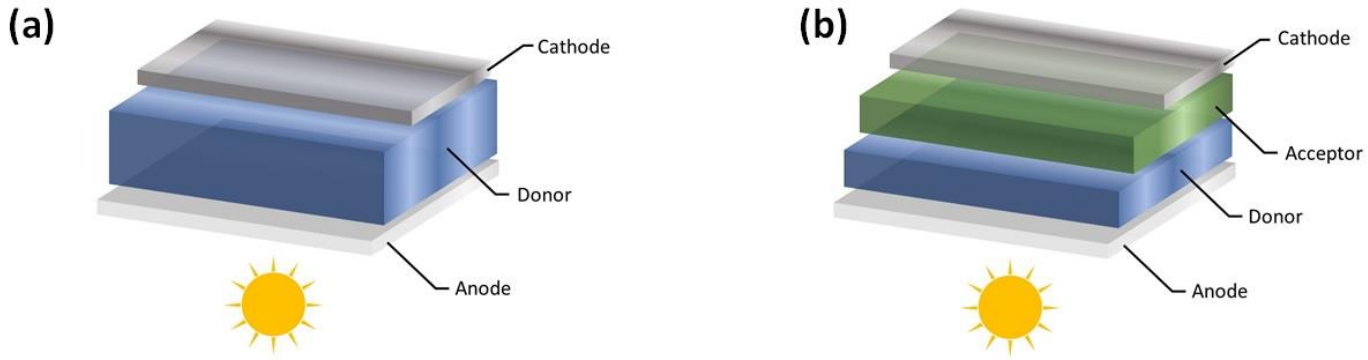

Figure 1. 2. OPV cells structures: (a) single layer device; (b) double layer device

The limited exciton diffusion length (L_D) in conjugated polymers problem was worked around with a third-generation active layer, which is composed of a blend of an electron donating polymer and an electron acceptor which can be either fullerene-based ($PC_{71}BM$, $PC_{61}BM$ or others) or a non-fullerene small organic molecule. This donor: acceptor blend is known as bulk-hetero-junction (BHJ). Figure 1.3a represents the typical band diagram for a donor: acceptor bulk-hetero-junction in an OPV device. Incident photons with energy higher than the bandgap (E_g) in both donor and acceptor but fundamentally in the donor polymer, that is, $E > E_g$, are absorbed by the BHJ causing the generation of excitons, that is, electron-hole pairs (step 1 in Figure 1.3a). Typical binding energy values for excitons are on the order of 0.5 eV or larger [21, 22]. Then, the excitons created must diffuse to a donor: acceptor interface where they dissociate efficiently into holes and electrons (steps 2 and 3 in Figure 1.3a). At this point, it is worth emphasizing that until a few years ago the LUMO-LUMO offset (ΔLUMO) between the donor and the acceptor was considered to be the driving force needed to split the tightly bound excitons and a ΔLUMO ≥ 0.3 V was regarded as the minimum necessary to ensure efficient charge transfer[23]. However, recent studies have shown that other factors also play their role and highly efficient OPVs can have ΔLUMO < 0.1 eV [24]. Finally, the separated electrons and holes must travel along the interpenetrating network towards the metal cathode and anode, respectively, where they are collected giving rise to a photocurrent and photo-voltage (step 4 in Figure 1.3a). Due to the low dielectric constant of conjugated polymers (a low dielectric constant leads to an increased difficulty of the exciton dissociation), the typical exciton diffusion length in a BHJ, i.e. the average distance an exciton can diffuse through the material before

recombination happens, is as low as ca. 10 nm [25-29], a length-scale that necessarily defines the optimal size of phase-separation for maximizing device efficiency.

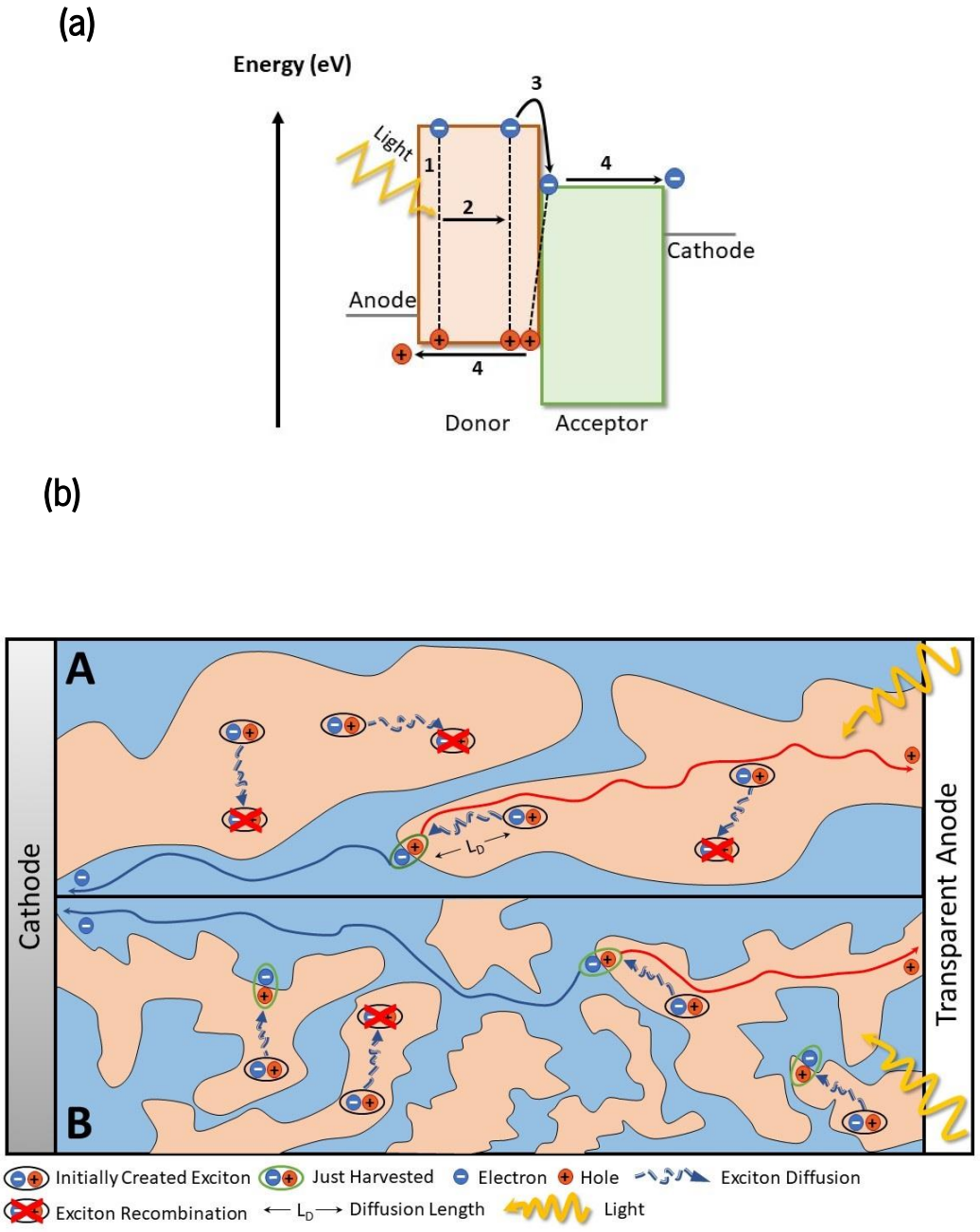

Figure 1. 3. a) Typical band diagram for a donor:acceptor bulk-heterojunction in organic solar cells: (1) Photon absorption and exciton generation; (2) exciton diffusion; (3) exciton dissociation; (4) carriers collection; **b)** Photocurrent generation processes in two bulk-heterojunctions with very different morphologies: a bad morphology (A) and a good morphology (B).

This is illustrated in Figure 1.3b where the processes occurring in two very different BHJ morphologies are represented. In the ideal morphology, most of the excitons created can find nearby (distance < L_D) a donor:acceptor interface where they dissociate generating free charge carriers and therefore the corresponding device has a high power conversion efficiency (PCE). By contrast, in the morphology with very large phase segregation most of the excitons when created are too far away (distance > L_D) from the nearest donor:acceptor interface and they recombine. Therefore, the ideal morphology for a BHJ is typically considered to be a bi-continuous and interpenetrating comb-like network morphology composed of donor-rich and acceptor-rich continuous phases, with the donor phase smallest dimension of ≈20 nm, allowing the minimization of bimolecular charges recombination. Electrical carrier mobility depends on those domains. As widely accepted, the better figures of merit result from a compromise between D:A interface total area and D:A domains bulk volume. It is worth mentioning, at this point, that different experimental techniques can be used to probe the nano-morphology of BHJs. These include: Atomic Force Microscopy [30], High Resolution Electron Microscopy [31], Near-Edge X-ray Absorption Fine Structure (NEXAFS) spectroscopy [32], Grazing Incidence Wide and Small Angle X-ray Scattering (GI-WAXS/GI-SAXS) [33], Resonant Soft X-Ray Scattering (RSoXS) [34], Spectroscopic Ellipsometry [35, 36],Neutron Reflectivity [37, 38] and Small Angle Neutron Scattering (SANS) [39-41].

1.3 Macroscopic Device Physics

Photovoltaics are fundamentally characterized by simple parameters that represents their figure of merit : V_{OC} (voltage under zero electrical current), J_{SC} (current density under zero electrical field), FF (representing the shape of J-V curve in the 4th quadrant) and η ($\frac{generated\ electrical\ power}{incident\ optical\ power}$).

Figure 1.4a shows the typical current density-potential (J-V) curve for an OPV device under dark and illumination conditions. The power conversion efficiency (PCE) of the device is the product of three figures of merit, namely short-circuit current (J_{sc}), open-circuit voltage (V_{oc}) and fill factor (FF) divided by the incident power radiation Pi, that is: $PCE = (J_{sc} \times V_{oc} \times FF)/Pi$.

Improving the figures of merit of an OPV requires a critical analysis of its macroscopic behaviour. Figure 1.4b shows the equivalent circuit for a solar cell. In this, J_{ph} is the photoinduced current density (all generated photocurrent from photon to electron energy transfer); R_s is the series resistance; R_{sh} is the shunt resistance; J is the current flow in the external load and V is the applied voltage.

The series resistance R_s originates from the bulk resistance of the active layer, the bulk resistance of the electrodes and the contact resistances of all interfaces in the device. The value of R_s determines where the current mainly flows (considering the potential range in the 4th quadrant): to the diode if R_s is high or to the external load if R_s is low. Therefore, in the fabrication of solar cells, ideally R_s should be as low as possible ($R_s \rightarrow 0$), as an effective way to improve the performance of the device. The shunt resistance R_{sh} may originate from manufacturing or natural intrinsic defects and includes current leakage from pinholes in the film, current leakage from the edge of the cell, current leakage by energy levels acting as traps or electron-hole recombination. It has the effect of dividing the current in the equivalent circuit and therefore ideally the value of R_{sh} should approach infinity so that there is no current loss in the device, that is, there is no current flow through R_{sh}.

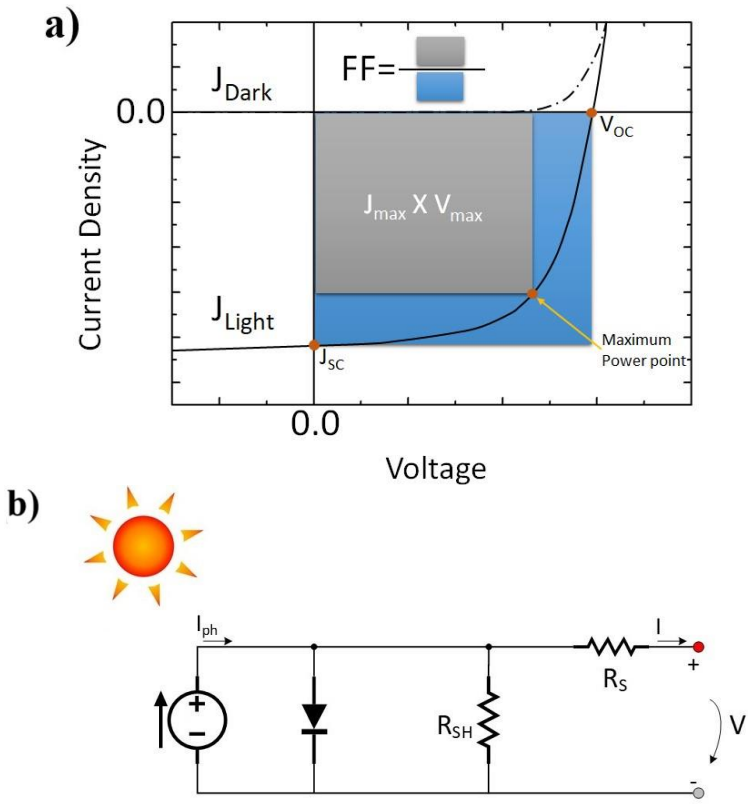

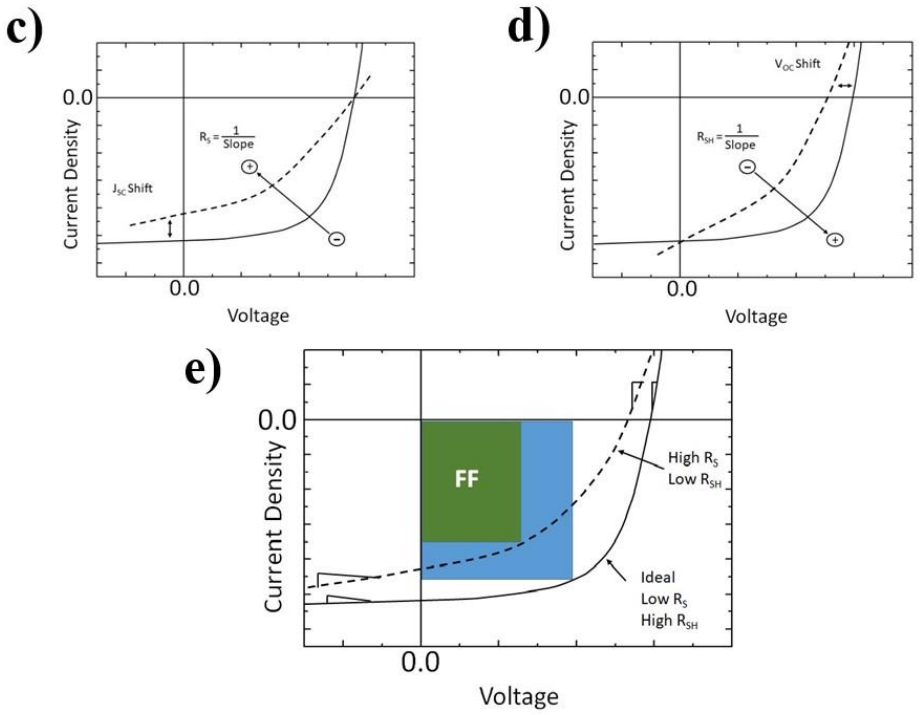

Figure 1. 4. a) Fundamental points in a solar cell I-V curve required for a full understanding of its figures of merit; b) The usual OPV equivalent electrical circuit; c) Impact of the variation of the series resistance (R_s) on *FF*; d) Impact of the variation of the shunt resistance (R_{sh}) on the *FF*; e) real I-V curve (as usually found) where both R_s and R_{sh} are not ideal.

Figure 1.4c and 1.4d represents the impact of the series resistance and shunt resistance on the fill factor, considering all the remaining parameters as constant. The FF represents how "rectangular" the J-V curve is and it characterizes how "difficult" or how "easy" the photogenerated carriers can be extracted from the solar cell. The ideal value for FF is 100% when the J-V curve is a perfect rectangle however in practice this never happens and in OPVs the FF values are typically in the range 40–80%. From Figure 1.4c it can be seen that at negative and low positive voltages the J-V curve is a straight line with slope $1/R_{sh}$; at intermediate positive voltages the J-V curve is an exponential line that is determined by the diode; and at higher positive voltages the J-V curve is another straight line with slope $1/R_s$. Therefore, to improve the FF value the shunt resistance should be as high as possible, and the series resistance should be as low as possible. It must be noted that in a real device R_s is higher than the ideal and R_{sh} is lower than the ideal. Therefore, the J-V curve as shown in Figure 1.4e is the usual. The V_{oc} [42-45] is primarily dependent on the energy difference between the LUMO level of the acceptor and the HOMO level of the donor: the higher the difference, the higher the V_{oc}. Therefore, the main strategy usually followed to increase V_{oc} consists in utilizing either fullerene acceptors with higher LUMO levels or donor polymers with lower HOMO levels. As long as the LUMO of the fullerene acceptor remains lower than the LUMO of the polymer donor by an amount sufficient to promote charge separation, raising the fullerene

LUMO level or lowering the polymer HOMO level should increase the V_{OC} and thus the PCE. The V_{OC} is prone to various loss mechanisms that affect the device efficiency, and these have recently received special attention [22, 46-48].

The J_{sc} [49-52] depends on several factors such as the amount of light absorbed, the efficiency of exciton and free charge generation, the charge-carrier mobility and the efficiency of charge extraction at the electrodes. The higher these variables are, the higher is the corresponding J_{sc} value.

The FF [53-56], as mentioned above, depends on the series resistance, shunt resistance and diode. However, these also depend on a large number of factors that interact with each other intricately and for this reason the FF is more complex and less understood than the V_{oc} and J_{sc} [48, 57-59]. Previous studies have shown that variables such as the blend composition, the blend morphology, the regioregularity of the conjugated polymer and the thickness of the BHJ influence significantly the FF affecting R_s and R_{sh} [53]. When the crystallinity of the blend layer increases, either by thermal annealing or through the use of a regioregular polymer, R_s decreases [53-56]. When the thickness of the blend layer increases, R_s increases and R_{sh} decreases [53, 60]. The quality of the two interfaces between the BHJ and the electrodes was also shown to play an important role in determining FF [53, 61]. In practice, FF depends on the J-V shape in the 4th quadrant. As the D:A junction degrades (by molecular conformation and orientation and/or energetically inappropriate levels of D:A materials) the J-V behaviour becomes more space charge limited (SCLC) dependent and the J-V curve displays a typical "s-shape." Common strategies to reduce R_s and increase R_{sh} include using buffer layers to reduce recombination [56], increasing the crystallinity of the BHJ materials [56, 62], changing the donor: acceptor mass ratios [63] and optimizing the size of phase domains in the BHJ [56, 62].

Among the several physical processes involved in the electrical power generation, the radiative (photons) absorption and charge collection at electrodes (involving the charge separation at D:A interfaces and electrical carriers transport in OPV volume) are often the most interesting for device improvement. In a simple model, the J_{sc} value should be close to the J_{Ph}, but from the equivalent electrical circuit it is easy to understand that J_{sc} decreases, in a primary way, by the effect of series resistance R_s. But, the I-V shape depends primarily on the R_{sh}. In fact, this resistance comprehends all physical effects responsible for the electrical carrier recombination from the exciton separation (charge state at interface domain) until the collection at electrodes (from the electrical charge transport in volume). The value of R_{sh} should, therefore, be as high as possible (as experimentally observed > 106 Ω). On other hand, increasing the photogenerated carriers should increase the J_{sc} value. We must therefore primarily search

for donors (polymers) with reduced (as possible) bandgap (HOMO—LUMO difference) to increase the solar light absorption in the visible spectrum.

Donor-Acceptor (D:A) interface is also a key factor in the OPV energy performance. As soon as the bonded excitons reach the D:A interface, an extremely competitive process between separation (charge transfer—CT—states) and recombination will take place, determining how much efficient will be the free (net) charge creation. Once again, this process is almost (besides energy levels) dominated by the molecular structure/conformation of the donor/acceptor materials in the active film. Regarding the bulk transport, a competitive framework between electrical carriers drift and recombination must occur. To allow the highest charge collection possible at electrodes, the drift time should be smaller as possible to a positive competition with the high probable electron-hole recombination due to the complex distribution of a high density of electrical active energy levels in the BHJ [64, 65]. As demonstrated from transient photoconductivity (see for example,[66]), the characteristic drift time is proportional to $\frac{d^3}{2\mu \mathrm{E}}$, where d is the organic layer thickness, μ the electrical carrier mobility and $E_i = (V_{OC} - V_{ext}) \times d^{-1}$ the internal electrical field, on the V_{oc} and the external applied voltage (V_{ext}). An important aspect is that the drift time is inversely proportional to the electrical carrier mobility. Increasing the degree of structural ordering of the D–A matrix, an increase of electrical charge mobility is expected (hopping process facilitated) with a consequent decrease of the drift time. This must allow the electrical carriers to drift towards electrodes before they can recombine, increasing the FF. Morphological ordering of the active layer is therefore desired. By the other side, the disorder molecular conformation gives rise to a high density of intrinsic defects that can act as traps for the electrical carriers under space charge conditions. The immediate consequence is the noticeable decrease of the electrical carrier mobility.

All the referred parameters are intrinsically related to the donor and acceptor compounds used and their interaction in the solid state. Optimization and incrementation of these parameters require a deep comprehension of the device operation and photocurrent generation (J_{ph}) as well as its limitations[67].

1.4 Polymers and fullerenes

In polymer:fullerene solar cells the role of light absorption has traditionally been assigned to the polymer donor, for the simple reason that fullerenes do not absorb strongly in the visible and near-infrared region of the spectrum. For this reason, a large amount of research in the OPV field has focused on synthesizing new polymers with a small optical bandgap E_g [68-70]. Besides the low optical bandgaps to broaden the absorption range into the infrared spectrum, polymers used as electron donors in polymer:fullerene solar cells should exhibit suitable LUMO energy levels for efficient electron transfer to the fullerene moieties and crystalline characteristics to ensure good charge mobility [68]. Three of the most recent and successful small band gap copolymers that, when compared with the "old reference" poly(3-hexylthiophene-2,5-diyl) (P3HT), E_g ca. 2.1 eV [71], have a smaller energy gap (allowing more of the sun's spectral emission to be harvested) and an higher ionization potential (leading to an increased V_{oc} and thus greater PCE) are: i) poly[[4,8-bis[(2-ethylhexyl)oxy] benzo[1,2-b:4,5-b']dithiophene-2,6-diyl][3-fluoro-2- [(2-ethylhexyl) carbonyl]thieno[3,4-b]thiophenedi-yl]], commonly known as PTB7 (E_g ca. 1.6 eV); ii) poly[4,8-bis(5-(2-ethylhexyl)thiophen-2-yl)benzo [1,2-b;4,5-b']dithiophene-2,6-diyl-alt-(4-(2-ethylhexyl)-3-fluorothieno[3,4-b]thiophene-)-2-carboxylate-2-6-diyl)], commonly known as PTB7-Th or PBDTTT-EFT (E_g ca. 1.6 eV) and iii) ((poly[(5,6-difluoro-2,1,3-benzothiadiazol-4,7-diyl)-alt-(3,3‴di(2-octyldodecyl) 2, 2′;5′,2″;5″,2‴-quaterthiophen-5,5‴-diyl), commonly known as PffBT4T-2OD (E_g = 1.65 eV). The E_g values indicated are only approximate as they depend on the polymer molecular weight [72].

Figure 1.5 depicts the chemical structure of these three very popular "post-P3HT" conjugated polymers used in OPVs. In this review only devices based on these three polymers (PTB7 [73], PTB7-Th and PffBT4T-2OD) will be discussed.

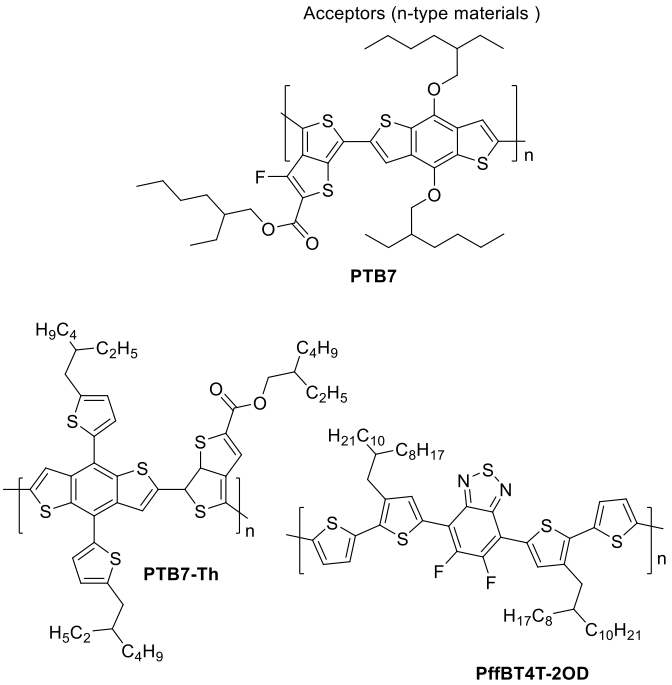

Figure 1. 5. Chemical structures of the polymer donors used in OPVs.

Buckminsterfullerene C_{60} was the first fullerene used in an OPV device, in the seminal work by Sariciftci *et al.* [74], where the authors report the photo-induced electron-transfer from a conducting polymer to C_{60}. However, the very low solubility of C_{60} in common organic solvents makes it very difficult to process and therefore, soon after its introduction in the OPV field, the strategy of functionalizing C_{60} with solubilizing moieties was adopted. For this reason the fullerenes $PC_{61}BM$ [75, 76] and its analogue [6,6]-Phenyl-C_{71}-butyric acid methyl ester ($PC_{71}BM$) [77] soon emerged as the two most widely used electron accepting materials in OPVs. These two fullerenes, $PC_{61}BM$ and $PC_{71}BM$, are now utilized as reference acceptors for all kinds of other fullerene acceptors, because of their good solubility, high electron mobility and high chemical stability. A key difference between $PC_{61}BM$ and $PC_{71}BM$ is the ellipsoidal shape of the latter, as compared to the more spherical C_{60} molecule [78]. The lower symmetry and more extended conjugation of C_{70} enables energetic transitions that are forbidden in C_{60}, leading to a broader photo-absorption profile in the visible region of the solar spectrum [79]. This allows increased photon harvesting and a potentially higher photocurrent for devices using $PC_{71}BM$ rather than $PC_{61}BM$, an important attribute that has brought the C_{70} analogue to the forefront of OPV research (despite its higher cost).

Although $PC_{61}BM$ and $PC_{71}BM$ are the most commonly used fullerenes in organic solar cells, several other modified fullerenes such as those depicted in Figure 1.6 are found in literature with specific

characteristics and have been assessed as acceptors in BHJs. This will be discussed below in combination with the corresponding polymers depicted in Figure 1.5.

As mentioned above, the V_{oc} of a polymer:fullerene solar cell increases when the energy difference between the LUMO level of the fullerene and the HOMO level of the polymer increases (Figure 1.3a). Therefore, using fullerenes with a higher LUMO level results in devices with higher V_{oc} values. A common synthetic approach used to increase the LUMO level of fullerenes consists in adding more substitutes to the fullerene cage in order to obtain fullerene multiadducts. Such strategy reduces the number of double bonds and the level of conjugation in the fullerene molecule and therefore increases the corresponding LUMO level. The fullerene bisadduct 1',1'',4',4''-tetrahydrodi [1,4] methanonaphthaleno[5,6]fullerene-C_{60}, commonly known as ICBA (Figure 1.6), has been the most popular bisadduct used in solar cells. However, as it will be seen along this review, most often although fullerene bisadducts such as ICBA produce devices with higher V_{oc} values, the corresponding PCE values are lower than those of reference devices with $PC_{71}BM$ and $PC_{61}BM$. The reasons for this are that fullerene multiadducts usually have much lower electron mobilities than monoadducts and this impacts the device's J_{sc} and FF adversely. Furthermore, these multiadducts are typically mixtures of several isomers and the small differences in the LUMO levels of these isomers contribute to increase the probability of exciton recombination, and thus further decrease J_{sc} (and indirectly the remaining parameters).

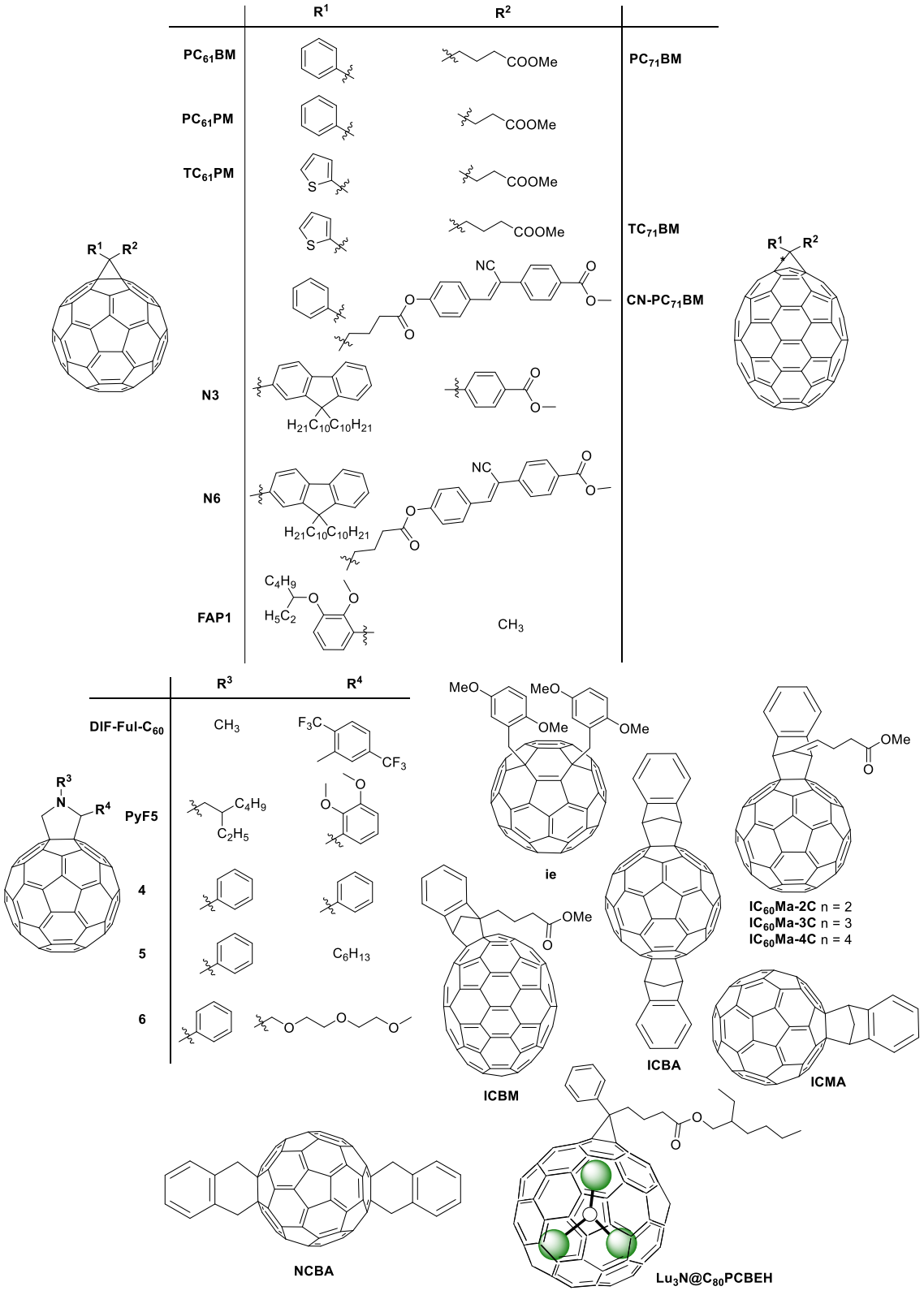

Figure 1. 6. Representative chemical structures of fullerene acceptors used in OPVs.

1.5 Additives

The processing conditions used in the preparation of a BHJ play a crucial role in the corresponding morphology and this also plays a critical role on the corresponding device energy efficiency. One of the most important issues in OPVs is the high probability of intrinsic defects formation due to the molecular disorder conformation. Additionally, molecular polymer stacking has a strong influence in the electrical behavior. The relevant situations strongly effect the carrier mobility under space charge conditions giving rise to overall decrease of performance. Therefore, decreasing such defects and promoting an efficient polymer molecular stacking, are, regardless other factors, important keys in OPV performance since these questions are strongly morphological dependent.

Several different approaches have been tested to optimize the morphology from the well-known thermal annealing process in the old P3HT based OPVs to the current and interesting process that is the inclusion of chemical additives.

The use of additives [80, 81] is by far the most popular processing methodology used to optimize the morphology and increase device performance in OPV devices using the small band gap copolymer systems PTB7, PTB7-Th and PffBT4T-2OD. This methodology consists in adding, before BHJ thin film deposition, a small amount of a high boiling point additive to the photovoltaic ink solution, typically 3% v/v. The most popular additives include 1,8-diiodooctane (DIO), 1-chloronaphthalene (CLN) and 1,8-octanedithiol (ODT), among others. In many instances, additives can more than duplicate the power conversion efficiency of the corresponding devices.

Despite the several studies performed using additives to improve the morphology of OPVs, these have been largely driven by empiricism as there is still a lack of fundamental scientific understanding of the relationship between the processing additive used, the resultant BHJ morphology and the corresponding device efficiency.

The primary role of additives such as DIO was, until recently, the object of some debate in the field. In a 2011 highly cited work, Lou *et al.* [82] used small-angle X-ray scattering (SAXS) to study the structure of $PC_{71}BM$ in chlorobenzene (CB), in a concentration of 15 $mg{\cdot}mL^{-1}$, and found that the addition of a small amount of DIO (3% v/v) to CB change the scattering signal of the fullerene solution. Their model-based analysis of the scattering data led them to interpret these results as evidence that the initial chlorobenzene solution, without DIO, contained $PC_{71}BM$ aggregates and that after the addition of DIO these were completely eliminated from solution due to an increased solubility of $PC_{71}BM$ in the CB:DIO

solution. This elimination of $PC_{71}BM$ agglomerates was hypothesized by Lou *et al.* to be the reason for the efficiency improvement in the OPV devices, when spin-coated with the polymer PTB7, as a result of the improved intercalation of the fullerene.

However, some more recent studies have cast considerable doubts upon this work by Lou *et al.* In 2014, Burgués-Ceballos *et al.* [83] reported that the solubility of $PC_{71}BM$ in CB was 207 mg·mL^{-1}, that is, much higher than the concentration of the solution (15 mg·mL^{-1}) in which Lou *et al.* [82] reported the presence of $PC_{71}BM$ agglomerates. Very recently Bernardo *et al.* [84, 85] carried out a full study aiming to understand the solution state of $PC_{71}BM$ in CB and CB with 3% DIO. Using both SAXS and SANS, these authors have shown that there is no change in the dissolution state of $PC_{71}BM$ upon the addition of DIO and in fact as shown in Figure 1.7, there is no aggregation of $PC_{71}BM$ in solution with or without the additive, contrary to the analysis previously reported by Lou *et al.*

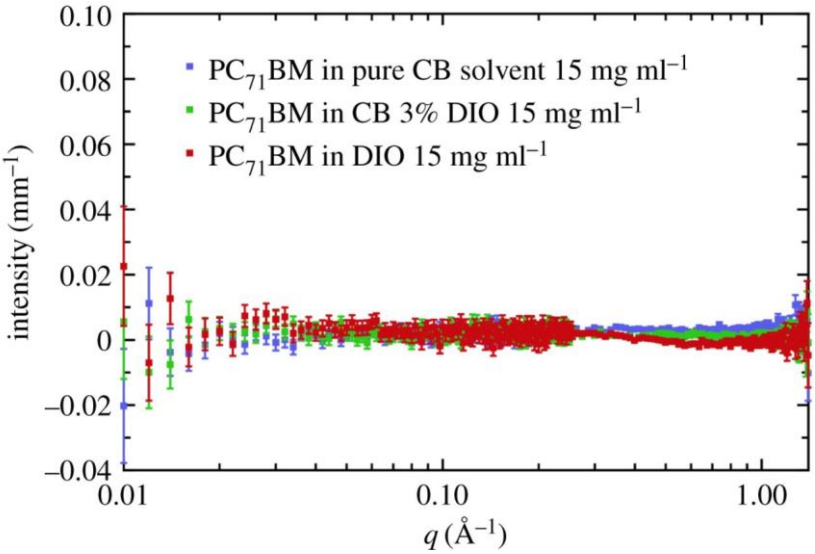

Figure 1. 7. SANS solution data for $PC_{71}BM$ at a concentration of 15 mg ml^{-1} in pure CB, CB with 3% v/v DIO, and also in pure DIO. Reprinted with permission from Ref. [84].

Furthermore, by studying the drying process of the spin-coated films using optical interferometry, these authors concluded that the high boiling point additive DIO plays its role by staying in the film after the spin coating process has finished. This allows increasing the molecular mobility of the DIO solvated fullerene on a much longer timescale than that of the film without DIO.

A similar conclusion was reached by Zhang *et al.* [40] studying PffBT4T-2OD:$PC_{71}BM$ based devices. Using spectroscopic ellipsometry, these authors showed that after spin-coating, a BHJ film processed using DIO is much thicker than a BHJ film processed without DIO, which clearly indicates that DIO largely remains in the film. Furthermore, upon annealing, the thickness of the film processed with DIO decreases

continuously due to DIO evaporation until reaching a thickness similar to the film processed without DIO (Figure 1.8a). Additionally, using SANS, these authors demonstrated that in these PffBT4T-2OD:$PC_{71}BM$ devices, DIO improves the efficiency as a result of the coarsening of the fullerene phase domains in the BHJ film induced by the transient plasticisation of the film during drying (Figure 1.8b).

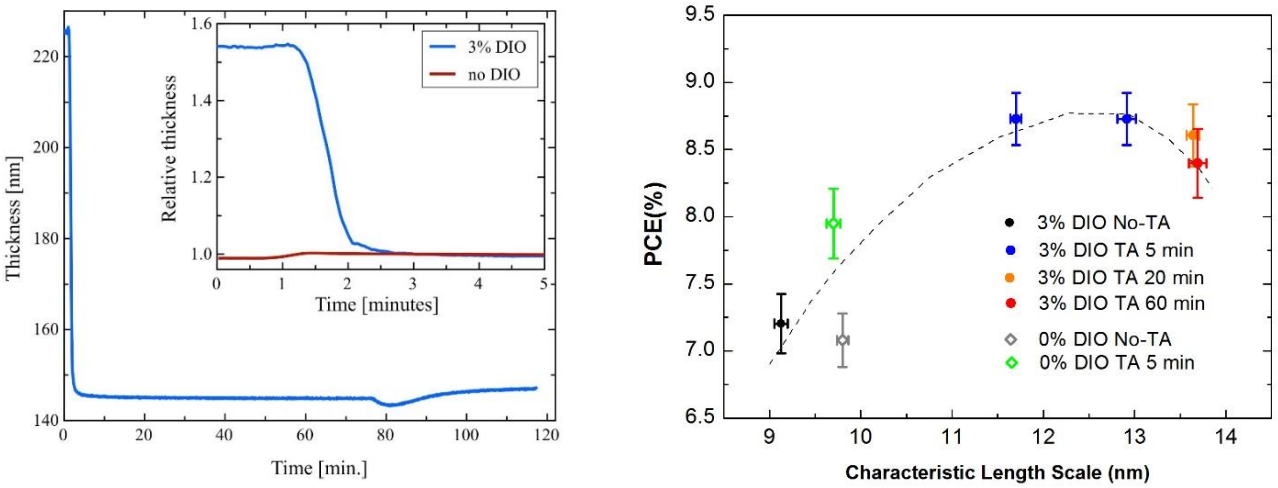

Figure 1. 8. (a) Dynamic spectroscopic ellipsometry data for the isothermal annealing of a PffBT4T-2OD:$PC_{71}BM$ blend film annealed at 100 °C. The heating stage was at 100 °C at time t = 1 min. The inset shows a zoomed in region at the beginning showing the dramatic drop in thickness within the first minute of being at temperature; (b) Correlation between PCE and characteristic length scale for samples processed in different ways, i.e. with/without DIO and with/without annealing. Reprinted with permission from Ref. [40].

1.6 Devices based on PTB7

PTB7 (Figure 1.5) is a copolymer containing an alternating electron rich benzodithiophene (BDT) unit and an electron deficient thienothiophene (TT) unit [73]. In this chapter Section 1.6.1 presents seminal research works on the improvement of the BHJ morphology and efficiency of PTB7:$PC_{71}CM$ (or $PC_{61}BM$) solar cells, discussing afterwards some of the most recent developments in this topic. Section 1.6.2 addresses the most recent and relevant studies involving BHJs of PTB7 with other fullerenes. In the end of this chapter, a compilation table (Table 1.1) summarizes the most relevant and most recent device efficiencies obtained with PTB7-based solar cells.

1.6.1 PTB7 devices with $PC_{61}BM$ and $PC_{71}BM$

The use of the polymer PTB7 in BHJ solar cells was first reported in 2010 in a seminal work by Liang *et al.* [86]. The best devices reported in this work were prepared with a D:A weight ratio of 1:1.5, using CB as solvent with 3 vol% of DIO as additive and exhibited a PCE of 7.40 % being, at the time, the first polymer solar cell showing a PCE over 7 %. Zhou *et al.* [87] reported short after a PCE to 7.94% after treating similar devices with methanol. Liu *et al.* [72] showed that it was possible to push the PCE values to 8.5 % using a PTB7 with high molecular weight (M_n) of 128 kg/mol and a low polydispersity (PDI) of 1.12. He *et al.* [88] fabricated devices, in the normal and inverted geometries, using the polymer PFN (poly[(9,9-bis(3'-(N,N-dimethylamino)propyl)2,7-fluorene)-alt-2,7-(9,9-dioctylfluorene)]) as a surface modifier to optimize the electrode work-function and increase the photocurrent. The reported PCE for the conventional and inverted geometries were respectively 8.24 % and 9.15 %.

In the last three years, the optimization of the efficiency of PTB7:$PC_{71}BM$ (or $PC_{61}BM$) devices progressed actively by improving the morphology of the BHJ.

Jhuo *et al.* studied the effect of new additive 1-naphthalenethiol (SH-na) on the morphology of PTB7:$PC_{71}BM$ BHJs. This additive was tested for bulk and surface morphology control, via a conventional spin-casting process and a novel SH-na solution dipping treatment [62]. Five different sets of devices were tested, namely: (i) reference device without additive; (ii) reference device with the conventional spin-cast DIO additive; (iii) device with spin-cast SH-na additive; (iv) device without spin-cast additive, but with solution dipped SH-na additive, and (v) device with both spin-cast SH-na additive and solution dipped SH-na additive. The top performing devices were those prepared by spin-casting SH-na additive and solution dipped SH-na additive and these exhibited a PCE of 8.42 %, a V_{oc} of 0.79 V, a J_{sc} of 15.7 mA.cm^{-2} and a FF of 0.70, which contrasted deeply with the corresponding values for a standard device without additive that were, respectively, 3.68 %, 0.70 V, 11.4 mA·cm^{-2} and 0.46.

The BHJ morphology and photovoltaic performance of PTB7:$PC_{71}BM$ devices was studied upon adding a series of bromine-terminated additives with different chain lengths in the range from 1,2-dibromoethane to 1,8-dibromooctane [89]. Despite the chemical similarity between the different additives, they were found to produce very different morphologies. Compared to devices without additive (PCE of 3.57 %), devices processed with the additive 1,4-dibromobutane originated the highest performances, although these were modest (PCE of 5.53 %). Interestingly, among all the additives tested 1,4-dibromobutane exhibited the closest solubility parameter to that of the classical DIO additive.

Others [90] tested the effect of additives and additive mixtures (including DIO, CLN and ODT) in the performance of PTB7:$PC_{61}BM$ devices prepared from solutions using chloroform as host solvent. The best devices reported had a PCE of 6.41 % and were obtained using a mixture of DIO and CLN as additive.

The use of a new solvent additive – diphenyl ether (DPE) – that facilitates the fabrication of thick (180 nm) PTB7:$PC_{71}BM$ BHJ layers and that, compared with additive-free devices, triplicates the PCE from 1.75 % to 6.19 % due to an increase in the crystallization of PTB7 that facilitates charge transport over longer distances, was reported by Zheng *et al.* [91]. Very recently, the same team reported [92] a novel binary solvent additive of DPE:DIO that, when added in the proportion of 2 vol.% DPE + 3 vol.% DIO to a CB ink solution, boosts the efficiency of inverted PTB7:$PC_{71}BM$ devices to over 9.5%, being this among the best results ever reported in the literature for PTB7-based devices. According to the authors, this improvement was due to the synergistic effect of both additives, with DPE promoting the crystallization of PTB7, and DIO favouring the phase separation between PTB7 and $PC_{71}BM$. This work highlighted the great potential of binary solvent additives for improving the performance of OPVs.

The effect of diiodoalkane additives with variable alkyl chain length, from 1,4-diiodobutane to 1,10-diiodododecane, on the performance of inverted PTB7:$PC_{71}BM$ devices was studied by Zhao *et al.* [93]. Compared with standard devices prepared from chlorobenzene ink solutions without additive (PCE of 2.3 %), all the diiodoalkane additives tested improved considerably the efficiency. However, the best performing devices with a PCE of 8.84 % were still obtained using the classical DIO (3 vol%), which shows that DIO has the optimal alkyl chain length to maximize the performance of these devices. Impedance spectroscopy results indicate that DIO maximizes the charge transfer from the BHJ to the electrode by minimizing the recombination rate at the donor/acceptor interface and increasing the charge carrier lifetime.

Formic acid (FA) was presented by Li *et al.* [94] as a novel additive capable of improving the efficiency of PTB7:$PC_{71}BM$ solar cells when used in combination with DIO in ink solutions using CB as host solvent. The device prepared using a solution prepared with 6 vol.% FA and 3 vol.% of DIO showed the best PCE of 9.04 % compared with a PCE of 7.25 % for the control device with 3 vol.% DIO and no FA. This increase in PCE observed upon the addition of FA was due to a dramatic increment of J_{sc} from 14.57 $mA \cdot cm^{-2}$ in the control device, to 24.11 $mA \cdot cm^{-2}$ in the devices with FA.

Chen et al. [95] introduced *o*-chlorobenzaldehyde (CBA) as a new solvent additive. PTB7:PC71BM devices were tested with different amounts of CBA and simultaneously standard devices without additive and devices with the standard DIO were also produced to be used as reference devices. Without any additive, the best devices exhibited a PCE of 3.87 %, and with DIO additive the best devices attained a

PCE of 7.53 %. However, the most efficient devices were those processed with CBA (5 vol %), which achieved an impressive PCE of 9.11 %. Charge carrier transport properties, determined with space-charge-limited current (SCLC) measurements, showed that the best devices processed with CBA had more ideal hole mobility (μ_h) and electron mobility (μ_e) than the other best devices: without any additive, $\mu_h = 7.3 \times 10^{-5}$ $cm^2V^{-1}s^{-1}$, $\mu_e = 5.9 \times 10^{-5}$ $cm^2V^{-1}s^{-1}$ and μ_h/μ_e =1.24; with DIO, $\mu_h = 8.4 \times 10^{-5}$ $cm^2V^{-1}s^{-1}$, $\mu_e = 1.6 \times 10^{-4}$ $cm^2V^{-1}s^{-1}$ and μ_h/μ_e =0.53; with CBA, $\mu_h = 1.3 \times 10_{-4}$ $cm^2V^{-1}s^{-1}$, $\mu_e = 4.0 \times 10^{-4}$ $cm^2V^{-1}s^{-1}$ and μ_h/μ_e = 0.33. Transient photovoltage (TPV) measurements revealed that devices processed with CBA displayed longer charge carrier lifetimes and shorter charge extraction times than devices processed with DIO or without additives. These are consistent with the higher FF and J_{sc} observed in the devices with CBA additive. These results can be a proof consequence of better local molecular conformation, due to a decrease of disorder that exhibits typically low electric carrier mobility. Besides producing devices with higher efficiencies, this work has also shown that CBA, when compared to DIO, has the additional advantage of possessing a much lower boiling point (b.p.= 212 °C vs b.p.= 350 °C for DIO), but still sufficiently higher than CB (b.p. = 132 °C). Thus, contrary to DIO, which requires high-vacuum post-treatments in order to be completely removed from the films, CBA evaporates during thin film processing, being therefore compatible with roll-to-roll processing.

Another topic related to the bulk-heterojunction, which has attracted some attention in recent years, is the morphological and lifetime stability of the PTB7-based solar cells.

The effect of two different host solvents (CB and ortho-xylene) containing 3 vol% DIO additive, on the morphology, efficiency and stability of inverted PTB7:PC_{61}BM devices was studied by Ciammaruchi *et al.* [96]. Devices processed with both solvents exhibited similar PCEs (7.54 % with CB and 7.05 % with ortho-xylene). Lifetime stability studies suggests that a complete removal of solvent traces as well as a proper UV filtering can largely improve the stability of cells processed with ortho-xylene and therefore eliminate the halogenated solvents from the process.

Dkhil *et al.* [97] reported that, depending on the fullerene size, there is a large difference in the morphological stability of PTB7:fullerene blends as a function of temperature. After 1 h of annealing at 140 °C, the PTB7:PC_{61}BM films showed the formation of fullerene crystals that increase in size and number after further annealing for 1 day. In contrast, PTB7:PC_{71}BM blends did not show any fullerene crystals visible by optical microscopy after one day thermal annealing at 140 ◦C. This clearly shows that there is a strong improvement in thermal stability of PTB7 polymer blends using the larger fullerene derivative PC_{71}BM. Furthermore, PTB7 devices with PC_{71}BM exhibited a remarkably high temperature

stability during permanent annealing at 140 ◦C for several days, which can be directly related to the intrinsically stability of the polymer blend.

The UV-induced degradation of PTB7:$PC_{71}BM$ solar cells in an inert atmosphere was studied by Bartesaghi *et al.* [98] who concluded that this degradation is due to a photochemical reaction that requires the presence of both PTB7 and $PC_{71}BM$. However, the exact mechanism of the photochemical degradation could not be determined.

1.6.2 PTB7 devices with other fullerenes

As primary indicated and spite of new non-fullerenes acceptors, the traditional acceptor based on fullerenes still being an interesting material for OPVs. In fact, the fullerene-based materials have been very well studied and it is relatively straight forward to design new derivatives structures that in a first approximation can be particularly interesting for OPVs. Besides such idea, is still paramount to try to explain the BHJ process framework.

A new fullerene acceptor (ICBM in Figure 1.6) was synthesized by He *et al.* using the cyclic addition reaction between an indene derivative (methyl 4-(1H-inden-3-yl) butanoate) and C_{70} [99]. Cyclic voltammetry results showed that the LUMO level of ICBM is 0.07 eV higher than that of $PC_{71}BM$. PTB7:ICBM devices, as well as PTB7:$PC_{71}BM$ reference devices, were prepared using polymer:fullerene weight ratio of 1:1.5 and 3vol % DIO as solvent additive to optimize the device morphologies. Compared to reference devices, ICBM-based devices showed higher V_{oc} (0.79 vs 0.74 V), as expected due to the higher LUMO level of ICBM, as well as higher J_{sc} (15.4 vs 14.2 $mA \cdot cm^{-2}$). However, the FF of PTB7/ICBM devices was slightly lower than that of PTB7/$PC_{71}BM$. Nevertheless, the final PCE of PTB7/ICBM devices (6.67 %) was higher than that of PTB7/$PC_{71}BM$ (6.30 %) due to the improvement of both J_{sc} and V_{oc}.

Novel [60] fulleropyrrolidine derivatives were synthetized by Karakawa *et al.*, where the replacement of the methyl butyrate group at C-2 on the pyrrolidine ring with phenyl, hexyl, and 2,5,8-trioxanonyl substituents lead to a series of N-phenyl derivatives 4, 5, and 6, respectively (Figure 1.6) [100]. The devices were made with inverted structure: ITO/PFN/BHJ/MoOx/Al, in which PFN is used as a cathode interlayer [88]. The 4-based device exhibited a higher J_{sc} compared with other devices, whereas the devices using C-2 alkylated 5 and 6 showed higher V_{oc} values than the 4-based and $PC_{61}BM$-based devices, probably due to their slightly higher LUMO energy levels. Overall, the device using the PTB7/4 blend film

exhibited the highest PCE of 7.34 % among these devices. It is worth noting that the PCE values of the PTB7/4 and PTB7/5 devices are both higher than that of the reference PTB7/$PC_{61}BM$ device (7.03 %).

Tseng *et al.* synthesized three $IC_{60}MA$ derivatives namely: $IC_{60}MA$-2C, $IC_{60}MA$-3C and $IC_{60}MA$-4C (Figure 1.6) with higher LUMO level than $PC_{61}BM$ and tested them in PTB7-based devices. As expected, the devices of PTB7 with ICMA derivatives all exhibited higher V_{oc} than the reference device of PTB7:$PC_{61}BM$ [101]. However, the best PCE was still obtained with the reference PTB7:$PC_{61}BM$ devices (6.8 %), while the devices with $IC_{60}MA$-2C, $IC_{60}MA$-3C and $IC_{60}MA$-4C displayed PCEs of 6.0 %, 5.1 % and 6.5 %, respectively.

Huang *et al.* studied 10 newly synthesized 1,4-fullerene bis-adducts (methoxylated 1,4-bisbenzyl fullerene adducts) [102], in which the two substituents are located at the "para" positions of a six-membered ring on the fullerene cage. These new fullerenes have a smaller π-conjugated system with reduced symmetry and, therefore, their LUMO level is slightly higher compared with 1,2-fullerene bis-adducts. These fullerenes were all initially tested with the standard P3HT polymer. Later, only the most successful (1e – Figure 1.6) was tested with PTB7 using a polymer:fullerene weight ratio of 1:1.5 and DIO as additive. For comparison, reference devices with PTB7:$PC_{61}BM$ were also prepared. Although the PTB7:1e device showed a much higher V_{oc} (0.83 vs 0.76 V) and a slightly higher J_{sc} (12.3 vs 12.1 $mA.cm^{-2}$) than the reference device, its overall PCE was slightly lower than in the reference device (5.4 vs 5.9 %) due to a considerably lower FF (53.3 vs 64.4 %), which may be due to a less efficient crystallization of derivative 1e compared to PCBM, changing the resultant BHJ morphology.

Two new fullerene acceptors, namely N3 and N6 in Figure 6, were synthetized by Nagarjuna *et al.* and tested in solar cells based on PTB7. The cyclopropane ring in N3 is attached to two aryl rings: one aryl ring consists in fluorene with two long decyl chains, which increase the solubility of the molecule in organic solvents and the other aryl ring is a methyl benzoate substituent, that has an electron withdrawing CO_2CH_3 group (EWG), which increases the electron accepting nature of the fullerene [103]. The fullerene N6 differs from N3 in that the methyl benzoate substituent is replaced by a long substituent containing NO_2 and CN groups, which are EWG. The highest PCE (4.1%) of devices with an inverted architecture was achieved with the system PTB7:N3 due to a slightly higher J_{sc} and V_{oc}. The poor shunt resistance in PTB7:N6 solar cells indicates more recombination of charge carriers in these devices. Lower solubility of N6 in 1,2-dichlorobenzene (*o*-DCB) may cause reduced donor-acceptor interface for excitons to be broken up into charges and insufficient percolation paths for charges to get collected at the electrode in PTB7:N6 films, resulting in higher recombination than in PTB7:N3 devices. On the other hand, series resistances were found to be 16.9 and 13.7 $\Omega \cdot cm^2$ for PTB7:N3 and PTB7:N6, respectively. A higher value of series

resistance in the PTB7:N3 device is possibly due to a higher thickness of the film (85 nm) compared to that of PTB7:N6 blend films (70 nm)[103]. In a later work, the same authors synthetized trifluoromethyl derived fulleropyrrolidine (DIF-ful-C_{60} in Figure 1.6) [104] fullerenes in which the attached –F and $-CF_3$ groups enhance the electron accepting character of the resultant fullerene due to the high electron deficient property of the ligands. The inverted devices with PTB7:DIF-full-C_{60} displayed a slightly higher efficiency than the control device of PTB7:$PC_{61}BM$ (6.8 vs 6.2 %) due to a higher V_{oc} (0.82 vs 0.70 V) and a higher J_{sc} (-15.97 vs -15. 40 $mA{\cdot}cm^{-2}$).

In a highly original work, the impact of the endohedral fullerene $Lu_3N@C_{80}$PCBEH (Figure 1.6) on the morphology and efficiency of PTB7-based devices was tested by Roehling *et al.* [105]. This endohedral fullerene has a lower electron affinity than standard fullerenes, which can raise the V_{oc} of photovoltaic devices. However, the PCE values obtained with standard devices processed with *o*-DCB solution without additives were very poor (PCE of 0.4 %) and, surprisingly, deteriorate further with the addition of additives. A morphological study showed that the poor performance results from a poor miscibility between PTB7 and $Lu_3N@C_{80}$PCBEH and in films with DIO added, the fullerene was observed to strongly aggregate into micrometer sized crystals.

Ternary polymer solar cells involving bulk-heterojunctions of PTB7 with $PC_{71}BM$ and other fullerene have also been investigated.

ICBA (Figure 1.6) was used by Cheng *et al.* [106] as an electron-cascade acceptor material in ternary blend devices of PTB7:PC_{71}BM:ICBA. Due to the higher LUMO level of ICBA relative to $PC_{71}BM$, the addition of ICBA leads to an increase in the open circuit voltage (V_{oc}). The best performing devices were those with a PC_{71}BM:ICBA ratio of 85:15 and exhibited a PCE of 8.24 % compared to 7.35 % for standard binary blend devices without ICBA.

Very recently Ma *et al.* [107] added a dihydronaphthyl-based C_{60} bis-adduct (NCBA in Figure 1.6) to a normal PTB7:$PC_{71}BM$ BHJ. NCBA has a LUMO between the LUMOs of PTB7 and $PC_{71}BM$ and, therefore, plays a bridging role allowing the acceptor energy level to be tuned by changing the ratio of NCBA:$PC_{71}BM$ in the blend acceptor material. The best devices were obtained with a 15% weight ratio of NCBA and exhibited a PCE of 9.85 %, compared with a PCE of 8.57 % for the reference device without NCBA.

Table 1.1. Summary of the most relevant device figures of merit and efficiency results obtained with PTB7:fullerene bulk-heterojunctions.

Acceptor	D:A Wt.	Solvent	Additive	J_{sc} (mA cm^{-2})	V_{oc} (V)	FF (%)	PCE (%) Best (average)	Device structure	Device Area (mm^2)	Obs.	Ref
$PC_{71}BM$	1:1.5	CB (100 vol%)	——	10.20	0.76	50.52	3.92	Standard ITO/PEDOT:PSS/BHJ/Ca/Al	10.0	—	[86]
		CB (97 vol%)	DIO (3 vol%)	14.50	0.74	68.97	7.40				
$PC_{71}BM$	1:1.5	CB (97 vol%)	DIO (3 vol%)	15.46	0.76	68 ± 1	7.94	Standard ITO/PEDOT:PSS/BHJ/Ca/Al	4.5	(a)	[87]
$PC_{71}BM$	1:1.5	o-DCB (100 vol%)	——	18.51	0.76	60	8.50	Standard ITO/PEDOT:PSS/BHJ/Ca/Al	4.5	(b)	[72]
$PC_{71}BM$	1:1.5	CB (97 vol%)	DIO (3 vol%)	15.4	0.759	70.6	8.24	Standard ITO/PEDOT:PSS/BHJ/PFN/Ca/Al	16	(c)	[88]
				17.2	0.740	72.0	9.15	Inverted ITO/PFN/BHJ/MoO_3/Al			
$PC_{71}BM$	1:1.5	CB (100vol%)	——	11.43	0.70	46	3.99 (3.68)	Standard ITO/PEDOT:PSS/BHJ/Ca/Al	7.5	(d)	[62]
		CB (97 vol%)	SH-na (3 vol%)	15.67	0.79	70	8.75 (8.42)	Standard ITO/PEDOT:PSS/BHJ/Ca/Al			
$PC_{71}BM$	1:1.5	CB (95 vol%)	DPE (2vol%) +DIO (3vol%)	18.1	0.72	71.0	9.55 (9.25)	Inverted ITO/ZnO/BHJ/MoO_3/Ag	—	—	[92]
$PC_{71}BM$	1:1.5	CB (97 vol%)	DIO (3 vol%)	17.49	0.764	66.1	8.84	Inverted ITO/PEIE/BHJ/MoO_3/Ag	9	—	[93]
$PC_{71}BM$	1:1.5	CB (91 vol%)	FA (6 vol%) + DIO (3 vol%)	24.11	0.72	52.11	9.04	Standard ITO/PEDOT:PSS/BHJ/Li/Al	4	(e)	[94]
$PC_{71}BM$	1:1.5	CB (97 vol%)	DIO (3 vol%)	15.2	0.73	67.8	7.53 (7.40)	Standard ITO/PEDOT:PSS/BHJ/PFN/Al	16	—	[95]
		CB (95 vol%)	CBA (5 vol%)	16.7	0.75	73.0	9.11 (8.99)	Standard ITO/PEDOT:PSS/BHJ/PFN/Al			
$PC_{71}BM$	1:1.5	o-DCB (97 vol%)	DIO (3 vol%)	14.2	0.74	60.0	6.30	Standard ITO/PEDOT:PSS/BHJ/Ca/Al	10	—	[99]
ICBM			CBA (5 vol %)	15.4	0.79	55.0	6.67				
Fullerene 4	1:1.5	CB (97 vol%)	DIO (3 vol%)	15.48	0.75	63.3	7.34	Inverted ITO/PFN/BHJ/MoOx/Al	9	—	[100]
Fullerene 5				14.21	0.76	67.3	7.27				
Fullerene 6				14.03	0.80	61.0	6.83				
$PC_{61}BM$				14.29	0.74	66.5	7.03				

Acceptor	D:A Wt.	Solvent	Additive	J_{sc} (mA cm^{-2})	V_{oc} (V)	FF (%)	PCE (%) Best (average)	Device structure	Device Area (mm^2)	Obs.	Ref
$IC_{60}MA$-2C	—	CB (97 vol%)	DIO (3 vol%)	14.2	0.77	55	6.0	Inverted ITO/ZnO/BHJ/MoO_3/Al	7	—	[101]
$IC_{60}MA$-3C				12.9	0.79	50	5.1				
$IC_{60}MA$-4C				13.7	0.77	61	6.5				
$PC_{61}BM$				14.6	0.76	62	6.8				
Fullerene 1e	1:1.5	CB 95 vol%	DIO 5 vol%	12.3	0.825	53.3	5.4	Standard ITO/PEDOT:PSS/BHJ/Ca/Al	7.2	—	[102]
$PC_{61}BM$				12.1	0.760	64.4	5.9				
Fullerene N3	1:1.5	o-DCB 97 vol%	DIO 3 vol%	9.73	0.812	52.1	4.12	Inverted ITO/ZnO/BHJ/MoO_3/Ag	—	—	[103]
Fullerene N6				9.06	0.805	50.2	3.64				
DIF-ful-C_{60}	1:1.5	o-DCB 97 vol%	DIO 3 vol%	15.97	0.82	51	6.8 (6.5)	Inverted ITO/ZnO/BHJ/MoO_3/Ag	—	(f)	[104]
$PC_{61}BM$				15.40	0.70	58	6.2 (5.9)				
$PC_{71}BM$	1:1.5	CB (97 vol%)	DIO (3 vol%)	14.99	0.701	68.8	7.35 (7.23)	Standard ITO/PEDOT:PSS/BHJ/Ca/Al	4	—	[106]
$PC_{71}BM$ (85%) +ICBA (15%)				16.32	0.720	69.2	8.24 (8.13)				
$PC_{71}BM$	1:1.5	o-DCB (97 vol%)	DIO (3 vol%)	17.4	0.76	64.8	8.57	Inverted ITO/ZnO/BHJ/MoO_3/Ag	9	—	[107]
$PC_{71}BM$ (85%) + NCBA (15%)				18.6	0.78	67.9	9.85				

Observations: (a) Methanol treatment; (b) PTB7 high Mw of 128 kg/mol; (c) PFN is used as surface modifier; (d) With solution dipping; (e) FA is Formic acid; (f) For PTB7:DIF-ful-C_{60} based OPVs, the D:A weight ratio was optimized and 1:1.5 showed the best performances.

1.7 Devices based on PTB7-Th

PTB7-Th (Figure 1.5) possesses a conjugated backbone structure identical to PTB7, only differing on the nature of the organic ligand connected to the benzodithiophene (BDT) unit: the ether group in PTB7 is replaced by a thiophene group in PTB7-Th. Due to this chemical modification, PTB7-Th can sustain higher temperatures than PTB7 without suffering decomposition [108]. In this chapter, Section 1.7.1 discusses the most relevant studies performed in the optimization of the BHJ morphology and efficiency of PTB7-Th:$PC_{71}BM$ (or $PC_{61}BM$) devices. Later, Section 1.7.2 addresses devices incorporating bulk-heterojunctions of PTB7-Th with other fullerenes. A compilation table, Table 1.2, is presented at the end of this chapter summarizing the most relevant and recent device efficiency results obtained with OPVs based on PTB7-Th.

1.7.1 PTB7-Th devices with $PC_{61}BM$ and $PC_{71}BM$

PTB7-Th synthesis and testing in polymer solar cells was first reported by Zhang *et al.* [109] in 2014. A PCE of 9.0 % was achieved in standard devices containing PTB7-Th:$PC_{71}BM$ in the ratio 1:1.5 and spin-coated from *o*-DCB solution with 3 vol% DIO. Devices processed with 1 vol.% DIO and 5 vol.% DIO were also tested but produced worse PCE results.

Huang *et al.* studied the effect of the solvent additive DIO on the BHJ morphology and efficiency of PTB7-Th:$PC_{71}BM$ devices with inverted architecture, using PEIE (Polyethylenimine ethoxylated) as interfacial layer on top of ITO [110]. The device prepared from a pure chlorobenzene solution, i.e. without additive, shows an efficiency of 6.4% with a J_{sc} of 16.2 mA.cm^{-2}, a V_{oc} of 0.80 V and FF of 49%. Incorporating 3 vol.% of DIO, the efficiency improves to 9.5 %, corresponding to J_{sc}, V_{oc} and FF values of 18.1 mA.cm^{-2}, 0.79 V and 66 %, respectively. AFM and TEM studies confirm the effectiveness of DIO in improving the dispersion of $PC_{71}BM$: the large aggregates ≈100 nm in diameter observed in films prepared without DIO are suppressed in films prepared with DIO [110].

A binary solvent additive made of DIO:N-methyl-pyrrolidone (NMP) (1.5%:1.5%) was employed by Wan *et al.* [111] to improve the PCE of PTB7-Th:$PC_{71}BM$ devices from 8.2 % (without additive) and 9.5 % (with 3 % DIO) to 10.8 %. Resonant Soft x-Ray Scattering analysis showed that, although all the bulk-heterojunctions exhibit similar domain sizes, the BHJ processed with DIO:NMP showed higher phase purity than the BHJs with single additives or without additives, which facilitates the charge transport and reduces charge recombination leading to the higher PCE observed.

Fan *et al.* [112] introduced a solid (melting point, m.p. = 125 °C) fluorescent inhibitor (1-bromo-4-nitrobenzene) into the PTB7:$PC_{71}BM$ BHJs to improve device efficiency. All the devices were spin-coated from a chlorobenzene solution with 3 vol.% DIO and the best devices were obtained with 15 wt.% of 1-bromo-4-nitrobenzene and exhibited a PCE of 8.95 % compared to 7.58 % for a reference device without 1-bromo-4-nitrobenzene. The increase in PCE was attributed to an improvement in charge transport and dissociation.

The effect of different polymer:fullerene blend mass ratios (1:0.5; 1:1; 1:1.5; 1:2 and 1:3) on the photovoltaic performance of PTB7-Th:$PC_{71}BM$ devices, with standard architecture, was investigated by Komilian *et al.* [63]. No additives were used and the surface of the BHJ was washed with ethanol before top electrode deposition. The best devices with a PCE of 9.38 % were obtained with a D:A mass ratio of 1:2.

Xiao *et al.* [113] reported highly efficient ternary cells based on PTB7-Th:CO_i8DFIC (Acceptor A1):$PC_{71}BM$ (Acceptor A2), where CO_i8DFIC is a non-fullerene small molecule acceptor. The LUMO for PTB7-Th (−3.12 eV), $PC_{71}BM$ (−3.67 eV) and CO_i8DFIC (−3.88 eV) show a stepwise alignment and therefore $PC_{71}BM$ facilitates electron transfer from PTB7-Th to CO_i8DFIC. The mass ratio between PTB7-Th and A1+A2 was fixed to 1:1.5, while the content of A2 in acceptors was varied from 0 to 100%. The best devices were obtained with (D:A1:A2) mass ratios of (1:1.05:0.45) and produced a remarkable PCE of 14.08%. These ternary cells combine the advantage of fullerene acceptors (high μ_e) and non-fullerene acceptors (strong visible or NIR absorption). Charge carrier mobilities were measured using the SCLC method. Compared with the binary blend film PTB7-Th:CO_i8DFIC ($\mu_h = 6.98 \times 10^{-4}$, $\mu e = 3.89 \times 10^{-5}$ and $\mu_h/\mu_e = 18$), the ternary blend film PTB7-Th: CO_i8DFIC:$PC_{71}BM$ (1:1.05:0.45) showed a similar μh and a much higher μ_e, which resulted in a decrease in the ratio μ_h/μ_e from 18 to 1.3 ($\mu_h = 6.35 \times 10-4$, $\mu_e = 4.80 \times 10-4$ and $\mu_h/\mu_e = 1.3$). As a result of the improved electron transport and more balanced charge transport in the active layer containing $PC_{71}BM$, J_{sc} and FF increased.

Jagadamma *et al.* [114] investigated the effect of ex-situ thermal annealing on the BHJ morphology of PTB7-Th:$PC_{71}BM$ devices and on the corresponding efficiency. Devices with an inverted architecture were used and the thermal annealing was performed over a range of temperatures ranging from room temperature to 150 °C. To exclude any negative influence from the possible degradation of charge selective layers and metal contacts, the ex-situ thermal annealing was applied only to the BHJ, that is, before metal anode deposition and not to the complete device. The unannealed devices displayed the highest PCE (9.1%) and this decreased gradually with the increase in thermal annealing temperature until it reached its lowest value (6.9%) for devices that had been annealed at 150 °C. A morphological

analysis using AFM showed that the BHJ morphology coarsens with increasing temperature and large scale phase separation is observed in BHJ annealed at 150 °C which partially supresses exciton dissociation and increases recombination losses with the consequent drops observed in J_{sc}, FF and in the PCE.

The effect of thickness variation of the BHJ (from 62 nm to 307 nm) on the photovoltaic performance of PTB7-Th:$PC_{71}BM$ devices, with both standard and inverted architectures, was studied by Kobori *et al.* [115]. In both device architectures, it was observed that FF decreased continuously with increasing the BHJ thickness. By contrast, the J_{sc} increases with the BHJ thickness but not monotonically. Furthermore, the J_{sc} of inverted devices were systematically higher than those of normal devices with identical thickness. In terms of overall PCE, for lower BHJ thickness (<100 nm) inverted devices perform considerably better than normal devices. However, for higher thicknesses the difference between the PCE of standard and inverted devices tends to fade away. The optimized devices were obtained in standard geometry with a BHJ thickness of 116 nm and a corresponding PCE of 9.25% and in inverted geometry with a BHJ thickness of 76 nm and a corresponding PCE of 10.4%. These results were explained by the difference of the simulated optical intensity distribution in the devices.

In a similar work, Zang *et al.* [60] also studied the effect of BHJ thickness (70, 90, 120, 180 and 270 nm) and polymer:fullerene (D:A) mass ratio (1:1.5 and 1:3) on the performance of PTB7-Th:$PC_{71}BM$ devices with an inverted architecture. For devices with a D:A mass ratio of 1:1.5, a BHJ thickness of 90 nm produced the highest efficiency with a PCE of 9.68%, a V_{oc} of 0.80 V, a J_{sc} of 16.55 $mA{\cdot}cm^{-2}$ and a FF of 71%. Although the devices with a thicker BHJ (270 nm) displayed a considerably higher J_{sc} (19.70 $mA{\cdot}cm^{-2}$), in agreement with the previous work by Kobori *et al.* [115], the corresponding PCE was lower (7.79%) due to a drastic drop in FF (50%) which offset the improved light absorption resultant from using thicker films. This decrease in FF was attributed to the less efficient charge carrier transport and dissociation in thicker films, due to the relatively low electron mobility in the BHJ. To improve the μ_e of the BHJ, the authors also tested devices in which they changed the D:A mass ratio to 1:3. In this case they observed that for thick devices with a BHJ thickness of 270 nm, the PCE was higher (8.15%) than the PCE of the corresponding devices with a D:A mass ratio of 1:1.5 (7.79%). Other researchers studied the effect of different processing treatments on bulk and interfacial disorder in inverted PTB7-Th:$PC_{71}BM$ devices [116]. Devices fabricated with and without DIO showed PCEs of 8.3% and 3.8%, respectively. The lifetime stability and degradation of the PTB7-Th based solar cells has also been a topic of interest in recent years.

Pearson et al. [117] measured the stability of reference PTB7-Th:$PC_{71}BM$ devices, with both standard and inverted architectures, over 70 h in an atmospheric chamber under continuous dry nitrogen flow, with typical oxygen and moisture levels of <5 ppm and <30 ppm respectively. Although devices with normal architecture exhibited a larger initial efficiency (PCE of 7.3% on average, vs. PCE of 6% for inverted cells), a PCE drop of more than 60% was observed in both device structures after only 24 h of light soaking under nitrogen. These results strongly suggest that BHJ degradation is driven by light-mediated processes rather than high levels of oxygen and moisture exposure. The large PCE reduction observed in both device configurations was mostly due to a large overall reduction in J_{sc}. Two different strategies were proposed for improving the stability of both standard and inverted devices. For standard devices, DIO was replaced by *o*-DCB as a co-solvent. Although the PCE of these new devices was slightly lower (6.5%), the device stability was greatly improved, which highlighted the detrimental stability effects associated with the use of DIO and previously identified by others in different BHJ systems. For inverted devices, placing a UV filter in front of the devices was also found to reduce considerably the extent of PCE degradation.

Liu *et al.* [118] demonstrated that in encapsulated devices, completely isolated from moisture and oxygen, the absorption of high energy UV photons by the PCBM molecules leads to a degradation of exciton diffusion and charge mobility in the fullerene phase. The μ_e measured by the SCLC method decreased by four orders of magnitude, from 2.43×10^{-3} to 2.16×10^{-7} $cm^2V^{-1}s^{-1}$ and the μ_h decreased by less than one order of magnitude, after 45 h of AM 1.5G non-UV-filtered 1-sun illumination. Transient Absorption (TA) measurements combined with UV wavelength cut-off degradation experiments suggest that the burn-in may be triggered by a spin flip at the donor/acceptor interface, leading to the formation of $PC_{71}BM$ triplet anions and the accumulation of electrostatic potential energy. The release of this excess electrostatic potential energy promotes a disordering of the weakly bonded nanomorphological order, mostly in the $PC_{71}BM$ domains near the donor/acceptor interface. To circumvent this problem, the authors proposed a strategy that consisted in replacing CB by DCB as master solvent, removing the DIO from the processing solution, replacing ZnO buffer layer (an oxidant source) by PFN and applying a thermal annealing treatment, prior to light soaking, to increase the crystallinity of the $PC_{71}BM$ domains in the BHJ (Figure 1.9). Using this strategy, these authors were able to produce organic cells that were simultaneously highly efficient and very stable.

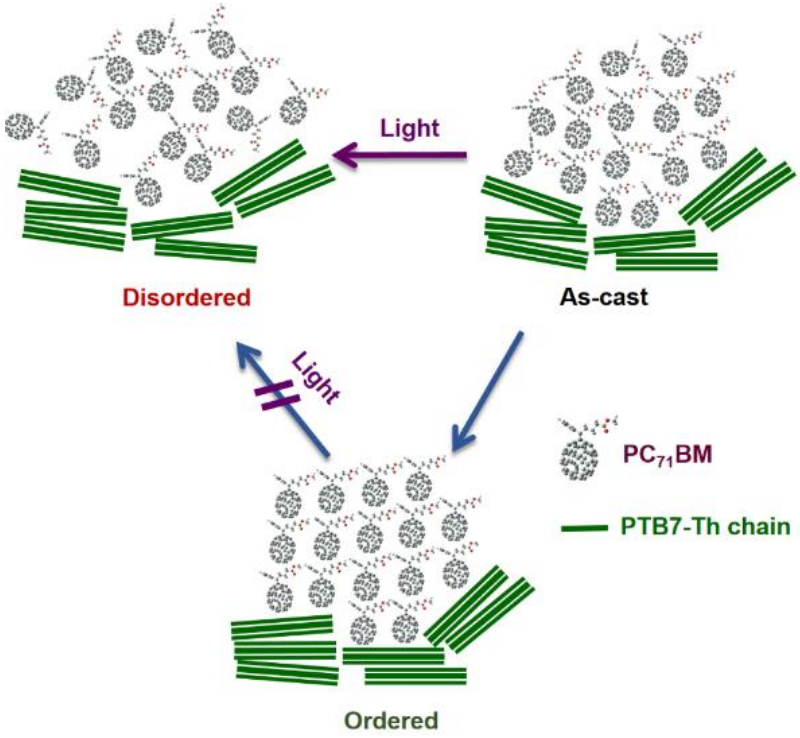

Figure 1. 9. Schematic of two possible paths for the nano-morphology evolution in the $PC_{71}BM$ acceptor phase: in the top one light induces disorder and in the bottom one light induced disorder is prevented in a highly crystalline configuration of the $PC_{71}BM$ molecules. Reprinted with permission from ref. [118].

Table 1. 2. Summary of the most relevant device figures of merit and efficiency results obtained with PTB7-Th:fullerene BHJs

Acceptor	D:A Wt.	Solvent	Additive	J_{sc} (mA cm^{-2})	V_{oc} (V)	FF (%)	PCE (%) Best (average)	Device structure	Device Area (mm^2)	Obs.	Ref
$PC_{71}BM$	1:1.5	o-DCB (99 vol%)	DIO (1 vol%)	16.03	0.786	65.12	8.21	Standard ITO/PEDOT:PSS/BHJ/Ca/Al	4	—	[109]
		o-DCB (97 vol%)	DIO (3 vol%)	16.86	0.784	68.16	9.00				
		o-DCB (95 vol%)	DIO (5 vol%)	14.59	0.779	64.73	7.35				
$PC_{71}BM$	1:1.5	CB (100 vol%)	——	16.2	0.80	49	6.4 (6.1)	Inverted ITO/PEIE/BHJ/MoO_3/Ag	4.5	—	[110]
		CB (97 vol%)	DIO (3 vol%)	18.1	0.79	66	9.5 (9.3)				
$PC_{71}BM$	1:1.5	o-DCB (100 vol%)	——	17.0	0.83	58.1	8.2 (8.1)	Standard ITO/PEDOT:PSS/BHJ/C_{60}-N/Al	4	(a)	[111]
		o-DCB (97 vol%)	NMP (3 vol%)	18.0	0.82	62.1	9.2 (8.9)				
		o-DCB (97 vol%)	DIO (3 vol%)	17.9	0.82	64.5	9.5 (9.2)				
		o-DCB (97 vol%)	DIO 1.5 vol% + NMP 1.5 vol%	19.1	0.82	69.1	10.8 (10.4)				
$PC_{71}BM$	1:1.5	CB (97 vol%)	DIO (3 vol%)	15.97	0.79	60.12	7.58 (7.51)	ITO/PEDOT:PSS/BHJ/BCP/Ag	12.56	(b)	[112]
				17.74	0.784	64.11	8.95 (8.89)				
$PC_{71}BM$	1:0.5	o-DCB	——	6.69	0.78	31	1.60	Standard ITO/PEDOT:PSS/BHJ/Ca/Al	13	(c)	[63]
	1:1			12.59	0.80	50	5.04				
	1:1.5			19.01	0.80	53	8.08				
	1:2			18.15	0.79	65	9.38				
	1:3			10.41	0.77	43	3.49				

Acceptor	D:A Wt.	Solvent	Additive	J_{sc} (mA cm^{-2})	V_{oc} (V)	FF (%)	PCE (%) Best (average)	Device structure	Device Area (mm^2)	Obs.	Ref
$PC_{71}BM$ (0.45 wt) + CO8DFIC (1.05 wt)	1:1.5	CB (99 vol%)	DIO (1 vol%)	28.20	0.70	71.0	14.08	Inverted ITO/ZnO/BHJ/MoO_3/Ag	4	—	[113]
$PC_{71}BM$	1:1.5	CB (97 vol%)	DIO (3 vol%)	16.6	0.77	71.3	9.1 (8.8)	Inverted ITO/ZnO/BHJ/MoO_3/Ag	8	(d)	[114]
$PC_{71}BM$	1:1.5	o-DCB (97 vol%)	DIO (3 vol%)	16.55	0.80	71	9.68 (9.42)	Inverted ITO/ZnO/BHJ/MoO_3/Ag	—	(e)	[60]
	1:3			14.53	0.80	73	8.73 (8.51)				
$PC_{71}BM$	1:1.8	CB (97 vol%)	DIO (3 vol%)	—	—	—	9.25	Standard ITO/PEDOT:PSS/BHJ/LiF/Al	8	(f)	[115]
				—	—	—	10.4	Inverted ITO/ZnO/BHJ/MoO_3/Ag			
$PC_{71}BM$	1:1.5	CB (100 vol%)	——	9.7	0.83	47.5	3.8 (3.3)	Inverted ITO/PEIE/BHJ/MoO_3/Ag	—	—	[116]
		CB (97 vol%)	DIO (3 vol%)	16.1	0.79	64.8	8.3 (8.1)				
$PC_{71}BM$	1:1.5	CB (97 vol%)	DIO (3 vol%)	—	—	—	—	Standard ITO/PEDOT:PSS/BHJ/Ca/Ag	4.5	—	[117]
				—	—	—	—	Inverted ITO/TiO_2/BHJ/MoO_3/Ag			
$PC_{71}BM$	1:1.5	CB (97 vol%)	DIO (3 vol%)	16.85	0.801	70.27	9.72 (9.49)	Inverted ITO/ZnO/BHJ/MoO_3/Ag	6	—	[118]
	1:1.5	1,2-DCB (100 vol%)	———	14.93	0.802	65.28	7.82	Inverted ITO/PFN/BHJ/MoO_3/Ag			
	1:2.0			16.01	0.802	72.28	9.59 (9.28)				
$PC_{61}BM$	1:1.5	CB (97 vol%)	DIO (3 vol%)	14.6	0.81	64	(7.6)	Inverted ITO/PEIE/BHJ/MoO_3/Ag	10	—	[119]
$PC_{71}BM$				17.7	0.80	66	(9.4)				
ICBA				13.3	1.0	53	(7.1)				

Acceptor	D:A Wt.	Solvent	Additive	J_{sc} (mA cm^{-2})	V_{oc} (V)	FF (%)	PCE (%) Best (average)	Device structure	Device Area (mm^2)	Obs.	Ref
$PC_{61}BM$	1:1.5	CB (97 vol%)	DIO (3 vol%)	14.0	0.80	65	7.3	Inverted ITO/ZnO/BHJ/MoOx/Ag	10.4	(g)	[120]
PyF5	1:2			13.7	0.84	56	6.5				
FAP1	1:2			12.7	0.87	55	6.1				
$PC_{61}BM$	1:1.5	o-DCB (97 vol%)	DIO (3 vol%)	15.14	0.84	62	7.9 (7.7)	Inverted ITO/ZnO/BHJ/MoO_3/Ag	—	—	[104]
DIF-full-C_{60}				16.01	0.82	65	8.6 (8.4)				
$PC_{71}BM$	1:1.5	CB (97 vol%)	CLN (3 vol%)	14.0	0.795	48.8	5.4	Inverted ITO/ZnO/BHJ/MoO_3/Ag	10	—	[121]
CN-$PC_{71}BM$				13.5	0.898	68.0	8.2				

Observations:(a) NMP is N-methyl pyrrolidone. (b) Reference device (lower PCE) without 1-bromo-4-nitrobenzene; device with higher PCE contains 1-bromo-4-nitrobenzene (15 wt% active layer). (c) The BHJ was surface washed with ethanol before top electrode deposition. (d) Devices subjected to different annealing temperatures were tested (RT, 70, 100, 120 and 150 °C). Best devices were obtained at RT. Only the performance of these is shown in this table. (e) For devices with D:A mass ratio 1:1.5, the following different BHJ thickness were tested: 70, 90, 120, 180 and 270 nm. Best devices were obtained with an optimized BHJ thickness of 90 nm. Only the performance of these is shown in this table. For devices with D:A ratio 1:3, the following different BHJ thickness were tested: 120, 180 and 270 nm. Best devices were obtained with an optimized BHJ thickness of 120 nm. Only the performance of these is shown in this table. (f) The performance data shown here were obtained with an optimized BHJ thickness of 116 nm in the standard devices and of 76 nm in the inverted devices. (g) The PTB7-Th:fullerene ratios were optimized and only devices with the highest efficiency ratios are shown: 1:1.5 for PC61BM and 1:2 for PyF5 and FAP1.

1.7.2 PTB7-Th devices with other fullerenes

Huang *et al.* [119] studied the BHJ morphology, photophysics and performance of inverted devices based on PTB7-Th blended with the indene-C_{60} bisadduct ICBA (Figure 1.6) and correlated it with similar devices using the two classical fullerenes $PC_{61}BM$ and $PC_{71}BM$. Although devices based on ICBA achieved, as expected, a higher V_{oc} (1.0 V) than devices based on $PC_{61}BM$ and $PC_{71}BM$ (0.81 V and 0.80 V respectively) consistent with the higher LUMO of ICBA, the corresponding efficiency was lower (average PCE of 7.1% for devices with ICBA compared with 7.6% and 9.4% for devices based on $PC_{61}BM$ and $PC_{71}BM$, respectively). Comparing the J_{sc} values, PTB7-Th devices based on $PC_{71}BM$ have a much higher J_{sc} (17.7 $mA{\cdot}cm^{-2}$) than similar devices based on $PC_{61}BM$ (14.6 $mA{\cdot}cm^{-2}$) and ICBA (13.3 $mA{\cdot}cm^{-2}$). This difference is largely explained by the fact that, in the visible region of the spectrum, $PC_{71}BM$ has a much higher absorption coefficient than both $PC_{61}BM$ and ICBA. ICBA BHJs are also characterized by lower polymer crystallinity, smaller domain sizes and better-mixed phases, which promotes a faster geminate recombination as revealed by transient absorption (TA) measurements. Overall this results in a poorer device performance of the ICBA-based devices.

The carrier transport loss mechanism in PTB7-Th BHJs based on the amorphous fullerene acceptor PyF5, as well as on the semi-crystalline fullerene acceptors FAP1 and $PC_{61}BM$ (see chemical structures of PyF5 and FAP1 in Figure 1.6) were studied by Zhang *et al.* [120]. The PCE of optimized PyF5 and FAP1 based devices (6.5% and 6.1% respectively) is slightly lower than that of optimized PC61BM based devices (7.3%), owing to the slightly lower fill factor and J_{sc}. Interestingly, optimized devices based on the fullerenes PyF5 and FAP1 require a higher fullerene mass loading (D:A = 1:2) than the optimized device based on $PC_{61}BM$ (D:A = 1:1.5). The charge carrier transport properties of pristine fullerenes and PTB7-Th:fullerene blends were determined with SCLC measurements. Although the three pristine fullerenes have very similar μ_e values (PyF5 = 4.0×10^{-3} $cm^2V^{-1}s^{-1}$; FAP1 = 4.4×10^{-3} $cm^2V^{-1}s^{-1}$; $PC_{61}BM$ = 4.5×10^{-3} $cm^2V^{-1}s^{-1}$), the μ_e values of the corresponding BHJ composites are very different due to the different nanoscale morphologies. For example, the μ_e of PTB7-Th:PyF5 (1:1) and PTB7-Th:FAP1 (1:1) are in the order of 10^{-7}–10^{-6} $cm^2V^{-1}s^{-1}$ and these are in sharp contrast with the much higher μe of PTB7-Th:$PC_{61}BM$ which is ≈10^{-4} $cm^2V^{-1}s^{-1}$. As the miscibility of PTB7-Th is higher with PyF5 and FAP1 than with $PC_{61}BM$, PTB7-Th:PyF5 and PTB7-Th:FAP1 blends require significantly higher fullerene loadings to reach comparably high electron mobilities as for PTB7-Th:$PC_{61}BM$ blends. The authors, therefore, concluded that BHJ composites with good polymer–fullerene miscibility require higher fullerene loadings than composites with a tendency to phase separate. Nagarjuna *et al.* [104] synthesized the fullerene DIF-ful-

C_{60} (Figure 1.6) and tested it with PTB7, as previously mentioned and with PTB7-Th. The optimized PTB7-Th: DIF-ful-C_{60} OPV devices showed a highest PCE of 8.6% with a J_{sc} of 16.01 mA·cm^{-2}, V_{oc} of 0.82 V and a high FF of 65.5%, whereas the reference solar cell made from PTB7-Th:PC_{61}BM blends showed a highest efficiency of 7.9%, with reduced J_{sc} of 15.14 mA·cm^{-2} and FF of 62.1%. In a different work, the same authors [119] synthesized the fullerene derivative CN-PC_{71}BM and optimized its application in PTB7-Th-based devices with an inverted structure. The best devices displayed a PCE of 8.2% and were obtained using a D:A mass ratio of 1:1.5, dissolved in CB and containing 3 vol % of CLN as additive.

1.8 Devices based on PffBT4T-2OD

The small band gap donor polymer poly[(5,6-difluoro-2,1,3-benzothiadiazol-4,7-diyl)-alt-(3,3'''di(2-octyldodecyl)2,2';5',2";5",2'''-quaterthiophen-5,5'''-diyl)] (PffBT4T-2OD) has recently attracted attention due to its potential to fabricate high performing OPV devices. PffBT4T-2OD, also known as PCE11, exhibits relatively high SCLC hole mobility of 1.5–3.0 × 10^{-2} cm^{2}V^{-1}s^{-1} [122] due to its high crystallinity. These properties, together with its tendency to form relatively pure polymer domains when blended with fullerenes, allow it to perform well in an OPV device, when used in relatively thick BHJ layers (≈300 nm) with higher light absorption capabilities. PffBT4T-2OD when in solution also exhibits a peculiarly strong temperature dependent aggregation behaviour, forming a gel at room temperature. Consequently, PffBT4T-2OD based devices need to be always cast from warm solutions (>60 ◦C), which then aggregate or crystallize during cooling and film forming processes. Table 1.3, at the end of this chapter, summarizes the most relevant and recent device efficiency results obtained with OPVs based on PffBT4T-2OD:fullerene BHJs.

1.8.1 PffBT4T-2OD Devices with $PC_{61}BM$ and $PC_{71}BM$

Ma *et al.* [123] investigated the influence of several processing parameters (solution temperature, concentration, spin-rate and solvent quality), as well as the influence of polymer molecular weight on the morphology and performance of PffBT4T-2OD:$PC_{71}BM$ devices. Here, it was found that the molecular orientation and molecular packing can be tuned by adjusting the solution temperature and the spin rate during spin-coating of the BHJ, with a low solution temperature and low spinning rate inducing highly ordered face-on polymer packing and a high solution temperature and a high spinning rate producing poorly ordered edge-on polymer packing. The best device performance (average PCE of 10.3%) was achieved using films spun-cast at 800 rpm from a solution at 100 ◦C, creating a smooth film containing sufficient aggregates to yield a favourable morphology.

Zhang *et al.* [124] studied the impact, on the morphology and efficiency of PffBT4T-2OD:$PC_{71}BM$ devices, of depositing the BHJ from different co-solvent mixtures namely: (i) o-xylene with 1 vol % *p*-anisaldehyde; (ii) CB with 3 vol % DIO; (iii) *o*-DCB with 3 vol % DIO and (iv) a mixture of 48.5 vol % CB and 48.5 vol % *o*-DCB with 3 vol % DIO. The best device efficiencies (average PCE = 9.07%) were obtained using the mixture CB:*o*-DCB:DIO. The authors attributed this higher efficiency to the higher crystallinity of PffBT4T-2OD and higher absorption density of the BHJ when processed with the ternary solvent combination.

The impact of four different additives (ODT, DIO, diphenylether (DPE) and CLN), added to the photovoltaic ink solution in 3 vol %, on the morphology and performance of the resultant PffBT4T-2OD:$PC_{71}BM$ devices, was studied by Zhao *et al.* [125]. The best devices displayed a PCE of 10.23% and were obtained using CN as additive. GIWAXS data showed that films processed with CN additive possess enhanced crystallinity of PffBT4T-2OD in the (100) direction corresponding to the alkyl stacking peak located at a q value of 0.29 $Å^{-1}$, which facilitates charge transport within the BHJ.

Zhang *et al.* [40] helped elucidating the mechanism of action of additives studying the effect of using 3 vol % of DIO in the preparation of PffBT4T-2OD:$PC_{71}BM$ devices. The results showed that PCE can increase by ≈20%, from 7.2% to above 8.95%, as a result of the coarsening of the phase domains induced in the film by DIO and thermal annealing, through a mechanism of transient plasticisation. Furthermore, the authors showed that DIO can be removed from the film by a thermal annealing process at temperatures below 100 °C and that there is an interplay between the evaporation rate of DIO and the rate of domain coarsening in the plasticized film. The effect of different isomers of $PC_{71}BM$ on the photovoltaic properties of PffBT4T-2OD:$PC_{71}BM$ blend films was investigated by Umeyama *et al.* [126].

It should be noted here that the $PC_{71}BM$ normally used in OPV devices consists of an isomer mixture of α-type isomers (80–90%) and β-type isomers (10–20%). The α-isomer is composed by two enantiomers, while the β-isomer consists of two diastereomers in which the phenyl group is extended toward opposite directions (Figure 1.10) [127]. Interestingly, the authors found that one of the diastereomers of the β-isomer (isomer β_1) shows an extraordinary cohesion in the blended film, deteriorating the OPV device performance. In fact, the PffBT4T-2OD devices based on β_1-$PC_{71}BM$ exhibited an extremely low PCE of 0.43%. By contrast, OPV devices using the remaining pure isomers exhibited much higher PCE, namely α-$PC_{71}BM$ (8.80%), β_2-$PC_{71}BM$ (8.75%) and these slightly surpass the device with using the normal $PC_{71}BM$ isomer mixture (8.46%) [126]. The authors concluded that decreasing the amount of a diastereoisomer of β_1-$PC_{71}BM$ with high aggregation tendency improves the photovoltaic performances[126].

Table 1. 3. Summary of the most relevant device figures of merit and efficiency results obtained with PffBT4T-2OD:fullerene BHJs**.**

Acceptor	D:A Wt.	Solvent	Additive	J_{sc} (mA cm^{-2})	V_{oc} (V)	FF (%)	PCE (%) Best (average)	Device structure	Device Area (mm^2)	Obs.	Ref
$PC_{71}BM$	1:1.2	CB (48.5 vol%) + DCB (48.5 vol%)	DIO (3 vol%)	18.5	0.79	71	10.3	Inverted ITO/ZnO/BHJ/MoO_3/Al	5.64	(a)	[123]
$PC_{71}BM$	1:1.2	CB (48.5 vol%) + DCB (48.5 vol%)	DIO (3 vol%)	18.19	0.76	66.6	9.16 (9.07)	Inverted ITO/ZnO/BHJ/MoO_3/Ag	2	(b)	[124]
$PC_{71}BM$	1:1.3	CB (48.5 vol%) + DCB (48.5 vol%)	CLN (3 vol%)	17.75	0.79	73.1	10.23 best	Standard ITO/PEDOT:PSS/BHJ/LiF/Al	4	(c)	[125]
$PC_{71}BM$	1:1.2	CB (50 vol%) + DCB (50 vol%)	———	16.13	0.72	62.93	7.29 (7.08)	Standard ITO/PEDOT:PSS/BHJ/Ca/Al	2.6	(d)	[40]
		CB (48.5 vol%) + DCB (48.5 vol%)	DIO (3 vol%)	17.33	0.75	68.34	8.90 (8.73)				
$PC_{71}BM$	——	CB (48.5 vol%) + DCB (48.5 vol%)	DIO (3 vol%)	19.5	0.75	72.2	10.57 (10.3)	Inverted ITO/TiO_2/BHJ/MoO_3/Ag	—	(e)	[128]
				18.8	0.79	74.7	11.17 (11.0)				
$TC_{71}BM$	1:1.2	CB (48.5 vol%) + DCB (48.5 vol%)	DIO (3 vol%)	18.8	0.77	75	10.8 (10.3)	Inverted ITO/ZnO/BHJ/MoO_3/Al	5.9	—	[122]
$PC_{71}BM$				18.4	0.77	74	10.5 (10.2)				
$PC_{61}PM$				17.7	0.77	76	10.4 (10.1)				
ICMA				16.4	0.78	77	9.8 (9.4)				
$TC_{61}PM$				17.4	0.75	74	9.7 (9.3)				
$PC_{61}BM$				17.1	0.77	73	9.6 (9.3)				
$PC_{71}BM$	1:1.2	CB (48.5 vol%) + DCB (48.5 vol%)	DIO (3 vol%)	17.3	0.76	70	9.31 (8.93)	Standard ITO/PEDOT:PSS/BHJ/Ca/Al	2.6	—	[129]
$PC_{61}BM$				16.3	0.77	67	8.46 (8.15)				
ICBA				7.5	0.94	45	3.19 (2.78)				

Observations:(a) Different processing conditions (spin-rate, solution temperature) were tested. Only the devices with the best performance are shown and these had a thickness of 300 nm and were obtained with a solution temperature of 100 °C and a spin rate of 800 rpm. (b) Different solvent combinations were tested. Only the devices with the best performance are shown and these were obtained using a mixture of CB:DCB (1:1 v/v) with 3 vol% DIO. (c) Different additives were tested. Only the device data with the best performance are shown and these were obtained using 1-chloro-naphthalene as additive. (d) Reference device without DIO was not annealed. Device with DIO was annealed for 5 minutes at 100 °C. (e) Reference device without PCDTBT8 shown on top and device with 15 wt% PCDTBT8 on bottom.

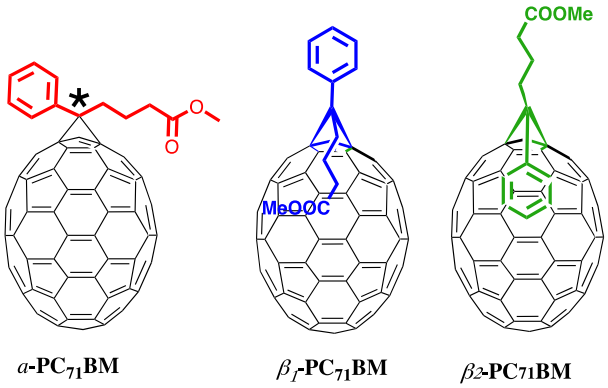

Figure 1. 10. Different isomers of $PC_{71}BM$. Adapted from reference [126].

Recently Li *et al.* [128] reported high efficiency ternary polymer solar cells, based on the system PffBT4T-2OD:$PC_{71}BM$ and containing the amorphous medium band gap conjugated polymer PCDTBT8 as a third minority component. Different mass fractions of PCDTBT8 were tested (0, 5, 10, 15, 20 and 30%) and the most efficient devices (average PCE of 11.0%) were prepared using 15 wt % of PCDTBT8. Morphological investigation showed that the third component PCDTBT8 locates at the interface between PffBT4T-2OD and $PC_{71}BM$, reduces the fullerene aggregation networks leading to increased exciton dissociation and additionally does not disrupt the crystallization of PffBT4T-2OD maintaining a good hole mobility (without PCDTBT8: μ_h = 0.0113 $cm^2V^{-1}s^{-1}$; with 15 wt % PCDTBT8: μ_h = 0.0092 $cm^2V^{-1}s^{-1}$).

1.8.2. PffBT4T-2OD devices with other fullerenes

In one of the most extensive polymer:fullerene combination studies ever reported in the organic photovoltaics literature, Liu *et al.* [122] have tested the use of a large number of different fullerene acceptors ($PC_{71}BM$, $PC_{61}BM$, $TC_{71}BM$, $PC_{61}PM$, $TC_{61}PM$ and ICMA—Figure 1.6) in devices based on the polymer PffBT4T-2OD and on other family related polymers. Their results have shown that the efficiency of the devices obtained using different fullerenes were all very similar (average values within the range 9.3–10.3%) and this observation led these authors to conclude that the aggregation behaviour of PffBT4T-2OD is insensitive to the presence of the fullerene acceptor and can be efficiently used to control the morphology of the corresponding BHJs. This has permitted a near-ideal polymer:fullerene morphology to be created (containing highly crystalline, preferentially orientated, yet small polymer domains) by control

over polymer aggregation during solution casting. The highest efficiency devices with an average PCE of 10.3% were obtained with the fullerene $TC_{71}BM$ (Figure 1.6).

More recently Zhang *et al.* [129] studied the effect of three different fullerene acceptors ($PC_{71}BM$, $PC_{61}BM$ and ICBA) on the performance of solar cells based on PffBT4T-2OD. Here it should be noted that the fullerene bisadduct ICBA has not been included in the previous extensive work by Liu et al. [122]. These authors have found that although PffBT4T-2OD:ICBA devices had a much higher V_{oc} (0.94 V) than the corresponding devices using $PC_{71}BM$ (0.76 V) and $PC_{61}BM$ (0.77 V), their efficiency (average PCE of 2.78%) was much lower than the efficiency of corresponding devices based on $PC_{71}BM$ (average PCE of 8.93%) and $PC_{61}BM$ (average PCE of 8.15%). Interestingly, these results do not seem to support the conclusions of Liu *et al.* Morphological characterization has shown that although the size of phase domains is very similar in the three different BHJs, the fullerene aggregates in the ICBA-based films have a reduced degree of order. Furthermore, due to the high LUMO level of ICBA, the corresponding BHJs are characterised by a lower initial exciton dissociation and this associated with the reduced ordering within the ICBA domains results in increased geminate recombination of the photogenerated electrons in the fullerene-rich domains and a consequently reduced PCE of the corresponding devices.

1.9 Summary and Outlook

Although non-fullerene acceptors have now surpassed fullerenes in terms of performance in OPVs, the research for developing new fullerenes and the morphological and efficiency optimization of polymer:fullerene solar cells, remains very intense. In this introduction the most relevant OPV studies, from a morphological viewpoint, involving BHJs of conjugated polymers PTB7, PTB7-Th and PffBT4T-2OD with fullerene acceptors, over the last 3 years (from 2016 onwards), were reviewed. Considering the efficiency improvements over the last three years, these were predominately driven by the optimization of the morphology at the nanoscale level of the photoactive blend. Some of the most relevant achievements reviewed include the development of single-junction OPVs with PCE > 14% based on ternary BHJs and also new developments on understanding the mechanism of the additives as morphological enhancers. Although many new different fullerenes have been synthesized and tested for OPV devices, in general these did not outperform the standard $PC_{71}BM$, which keeps unthreatened its leading position, as the most reliable and popular fullerene within the OPV research. The addition of two or more addends to the fullerene buckyball is known to increase its LUMO level and consequently

increase the V_{oc} of the corresponding OPV devices. However, most devices based on these multi-adduct fullerenes fail to maintain high J_{sc} and FF values and as a result the overall device efficiency is usually worse than in reference devices with the standard $PC_{71}BM$. The addition of two or more adducts usually degrades the device efficiency for two main reasons: they decrease the overall crystallinity of the fullerene and as a result the electron mobility decreases; and, second, they affect drastically the degree of phase separation from the polymer and the consequent polymer:fullerene morphology at the nanoscale. The major challenge in this topic lies in finding the optimal compromise among a combination of fullerene properties that often works in opposite directions.

As indicated, the strategies followed, so far, for synthesizing new fullerene acceptors for OPVs have been largely based on single-molecule properties and nowadays theoretical calculations (*ab initio*) can, for example, estimate with high accuracy the HOMO-LUMO levels of new fullerene acceptors. However, single-molecule properties cannot account for the whole story, as they completely neglect all aspects related to molecular interactions and structural organization in the solid state, including degree of crystallinity and crystallographic structure, which are crucially important for properties such as the electron mobility. Therefore, one research direction that is still clearly underexplored and poorly understood concerns the fundamental study of the relationship between the chemical structure of single fullerene molecules, their 3-D molecular packing in the solid state and the corresponding electrical properties. This will require the combination of a battery of experimental and theoretical techniques including: organic synthesis of new fullerenes; X-ray diffraction characterization of solid-state structures; computational modelling (ab initio, molecular dynamics); and measurement of charge mobilities, among others. This fundamental knowledge will certainly prove very useful in designing better strategies for the synthesis of new fullerenes for highly efficient OPV applications. In this way, one of the priority work will be in new fullerene acceptors, mostly focused in how the new molecular structures can influence the overall OPV figures of merit.

Most optimized morphologies still cannot remain stable for long periods of time due to molecular diffusion and molecular degradation of the BHJ components under real device operation. Therefore, further research is needed for improving the morphological stability of these BHJs. Moreover, and besides new acceptor materials, the morphological conformation of OPV active layer, needs to be improved. As mentioned above, the use of additives is currently one of the most interesting processes to attain more favorable morphologies.

The development and commercialization of next-generation OPVs is a highly multidisciplinary research subject and only through a sustained cooperative effort involving the expertise of material chemists, physicists and engineers it will be possible to succeed.

Considering these ideas, the work in this thesis will be organized as follows:

In this first Chapter, the basic concepts on OPVs was presented. Additionally, a state of art of the most important BHJ-OPVs structures and materials was also made with a particular focus in considering both new fullerene derivatives acceptors and the use of additivess to improve the morphology of the active layer. All these concepts introduce the main focus of this thesis.

In Chapter II, a first set of eight phenyl-substituted N-methyl-fulleropyrrolidine acceptors (four C_{60} and four C_{70} derivatives) is presented, that were synthetized for the first time. OPVs with these new acceptors were fabricated, fully characterized and the corresponding J-V curves were simulated. A correlation between fullerene structure and device performance is performed allowing an assessment of the influence of new structures in the overall OPV performance.

A second group of eight novel N-methyl-fulleropyrrolidine acceptors (four C_{60} and four C_{70} derivatives) containing thiophene and carbazole pendant groups is presented in Chapter three. These fullerenes were synthetized following the same chemical routes as the previous set. The fabricated OPVs with these new set of acceptors exhibits similar overall performance to the first set of acceptors.

Chapter IV is focused in studying the impact of several different additives on the active layer morphology and photovoltaic performance of devices based on the system PffBT4T-2OD:PC_{71}BM. Whilst some of the additives improve device performance, other additives were deliberately chosen that degrade the morphology and device efficiency. A deep structural analysis is presented and correlated with the electrical properties. A general understanding of the relationship between type of additive, device morphology and efficiency is developed.

References

[1] Y.-C. Huang, H.-C. Cha, C.-Y. Chen, C.-S. Tsao, A universal roll-to-roll slot-die coating approach towards high-efficiency organic photovoltaics, Progress in Photovoltaics: Research and Applications, 25 (2017) 928-935.
[2] D. Vak, H. Weerasinghe, J. Ramamurthy, J. Subbiah, M. Brown, D.J. Jones, Reverse gravure coating for roll-to-roll production of organic photovoltaics, Solar Energy Materials and Solar Cells, 149 (2016) 154-161.
[3] T.R. Andersen, N.A. Cooling, F. Almyahi, A.S. Hart, N.C. Nicolaidis, K. Feron, M. Noori, B. Vaughan, M.J. Griffith, W.J. Belcher, P.C. Dastoor, Fully roll-to-roll prepared organic solar cells in normal geometry with a sputter-coated aluminium top-electrode, Solar Energy Materials and Solar Cells, 149 (2016) 103-109.
[4] R. Søndergaard, M. Hösel, D. Angmo, T.T. Larsen-Olsen, F.C. Krebs, Roll-to-roll fabrication of polymer solar cells, Materials Today, 15 (2012) 36-49.
[5] C. Kapnopoulos, E.D. Mekeridis, L. Tzounis, C. Polyzoidis, A. Zachariadis, S. Tsimikli, C. Gravalidis, A. Laskarakis, N. Vouroutzis, S. Logothetidis, Fully gravure printed organic photovoltaic modules: A straightforward process with a high potential for large scale production, Solar Energy Materials and Solar Cells, 144 (2016) 724-731.
[6] Y. Galagan, H. Fledderus, H. Gorter, H.H. t Mannetje, S. Shanmugam, R. Mandamparambil, J. Bosman, J. Rubingh, J.P. Teunissen, A. Salem, I.G. de Vries, R. Andriessen, W.A. Groen, Roll-to-Roll Slot-Die Coated Organic Photovoltaic (OPV) Modules with High Geometrical Fill Factors, Energy Technol., 3 (2015) 834-842.
[7] Y. Cui, H.F. Yao, J.Q. Zhang, T. Zhang, Y.M. Wang, L. Hong, K.H. Xian, B.W. Xu, S.Q. Zhang, J. Peng, Z.X. Wei, F. Gao, J.H. Hou, Over 16% efficiency organic photovoltaic cells enabled by a chlorinated acceptor with increased open-circuit voltages, Nature Communications, 10 (2019) 8.
[8] L. Meng, Y. Zhang, X. Wan, C. Li, X. Zhang, Y. Wang, X. Ke, Z. Xiao, L. Ding, R. Xia, H.-L. Yip, Y. Cao, Y. Chen, Organic and solution-processed tandem solar cells with 17.3% efficiency, Science, (2018).
[9] P. Cheng, G. Li, X.W. Zhan, Y. Yang, Next-generation organic photovoltaics based on non-fullerene acceptors, Nature Photonics, 12 (2018) 131-142.
[10] J.Q. Zhang, H.S. Tan, X.G. Guo, A. Facchetti, H. Yan, Material insights and challenges for non-fullerene organic solar cells based on small molecular acceptors, Nat. Energy, 3 (2018) 720-731.
[11] C.Q. Yan, S. Barlow, Z.H. Wang, H. Yan, A.K.Y. Jen, S.R. Marder, X.W. Zhan, Non-fullerene acceptors for organic solar cells, Nature Reviews Materials, 3 (2018).
[12] J. Hou, O. Inganäs, R.H. Friend, F. Gao, Organic solar cells based on non-fullerene acceptors, Nat. Mater., 17 (2018) 119.
[13] W.Q. Chen, Q.C. Zhang, Recent progress in non-fullerene small molecule acceptors in organic solar cells (OSCs), Journal of Materials Chemistry C, 5 (2017) 1275-1302.
[14] Y.Z. Lin, X.W. Zhan, Non-fullerene acceptors for organic photovoltaics: an emerging horizon, Materials Horizons, 1 (2014) 470-488.

[15] A. Määttänen, P. Ihalainen, P. Pulkkinen, S. Wang, H. Tenhu, J. Peltonen, Inkjet-Printed Gold Electrodes on Paper: Characterization and Functionalization, ACS Applied Materials & Interfaces, 4 (2012) 955-964.
[16] Y. Noguchi, T. Sekitani, T. Yokota, T. Someya, Direct inkjet printing of silver electrodes on organic semiconductors for thin-film transistors with top contact geometry, Applied Physics Letters, 93 (2008).
[17] S. Norita, D. Kumaki, Y. Kobayashi, T. Sato, K. Fukuda, S. Tokito, Inkjet-printed copper electrodes using photonic sintering and their application to organic thin-film transistors, Organic Electronics, 25 (2015) 131-134.
[18] K. Wang, C. Liu, T. Meng, C. Yi, X. Gong, Inverted organic photovoltaic cells, Chem. Soc. Rev., 45 (2016) 2937-2975.
[19] M. Dekker, Handbook of Conducting Polymers, 1 ed., New York, 1985.
[20] S. Karg, W. Riess, V. Dyakonov, M. Schwoerer, ELECTRICAL AND OPTICAL CHARACTERIZATION OF POLY(PHENYLENE-VINYLENE) LIGHT-EMITTING-DIODES, Synthetic Metals, 54 (1993) 427-433.
[21] J.H. Seo, Y. Jin, J.Z. Brzezinski, B. Walker, T.Q. Nguyen, Exciton Binding Energies in Conjugated Polyelectrolyte Films, Chemphyschem, 10 (2009) 1023-1027.
[22] S.M. Menke, N.A. Ran, G.C. Bazan, R.H. Friend, Understanding Energy Loss in Organic Solar Cells: Toward a New Efficiency Regime, Joule, 2 (2018) 25-35.
[23] M.C. Scharber, N.S. Sariciftci, Efficiency of bulk-heterojunction organic solar cells, Progress in Polymer Science, 38 (2013) 1929-1940.
[24] D. Baran, T. Kirchartz, S. Wheeler, S. Dimitrov, M. Abdelsamie, J. Gorman, R.S. Ashraf, S. Holliday, A. Wadsworth, N. Gasparini, P. Kaienburg, H. Yan, A. Amassian, C.J. Brabec, J.R. Durrant, I. McCulloch, Reduced voltage losses yield 10% efficient fullerene free organic solar cells with > 1 V open circuit voltages, Energy & Environmental Science, 9 (2016) 3783-3793.
[25] W.A. Luhman, R.J. Holmes, Investigation of Energy Transfer in Organic Photovoltaic Cells and Impact on Exciton Diffusion Length Measurements, Advanced Functional Materials, 21 (2011) 764-771.
[26] O.V. Mikhnenko, H. Azimi, M. Scharber, M. Morana, P.W.M. Blom, M.A. Loi, Exciton diffusion length in narrow bandgap polymers, Energy & Environmental Science, 5 (2012) 6960-6965.
[27] S.M. Menke, R.J. Holmes, Exciton diffusion in organic photovoltaic cells, Energy & Environmental Science, 7 (2014) 499-512.
[28] Y. Tamai, H. Ohkita, H. Benten, S. Ito, Exciton Diffusion in Conjugated Polymers: From Fundamental Understanding to Improvement in Photovoltaic Conversion Efficiency, The Journal of Physical Chemistry Letters, 6 (2015) 3417-3428.
[29] B. Siegmund, M.T. Sajjad, J. Widmer, D. Ray, C. Koerner, M. Riede, K. Leo, I.D.W. Samuel, K. Vandewal, Exciton Diffusion Length and Charge Extraction Yield in Organic Bilayer Solar Cells, Advanced Materials, 29 (2017) 1604424.
[30] C. Groves, O.G. Reid, D.S. Ginger, Heterogeneity in Polymer Solar Cells: Local Morphology and Performance in Organic Photovoltaics Studied with Scanning Probe Microscopy, Accounts of Chemical Research, 43 (2010) 612-620.
[31] R.M. Beal, A. Stavrinadis, J.H. Warner, J.M. Smith, H.E. Assender, A.A.R. Watt, The Molecular Structure of Polymer-Fullerene Composite Solar Cells and Its Influence on Device Performance, Macromolecules, 43 (2010) 2343-2348.

[32] A.F. Tillack, K.M. Noone, B.A. MacLeod, D. Nordlund, K.P. Nagle, J.A. Bradley, S.K. Hau, H.L. Yip, A.K.Y. Jen, G.T. Seidler, D.S. Ginger, Surface Characterization of Polythiophene:Fullerene Blends on Different Electrodes Using Near Edge X-ray Absorption Fine Structure, Acs Applied Materials & Interfaces, 3 (2011) 726-732.
[33] P. Müller-Buschbaum, The Active Layer Morphology of Organic Solar Cells Probed with Grazing Incidence Scattering Techniques, Advanced Materials, 26 (2014) 7692-7709.
[34] Y. Wu, Z.Y. Wang, X.Y. Meng, W. Ma, Morphology Analysis of Organic Solar Cells with Synchrotron Radiation Based Resonant Soft X-Ray Scattering, Progress in Chemistry, 29 (2017) 93-101.
[35] C. Kapnopoulos, E.D. Mekeridis, L. Tzounis, C. Polyzoidis, S. Tsimikli, C. Gravalidis, A. Zachariadis, A. Laskarakis, S. Logothetidis, Gravure printed organic photovoltaic modules onto flexible substrates consisting of a P3HT:PCBM photoactive blend, Mater. Today-Proc., 3 (2016) 746-757.
[36] A.J. Pearson, T. Wang, A.D.F. Dunbar, H.N. Yi, D.C. Watters, D.M. Coles, P.A. Staniec, A. Iraqi, R.A.L. Jones, D.G. Lidzey, Morphology Development in Amorphous Polymer: Fullerene Photovoltaic Blend Films During Solution Casting, Advanced Functional Materials, 24 (2014) 659-667.
[37] A.J. Parnell, A.D.F. Dunbar, A.J. Pearson, P.A. Staniec, A.J.C. Dennison, H. Hamamatsu, M.W.A. Skoda, D.G. Lidzey, R.A.L. Jones, Depletion of PCBM at the Cathode Interface in P3HT/PCBM Thin Films as Quantified via Neutron Reflectivity Measurements, Advanced Materials, 22 (2010) 2444-2447.
[38] Y. Yan, X. Liu, T. Wang, Conjugated-Polymer Blends for Organic Photovoltaics: Rational Control of Vertical Stratification for High Performance, Advanced Materials, 29 (2017) 22.
[39] D.A. Chen, A. Nakahara, D.G. Wei, D. Nordlund, T.P. Russell, P3HT/PCBM Bulk Heterojunction Organic Photovoltaics: Correlating Efficiency and Morphology, Nano Letters, 11 (2011) 561-567.
[40] Y. Zhang, A.J. Parnell, F. Pontecchiani, J.F.K. Cooper, R.L. Thompson, R.A.L. Jones, S.M. King, D.G. Lidzey, G. Bernardo, Understanding and controlling morphology evolution via DIO plasticization in PffBT4T-2OD/PC71BM devices, Sci. Rep., 7 (2017) 44269.
[41] M.J. Hollamby, Practical applications of small-angle neutron scattering, Physical Chemistry Chemical Physics, 15 (2013) 10566-10579.
[42] N.K. Elumalai, A. Uddin, Open circuit voltage of organic solar cells: an in-depth review, Energy & Environmental Science, 9 (2016) 391-410.
[43] C.J. Brabec, A. Cravino, D. Meissner, N.S. Sariciftci, T. Fromherz, M.T. Rispens, L. Sanchez, J.C. Hummelen, Origin of the open circuit voltage of plastic solar cells, Advanced Functional Materials, 11 (2001) 374-380.
[44] M.C. Scharber, D. Wuhlbacher, M. Koppe, P. Denk, C. Waldauf, A.J. Heeger, C.L. Brabec, Design rules for donors in bulk-heterojunction solar cells - Towards 10 % energy-conversion efficiency, Advanced Materials, 18 (2006) 789-+.
[45] K. Vandewal, K. Tvingstedt, A. Gadisa, O. Inganas, J.V. Manca, On the origin of the open-circuit voltage of polymer-fullerene solar cells, Nature Materials, 8 (2009) 904-909.
[46] D. Qian, Z. Zheng, H. Yao, W. Tress, T.R. Hopper, S. Chen, S. Li, J. Liu, S. Chen, J. Zhang, X.-K. Liu, B. Gao, L. Ouyang, Y. Jin, G. Pozina, I.A. Buyanova, W.M. Chen, O. Inganäs, V. Coropceanu, J.-L. Bredas, H. Yan, J. Hou, F. Zhang, A.A. Bakulin, F. Gao, Design rules for minimizing voltage losses in high-efficiency organic solar cells, Nature Materials, 17 (2018) 703-709.

[47] Y.M. Wang, D.P. Qian, Y. Cui, H.T. Zhang, J.H. Hou, K. Vandewal, T. Kirchartz, F. Gao, Optical Gaps of Organic Solar Cells as a Reference for Comparing Voltage Losses, Advanced Energy Materials, 8 (2018).
[48] I. Ramirez, M. Causa, Y.F. Zhong, N. Banerji, M. Riede, Key Tradeoffs Limiting the Performance of Organic Photovoltaics, Advanced Energy Materials, 8 (2018).
[49] S. Banerjee, S.S.K. Iyer, Short-circuit current density and spectral response modelling of bulk-heterojunction solar cells, Organic Electronics, 11 (2010) 2032-2036.
[50] F. Cheng, G. Fang, X. Fan, N. Liu, N. Sun, P. Qin, Q. Zheng, J. Wan, X. Zhao, Enhancing the short-circuit current and efficiency of organic solar cells using MoO3 and CuPc as buffer layers, Solar Energy Materials and Solar Cells, 95 (2011) 2914-2919.
[51] J.C. Wang, S.Q. Shi, C.W. Leung, S.P. Lau, K.Y. Wong, P.K.L. Chan, Short circuit current improvement in planar heterojunction organic solar cells by multijunction charge transfer, Applied Physics Letters, 100 (2012).
[52] N. Lu, L. Li, P. Sun, M. Liu, Short-circuit current model of organic solar cells, Chemical Physics Letters, 614 (2014) 27-30.
[53] M.S. Kim, B.G. Kim, J. Kim, Effective Variables To Control the Fill Factor of Organic Photovoltaic Cells, Acs Applied Materials & Interfaces, 1 (2009) 1264-1269.
[54] B.Y. Qi, J.Z. Wang, Fill factor in organic solar cells, Physical Chemistry Chemical Physics, 15 (2013) 8972-8982.
[55] D. Gupta, S. Mukhopadhyay, K.S. Narayan, Fill factor in organic solar cells, Solar Energy Materials and Solar Cells, 94 (2010) 1309-1313.
[56] M.-H. Jao, H.-C. Liao, W.-F. Su, Achieving a high fill factor for organic solar cells, Journal of Materials Chemistry A, 4 (2016) 5784-5801.
[57] V.A. Trukhanov, V.V. Bruevich, D.Y. Paraschuk, Fill factor in organic solar cells can exceed the Shockley-Queisser limit, Scientific Reports, 5 (2015).
[58] R.S. Gebhardt, P.F. Du, O. Wodo, B. Ganapathysubramanian, A data-driven identification of morphological features influencing the fill factor and efficiency of organic photovoltaic devices, Computational Materials Science, 129 (2017) 220-225.
[59] J.K. Tan, R.Q. Png, C. Zhao, P.K.H. Ho, Ohmic transition at contacts key to maximizing fill factor and performance of organic solar cells, Nature Communications, 9 (2018).
[60] Y. Zang, Q. Xin, J. Zhao, J. Lin, Effect of Active Layer Thickness on the Performance of Polymer Solar Cells Based on a Highly Efficient Donor Material of PTB7-Th, Journal of Physical Chemistry C, 122 (2018) 16532-16539.
[61] W. Huang, B. Zhu, S.-Y. Chang, S.L. Zhu, P. Cheng, Y.-T. Hsieh, L. Meng, R. Wang, C. Wang, C. Zhu, C. McNeill, M. Wang, Y. Yang, High Mobility Indium Oxide Electron Transport Layer for an Efficient Charge Extraction and Optimized Nanomorphology in Organic Photovoltaics, Nano Letters, 18 (2018) 5805-5811.
[62] H.J. Jhuo, S.H. Liao, Y.L. Li, P.N. Yeh, S.A. Chen, W.R. Wu, C.J. Su, J.J. Lee, N.L. Yamada, U.S. Jeng, The Novel Additive 1-Naphthalenethiol Opens a New Processing Route to Efficiency-Enhanced Polymer Solar Cells, Advanced Functional Materials, 26 (2016) 3094-3104.

[63] S. Komilian, O. Oklobia, T. Sadat-Shafai, Controlling intercalations of PBDTTT-EFT side chain to initiate suitable network for charge extraction in PBDTTT-EFT:PC71BM blended bulk heterojunction solar cell, Solar Energy Materials and Solar Cells, 175 (2018) 35-40.
[64] L. Schmidt-Mende, J. Weickert, Organic and Hybrid Solar Cells: An Introduction, de Gruyter, Berlin, Germany, 2016.
[65] P. Wurfel, Physics of Solar Cells: From Basic Principles to Advanced Concepts, Wiley-VCH, Weinheim, Germany, 2009.
[66] S.R. Cowan, R.A. Street, S.N. Cho, A.J. Heeger, Transient photoconductivity in polymer bulk heterojunction solar cells: Competition between sweep-out and recombination, Physical Review B, 83 (2011) 8.
[67] P. Cheng, X. Zhan, Stability of organic solar cells: challenges and strategies, Chem. Soc. Rev., 45 (2016) 2544-2582.
[68] T. Xu, L. Yu, How to design low bandgap polymers for highly efficient organic solar cells, Mater. Today, 17 (2014) 11-15.
[69] C. Liu, K. Wang, X. Gong, A.J. Heeger, Low bandgap semiconducting polymers for polymeric photovoltaics, Chem. Soc. Rev., 45 (2016) 4825-4846.
[70] S. Holliday, Y.L. Li, C.K. Luscombe, Recent advances in high performance donor-acceptor polymers for organic photovoltaics, Progress in Polymer Science, 70 (2017) 34-51.
[71] G. Bernardo, D.G. Bucknall, Recent Progress in the Understanding and Manipulation of Morphology in Polymer: Fullerene Photovoltaic Cells, IntechOpen2013.
[72] C. Liu, K. Wang, X.W. Hu, Y.L. Yang, C.H. Hsu, W. Zhang, S. Xiao, X. Gong, Y. Cao, Molecular Weight Effect on the Efficiency of Polymer Solar Cells, Acs Applied Materials & Interfaces, 5 (2013) 12163-12167.
[73] L.Y. Lu, L.P. Yu, Understanding Low Bandgap Polymer PTB7 and Optimizing Polymer Solar Cells Based on It, Adv. Mater., 26 (2014) 4413-4430.
[74] N.S. Sariciftci, L. Smilowitz, A.J. Heeger, F. Wudl, Photoinduced Electron-Transfer From a Conducting Polymer to Buckminsterfullerene, Science, 258 (1992) 1474-1476.
[75] J.C. Hummelen, B.W. Knight, F. Lepeq, F. Wudl, J. Yao, C.L. Wilkins, PREPARATION AND CHARACTERIZATION OF FULLEROID AND METHANOFULLERENE DERIVATIVES, J. Org. Chem., 60 (1995) 532-538.
[76] G. Yu, J. Gao, J.C. Hummelen, F. Wudl, A.J. Heeger, Polymer Photovoltaic Cells: Enhanced Efficiencies via a Network of Internal Donor-Acceptor Heterojunctions, Science, 270 (1995) 1789-1791.
[77] M.M. Wienk, J.M. Kroon, W.J.H. Verhees, J. Knol, J.C. Hummelen, P.A. van Hal, R.A.J. Janssen, Efficient methano 70 fullerene/MDMO-PPV bulk heterojunction photovoltaic cells, Angew. Chem. Int. Ed., 42 (2003) 3371-3375.
[78] M. Williams, N.R. Tummala, S.G. Aziz, C. Risko, J.L. Bredas, Influence of Molecular Shape on Solid-State Packing in Disordered PC61BM and PC71BM Fullerenes, Journal of Physical Chemistry Letters, 5 (2014) 3427-3433.
[79] F. Zhang, Z. Zhuo, J. Zhang, X. Wang, X. Xu, Z. Wang, Y. Xin, J. Wang, J. Wang, W. Tang, Z. Xu, Y. Wang, Influence of PC60BM or PC70BM as electron acceptor on the performance of polymer solar cells, Solar Energy Materials and Solar Cells, 97 (2012) 71-77.

[80] C. McDowell, M. Abdelsamie, M.F. Toney, G.C. Bazan, Solvent Additives: Key Morphology-Directing Agents for Solution-Processed Organic Solar Cells, Advanced Materials, 30 (2018) 1707114.
[81] H.C. Liao, C.C. Ho, C.Y. Chang, M.H. Jao, S.B. Darling, W.F. Su, Additives for morphology control in high-efficiency organic solar cells, Materials Today, 16 (2013) 326-336.
[82] S.J. Lou, J.M. Szarko, T. Xu, L. Yu, T.J. Marks, L.X. Chen, Effects of Additives on the Morphology of Solution Phase Aggregates Formed by Active Layer Components of High-Efficiency Organic Solar Cells, Journal of the American Chemical Society, 133 (2011) 20661-20663.
[83] I. Burgués-Ceballos, F. Machui, J. Min, T. Ameri, M.M. Voigt, Y.N. Luponosov, S.A. Ponomarenko, P.D. Lacharmoise, M. Campoy-Quiles, C.J. Brabec, Solubility Based Identification of Green Solvents for Small Molecule Organic Solar Cells, Advanced Functional Materials, 24 (2014) 1449-1457.
[84] G. Bernardo, A.L. Washington, Y. Zhang, S.M. King, D.T.W. Toolan, M.P. Weir, A.D.F. Dunbar, J.R. Howse, R. Dattani, J.P.A. Fairclough, A.J. Parnell, Does 1,8-diiodooctane affect the aggregation state of PC₇₁BM in solution?, Royal Society Open Science, 5 (2018).
[85] G. Bernardo, A.L. Washington, Y. Zhang, S.M. King, D.T.W. Toolan, M.P. Weir, A.D.F. Dunbar, J.R. Howse, R. Dattani, J.P.A. Fairclough, A.J. Parnell, Data from: Does 1,8-Diiodooctane affect the aggregation state of PC71BM in solution?, Dryad Digital Repository2018.
[86] Y.Y. Liang, Z. Xu, J.B. Xia, S.T. Tsai, Y. Wu, G. Li, C. Ray, L.P. Yu, For the Bright Future-Bulk Heterojunction Polymer Solar Cells with Power Conversion Efficiency of 7.4%, Advanced Materials, 22 (2010) E135-+.
[87] H.Q. Zhou, Y. Zhang, J. Seifter, S.D. Collins, C. Luo, G.C. Bazan, T.Q. Nguyen, A.J. Heeger, High-Efficiency Polymer Solar Cells Enhanced by Solvent Treatment, Advanced Materials, 25 (2013) 1646-1652.
[88] Z. He, C. Zhong, S. Su, M. Xu, H. Wu, Y. Cao, Enhanced power-conversion efficiency in polymer solar cells using an inverted device structure, Nat. Photonics, 6 (2012) 591-595.
[89] M. Li, W. Zhang, X. Tang, J. Jin, H. Wang, L. Chen, W. Lv, R. Chen, W. Huang, Bromine-Terminated Additives for Phase-Separated Morphology Control of PTB7:PC71BM-Based Polymer Solar Cells, ACS Sustainable Chemistry & Engineering, 5 (2017) 11668-11675.
[90] S.O. Oseni, G.T. Mola, The effect of uni- and binary solvent additives in PTB7:PC61BM based solar cells, Solar Energy, 150 (2017) 66-72.
[91] Y.F. Zheng, T. Goh, P. Fan, W. Shi, J.S. Yu, A.D. Taylor, Toward Efficient Thick Active PTB7 Photovoltaic Layers Using Diphenyl Ether as a Solvent Additive, Acs Applied Materials & Interfaces, 8 (2016) 15724-15731.
[92] Y. Zheng, G. Wang, D. Huang, J. Kong, T. Goh, W. Huang, J. Yu, A.D. Taylor, Binary Solvent Additives Treatment Boosts the Efficiency of PTB7:PCBM Polymer Solar Cells to Over 9.5%, Solar RRL, 2 (2018) 1700144.
[93] X. Zhao, J. Xiang, D. Liu, D. Zhou, G. Wang, G. Zhou, K. Alameh, B. Ding, Q. Song, Impact of alkyl chain length of 1,n-diiodoalkanes on PC71BM distribution in both bulk and air surface of PTB7:PC71BM film, Organic Electronics, 37 (2016) 358-365.
[94] Y. Li, Z. Xu, S. Zhao, D. Huang, L. Zhao, C. Zhang, J. Zhao, P. Wang, Y. Zhu, Enhanced carrier dynamics of PTB7:PC71BM based bulk heterojunction organic solar cells by the incorporation of formic acid, Organic Electronics, 28 (2016) 275-280.

[95] J. Chen, L. Zhang, X. Jiang, K. Gao, F. Liu, X. Gong, J. Chen, Y. Cao, Using o-Chlorobenzaldehyde as a Fast Removable Solvent Additive during Spin-Coating PTB7-Based Active Layers: High Efficiency Thick-Film Polymer Solar Cells, Advanced Energy Materials, 7 (2017) 1601344.
[96] L. Ciammaruchi, F. Brunetti, I. Visoly-Fisher, Solvent effects on the morphology and stability of PTB7:PCBM based solar cells, Solar Energy, 137 (2016) 490-499.
[97] S.B. Dkhil, M. Pfannmöller, M.I. Saba, M. Gaceur, H. Heidari, C. Videlot-Ackermann, O. Margeat, A. Guerrero, J. Bisquert, G. Garcia-Belmonte, A. Mattoni, S. Bals, J. Ackermann, Toward High-Temperature Stability of PTB7-Based Bulk Heterojunction Solar Cells: Impact of Fullerene Size and Solvent Additive, Advanced Energy Materials, 7 (2017) 1601486.
[98] D. Bartesaghi, G. Ye, R.C. Chiechi, L.J.A. Koster, Compatibility of PTB7 and [70]PCBM as a Key Factor for the Stability of PTB7:[70]PCBM Solar Cells, Advanced Energy Materials, 6 (2016) 1502338.
[99] Y.J. He, M. Shao, K. Xiao, S.C. Smith, K.L. Hong, High-performance polymer photovoltaics based on rationally designed fullerene acceptors, Sol. Energy Mater. Sol. Cells, 118 (2013) 171-178.
[100] M. Karakawa, T. Nagai, K. Adachi, Y. Ie, Y. Aso, N-phenyl 60 fulleropyrrolidines: alternative acceptor materials to PC61BM for high performance organic photovoltaic cells, J. Mater. Chem. A, 2 (2014) 20889-20895.
[101] N.W. Tseng, Y. Yu, Y.K. Li, J.B. Zhao, S.K. So, H. Yan, K.M. Ng, Isobenzofulvene-fullerene mono-adducts for organic photovoltaic applications, J. Mater. Chem. C, 3 (2015) 977-980.
[102] S.H. Huang, G.Y. Zhang, N.S. Knutson, M.T. Fontana, R.C. Huber, A.S. Ferreira, S.H. Tolbert, B.J. Schwartz, Y. Rubin, Beyond PCBM: methoxylated 1,4-bisbenzyl 60 fullerene adducts for efficient organic solar cells, J. Mater. Chem. A, 4 (2016) 416-424.
[103] P. Nagarjuna, A. Bagui, J.H. Hou, S.P. Singh, New Electron Acceptor Derived from Fluorene: Synthesis and Its Photovoltaic Properties, J. Phys. Chem. C, 120 (2016) 13390-13397.
[104] P. Nagarjuna, A. Bagui, A. Garg, V. Gupta, S.P. Singh, One-Step Synthesis of New Electron Acceptor for High Efficiency Solution Processable Organic Solar Cells, J. Phys. Chem. C, 121 (2017) 26615-26621.
[105] J.D. Roehling, D. Baran, J. Sit, T. Kassar, T. Ameri, T. Unruh, C.J. Brabec, A.J. Moulé, Nanoscale Morphology of PTB7 Based Organic Photovoltaics as a Function of Fullerene Size, Scientific Reports, 6 (2016) 30915.
[106] P. Cheng, Y.F. Li, X.W. Zhan, Efficient ternary blend polymer solar cells with indene-C-60 bisadduct as an electron-cascade acceptor, Energy & Environmental Science, 7 (2014) 2005-2011.
[107] G. Ma, Z. Liu, N. Wang, Efficient ternary polymer solar cells with dihydronaphthyl-based C60 bisadduct as an third component material, Solar Energy, 170 (2018) 164-173.
[108] L. Fernandes, H. Gaspar, J.P.C. Tome, F. Figueira, G. Bernardo, Thermal stability of low-bandgap copolymers PTB7 and PTB7-Th and their bulk heterojunction composites, Polymer Bulletin, 75 (2018) 515-532.
[109] S.Q. Zhang, L. Ye, W.C. Zhao, D.L. Liu, H.F. Yao, J.H. Hou, Side Chain Selection for Designing Highly Efficient Photovoltaic Polymers with 2D-Conjugated Structure, Macromolecules, 47 (2014) 4653-4659.
[110] W.C. Huang, E. Gann, L. Thomsen, C.K. Dong, Y.B. Cheng, C.R. McNeill, Unraveling the Morphology of High Efficiency Polymer Solar Cells Based on the Donor Polymer PBDTTT-EFT, Adv. Energy Mater., 5 (2015) 11.

[111] Q. Wan, X. Guo, Z. Wang, W. Li, B. Guo, W. Ma, M. Zhang, Y. Li, 10.8% Efficiency Polymer Solar Cells Based on PTB7-Th and PC71BM via Binary Solvent Additives Treatment, Advanced Functional Materials, 26 (2016) 6635-6640.
[112] R. Fan, Z.X. Huai, Y.S. Sun, X.W. Li, G.S. Fu, S.H. Huang, L.X. Wang, S.P. Yang, Enhanced performance of polymer solar cells based on PTB7-Th: PC71BM by doping with 1-bromo-4-nitrobenzene, Journal of Materials Chemistry C, 5 (2017) 10985-10990.
[113] Z. Xiao, X. Jia, L.M. Ding, Ternary organic solar cells offer 14% power conversion efficiency, Science Bulletin, 62 (2017) 1562-1564.
[114] L.K. Jagadamma, M.T. Sajjad, V. Savikhin, M.F. Toney, I.D.W. Samuel, Correlating photovoltaic properties of a PTB7-Th:PC71BM blend to photophysics and microstructure as a function of thermal annealing, Journal of Materials Chemistry A, 5 (2017) 14646-14657.
[115] T. Kobori, T. Fukuda, Effect of optical intensity distribution on device performances of PTB7-Th:PC71BM-based organic photovoltaic cells, Organic Electronics, 51 (2017) 76-85.
[116] N. Jain, N. Chandrasekaran, A. Sadhanala, R.H. Friend, C.R. McNeill, D. Kabra, Interfacial disorder in efficient polymer solar cells: the impact of donor molecular structure and solvent additives, J. Mater. Chem. A, 5 (2017) 24749-24757.
[117] A.J. Pearson, P.E. Hopkinson, E. Couderc, K. Domanski, M. Abdi-Jalebi, N.C. Greenham, Critical light instability in CB/DIO processed PBDTTT-EFT:PC71BM organic photovoltaic devices, Org. Electron., 30 (2016) 225-236.
[118] Q. Liu, J. Toudert, F. Liu, P. Mantilla-Perez, M.M. Bajo, T.P. Russell, J. Martorell, Circumventing UV Light Induced Nanomorphology Disorder to Achieve Long Lifetime PTB7-Th:PCBM Based Solar Cells, Advanced Energy Materials, 7 (2017) 1701201.
[119] W.C. Huang, E. Gann, N. Chandrasekaran, S.K.K. Prasad, S.Y. Chang, L. Thomsen, D. Kabra, J.M. Hodgkiss, Y.B. Cheng, Y. Yang, C.R. McNeill, Influence of Fullerene Acceptor on the Performance, Microstructure, and Photophysics of Low Bandgap Polymer Solar Cells, Adv. Energy Mater., 7 (2017) 10.
[120] C.H. Zhang, S. Langner, A.V. Mumyatov, D.V. Anokhin, J. Min, J.D. Perea, K.L. Gerasimov, A. Osvet, D.A. Ivanov, P. Troshin, N. Li, C.J. Brabec, Understanding the correlation and balance between the miscibility and optoelectronic properties of polymer-fullerene solar cells, J. Mater. Chem. A, 5 (2017) 17570-17579.
[121] P. Nagarjuna, A. Bagui, V. Gupta, S.P. Singh, A highly efficient PTB7-Th polymer donor bulk hetero-junction solar cell with increased open circuit voltage using fullerene acceptor CN-PC70BM, Org. Electron., 43 (2017) 262-267.
[122] Y. Liu, J. Zhao, Z. Li, C. Mu, W. Ma, H. Hu, K. Jiang, H. Lin, H. Ade, H. Yan, Aggregation and morphology control enables multiple cases of high-efficiency polymer solar cells, Nature Communications, 5 (2014).
[123] W. Ma, G. Yang, K. Jiang, H. Carpenter Joshua, Y. Wu, X. Meng, T. McAfee, J. Zhao, C. Zhu, C. Wang, H. Ade, H. Yan, Influence of Processing Parameters and Molecular Weight on the Morphology and Properties of High-Performance PffBT4T-2OD:PC71BM Organic Solar Cells, Adv. Energy Mater., 5 (2015) 1501400.

[124] X. Zhang, D. Zheng, S. Xing, H. Wang, J. Huang, J. Yu, Precisely control the morphology and crystallization of temperature-dependent aggregation bulk heterojunction by using co-solvent system for optimized light intensity distribution and its effect on thick active layer polymer solar cells, Sol. Energy, 147 (2017) 106-112.
[125] J. Zhao, S. Zhao, Z. Xu, B. Qiao, D. Huang, L. Zhao, Y. Li, Y. Zhu, P. Wang, Revealing the Effect of Additives with Different Solubility on the Morphology and the Donor Crystalline Structures of Organic Solar Cells, ACS Appl. Mater. Interfaces, 8 (2016) 18231-18237.
[126] T. Umeyama, K. Igarashi, D. Sakamaki, S. Seki, H. Imahori, Unique cohesive nature of the [small beta]1-isomer of [70]PCBM fullerene on structures and photovoltaic performances of bulk heterojunction films with PffBT4T-2OD polymers, Chem. Commun., 54 (2018) 405-408.
[127] S. Vidal, M. Izquierdo, W.K. Law, K. Jiang, S. Filippone, J. Perles, H. Yan, N. Martin, Photochemical site-selective synthesis of [70]methanofullerenes, Chem. Commun., 52 (2016) 12733-12736.
[128] W. Li, J. Cai, F. Cai, Y. Yan, H. Yi, R.S. Gurney, D. Liu, A. Iraqi, T. Wang, Achieving over 11% power conversion efficiency in PffBT4T-2OD-based ternary polymer solar cells with enhanced open-circuit-voltage and suppressed charge recombination, Nano Energy, 44 (2018) 155-163.
[129] Y. Zhang, A.J. Parnell, O. Blaszczyk, A.J. Musser, I.D.W. Samuel, D.G. Lidzey, G. Bernardo, Effect of fullerene acceptor on the performance of solar cells based on PffBT4T-2OD, Physical Chemistry Chemical Physics, 20 (2018) 19023-19029.

Chapter II. PffBT4T-2OD based solar cells with phenyl-substituted N-methyl - fulleropyrrolidine acceptors

Abstract:

Novel C_{60} and C_{70} N-methyl-fulleropyrrolidine derivatives, containing both electron withdrawing and electron donating substituent groups, were synthesized by the well-known Prato reaction. The corresponding HOMO/LUMO energy levels were determined by cyclic voltammetry, from the onset oxidation and reduction potentials, respectively. Some of the novel fullerenes have higher LUMO levels than the standards $PC_{61}BM$ and $PC_{71}BM$. When tested in PffBT4T-2OD based polymer solar cells, these fullerenes do not bring about any efficiency improvements compared to the standard $PC_{71}BM$ system, however they show how the electronic nature of the different substituents strongly affects the efficiency of the corresponding OPV devices. The functionalization of C_{70} yields a mixture of regioisomers and DFT calculations show that these have systematically different electronic properties. This electronic inhomogeneity is likely responsible for the lower performance observed in devices containing C_{70} derivatives. These results help to understand how new fullerene acceptors can affect the performance of OPV devices.

2.1 Introduction

The work reported in this chapter is based in the article "*PffBT4T-2OD Based Solar Cells with Aryl-Substituted N-Methyl-Fulleropyrrolidine Acceptors, Materials, 12(24),* ***2019****".*

Standard inorganic solar cells can achieve high efficiencies, but they possess some disadvantages including an elaborated and costly production. To overcome these drawbacks many efforts were made to develop several third-generation thin film solar technologies. As an example, organic photovoltaic cells (OPVs) [1-5] can be low-cost production since they can be manufactured in larger areas on flexible and lightweight plastic substrates via solution and printed using high-throughput roll-to-roll methods (R2R) [6]. In recent years, the OPVs have experienced significant developments in power conversion efficiency (PCE), attaining recently over 16 % for single junction devices [7-9] and PCE over 17% for tandem cells [10]

The small band gap donor polymer PffBT4T-2OD, poly[(5,6-difluoro-2,1,3-benzothiadiazol-4,7-diyl)-alt-(3,3'''-di(2-octyldodecyl)-2,2';5',2'';5'',2'''-quaterthio phen-5,5'''-diyl)], also commonly known as PCE11, has been attracting large interest due to its potential to fabricate high performing OPV devices [11-16]

Its high crystallinity and relatively high SCLC hole mobility (1.5–3.0 × 10^{-2} $cm^2V^{-1}s^{-1}$), allow its good performance in an OPV device, when used in relatively thick (~300 nm) bulk-heterojunction (BHJ) layers with higher light absorption capabilities. PffBT4T-2OD exhibits a strong tendency to aggregate in solution [13] characterized by the formation of a gel at room temperature. Therefore, PffBT4T-2OD based devices are usually cast from warm solutions (>60 °C), which then aggregate or crystallize during cooling and film forming processes.

The effect of different processing parameters (solution temperature, concentration, spin-rate, solvent quality and polymer M_w) on the morphology and performance of PffBT4T-2OD:$PC_{71}BM$ devices was studied by Ma *et al.* [12]. The adjustment of solution temperature and spin rate, allows the tuning of the molecular orientation and packing during spin-coating of the BHJ. A low solution temperature and low spinning rate induce highly ordered face-on polymer packing and a high solution temperature and a high spinning rate produce poorly ordered edge-on polymer packing. The best device performance (average PCE of 10.3%) was achieved using films spun-cast at 800 rpm from a solution at 100 ◦C, creating a smooth film containing sufficient aggregates to yield a favourable morphology.

Zhao *et al.* [25] studied the impact of four different additives (1,8-octanedithiol, 1,8-diiodooctane, diphenylether and chloronaphthalene) on the performance of PffBT4T-2OD:$PC_{71}BM$ devices. Chloronaphthalene produced the best devices (PCE = 10.23%), with enhanced polymer crystallinity in the (100) direction corresponding to the alkyl stacking peak located at a q value of 0.29 $Å^{-1}$, which facilitates charge transport within the BHJ.

The effect of different isomers of $PC_{71}BM$ on the photovoltaic properties of PffBT4T-2OD:$PC_{71}BM$ blend films was investigated by Umeyama et al. [16]. It should be noted that the $PC_{71}BM$ used in OPV devices normally consists of a mixture of α- and β-type isomers (in approximately 80–90% and 10–20%, respectively). The α-isomer is composed by two enantiomers, while the β-isomer consists of two diastereomers in which the phenyl group is extended toward opposite directions [26]. Interestingly, the authors found that one of the diastereomers of the β-isomer (isomer β1) shows an extraordinary cohesion in the blended film, deteriorating the OPV device performance. In fact, the PffBT4T-2OD devices based on β1-$PC_{71}BM$ exhibited an extremely low PCE of 0.43%. By contrast, OPV devices using the remaining pure isomers exhibited much higher PCE, namely α-$PC_{71}BM$ (8.80%), β2-$PC_{71}BM$ (8.75%) and these

slightly surpass the device with using the normal $PC_{71}BM$ isomer mixture (8.46%) [16]. The authors concluded that decreasing the amount of a diastereomers of β1-$PC_{71}BM$ with high aggregation tendency improves the photovoltaic performances [16].

Although $PC_{71}BM$ is the most commonly used fullerene in organic solar cells, several other modified fullerenes are found in literature with specific characteristics and have been assessed as acceptors in BHJs.

Liu *et al.* [13] performed an extensive polymer:fullerene combination, testing the use of a large number of different fullerene acceptors ($PC_{71}BM$, $PC_{61}BM$, $TC_{71}BM$, $PC_{61}PM$, $TC_{61}PM$ and ICMA) in devices based on the polymer PffBT4T-2OD and on other family related polymers. The highest efficiency devices with an average PCE of 10.3% were obtained with the fullerene $TC_{71}BM$.

More recently, Zhang *et al.* [15] studied the effect of three different fullerene acceptors ($PC_{71}BM$, $PC_{61}BM$ and ICBA) on the performance of solar cells based on PffBT4T-2OD. The investigation showed that despite PffBT4T-2OD:ICBA devices had a much higher V_{oc} (0.94 V) than the corresponding devices using $PC_{71}BM$ and $PC_{61}BM$ (0.77 V, 0.76 V, respectively), their efficiency (average PCE of 2.78%) was much lower than the efficiency of corresponding devices based on $PC_{71}BM$ and $PC_{61}BM$ (average PCE of 8.93% and 8.15% respectively). Morphological characterization allowed to elucidate that although the size of phase domains is very similar in the three different BHJs, the fullerene aggregates in the ICBA-based films have a reduced degree of order. The high LUMO level of ICBA of the corresponding BHJs are an indicator of a lower initial exciton dissociation and associated with the reduced ordering within the ICBA domains results in increased geminate recombination of the photogenerated electrons in the fullerene-rich domains and a consequently reduced PCE of the corresponding devices.

Fullerene derivatives display a wide range of physical and chemical properties that make them attractive for the preparation of supramolecular assemblies and for organic photovoltaics [27-29]. For instance, attaching the proper organic addends on fullerenes, it is possible to tune their solubility, energy levels, molecular interactions, surface energy, orientation in the solid state as well as electron mobility [5, 30]. However, systematic studies testing newly synthesized fullerenes in low band gap polymers such as PffBT4T-2OD, are still scarce in the literature.

In this work we synthesize some new C_{60}-based and C_{70}-based fullerenes, bearing electron donating and electron withdrawing functionalities, and we test their effect as electron acceptors in the figures of merit of polymer solar cells based on the polymer PffBT4T-2OD. Although the PCE results are not among the best found in literature, the complete characterization of the materials and respective devices can

help to further understand the role of the different fullerene acceptor structures in the performance of OPVs.

2.2 Materials and Methods

2.2.1 Materials

The starting materials used for the synthesis of novel fullerene derivatives were purchased from Solenne BV, namely: C_{60} (> 99.5% purity) with M_w= 720.64 g.mol^{-1} and C_{70} (> 99% purity) with M_w= 840.77 g.mol^{-1}. The reference fullerene $PC_{61}BM$ was also purchased from Solenne BV.

The following materials, used in device fabrication, were purchased from Ossila Ltd.: i) Poly(3,4-ethylenedioxy-thiophene):poly(styrene sulfonic acid) (PEDOT:PSS, Heraeus Clevios AI4083); ii) the polymer PffBT4T-2OD (M302) with M_n = 83,008 g.mol^{-1} and M_w = 172,033 g.mol^{-1} and iii) the reference fullerene $PC_{71}BM$ (M113), with empirical formula $C_{82}H_{14}O_2$ and M_w = 1030.99 g mol^{-1}. The solvent used in the device fabrication was *o*-dichlorobenzene (DCB) with high purity grade and was purchased from Sigma-Aldrich. All these materials and solvent were used as received without further purification.

2.2.2 NMR spectroscopy

^{1}H and ^{13}C solution NMR spectra of the functionalized fullerenes were recorded on a Bruker Avance 500 (500.13 and 125.76 MHz for ^{1}H and ^{13}C, respectively) spectrometer. CS_2, deuterated acetone and deuterated chloroform (99.6 %, TCI Chemicals) were used as solvents and tetramethylsilane (TMS) as internal reference. The chemical shifts are expressed in (ppm).

2.2.3 Preparation of compounds 60a, 60b, 60c, 70a, 70b and 70c.

A mixture of C_{60} (100 mg, 0.14 mmol, 1 eq.) or C_{70} (100 mg, 0.12 mmol), *N*-methylglycine (0.35 mmol) and the corresponding aldehyde (0.70 mmol) in a toluene solution (100 ml) was stirred at reflux temperature for 8 h and then the solvent was removed under vacuum. The solid residue was purified by flash column chromatography (eluent: toluene/hexanes 1:3 with increasing amounts of toluene until purification of the first brown band) affording roughly 30-40% of the *N*-methyl-3,4-fulleropyrrolidine derivatives **60a**, **60b**, **60c**, **70a**, **70b** and **70c** (Figure 2.25). The ^{1}H, ^{13}C NMR and HSQC spectra for **60b**, **60c**, **70a**, **70b** and **70c** are displayed in **APPENDIX I**.

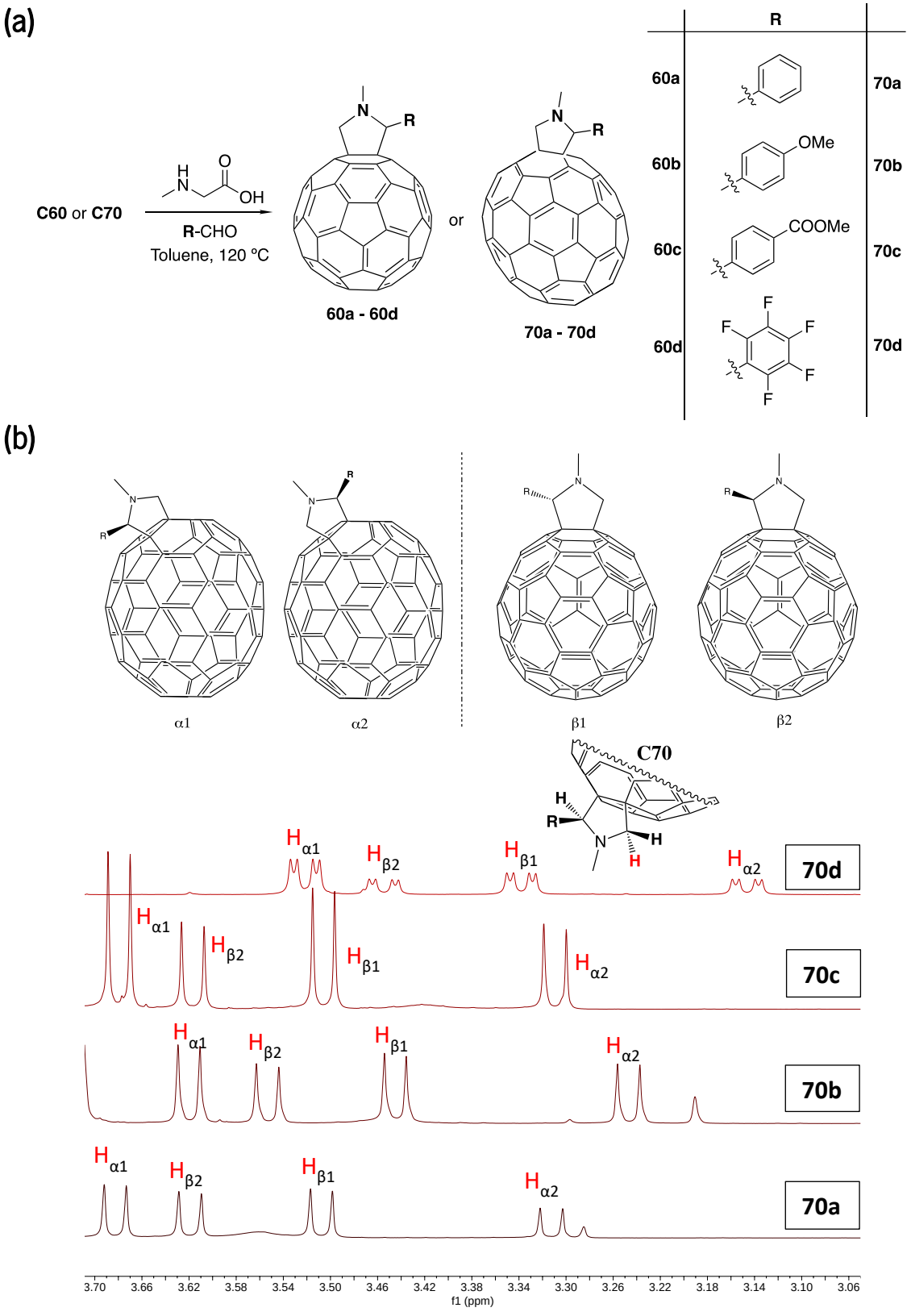

Figure 2. 1. (a) Preparation method used in the synthesis of compounds 60a to 60d and 70a to 70d; (b) Structures and ^{1}H NMR of the isomers present in the C_{70} derivatives 70a to 70d.

60a: ^{1}H NMR (300 MHz, CS_2 + Acetone-d6): δ 7.81 (d, *J* = 7.3 Hz, 2H), 7.43 (td, *J* = 7.3, 1.3 Hz, 2H), 7.39 – 7.30 (m, 1H), 5.04 (d, *J* = 9.4 Hz, 1H), 5.00 (s, 1H), 4.34 (d, *J* = 9.4 Hz, 1H), 2.86 (s, 3H); ^{13}C NMR (126 MHz, CS_2 + Acetone-d6): δ 156.96, 154.05, 154.01, 147.75, 147.33, 147.07, 146.78, 146.73, 146.69, 146.66, 146.59, 146.56, 146.41, 146.28, 146.08, 146.04, 146.01, 145.86, 145.77, 145.70, 145.66, 145.62, 145.21, 145.14, 144.90, 143.63, 143.50, 143.17, 143.09, 143.07, 143.05, 142.80, 142.67, 142.61, 142.29, 142.19, 140.64, 139.95, 137.46, 137.38, 137.10, 136.45, 136.32, 129.34, 129.08, 83.94, 77.73, 70.41, 69.55, 40.30. (Figures 2.1, 2.2 and 2.3)

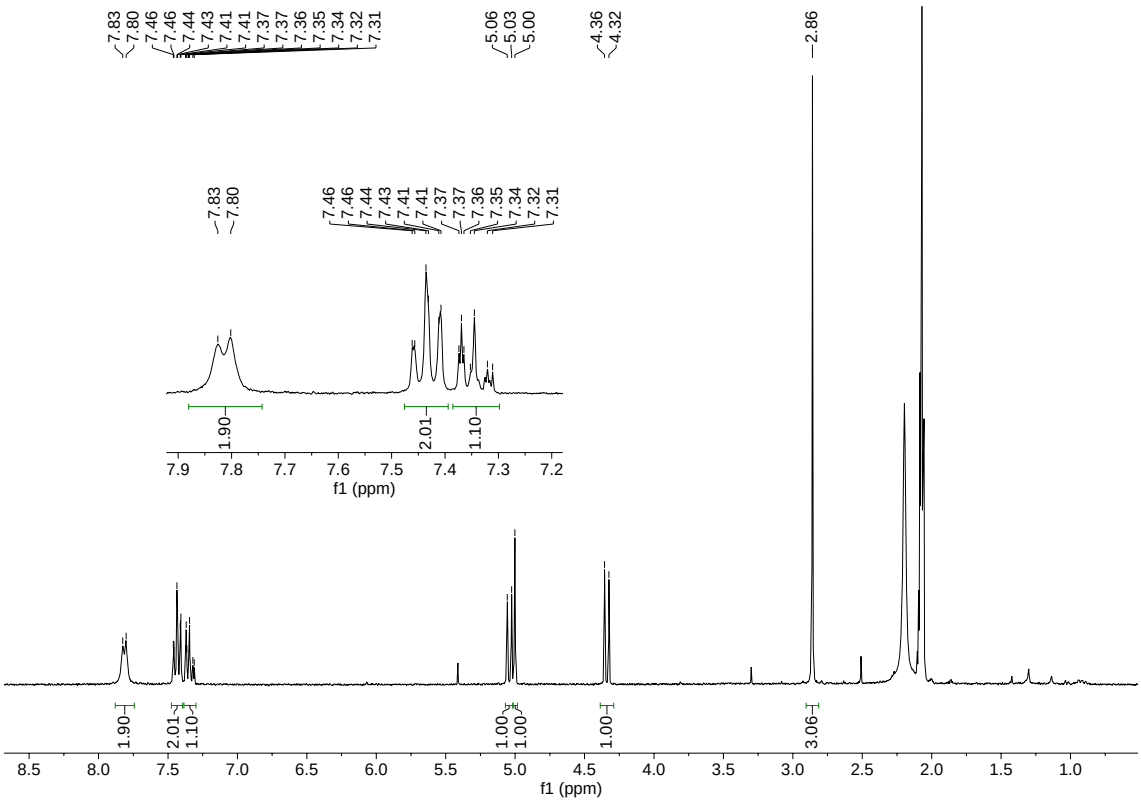

Figure 2. 2. ^{1}H NMR spectra of compound **60a** in a mixture of CS_2 and acetone-d6.

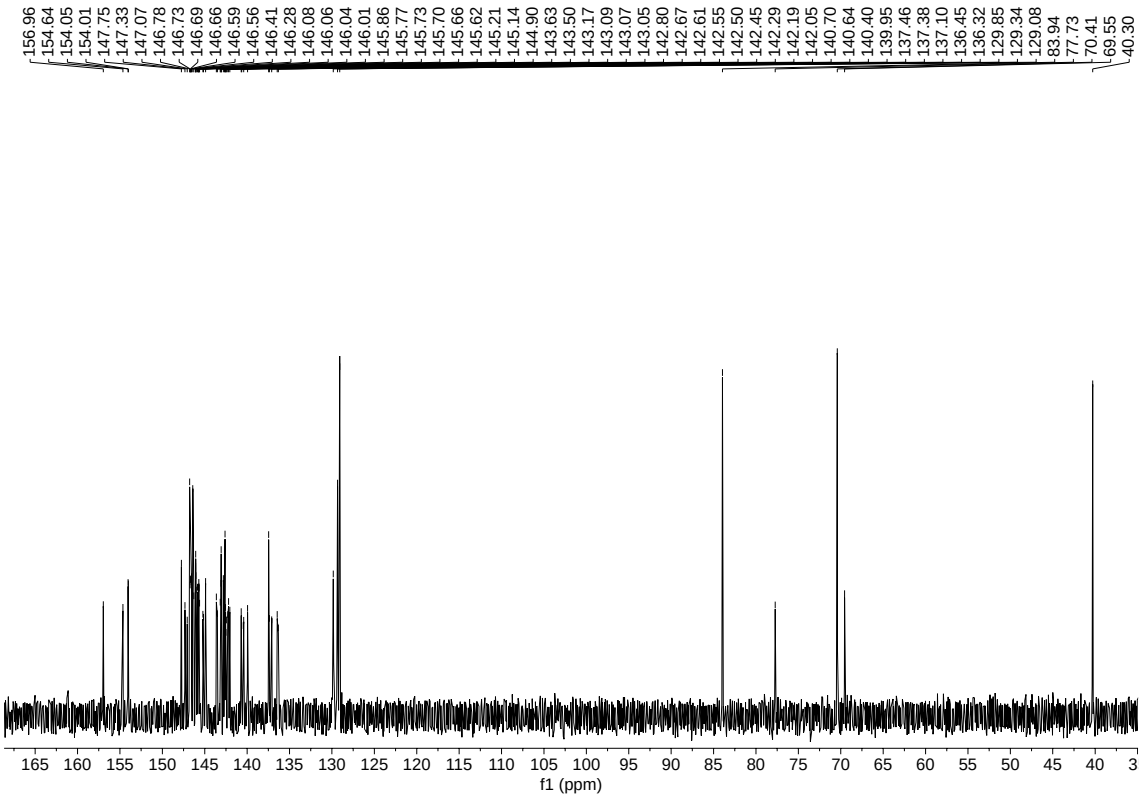

Figure 2. 3. ^{13}C NMR spectra of compound **60a** in a mixture of CS_2 and acetone-d6.

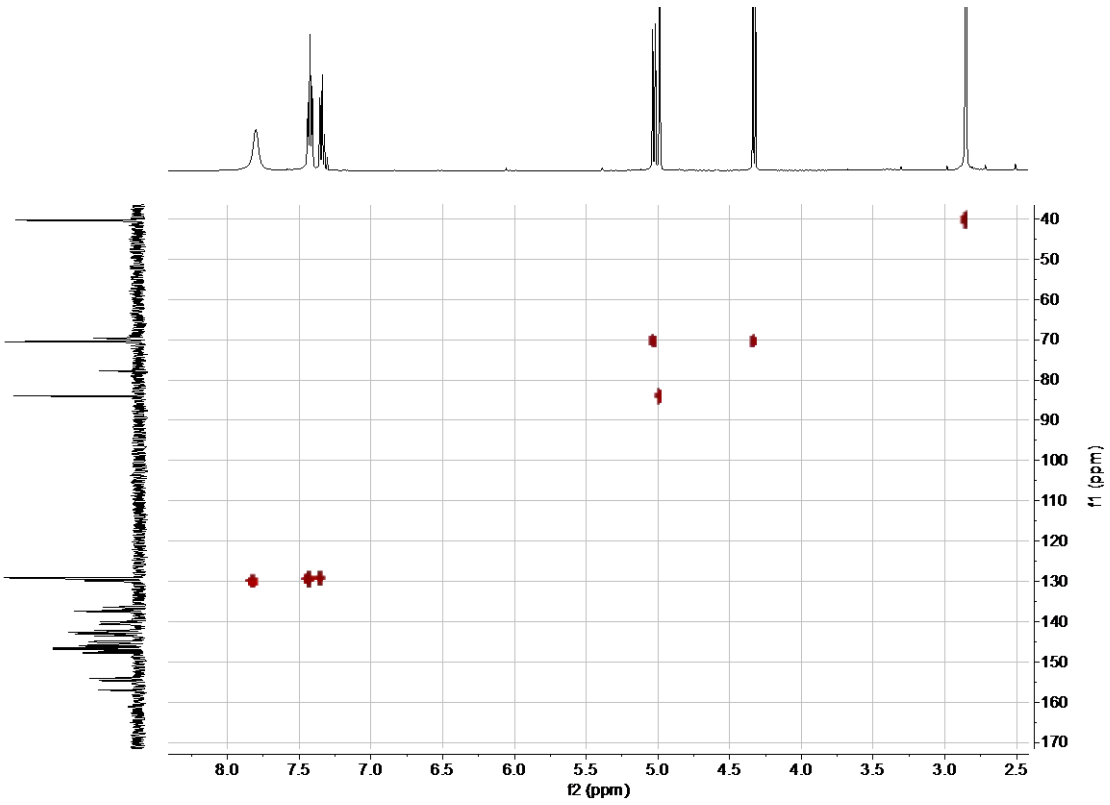

Figure 2. 4. HSQC spectra of compound **60a** in a mixture of CS_2 and acetone-d6

2.2.4 Preparation of compounds 60d and 70d.

A toluene solution (100 mL) containing C_{60} (100 mg, 0.14 mmol) or C_{70}, (0.12 mmol), *N*-methylglycine (0.35 mmol) and the corresponding aldehyde (0.70 mmol) was stirred until reflux temperature. After this, 0.67 mmol of the corresponding aldehyde was added to the reaction every three hours (3 times) and the reaction was maintained for another 15 h at reflux temperature. The reaction mixture was then concentrated and purified by flash column chromatography, using toluene/hexanes (1:3) as eluent, with increasing amounts of toluene until purification of the first brown band, affording roughly 30-40% of the *N*-methyl-3,4-fulleropyrrolidine derivatives **60d** and **70d** (Figure 2.25). The ^{1}H, ^{13}C NMR and HSQC spectra for **60d** and **70d** are displayed in **APPENDIX I**.

2.2.5 Cyclic Voltammetry

Autolat PGSTAT302N potentiostat was used in electrochemical experiments. Voltammograms were recorded using a three-electrode cell arrangement; a polished glassy-carbon (GC) pin (3 mm in diameter) served as a working electrode, a platinum wire as a counter electrode, and the reference electrode was acetonitrile Ag|Ag+. Acetonitrile solution of $AgNO_3$ (0.01 M) with the addition of 0.1 M of Bu_4NPF_6 was used in the compartment of the reference electrode. The fullerenes (ca. 0.6 mg/mL) were dissolved in a solvent mixture of 4:1 (by volume) chlorobenzene:acetonitrile with the addition of 0.1 M Bu_4NPF_6 as a supporting electrolyte. Before measurements, the solutions were deaerated by purging high purity Argon for 7 minutes. Cyclic voltammograms were recorded at a potential scan rate of 100 mV/s. During the measurements, the Argon flow was kept above the solution in the cell. All electrode potentials were quoted with respect to equilibrium potential ($E_{1/2}$) of Fc+/Fc redox couple in the same solvent mixture. The LUMO and HOMO energy levels were estimated from the onset potential of the reduction (E_{Red}^{on}) and oxidation (E_{Ox}^{on}) respectively: ELUMO = -4.9 - E_{Red}^{on}; EHOMO = -4.9-E_{Ox}^{on}.

2.2.6 Ab initio DFT calculations

Density Functional Theory calculations at the PBEh-3c level were performed to derive all molecular structures [31]. To compare with voltammetry experiments, PBE-def2-TZVP level calculations were used as they show larger accuracy than hybrid functionals [32-34]. For C70 systems both isomers, α and β, were computed. For simplicity, only one diasteroisomer for each isomer was considered after preliminary calculations showed similar results for both diasterisomeric forms. All calculations were performed with the ORCA 4.2 program [35].

2.2.7 Absorption Spectroscopy

In a first stage, UV-Vis absorption spectroscopy was used to characterize the optical properties of the pure fullerenes in *o*-dichlorobenzene solution. Although attempts have also been made to measure the UV-Vis spectra of spin-coated thin films of the pure fullerenes on quartz windows, these were not successful due to the difficulty in preparing homogeneous thin films.

In a posterior stage, UV-Vis absorption spectroscopy was used to evaluate the effect of fullerenes in the light absorption of the different blends, which is one of the first steps to charge generation. Absorption spectra (UV-Vis) were obtained on a Shimadzu UV-2501PC spectrophotometer, in the 350–800 nm range in solid-state film deposited in quartz substrates.

2.2.8 Device fabrication

The OPV devices employ a standard structure ITO/HTL/Active layer/Ca/Al. PEDOT:PSS was used as hole transport layer (HTL). ITO (Indium Tin Oxide) has a sheet resistance of 20 Ω/□. The active layers were all spin-coated from a solution of *o*-dichlorobenzene with the polymer PffBT4T-2OD and several fullerene derivatives shown in Figure 2.25, having concentrations of 4.0 mg·mL^{-1} and 4.8 mg·mL^{-1} respectively (1:1.2 mass ratio). At this point, it is worth mentioning that other polymer:fullerene mass ratios were initially screened (namely 1:3 and 3:1) but later discarded because the corresponding devices exhibited lower figures of merit. Although the majority of the previous works use a solvent mixture of chlorobenzene:*o*-dichlorobenzene (1:1) to dissolve the polymer, in the present work due to the relatively high *Mw* of the polymer used, it proved to be more appropriate the use of pure *o*-dichlorobenzene which has a stronger solubilizing power than the chlorobenzene/*o*-dichlorobenzene mixture. Due to the strong aggregation and gelation tendency of the polymer PffBT4T-2OD in solution, the active layers were spin coated from pre-heated solutions (120 °C) at a spin speed of 800 rpm onto the PEDOT:PSS/glass substrate that was pre-heated to 120 °C. The active layer was spin-cast in a nitrogen filled glove box. The films were then left inside the glove box for 1 hour to dry. The cathode evaporation was then made sequentially composed by 5 nm Calcium (Ca) and 100 nm Aluminium (Al) on top of the active layer under a vacuum < 2×10^{-6} mbar to form the top electrode contact. The average fabrication number for each fullerene derivatives was approximately 15 devices (8 pixels per device).

2.2.9 Device performance characterization

Photovoltaic properties of the devices were determined using a Newport-Oriel 96000 AM 1.5 Global solar simulator which was calibrated using an NREL standard silicon solar cell to ensure an irradiance level of 1000 W/m^2. An aperture mask was used to limit the light-exposed area of the device to 2.6 mm^2, avoiding edge effects. All measurements were made at room temperature and ambient atmosphere.

2.2.10 Morphological characterization using Atomic Force Microscopy (AFM)

Atomic Force Microscopy (AFM) in tapping mode was used to image the surface morphology of the PffBT4T-2OD:fullerene thin films. AFM experiments were performed using a Molecular Imaging PicoLE AFM and several scans were imaged in flattened mode data to remove the background slope. The scan size of topographic AFM images presented in all experiments is 5x5 μm.

2.3 Results and Discussion

In this work, we started by synthesizing mono-functionalized C_{60} and C_{70} fullerenes containing electron donating and withdrawing groups, as shown in Figure 2.25(a). This was achieved by the well-known Prato reaction, a controlled cycloaddition reaction in which a pyrrolidine ring is fused with a 6,6 ring junction of both C_{60} or C_{70} [13, 36]. Compounds **60a-60d** and **70a-70d** were prepared by reaction of the appropriate azomethine ylide precursors respectively with C_{60} and C_{70}. The reactive 1,3-dipoles were generated *in situ* and compounds **60a-60d** and **70a-70d** were synthesized according to Figure 2.25(a), using *N*-methyl glycine (sarcosine) and the corresponding aldehyde. Due to the large variety of substituted azomethine ylides that can be generated from readily accessible starting materials, highly functionalized pyrrolidine rings in C_{60} and C_{70} can be easily obtained in moderate to good yields [36].

We observed that the solubility of the resulting C_{70} derivatives was greatly improved when compared with the solubility of the C_{60} derivatives: while derivatives **70a-70d** [37] were soluble in dichloromethane, derivatives **60a-60d** where far less soluble, and only solvents such as toluene and CS_2 could dissolve them. The final products were separated from unreacted starting material (C_{60} or C_{70}) and other by-products by silica gel chromatography using a mixture of toluene/hexane. Most of the substituents introduced on the fullerenes provided enough polarity to easily separate the final materials from the starting materials as the second coloured band eluted from the silica gel chromatography.

The structures of **60a-60d** and **70a-70d** derivatives were all confirmed by ^{1}H NMR spectroscopy (Figures 2.1 to 2.24). However, it is important to note that the ^{1}H NMR spectra of the C_{70} derivatives

displays four signals attributed to the pyrrolidine protons as a characteristic feature of four distinct C_{70} isomeric products. Indeed, unlike C_{60}, in which all carbon atoms and double bonds are initially equivalent, the lower symmetry of C_{70} gives rise to a mixture of four isomers. As shown in Figure 2.25(b), two sets of [6-6] mono-adducts are expected and the integration based on one of these protons (^{1}H, Figure 2.25(b)) allowed us to estimate the fractions of each isomer in the C_{70} derivatives **70a** to **70d**. The singlet signal of the ^{1}H proton is clearly split into four signals, corresponding to the α1, α2, β1 and β2 C_{70} mono-adducts in a ratio where the α isomers tend to increase with the electron withdrawing effect around the phenyl substituent. The ^{1}H NMR data of the pyrrolidine is summarized in Table 2.1. Other techniques such as HPLC can further confirm the isomeric nature of these mixtures. For instance, Urbani et al. [37] has prepared C_{70}-fuleropyrrodines with a similar approach here described and confirmed the presence of two kinds of isomeric products, namely, α and the β-types. However, differentiation within the α isomers or the β isomers was not possible. The same authors also found that under Prato experimental conditions, only [6-6] C_{70} mono-adducts were isolated and the presence of the [5-6] isomeric products could not be detected by classical analytical methods (HPLC and NMR).

Table 2. 1. Fraction in percentage of the isomers present in derivatives 70a-70d

	α1 (%)	α2 (%)	β1(%)	β2 (%)	α:β (%)
70a	30	17	27	26	47:53
70b	28	21	29	22	49:51
70c	36	19	26	19	55:45
70d	39	18	24	18	57:43

The electrochemical properties of the synthesized fullerenes were then determined using cyclic voltammetry. Figure 2.26(a) shows the Cyclic Voltammetry (CV) curves for all samples. The experimentally determined energy levels are summarized in Table 2.2 and represented graphically in Figure 2.26(b). In Figure 2.26(b), we also represent the HOMO/LUMO levels of PffBT4T-2OD as taken from the literature [13]. We note that our experimentally determined HOMO/LUMO levels for the standard fullerenes $PC_{61}BM$ and $PC_{71}BM$ are in very good agreement with literature data [38, 39] which guarantees the reliability of our measurements for all the remaining fullerenes. We note that some of the novel fullerenes (**60a**, **60b**, **60c** and **70c**) have slightly higher LUMO levels than the standards $PC_{71}BM$ and $PC_{61}BM$, which in theory should favour higher V_{OC} and *PCE* assuming that all other factors remain unchanged.

Table 2. 2. HOMO and LUMO levels for all materials as calculated from cyclic voltammetry. The potential onsets used for the calculations are also indicated.

Material	E_{ox}^{onset} (V)	HOMO (eV)	E_{red}^{onset} (V)	LUMO (eV)
PffBT4T-2OD	-	-5.34	-	-3.69
$PC_{61}BM$	1.07	-5.97	-1.01	-3.89
$PC_{71}BM$	0.97	-5.87	-1.01	-3.89
60a	0.84	-5.74	-1.03	-3.87
60b	0.82	-5.72	-1.04	-3.86
60c	0.64	-5.54	-1.03	-3.87
60d	0.93	-5.83	-0.93	-3.97
70a	0.78	-5.68	-0.91	-3.99
70b	0.74	-5.64	-0.85	-4.05
70c	0.81	-5.71	-1.03	-3.87
70d	0.87	-5.77	-0.99	-3.91

(a)

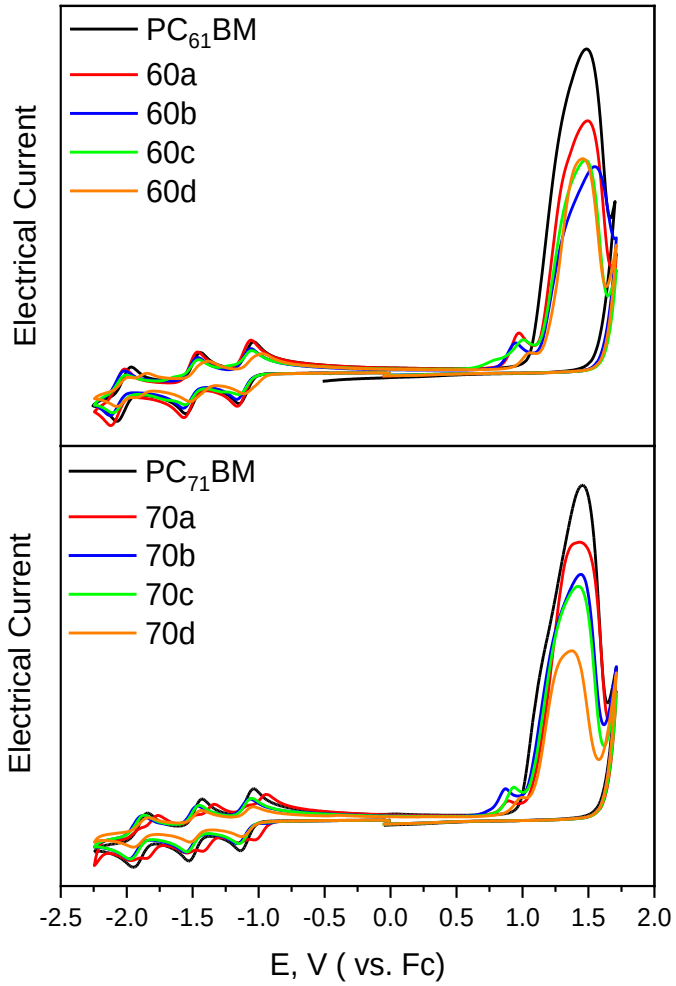
PC61BM
60a
60b
60c
60d
Electrical Current
PC71BM
70a
70b
70c
70d
Electrical Current
-2.5
-2.0
-1.5
-1.0
-0.5
0.0
0.5
1.0
1.5
2.0
E, V (vs. Fc)

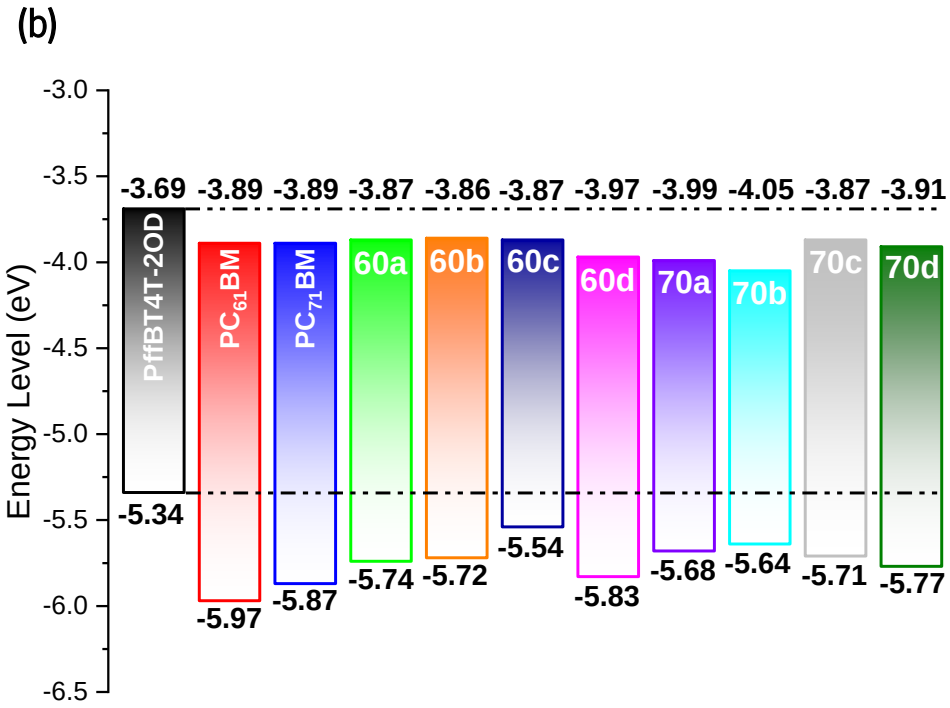

Figure 2. 5. (a) Cyclic Voltammetry curves for all different materials. The Electrical Current scale is arbitrary shifted in order to show all curves. (b) Scheme of HOMO and LUMO levels for all materials as calculated from cyclic voltammetry. The HOMO and LUMO levels for PffBT4T-2OD as indicated in [16] are also shown.

The HOMO and LUMO energies were computed with DFT and show a reasonable agreement with the voltammetry derived values, Table 2.3 In detail, LUMO energies show a remarkable agreement with only **70a** and **70b** molecules showing differences larger than 0.1 eV, while HOMOs show generally larger divergences. Interestingly, when the energies of the frontier orbitals of α and β C_{70} isomers are compared, HOMOs are stabilized while LUMOs are destabilized. Consequently, all α isomers have systematically larger HOMO-LUMO gaps than β isomers. Also, for all functionalized C_{60} and some C_{70} molecules both frontier orbitals have most electron density localized in the fullerene moieties, Figure 2.27. There are only two exceptions: **70a** and **70b** where there is also density on the functional group.

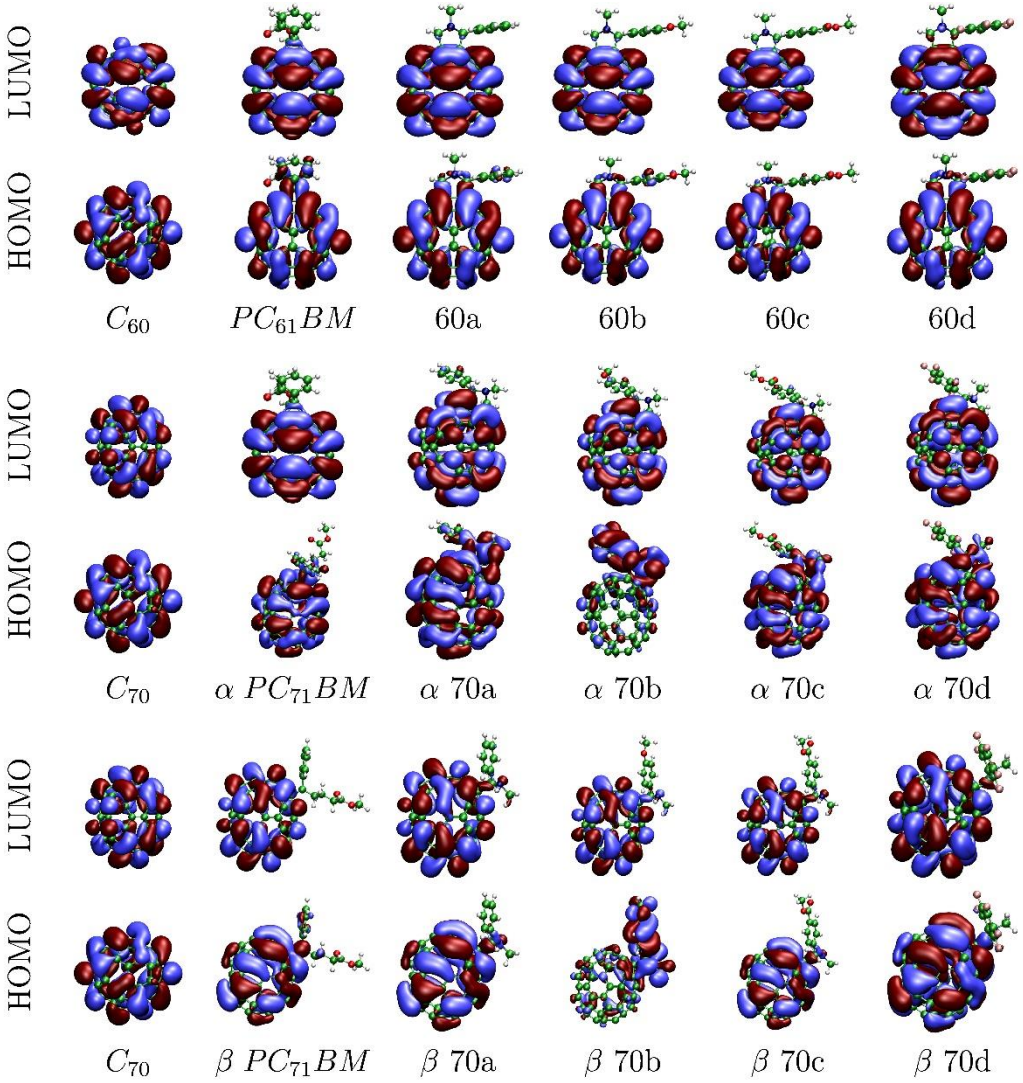

Figure 2. 6. Frontier orbitals of pristine and functionalized C_{60} and C_{70} molecules.

Table 2. 3. Experimental and computed HOMO and LUMO energies at the PBE-def2-TZVP/PBEh-3c level. All values in eV.

	HOMO			LUMO		
	Exp.	**α**	**β**	**Exp.**	**α**	**β**
$PC_{61}BM$	-5.97	-5.47		-3.89	-3.94	
$PC_{71}BM$	-5.87	-5.52	-5.44	-3.89	-3.85	-3.87
60a	-5.74	-5.42		-3.87	-3.90	
60b	-5.72	-5.38		-3.86	-3.87	
60c	-5.54	-5.46		-3.87	-3.94	
60d	-5.83	-5.53		-3.97	-4.00	
70a	-5.68	-5.47	-5.40	-3.99	-3.80	-3.85
70b	-5.64	-5.38	-5.34	-4.05	-3.76	-3.81
70c	-5.51	-5.52	-5.45	-3.87	-3.85	-3.90
70d	-5.77	-5.56	-5.48	-3.91	-3.88	-3.92

The UV-Vis absorption spectra of pure solutions of each fullerene in o-dichlorobenzene were recorded and are shown in Figure 2.28. As expected, the C_{70}-based fullerenes display a broader photo-absorption profile in the visible region of the solar spectrum and this is due to the lower and more extended conjugation of the C_{70} cage that enables energetic transitions that are forbidden in C_{60} [24]. Although the main exciton creation is assumed to occur in the polymer, such increased photon harvesting potentially allows higher photocurrents for devices using C_{70}-based fullerenes than for their C_{60}-based analogues.

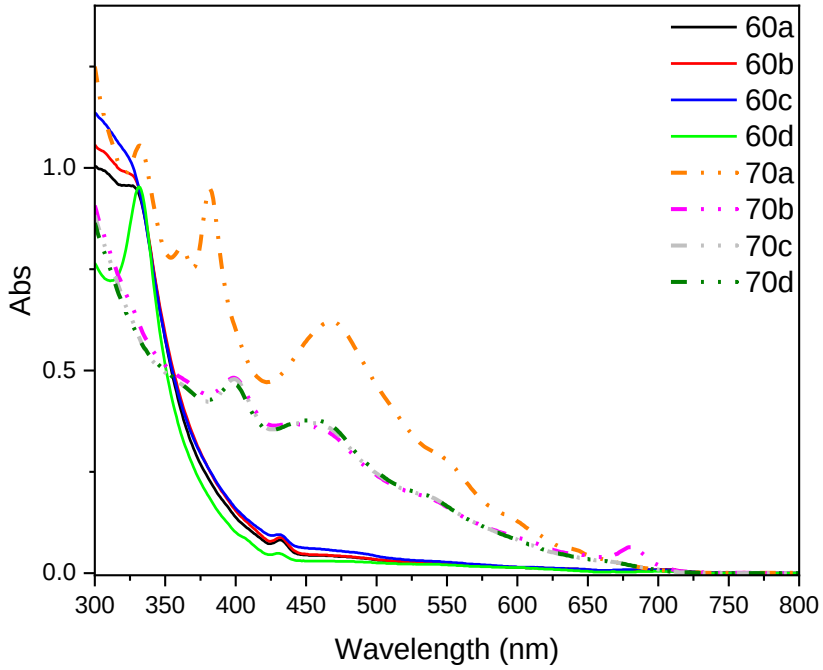

Figure 2. 7. UV-Vis spectroscopy of the fullerenes in 1,2-dichlorobenzene.

The current density-voltage (J-V) curves of devices with standard architecture, as shown in Figure 2.29(a), and processed with the eight different fullerenes, as well as a control device using the standard $PC_{71}BM$, are shown in Figure 2.29(b). Although device data using the standard, but less common, $PC_{61}BM$ has not been included, according to literature the *PCE* of PffBT4T-2OD:$PC_{61}BM$ devices in only ~10 % lower than the *PCE* of PffBT4T-2OD:$PC_{71}BM$ devices [15]. We note that, in order to guarantee the reproducibility and the reliable comparison of device data between different fabrication batches, every time a new batch of devices was made, a few devices with $PC_{71}BM$ were included as a control of the general quality of the whole device fabrication process. As shown in Figure 2.29(b), all the new fullerenes produced devices with considerably lower figures of merit than the reference devices with $PC_{71}BM$, even though most of the novel fullerenes possess favourable LUMO levels. Interestingly, we also observe that despite their higher light absorption, C_{70}-based fullerenes (open triangles in Figure 2.29(b)) in general

produce lower efficiencies (best PCE of 1.76% for 70c) than the C_{60}-based fullerenes (open squares – best PCEs of 2.84% for **60a** and 2.04% for **60b**). When comparing fullerenes with identical functionalization we observe that **60a**, **60b** and **60d** produce devices with better figures of merit than respectively **70a**, **70b** and **70d**. Only in the case of **60c** and **70c** the opposite relationship is observed. The inferior performance that we generally observe in our C_{70}-based devices, compared to C_{60}-based devices, is most likely due to the energetic disorder introduced in these systems by the presence of several isomers, as our DFT calculations clearly show that the C_{70} isomers have different electronic properties. This effect has been previously observed in the case of $PC_{71}BM$ isomers, in a study where the authors concluded that one of the β-isomers present in the mixture of four isomers (α1, α2, β1 and β2) does not contribute to the efficiency of the overall mixture [16]. In particular, Umeyama and co-workers found that devices prepared using a blend of PffBT4T-2OD with the purified β1-$PC_{71}BM$ isomer exhibited an extremely low PCE of 0.43 %, due to the high aggregation tendency of β1-$PC_{71}BM$ in the blend film. In our present work, this effect can be even more pronounced since the synthetic methodologies employed produced amounts of β1-isomer up to 30% [37, 40]. It is worth mentioning that the effect of isomers of C_{70}-based mono-adducts in OPVs has been receiving special attention [16, 41-44] by the group of Prof Imahori at Kyoto University and a very recent review by this group [41] calls the attention of the research community to the great importance of this issue which has been so far largely ignored.

In Figure 2.29(b) it is noticeable the change in the shape of some J-V curves compared to the data when conventional $PC_{71}BM$ is employed in the active layer. For instance, and regardless the clear decrease in the main figures of merit, devices with fullerene **60c** exhibit a very pronounced influence of a space charge limited current (SCLC) [45], although some similar behaviour is also observed in the other devices with the prepared fullerenes. Together with the decrease of V_{oc} and J_{sc} for all devices (compared to the $PC_{71}BM$) the fill-factor FF also decreases due to the mentioned J-V shape. The main figures of merit for each different kind of devices are represented schematically in Figure 2.29(c) and indicated in Table 2.4. At this point it is worth noting that a large number of previous studies in the literature have reported new fullerenes that despite exhibiting enhanced LUMO levels with respect to $PC_{61}BM$ or $PC_{71}BM$, originated devices with considerably lower PCE [46-55] and also with simultaneously lower *PCE* and V_{OC} [50-55] than reference devices based on $PC_{61}BM$ or $PC_{71}BM$.

(a)

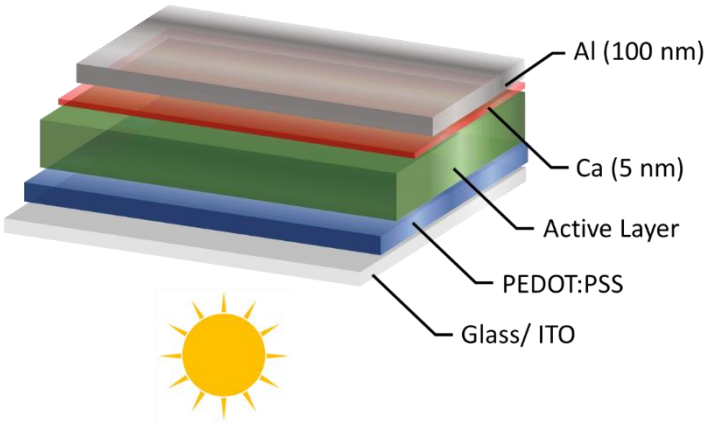
Al (100 nm)
Ca (5 nm)
Active Layer
PEDOT:PSS
Glass/ ITO

(b)

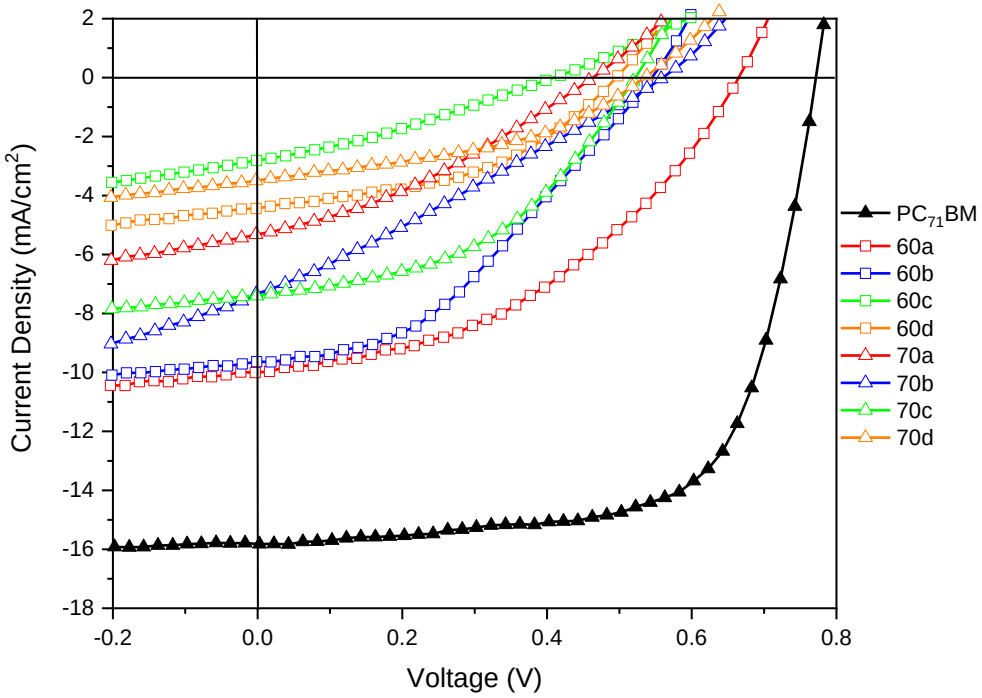
Current Density (mA/cm^2)
Voltage (V)
2
0
-2
-4
-6
-8
-10
-12
-14
-16
-18
-0.2
0.0
0.2
0.4
0.6
0.8
PC$_{71}$BM
60a
60b
60c
60d
70a
70b
70c
70d

(c)

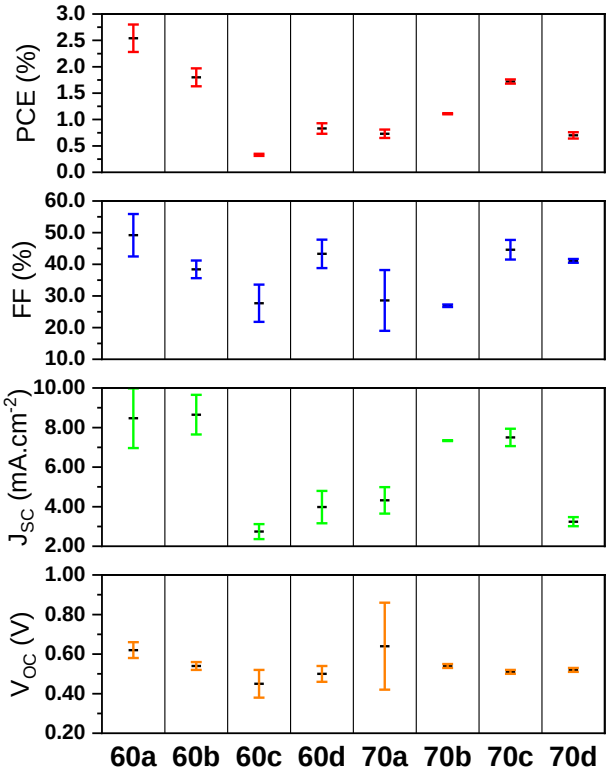

Figure 2. 8. (a) A schematic of the standard device structure used in the fabrication of devices; (b) Representative electrical current density – applied voltage (J-V) curves for PffBT4T-2OD based devices with each particular type of fullerene species 60a-60d and 70a-70d; (c) Overall device metrics for PffBT4T-2OD based devices using the different fullerenes 60a-60d and 70a-70d.

UV-Vis spectra of the blends and pure polymer, normalized based on the intensity of their 0-1 transition peak at ~700 nm, are depicted in Figure 2.30. The polymer PffBT4T-2OD is the main responsible for the light absorption and the fullerenes contribute only a minor part to the total absorbance of the active layer in the visible region. As shown in Figure 2.30, the pure polymer PffBT4T-2OD has essentially three main absorption bands in the visible region, with maxima located at ~460, 640 and 700 nm. The band at lower energy exhibits an absorption edge at ~750 nm, corresponding to an optical bandgap of ~1.65 eV [56], which is in perfect agreement with the literature [13]. Comparing Figures 2.30(a) and 2.30(b) it is evident that the BHJs using C_{70}-based fullerenes display, in the 400–700 nm range, a stronger light absorption than the BHJs using C_{60}-based fullerenes. This observation is expected considering that, as shown in Figure 2.28, the pure C_{70}-based fullerenes display a stronger light absorption

in the visible range. The higher light absorption of the C_{70}-based BHJs should be a factor that, per se, obviously favours device efficiency assuming that all other factors remain the same.

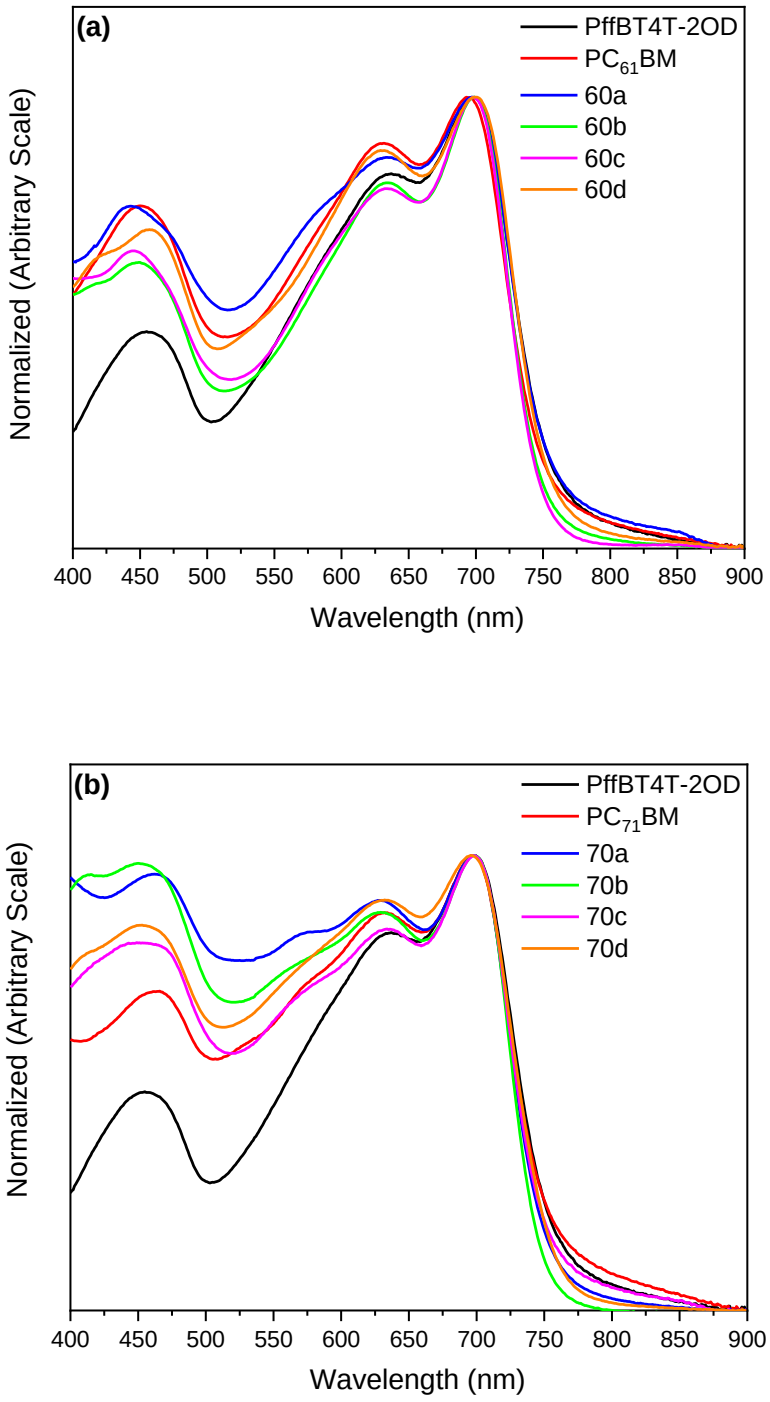

Figure 2. 9. UV-Vis absorption spectra of a PffBT4T-2OD pristine film and of PffBT4T-2OD:fullerene blend films with: (a) C_{60} based fullerenes and (b) C_{70} based fullerenes. All spectra are normalized based on the intensity of their 0-1 transition peak at ≈700 nm.

The current density-voltage (J-V) curves of devices were fitted to the usual OPV equivalent circuit employing genetic algorithms as previously described [57]. Figure 2.31 shows the most significant results. The full data is present in Table 2.4.

.

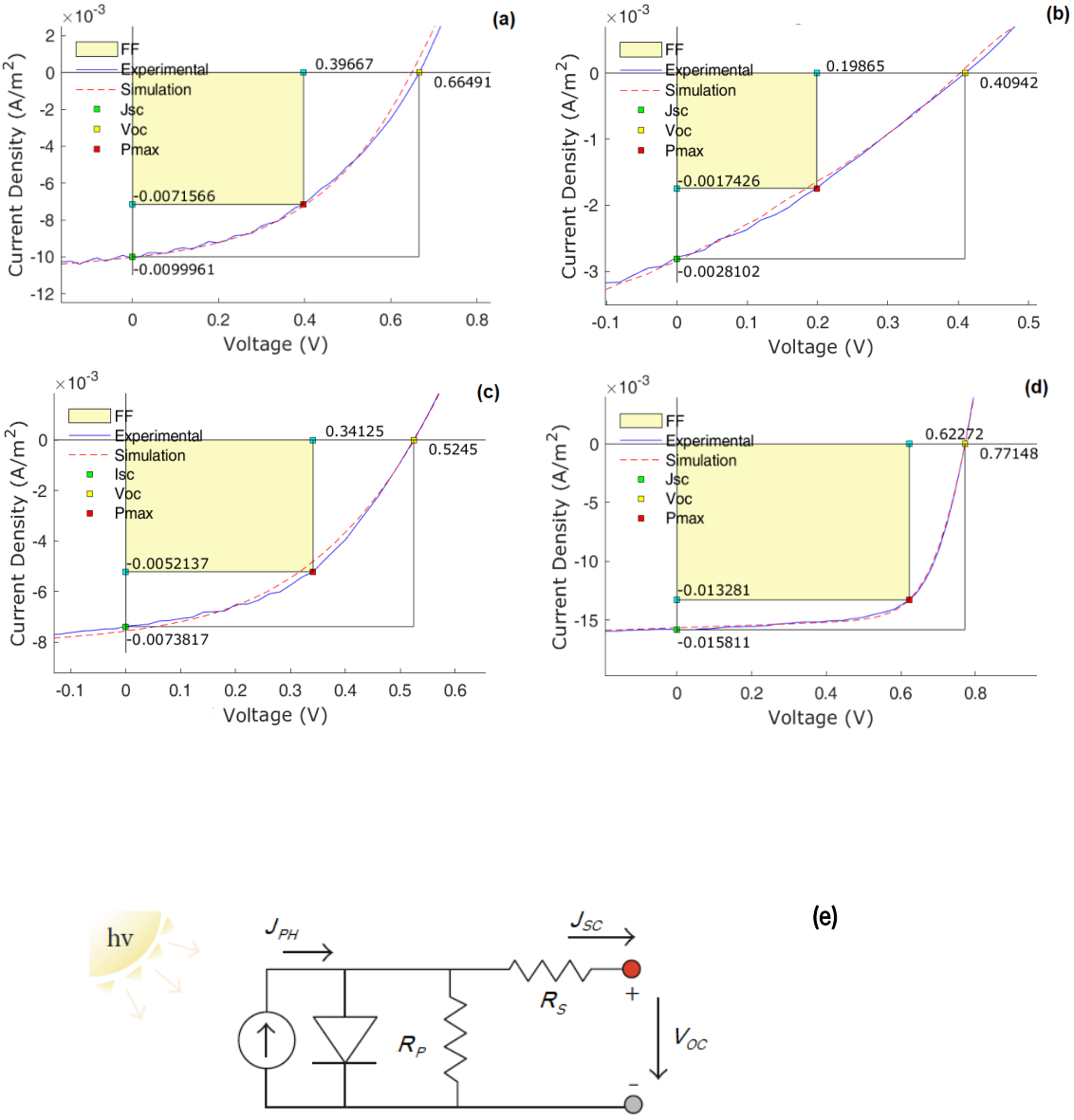

Figure 2. 10. Full simulation data (dashed lines) for the electrical current density – applied voltage (J-V) for OPVs based in donors: a) 60a, b) 60c, c) 70c and d) $PC_{71}BM$. The general equivalent electric circuit used for simulation of the experimental data is represented in e).

Table 2. 4. Device metrics showing the peak and (average) values for PCE for devices prepared using different fullerene derivatives. Generated photocurrent (J_{ph}) and parallel (R_p) and series resistances (R_s) obtained by the equivalent circuit fit with experimental data

PffBT4T-2OD					Simulation		
	PCE (%)	V_{oc} (V)	FF (%)	J_{sc} (mA/cm²)	J_{ph} (mA/cm²)	R_s (Ω)	R_p (Ω)
$PC_{71}BM$	8.41 (8.19±0.24)	0.77 (0.74±0.02)	71.2 (69.8±1.7)	16.42 (15.87±0.40)	15.66	159	9.72×10^4
60a	2.84 (2.54±0.26)	0.66 (0.62±0.04)	42.9 (49.2±6.7)	9.96 (8.47±1.51)	10.20	579	2.00×10^4
60b	2.04 (1.80±0.17)	0.54 (0.54±0.02)	38.8 (38.4±2.8)	9.65 (8.65±1.00)	9.64	475	1.69×10^4
60c	0.36 (0.33±0.02)	0.56 (0.45±0.07)	20.5 (27.7±5.9)	3.16 (2.74±0.38)	3.67	3724	1.00×10^4
60d	0.98 (0.83±0.10)	0.50 (0.50±0.04)	44.8 (43.3±4.5)	4.41 (3.98±0.82)	4.76	866	1.49×10^4
70a	0.82 (0.73±0.08)	0.54 (0.64±0.22)	28.6 (28.6±9.6)	5.30 (4.32±0.67)	5.98	1771	0.84×10^4
70b	1.12 (1.11±0.01)	0.56 (0.54±0.01)	27.2 (26.9±0.4)	7.33 (7.34±0.02)	7.93	1028	0.56×10^4
70c	1.76 (1.72±0.04)	0.52 (0.51±0.01)	45.9 (44.6±3.1)	7.36 (7.50±0.44)	7.69	587	2.04×10^4
70d	0.77 (0.70±0.06)	0.54 (0.52±0.01)	41.1 (41.1±0.6)	3.48 (3.24±0.23)	3.67	1139	1.55×10^4

Several issues should be discussed regarding our macroscopic device physics data, as the influence of the space charge in the J-V data, mentioned above, reveals a departure from the ideal equivalent electrical circuit for the OPVs.

Concerning the values of J_{SC}, it is clear that all of them are considerably lower than the value obtained with the standard $PC_{71}BM$. In condition of $V = 0$, J should be given by $J = qdGP_c$ where q is the electronic charge, d the film thickness, G (depending on electrical current I) the photon flux by volume absorbed by the OPV and P_c (depending on both electrical current I and applied voltage V) the conventional charge collection probability. The easiest way to estimate P_c is by the ratio between the J_{SC} and the reverse saturation current J_{PH}. In our case, and due to the significant component of space charge J-V curve under high reverse bias, it is difficult to obtain experimentally the value of J_{PH}. Therefore, the estimated values obtained from the equivalent circuit simulation with experimental data, were used. As usual in OPVs, the values of P_c are almost near 1 (considering the experimental error) but for the case of fullerene **60c**, a clear low value of $Pc = 0.76$ is obtained, corresponding also to the sample that provides the lower value of efficiency. With exception of the sample **70a** ($P_c = 0.89$, $\eta = 0.82$), all the remaining values of the charge collection probability are higher than 0.92, with some absence of correlation with efficiency for some samples. Regarding the V_{OC} values for devices with the new fullerenes, all these are also lower than the value obtained with the standard $PC_{71}BM$. A well-known [58] simple empirical relationship between V_{OC} and the HOMO / LUMO levels of respectively donor / acceptor can be establish, leading to $V_{OC} \approx (E^A_{LUMO} - E^D_{HOMO}) - 0.3$. In practice, the search for a suitable explanation for the empirical 0.3 (V) in V_{OC} equation, has shown that open circuit voltage is dependent on the quasi-Fermi levels in both donor and acceptor materials. Cowan *et al.* [59] proposed a model that takes into account such quasi-Fermi levels influence, that can be described by

$$V_{OC} = \frac{1}{q}(E^A_{LUMO} - E^D_{HOMO} - \Delta) - \frac{kT}{q}\ln\left(\frac{n_e n_h}{N_c^2}\right)$$

where n_e and n_h are respectively, the electron and hole densities in the fullerene and polymer domains at open circuit, and N_c is the density of conduction states of the polymer and fullerene (assumed here to be equal) and Δ is an energy shift that originates from disorder within the phase separated polymer and fullerene regions.

From the experimental data of our samples, and considering the HOMO / LUMO levels determined, we should expect significantly high values for V_{OC}. However, the noticeable SCLC contribution in the J-V data, predicts a significant disorder in phase separation, as the simulation data indicates (a clear

departing, in some samples, from the theoretical simple equivalent electrical circuit) due to the poor fit to the perfect diode model. This means that, in spite of interesting expectations for figures of merit based in the HOMO / LUMO levels of some materials, the degradation of the active layer with further phase disorder, should be the suitable explanation for the low V_{oc} values, as the energetic disorder contribution Δ must be significant high. Additionally, the departing of the pure diode model (for phase separation) toward a device that becomes electrically governed by a space charge contribution gives rise to several other implications. In fact, the space charge influence in organic devices suggests an existence of intrinsic defects acting as energy traps for electrical carriers (see, for instance in our data, the clear lower values of R_P obtained in all devices with new fullerenes compared to the $PC_{71}BM$), that should imply a decrease of J_{sc} and a lowering of the fill-factor. Interfacial trap energy levels at D:A phase is one of the most critical contribution for the OPV figures of merit. In practice, a high density of such trap states should reduce the J_{sc} with further reduction of fill-factor FF, additionally to the more closed J-V curve and giving experimental results sometimes far from the expected. Additionally, the presence of traps arising from intrinsic defects have another main consequence that is the decrease of electrical carrier mobility, as the trap-free Poole-Frenkel mobility becomes lower, affected by the final traps density. This should further decrease J_{sc} and contribute negatively to the efficiency.

Aiming to shed some light on the relationship between the nanoscopic BHJ morphology and the macroscopic device physics performance, the surface morphology of the PffBT4T-2OD:fullerene films was assessed using atomic force microscopy (AFM), Figure 2.32. However, the interpretation of these AFM images is very ambiguous and should be made with great caution. For example, if in one hand we can argue that BHJs with **60b** and **70c** have relatively higher efficiencies because they are among the smoother films (supposedly with smaller fullerenes agglomerates); on the other hand, and in light of the same argument, it is hard to explain the higher efficiency of film **60a** which is rougher. We note however that AFM only probes the surface morphology of the film that may be very different from that of the underlying bulk material. Furthermore, as we explain in more detail below, the interpretation of an apparently coarse- or fine-grained physical microstructure alone can lead to incorrect conclusions regarding its effect on device performance. In fact, BHJs are morphologically complex systems and, beyond the measurement of the size of phase domains, their detailed characterization would also require the measurement of the degree of purity of the phase domains and the degree of orientation (crystallinity) inside those phase domains. However, such a detailed morphological characterization would require the use of some hardly accessible techniques such as Resonant Soft X-Ray Scattering (RSoXS) [60], Small

Angle Neutron Scattering (SANS) [14, 61], Grazing-Incidence Wide-Angle X-ray Scattering (GIWAXS) [62] and Neutron Reflectivity [63] and this is beyond the scope of our present work.

Finally, at this point, in order to better understand our results we make some important general considerations, based on literature, on the relationship between the nanoscale morphology of polymer:fullerene films and the efficiency of the devices.

According to the currently prevailing morphological paradigm in BHJ solar cells, the morphology of a polymer:fullerene BHJ should consist of at least three distinct phases: an ordered polymer-rich phase (responsible for hole transport); a disordered amorphous phase composed of intimately mixed polymer and fullerene (with very high D:A interfacial area to favour exciton dissociation); and a fullerene-rich phase (responsible for the electron transport) [64]. Fullerene derivatives are usually not miscible in highly ordered (i.e. crystalline) polymer domains, but they are miscible in disordered amorphous polymer phases up to a certain thermodynamic equilibrium that depends on the polymer-fullerene interaction [65-67].

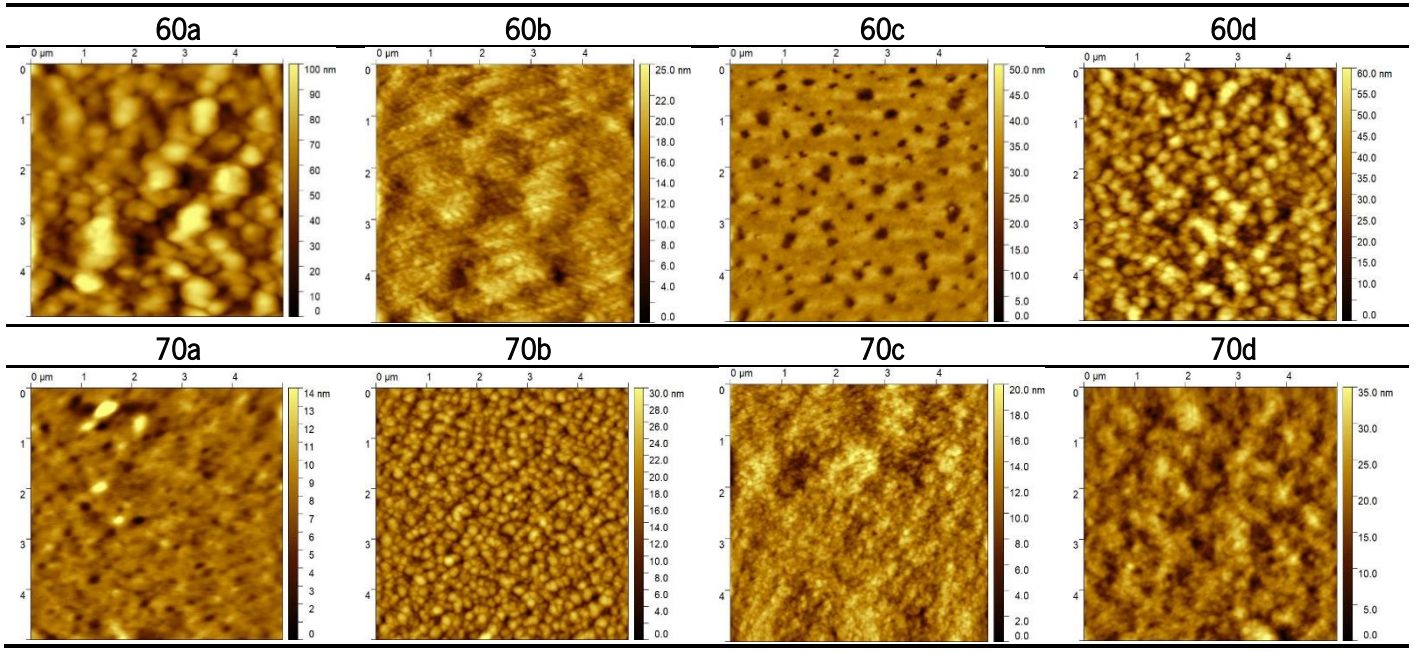

Figure 2.11. AFM morphology images of PffBT4T-2OD based bulk-heterojunction films with different fullerenes.

Therefore, BHJs blends with good polymer-fullerene miscibility may require higher fullerene loadings than less miscible blends so as to result in the formation of fullerene-rich domains.

The degree of fullerene dispersion in a polymer can affect its LUMO level (relatively to standard values determined by CV). According to Durrant *et al.* [68], pure solid $PC_{61}BM$ has a 100–200 meV higher electron affinity than $PC_{61}BM$ finely dispersed in polystyrene, suggesting that fullerene aggregation consistently lowers its LUMO value. These authors concluded [69] that variations in the film microstructure can modulate the device V_{OC} by up ~0.2 V. This modulation likely accounts for much of the observed variation in the recombination rate between systems which, leads to deviations in V_{OC} by up to ± 0.1 V from those predicted by consideration of material energetics alone. Similarly, Lange *et al.* [70] suggested that the intimate contact between fullerenes and polymer chains in highly intermixed blends may reduce the LUMO level of fullerenes and cause a reduced V_{OC}. Piersimoni *et al.* [71] reported that the crystallization of fullerene molecules lowers the energy of the charge transfer state (E_{CT}) and this is directly manifested in a reduced V_{OC}. Several studies have also found that a large degree of energetic disorder can cause significant reductions in the achievable V_{OC} in OPVs [72, 73], as we have already discussed. Troshin *et al.* [74] studied a broad range of fullerene derivatives having very similar LUMO levels but different solubilities in chlorobenzene and observed that the fullerene solubility strongly affects the BHJ morphology and consequently the solar cell figures of merit including the V_{OC}. This can be attributed to the density of states (DOS) near the HOMO/LUMO levels at D:A interface, changed by the bulk phase separation morphology (and consequently with intrinsic defects formation) and modifying the quasi-Fermi levels with further change in V_{OC}. V_{OC} was shown to attain maximum values for fullerene solubilities ≥ 30 $mg{\cdot}mL^{-1}$.

Different functional groups attached to the C_{60} and C_{70} cages, can severely change the electronic coupling between adjacent fullerenes through steric and/or electronic effects as well as their solid-state packing and crystallization properties, causing a significant decrease in their local electron mobility [75]. Furthermore, different fullerene functional groups can alter significantly the polymer:fullerene compatibility, causing significant changes in the nanoscale morphology. As a result, fullerenes with similar μ_e values in their pure state may originate BHJs with very different μ_e values due to different nanoscale morphologies [76, 77]. Additionally, the structural and energetic disorder that results from the presence of different fullerene isomers, as we have found in our C_{70}-based fullerenes, was also shown to contribute to the low electron mobility often observed in the fullerene-rich phase [50, 78, 79] with the consequent detrimental effect in the performance of devices. As such, efforts are underway to devise regioselective synthetic pathways [43, 44, 80-82].

Finally, and as an additional factor that can eventually help explaining our results, we mention that a relatively recent study suggests that fulleropyrrolidines due to their intrinsic basicity can have a detrimental interaction with the acidic PEDOT:PSS that may result in the degradation of the photovoltaic performance [83]. However, we also note that several other studies in literature [54, 84-86] have previously reported fulleropyrrolidine-based devices, with a standard geometry ITO/PEDOT:PSS/BHJ /Cathode, and exhibiting similar or higher performances than reference devices with $PC_{61}BM$ or $PC_{71}BM$. Therefore, this issue is certainly still open for debate.

All these studies above show that besides the energy levels of donor (HOMO) and acceptor (LUMO), several other factors also play an important role in the determination of the values of V_{OC} as well as of JSC, FF and PCE.

2.4 Conclusions

Novel C_{60} and C_{70} fullerene derivatives were synthesized by the well-known Prato reaction and the corresponding HOMO / LUMO levels measured by voltammetry. Despite the favourable LUMO levels of some of these novel fullerenes, compared to $PC_{71}BM$, all of them originated PffBT4T-2OD-based devices with poorer performances than reference devices based on the standard $PC_{71}BM$. The functionalization of C_{70} yielded a mixture of 4 regioisomers ($\alpha1$, $\alpha2$, $\beta1$, $\beta2$) that have different HOMO/LUMO levels as determined by DFT calculations. Interestingly, these C_{70} derivatives despite their higher light absorption in the visible range originated devices with lower performances than the corresponding C_{60} derivatives. This lower performance of devices based on C_{70} derivatives is most likely a consequence of both the energetic disorder introduced by the mixture of regioisomers and the presence in a relatively high amount of the $\beta1$-isomer which, according to recent reports, is known to be particularly harmful for device performance. In fact, energetic disorder, especially at D:A interface, tends to degrade the V_{OC}, and (also in the bulk) introduces intrinsic defects responsible for low J_{SC} (including a high influence of SCLC trap-dependent behaviour with also further decrease of carrier mobility) and increasing the exciton loss by recombination. While is not possible to make any straightforward correlation between the quantity of $\beta1$-isomer and the values of efficiency observed for each C_{70} derivative, it is possible to note that the amounts of $\beta1$ are high enough to interact negatively in the film blends decreasing their overall efficiency when compared with C_{60} derivatives.

References

[1] H. Gaspar, F. Figueira, L. Pereira, A. Mendes, C.J. Viana, G. Bernardo, Recent Developments in the Optimization of the Bulk Heterojunction Morphology of Polymer: Fullerene Solar Cells, Materials, 11 (2018).
[2] J.Q. Zhang, H.S. Tan, X.G. Guo, A. Facchetti, H. Yan, Material insights and challenges for non-fullerene organic solar cells based on small molecular acceptors, Nat. Energy, 3 (2018) 720-731.
[3] P. Cheng, G. Li, X.W. Zhan, Y. Yang, Next-generation organic photovoltaics based on non-fullerene acceptors, Nature Photonics, 12 (2018) 131-142.
[4] J.H. Hou, O. Inganas, R.H. Friend, F. Gao, Organic solar cells based on non-fullerene acceptors, Nature Materials, 17 (2018) 119-128.
[5] R. Ganesamoorthy, G. Sathiyan, P. Sakthivel, Review: Fullerene based acceptors for efficient bulk heterojunction organic solar cell applications, Solar Energy Materials and Solar Cells, 161 (2017) 102-148.
[6] R. Sondergaard, M. Hosel, D. Angmo, T.T. Larsen-Olsen, F.C. Krebs, Roll-to-roll fabrication of polymer solar cells, Materials Today, 15 (2012) 36-49.
[7] Z. Xiao, X. Jia, L.M. Ding, Ternary organic solar cells offer 14% power conversion efficiency, Sci. Bull., 62 (2017) 1562-1564.
[8] S.S. Li, L. Ye, W.C. Zhao, H.P. Yan, B. Yang, D.L. Liu, W.N. Li, H. Ade, J.H. Hou, A Wide Band Gap Polymer with a Deep Highest Occupied Molecular Orbital Level Enables 14.2% Efficiency in Polymer Solar Cells, J. Am. Chem. Soc., 140 (2018) 7159-7167.
[9] Y. Cui, H.F. Yao, J.Q. Zhang, T. Zhang, Y.M. Wang, L. Hong, K.H. Xian, B.W. Xu, S.Q. Zhang, J. Peng, Z.X. Wei, F. Gao, J.H. Hou, Over 16% efficiency organic photovoltaic cells enabled by a chlorinated acceptor with increased open-circuit voltages, Nature Communications, 10 (2019) 8.
[10] L.X. Meng, Y.M. Zhang, X.J. Wan, C.X. Li, X. Zhang, Y.B. Wang, X. Ke, Z. Xiao, L.M. Ding, R.X. Xia, H.L. Yip, Y. Cao, Y.S. Chen, Organic and solution-processed tandem solar cells with 17.3% efficiency, Science, 361 (2018) 1094-+.
[11] S.Q. Zhang, L. Ye, W.C. Zhao, D.L. Liu, H.F. Yao, J.H. Hou, Side Chain Selection for Designing Highly Efficient Photovoltaic Polymers with 2D-Conjugated Structure, Macromolecules, 47 (2014) 4653-4659.
[12] W. Ma, G.F. Yang, K. Jiang, J.H. Carpenter, Y. Wu, X.Y. Meng, T. McAfee, J.B. Zhao, C.H. Zhu, C. Wang, H. Ade, H. Yan, Influence of Processing Parameters and Molecular Weight on the Morphology and Properties of High-Performance PffBT4T-2OD:PC71BM Organic Solar Cells, Advanced Energy Materials, 5 (2015) 9.
[13] Y. Liu, J. Zhao, Z. Li, C. Mu, W. Ma, H. Hu, K. Jiang, H. Lin, H. Ade, H. Yan, Aggregation and morphology control enables multiple cases of high-efficiency polymer solar cells, Nature Communications, 5 (2014) 5293.
[14] Y. Zhang, A.J. Parnell, F. Pontecchiani, J.F.K. Cooper, R.L. Thompson, R.A.L. Jones, S.M. King, D.G. Lidzey, G. Bernardo, Understanding and controlling morphology evolution via DIO plasticization in PffBT4T-2OD/PC71BM devices, Scientific Reports, 7 (2017) 44269.
[15] Y.W. Zhang, A.J. Parnell, O. Blaszczyk, A.J. Musser, I.D.W. Samuel, D.G. Lidzey, G. Bernardo, Effect of fullerene acceptor on the performance of solar cells based on PffBT4T-2OD, Physical Chemistry Chemical Physics, 20 (2018) 19023-19029.
[16] T. Umeyama, K. Igarashi, D. Sakamaki, S. Seki, H. Imahori, Unique cohesive nature of the β1-isomer of [70]PCBM fullerene on structures and photovoltaic performances of bulk heterojunction films with PffBT4T-2OD polymers, Chemical Communications, 54 (2018) 405-408.
[17] H. Kang, G. Kim, J. Kim, S. Kwon, H. Kim, K. Lee, Bulk-Heterojunction Organic Solar Cells: Five Core Technologies for Their Commercialization, Advanced Materials, 28 (2016) 7821-7861.

[18] C.J. Brabec, M. Heeney, I. McCulloch, J. Nelson, Influence of blend microstructure on bulk heterojunction organic photovoltaic performance, Chemical Society Reviews, 40 (2011) 1185-1199.
[19] H. Hoppe, N.S. Sariciftci, Morphology of polymer/fullerene bulk heterojunction solar cells, Journal of Materials Chemistry, 16 (2006) 45-61.
[20] J.C. Hummelen, B.W. Knight, F. Lepeq, F. Wudl, J. Yao, C.L. Wilkins, PREPARATION AND CHARACTERIZATION OF FULLEROID AND METHANOFULLERENE DERIVATIVES, J. Org. Chem., 60 (1995) 532-538.
[21] G. Yu, J. Gao, J.C. Hummelen, F. Wudl, A.J. Heeger, Polymer photovoltaic cells - Enhanced efficiencies via a network of internal donor-acceptor heterojunctions, Science, 270 (1995) 1789-1791.
[22] M.M. Wienk, J.M. Kroon, W.J.H. Verhees, J. Knol, J.C. Hummelen, P.A. van Hal, R.A.J. Janssen, Efficient methano 70 fullerene/MDMO-PPV bulk heterojunction photovoltaic cells, Angewandte Chemie-International Edition, 42 (2003) 3371-3375.
[23] M. Williams, N.R. Tummala, S.G. Aziz, C. Risko, J.L. Bredas, Influence of Molecular Shape on Solid-State Packing in Disordered PC61BM and PC71BM Fullerenes, Journal of Physical Chemistry Letters, 5 (2014) 3427-3433.
[24] F.J. Zhang, Z.L. Zhuo, J. Zhang, X. Wang, X.W. Xu, Z.X. Wang, Y.S. Xin, J. Wang, W.H. Tang, Z. Xu, Y.S. Wang, Influence of PC60BM or PC70BM as electron acceptor on the performance of polymer solar cells, Solar Energy Materials and Solar Cells, 97 (2012) 71-77.
[25] J. Zhao, S.L. Zhao, Z. Xu, B. Qiao, D. Huang, L. Zhao, Y. Li, Y.Q. Zhu, P. Wang, Revealing the Effect of Additives with Different Solubility on the Morphology and the Donor Crystalline Structures of Organic Solar Cells, Acs Applied Materials & Interfaces, 8 (2016) 18231-18237.
[26] S. Vidal, M. Izquierdo, W.K. Law, K. Jiang, S. Filippone, J. Perles, H. Yan, N. Martín, Photochemical site-selective synthesis of [70]methanofullerenes, Chemical Communications, 52 (2016) 12733-12736.
[27] Z.Q. Liu, Modification on Fullerene, Curr Org Synth, 14 (2017) 999-1021.
[28] A. Kausar, Advances in Polymer/Fullerene Nanocomposite: A Review on Essential Features and Applications, Polymer-Plastics Technology and Engineering, 56 (2017) 594-605.
[29] M. Chen, R. Guan, S. Yang, Hybrids of Fullerenes and 2D Nanomaterials, Advanced Science, 6 (2019) 1800941.
[30] C.-Z. Li, H.-L. Yip, A.K.Y. Jen, Functional fullerenes for organic photovoltaics, Journal of Materials Chemistry, 22 (2012) 4161-4177.
[31] S. Grimme, J.G. Brandenburg, C. Bannwarth, A. Hansen, Consistent structures and interactions by density functional theory with small atomic orbital basis sets, The Journal of Chemical Physics, 143 (2015) 054107.
[32] A. Karton, S.L. Waite, A.J. Page, Performance of DFT for C60 Isomerization Energies: A Noticeable Exception to Jacob's Ladder, The Journal of Physical Chemistry A, 123 (2019) 257-266.
[33] H. Wang, Y. He, Y. Li, H. Su, Photophysical and Electronic Properties of Five PCBM-like C60 Derivatives: Spectral and Quantum Chemical View, The Journal of Physical Chemistry A, 116 (2012) 255-262.
[34] T.A. Beu, J. Onoe, A. Hida, First-principles calculations of the electronic structure of one-dimensional C-60 polymers, Physical Review B, 72 (2005) 155416.
[35] F. Neese, The ORCA program system, Wiley Interdisciplinary Reviews: Computational Molecular Science, 2 (2012) 73-78.
[36] M. Prato, M. Maggini, C. Giacometti, G. Scorrano, G. Sandona, G. Farnia, Synthesis and electrochemical properties of substituted fulleropyrrolidines, Tetrahedron, 52 (1996) 5221-5234.
[37] M. Urbani, B. Pelado, P. de la Cruz, K.-i. Yamanaka, O. Ito, F. Langa, Synthesis and Photoinduced Energy- and Electron-Transfer Processes of C60–Oligothienylenevinylene–C70 Dumbbell Compounds, Chemistry – A European Journal, 17 (2011) 5432-5444.

[38] L.Y. Lu, W. Chen, T. Xu, L.P. Yu, High-performance ternary blend polymer solar cells involving both energy transfer and hole relay processes, Nature Communications, 6 (2015).
[39] M.-A. Pan, T.-K. Lau, Y. Tang, Y.-C. Wu, T. Liu, K. Li, M.-C. Chen, X. Lu, W. Ma, C. Zhan, 16.7%-efficiency ternary blended organic photovoltaic cells with PCBM as the acceptor additive to increase the open-circuit voltage and phase purity, Journal of Materials Chemistry A, 7 (2019) 20713-20722.
[40] F. Langa, P. de la Cruz, A. de la Hoz, E. Espíldora, F.P. Cossío, B. Lecea, Modification of Regioselectivity in Cycloadditions to C70 under Microwave Irradiation, The Journal of Organic Chemistry, 65 (2000) 2499-2507.
[41] T. Umeyama, H. Imahori, Isomer Effects of Fullerene Derivatives on Organic Photovoltaics and Perovskite Solar Cells, Accounts of Chemical Research, 52 (2019) 2046-2055.
[42] T. Umeyama, S. Takahara, S. Shibata, K. Igarashi, T. Higashino, K. Mishima, K. Yamashita, H. Imahori, cis-1 Isomers of tethered bismethano 70 fullerene as electron acceptors in organic photovoltaics, Rsc Advances, 8 (2018) 18316-18326.
[43] T. Umeyama, S. Shibata, K. Igarashi, S. Takahara, T. Higashino, S. Seki, H. Imahori, Enantiomerically Separated α-[70]PCBM for Organic Photovoltaics, Chemistry Letters, 46 (2017) 1001-1003.
[44] T. Umeyama, T. Miyata, A.C. Jakowetz, S. Shibata, K. Kurotobi, T. Higashino, T. Koganezawa, M. Tsujimoto, S. Gélinas, W. Matsuda, S. Seki, R.H. Friend, H. Imahori, Regioisomer effects of [70]fullerene mono-adduct acceptors in bulk heterojunction polymer solar cells, Chemical Science, 8 (2017) 181-188.
[45] V.D. Mihailetchi, J. Wildeman, P.W.M. Blom, Space-Charge Limited Photocurrent, Physical Review Letters, 94 (2005) 126602.
[46] Y.-J. Cheng, M.-H. Liao, C.-Y. Chang, W.-S. Kao, C.-E. Wu, C.-S. Hsu, Di(4-methylphenyl)methano-C-60 Bis-Adduct for Efficient and Stable Organic Photovoltaics with Enhanced Open-Circuit Voltage, Chemistry of Materials, 23 (2011) 4056-4062.
[47] H.U. Kim, D. Mi, J.H. Kim, J.B. Park, S.C. Yoon, U.C. Yoon, D.H. Hwang, Carbazole-containing fullerene derivatives for P3HT-based bulk-heterojunction solar cells, Sol. Energy Mater. Sol. Cells, 105 (2012) 6-14.
[48] N.-W. Tseng, Y. Yu, Y. Li, J. Zhao, S.K. So, H. Yan, K.M. Ng, Isobenzofulvene-fullerene mono-adducts for organic photovoltaic applications, Journal of Materials Chemistry C, 3 (2015) 977-980.
[49] G.X. Liu, T.T. Cao, Y.J. Xia, B. Song, Y. Zhou, N. Chen, Y.F. Li, Dihydrobenzofuran-C-60 bisadducts as electron acceptors in polymer solar cells: Effect of alkyl substituents, Synthetic Met, 215 (2016) 176-183.
[50] S. Kitaura, K. Kurotobi, M. Sato, Y. Takano, T. Umeyama, H. Imahori, Effects of dihydronaphthyl-based 60 fullerene bisadduct regioisomers on polymer solar cell performance, Chemical Communications, 48 (2012) 8550-8552.
[51] F. Nisic, A. Colombo, C. Dragonetti, A. Cominetti, A. Pellegrino, N. Perin, R. Po, A. Tacca, Novel Terthiophene-Substituted Fullerene Derivatives as Easily Accessible Acceptor Molecules for Bulk-Heterojunction Polymer Solar Cells, International Journal of Photoenergy, (2014).
[52] J.H. Choi, K.I. Son, T. Kim, K. Kim, K. Ohkubo, S. Fukuzumi, Thienyl-substituted methanofullerene derivatives for organic photovoltaic cells, J. Mater. Chem., 20 (2010) 475-482.
[53] R. Tao, T. Umeyama, K. Kurotobi, H. Imahori, Effects of Alkyl Chain Length and Substituent Pattern of Fullerene Bis-Adducts on Film Structures and Photovoltaic Properties of Bulk Heterojunction Solar Cells, Acs Applied Materials & Interfaces, 6 (2014) 17313-17322.
[54] Y.L. Liang, Y.J. Hao, X.D. Liu, L. Feng, M.Z. Chen, Q.Q. Tang, N. Chen, M.L. Tang, B.B. Sun, Y. Zhou, B. Song, Efficiency enhancement from 60 fulleropyrrolidine-based polymer solar cells through N-substitution manipulation, Carbon, 92 (2015) 185-192.

[55] S. Yamane, J. Mizukado, T. Takahashi, Y. Suzuki, M. Sakurai, H. Hagihara, H. Suda, Fulleropyrrolidine Derivatives with Benzophenone Moiety as Electron Acceptors in Thermally Stable Organic Photovoltaic Devices, Chemistry Letters, 44 (2015) 527-529.
[56] J.C.S. Costa, R.J.S. Taveira, C.F.R.A.C. Lima, A. Mendes, L.M.N.B.F. Santos, Optical band gaps of organic semiconductor materials, Optical Materials, 58 (2016) 51-60.
[57] A.J. Trindade, L. Pereira, Bulk Heterojunction Organic Solar Cell Area-Dependent Parameter Fluctuation, Int. J. Photoenergy, (2017) 10.
[58] C.J. Brabec, A. Cravino, D. Meissner, N.S. Sariciftci, T. Fromherz, M.T. Rispens, L. Sanchez, J.C. Hummelen, Origin of the open circuit voltage of plastic solar cells, Advanced Functional Materials, 11 (2001) 374-380.
[59] S.R. Cowan, A. Roy, A.J. Heeger, Recombination in polymer-fullerene bulk heterojunction solar cells, Physical Review B, 82 (2010).
[60] Y. Wu, Z.Y. Wang, X.Y. Meng, W. Ma, Morphology Analysis of Organic Solar Cells with Synchrotron Radiation Based Resonant Soft X-Ray Scattering, Progress in Chemistry, 29 (2017) 93-101.
[61] M.J. Hollamby, Practical applications of small-angle neutron scattering, Phys. Chem. Chem. Phys., 15 (2013) 10566-10579.
[62] P. Muller-Buschbaum, The Active Layer Morphology of Organic Solar Cells Probed with Grazing Incidence Scattering Techniques, Advanced Materials, 26 (2014) 7692-7709.
[63] Y. Yan, X. Liu, T. Wang, Conjugated-Polymer Blends for Organic Photovoltaics: Rational Control of Vertical Stratification for High Performance, Adv. Mater., 29 (2017).
[64] S. Mukherjee, C.M. Proctor, G.C. Bazan, T.Q. Nguyen, H. Ade, Significance of Average Domain Purity and Mixed Domains on the Photovoltaic Performance of High-Efficiency Solution-Processed Small-Molecule BHJ Solar Cells, Adv. Energy Mater., 5 (2015).
[65] G. Bernardo, N. Deb, S.M. King, D.G. Bucknall, Phase behavior of blends of PCBM with amorphous polymers with different aromaticity, Journal of Polymer Science Part B: Polymer Physics, 54 (2016) 994-1001.
[66] G. Bernardo, D.G. Bucknal, Recent Progress in the Understanding and Manipulation of Morphology in Polymer: Fullerene Photovoltaic Cells, in: S.L. Pyshkin, John M. Ballato (Eds.) Optoelectronics - Advanced Materials and Devices, IntechOpen2013, pp. 207 - 227.
[67] N.D. Treat, A. Varotto, C.J. Takacs, N. Batara, M. Al-Hashimi, M.J. Heeney, A.J. Heeger, F. Wudl, C.J. Hawker, M.L. Chabinyc, Polymer-Fullerene Miscibility: A Metric for Screening New Materials for High-Performance Organic Solar Cells, J. Am. Chem. Soc., 134 (2012) 15869-15879.
[68] F.C. Jamieson, E.B. Domingo, T. McCarthy-Ward, M. Heeney, N. Stingelin, J.R. Durrant, Fullerene crystallisation as a key driver of charge separation in polymer/fullerene bulk heterojunction solar cells, Chemical Science, 3 (2012) 485-492.
[69] D. Credgington, J.R. Durrant, Insights from Transient Optoelectronic Analyses on the Open-Circuit Voltage of Organic Solar Cells, J. Phys. Chem. Lett., 3 (2012) 1465-1478.
[70] I. Lange, J. Kniepert, P. Pingel, I. Dumsch, S. Allard, S. Janietz, U. Scherf, D. Neher, Correlation between the Open Circuit Voltage and the Energetics of Organic Bulk Heterojunction Solar Cells, J. Phys. Chem. Lett., 4 (2013) 3865-3871.
[71] F. Piersimoni, S. Chambon, K. Vandewal, R. Mens, T. Boonen, A. Gadisa, M. Izquierdo, S. Filippone, B. Ruttens, J. D'Haen, N. Martin, L. Lutsen, D. Vanderzande, P. Adriaensens, J.V. Manca, Influence of Fullerene Ordering on the Energy of the Charge-Transfer State and Open-Circuit Voltage in Polymer:Fullerene Solar Cells, The Journal of Physical Chemistry C, 115 (2011) 10873-10880.
[72] G. Garcia-Belmonte, Carrier recombination flux in bulk heterojunction polymer:fullerene solar cells: Effect of energy disorder on ideality factor, Solid-State Electronics, 79 (2013) 201-205.
[73] J.C. Blakesley, D. Neher, Relationship between energetic disorder and open-circuit voltage in bulk heterojunction organic solar cells, Physical Review B, 84 (2011).

[74] P.A. Troshin, H. Hoppe, J. Renz, M. Egginger, J.Y. Mayorova, A.E. Goryochev, A.S. Peregudov, R.N. Lyubovskaya, G. Gobsch, N.S. Sariciftci, V.F. Razumov, Material Solubility-Photovoltaic Performance Relationship in the Design of Novel Fullerene Derivatives for Bulk Heterojunction Solar Cells, Adv. Funct. Mater., 19 (2009) 779-788.
[75] J. Ide, D. Fazzi, M. Casalegno, S.V. Meille, G. Raos, Electron transport in crystalline PCBM-like fullerene derivatives: a comparative computational study, Journal of Materials Chemistry C, 2 (2014) 7313-7325.
[76] C. Zhang, S. Langner, A.V. Mumyatov, D.V. Anokhin, J. Min, J.D. Perea, K.L. Gerasimov, A. Osvet, D.A. Ivanov, P. Troshin, N. Li, C.J. Brabec, Understanding the correlation and balance between the miscibility and optoelectronic properties of polymer–fullerene solar cells, Journal of Materials Chemistry A, 5 (2017) 17570-17579.
[77] G.K. Long, R. Shi, Y.C. Zhou, A.L. Li, B. Kan, W.R. Wu, U.S. Jeng, T. Xu, T.Y. Yan, M.T. Zhang, X. Yang, L.T. Sun, A. Gray-Weale, X.J. Wan, H.T. Zhang, C.X. Li, Y.T. Wang, Y.S. Chen, Molecular Origin of Donor- and Acceptor-Rich Domain Formation in Bulk-Heterojunction Solar Cells with an Enhanced Charge Transport Efficiency, Journal of Physical Chemistry C, 121 (2017) 5864-5870.
[78] F. Steiner, S. Foster, A. Losquin, J. Labram, T.D. Anthopoulos, J.M. Frost, J. Nelson, Distinguishing the influence of structural and energetic disorder on electron transport in fullerene multi-adducts, Materials Horizons, 2 (2015) 113-119.
[79] M. Lenes, S.W. Shelton, A.B. Sieval, D.F. Kronholm, J.C. Hummelen, P.W.M. Blom, Electron Trapping in Higher Adduct Fullerene-Based Solar Cells, Adv. Funct. Mater., 19 (2009) 3002-3007.
[80] B.L. Zhang, J.M. White, D.J. Jones, W.W.H. Wong, Regioselective synthesis of fullerene multiadducts via tether-directed 1,3-dipolar cycloaddition, Organic & Biomolecular Chemistry, 13 (2015) 10505-10510.
[81] M.R. Ceron, L. Echegoyen, Recent progress in the synthesis of regio-isomerically pure bis-adducts of empty and endohedral fullerenes, Journal of Physical Organic Chemistry, 29 (2016) 613-619.
[82] B.L. Zhang, J. Subbiah, Y.Y. Lai, J.M. White, D.J. Jones, W.W.H. Wong, One-pot selective synthesis of a fullerene bisadduct for organic solar cell applications, Chemical Communications, 51 (2015) 9837-9840.
[83] M. Karakawa, T. Nagai, Interfacial Reaction of Fulleropyrrolidines Affecting Organic Photovoltaic Performance, ACS Applied Materials & Interfaces, 9 (2017) 21338-21345.
[84] K. Matsumoto, K. Hashimoto, M. Kamo, Y. Uetani, S. Hayase, M. Kawatsura, T. Itoh, Design of fulleropyrrolidine derivatives as an acceptor molecule in a thin layer organic solar cell, J. Mater. Chem., 20 (2010) 9226-9230.
[85] M. Karakawa, T. Nagai, K. Adachi, Y. Ie, Y. Aso, N-phenyl 60 fulleropyrrolidines: alternative acceptor materials to PC61BM for high performance organic photovoltaic cells, Journal of Materials Chemistry A, 2 (2014) 20889-20895.
[86] P. Pitliya, Y. Sun, J.C. Garza, C. Liu, X. Gong, A. Karim, D. Raghavan, Synthesis and characterization of novel fulleropyrrolidine in P3HT blended bulk heterojunction solar cells, Polymer, 55 (2014) 1769-1781

Chapter III. Thiophene- and carbazole-substituted N-methyl-fulleropyrrolidine acceptors in PffBT4T-2OD based solar cells

Abstract

The impact of fullerene side chain functionalization with thiophene and carbazole groups on the device properties of bulk-heterojunction polymer:fullerene solar cells is discussed through a systematic investigation of material blends consisting of the conjugated polymer poly[(5,6-difluoro-2,1,3-benzothiadiazol-4,7-diyl)-alt-(3,3'''-di(2-octyldodecyl)-2,2';5',2'';5'',2'''-quaterthiophen-5,5'''-diyl)] (PffBT4T-2OD) as donor and C_{60} and C_{70} based fulleropyrrolidines as acceptor. The photovoltaic performance clearly depended on the molecular structure of the fulleropyrrolidine substituents although no direct correlation with the BHJ surface morphology, as determined by AFM, could be established. Despite possessing some favorable LUMO levels, when compared to the standard $PC_{71}BM$, all the synthesized fulleropyrrolidine acceptors produced OPV devices with inferior performances than reference devices based on $PC_{71}BM$. Fulleropyrrolidines based on C_{60} produced, in general, better devices than those based on C_{70}, most likely due to the energetic and structural disorder in the regioisomer mixtures of C_{70}-based fullerenes. The results provide new knowledge on the effect of the fullerene functionalization on the efficiency of BHJ solar cells.

3.1 Introduction

The work reported in this chapter is based in the article "*Thiophene-and Carbazole-Substituted N-Methyl-Fulleropyrrolidine Acceptors in PffBT4T-2OD Based Solar Cells, Materials, 13(6), 2020".*

Organic Photovoltaic (OPV) cells are a promising solar energy harvesting technology because of their flexibility, lightweight and compatibility with large-scale production using high-throughput roll-to-roll methods (R2R) that are expected to reduce the module fabrication cost and the energy payback time [1-3]. Much efforts have been made in the last two decades focusing in the material design, device engineering and morphology optimization, aiming to increase the power conversion efficiencies (PCE) of the OPV device. In recent years, the OPVs have experienced significant developments, attaining recently PCE values > 16 % for single junction devices [4-6] and > 17% for tandem cells [7]. The active layer in a OPV device is made of a blend of a p-type polymer and an n-type acceptor forming a bicontinuous interpenetrating network.

The p-type small band gap polymer PffBT4T-2OD, also known as PCE11, has recently become popular in the OPV field [8-15] due to its high hole mobility of 1.5–3.0 × 10^{-2} $cm^2V^{-1}s^{-1}$ [10], associated with its high crystallinity, that allows its use in relatively thick (~300 nm) and high efficient solar cells. The n-type acceptors used in OPVs can be either fullerene derivatives or non-fullerene small molecules. Although the performance of OPVs using non-fullerene acceptors has already outperformed its fullerene-based counterpart, the research in polymer:fullerene solar cells using new "non-standard" fullerenes remains very active [16-22].

Buckminsterfullerene C_{60} was the first fullerene used in an OPV device, in the seminal work by Sariciftci et al. [23] reporting the discovery of the photo-induced electron-transfer from a conducting polymer to C_{60}. However, the very low solubility of C_{60} in common organic solvents makes it very difficult to process and therefore, soon after its introduction in the OPV field, the strategy of functionalizing C_{60} with solubilizing moieties was adopted. For this reason, the fullerenes $PC_{61}BM$ [24, 25] and its analogue $PC_{71}BM$ [26] soon emerged as the two most widely used electron accepting materials in OPVs. These two fullerenes, $PC_{61}BM$ and $PC_{71}BM$, are now utilized as reference acceptors for all kinds of other fullerene acceptors, because of their good solubility, high electron mobility and high chemical stability. A key difference between $PC_{61}BM$ and $PC_{71}BM$ is the broader photo-absorption profile of $PC_{71}BM$ in the visible region of the solar spectrum that allows increased photon harvesting and a potentially higher photocurrent for devices using $PC_{71}BM$ rather than $PC_{61}BM$, an important attribute that has brought the C_{70} analogue to the forefront of OPV research (despite its higher cost) [27, 28].

Fullerene derivatives display a wide range of physical and chemical properties that make them appealing for use in OPVs. Fullerenes with proper organic moieties can be tuned on their solubility, energy levels, molecular interactions, orientation in the solid state, as well as on their surface energy [29]. Several different fullerene functionalization strategies have been previously tested aiming to improve the performance of polymer:fullerene solar cells [16, 17, 30]. Some important examples of alternative fullerene acceptor families include dihydronaphthyl-based fullerenes [31-34] and fulleropyrrolidines [35-44].

Fulleropyrrolidines have several attractive features namely: they can be synthesized from pristine C_{60} and C_{70} in a simple one-step synthetic procedure under Prato reaction conditions; ease of modification of the substituents linked to the pyrrolidine ring by using commercially available or easily prepared glycine and aldehyde derivatives as reactants; and a good chemical stability. One of the first reports on the use of fulleropyrrolidine acceptors in OPVs, was made by Lee et al. [35] in 2007. These authors synthesized fulleropyrrolidine derivatives substituted with different chain lengths and tested them in OPVs with

standard geometry and using the polymer MEH-PPV. The efficiencies obtained were all very low (≤ 0.47%) and no comparison was made with reference devices using $PC_{61}BM$. Matsumoto et al. [36] synthesized and tested a series of fulleropyrrolidine derivatives in P3HT-based OPV cells with standard geometry. Several of the fulleropyrrolidine derivatives originated devices that outperformed reference devices with $PC_{61}BM$. The best fulleropyrrolidine-based devices attained a PCE of 3.44% compared to 2.53% for $PC_{61}BM$-based reference devices. A new phenothiazine-containing fulleropyrrolidine derivative was synthesized and tested by Mi et al. [37] in P3HT-based devices with standard geometry. However, the devices achieved the best modest efficiency of only 1.42 %. Saravanan et al. [38] synthesized two fullerene-terthiophene dyads without (3T-C_{60}) and with (3TH-C_{60}) hexyl chains on the terthiophene substituent and tested them in P3HT devices with standard geometry. The 3TH-C_{60} fullerenes originated better devices (max PCE of 2.54 %) than 3T-C60 due to their higher miscibility with the P3HT matrix. Zhang et al. [39] synthesized two indole-containing fullerene derivatives and tested them in inverted solar cells with the structure of ITO/ZnO/P3HT:fullerene/MoO_3/Ag. The best devices showed a PCE of 3.32%, very similar to the PCE of 3.28% for reference $PC_{61}BM$ based devices. Six novel soluble [60]fulleropyrrolidine derivatives were synthesized by Karakawa et al. [40] and tested in OPVs with P3HT and with PTB7. Devices with P3HT were made with the standard geometry ITO/PEDOT:PSS/BHJ/Al and devices with PTB7 were made with inverted geometry ITO/PFN/BHJ/MoOx/Al. The best P3HT-based devices using fulleropyrrolidine derivatives achieved a max. PCE of 2.41 % comparable to the value of 2.30 % obtained for reference P3HT devices with $PC_{61}BM$. Interestingly, the authors also observed that although the LUMO levels of all the fulleropyrrolidines closely resemble each other and those of $PC_{61}BM$, devices with P3HT displayed a large variety of PCEs ranging from 0.02% to 2.41% depending on the acceptor. In the case of PTB7-based devices using fulleropyrrolidines a max PCE of 7.34% was achieved, slightly above the value of 7.03 % obtained for reference PTB7 devices with $PC_{61}BM$. Kaunisto et al. [41] synthesized eight fulleropyrrolidine derivatives with thiophene substituents ranging from 1 to 4 thiophene units and tested them in inverted BHJs using P3HT as p-type material. Fulleropyrrolidine derivatives with one or two thiophene units performed better as acceptor materials than those with three or four thiophene units. Interestingly, even though all the devices with different fulleropyrrolidine derivatives exhibited very similar BHJ surface morphologies, as determined by AFM, and all the fulleropyrrolidine derivatives exhibited very similar LUMO levels (either -3.7 eV or -3.6 eV), as determined by cyclic voltammetry, the produced devices exhibited largely different PCEs ranging from < 0.01 % to 2.0 %, and all of them inferior to the PCE of reference P3HT:$PC_{61}BM$ devices. Pitliya et al. [42] synthesized a novel fulleropyrrolidine derivative C_{60}-fused N-(3methoxypropyl)-2-(carboxyethyl)-5-(4-cyanophenyl)fulleropyrrolidine (NCPF) and

tested it in P3HT-based OPV devices with standard geometry ITO/PEDOT:PSS/BHJ/Al. Fulleropyrrolidine-based devices achieved a PCE of 1.77% comparable to 2.14% for reference devices based on $PC_{61}BM$. Eight fulleropyrrolidine derivatives with alternating N-phenyl or N-methyl group were synthesized by Liang et al. [43] and tested in P3HT-based OPVs with standard geometry ITO/PEDOT:PSS/BHJ/Ca/Al. The devices produced using different fulleropyrrolidine derivatives exhibited very different photovoltaic properties with PCEs ranging from 0.70 % to 3.19 %, compared with the PCE value of 3.32 % for reference devices with $PC_{61}BM$. Interestingly, even though some of the fullerenes exhibited more favourable LUMO levels than $PC_{61}BM$, they originated devices with considerably lower V_{oc} and PCE values. Yamane et al. [44] synthesized two fulleropyrrolidine derivatives with the benzophenone moiety that can supress their crystallization and tested them in P3HT-based OPV devices with structure ITO/MoO_3/BHJ/Al. The devices exhibited higher thermal stability but lower PCE than reference devices with $PC_{61}BM$.

In this work we synthesize some novel thiophene- and carbazole-substituted N-methyl-fulleropyrrolidine acceptors and test their impact on the performance of polymer solar cells based on the polymer PffBT4T-2OD.

3.2 Materials and Methods

3.2.1 Materials

The pristine fullerenes C_{60} (> 99.5% purity) with M_w= 720.64 g.mol^{-1} and C_{70} (> 99% purity) with M_w= 840.77 g.mol^{-1}, used in the synthesis of novel fullerene derivatives were purchased from Solenne BV, as well as the $PC_{61}BM$ (M_w = 910.88 g·mol^{-1}, 99% purity) used in cyclic voltammetry measurements.

The following materials, used in device fabrication, were purchased from Ossila Ltd.: i) Poly(3,4-ethylenedioxy-thiophene):poly(styrene sulfonic acid) (PEDOT:PSS, Heraeus Clevios AI4083); ii) the polymer poly[(5,6-difluoro-2,1,3-benzothiadiazol-4,7-diyl)-alt-(3,3'''-di(2-octyldodecyl)-2,2';5',2'';5'',2'''-quaterthiophen-5,5'''-diyl)], commonly known as PffBT4T-2OD or PCE11 with M_n = 83,008 g.mol^{-1} and M_w = 172,033 g.mol^{-1} (catalogue # M302) and iii) the reference fullerene $PC_{71}BM$ (M113), [6,6]-phenyl-C_{71} butyric acid methyl ester, with empirical formula $C_{82}H_{14}O_2$ and M_w = 1030.99 g mol^{-1}. The solvent used in device fabrication, *o*-dichlorobenzene (DCB), has high purity grade and was purchased from Sigma-Aldrich. All these materials and solvent were used as received without further purification.

3.2.2 NMR spectroscopy

^{1}H and ^{13}C solution NMR spectra of the functionalized fullerenes were recorded on a Bruker Avance 500 (500.13 and 125.76 MHz for ^{1}H and ^{13}C, respectively) spectrometer. CS_2, deuterated acetone and deuterated chloroform (99.6 %, TCI Chemicals) were used as solvents and tetramethylsilane (TMS) as internal reference. The chemical shifts are expressed in (ppm).

*3.2.3 Preparation of compounds **60A-60D** and **70A-70D***

A solution of toluene containing 100 mg (0.14 mmol) of C_{60} or C_{70}, *N*-methylglycine (0.35 mmol) and of the corresponding aldehyde (0.67 mmol) was stirred until reflux temperature. After this 0.67 mmol of the corresponding aldehyde was added to the reaction every three hours (3 times) and the reaction was maintained for 24 h, then the solvent was removed in vacuum. The solid residue was purified by flash column chromatography (eluent: toluene/hexanes 1:3 with increasing amounts of toluene until purification of the first brown band) affording roughly 30-40% of the *N*-methyl-3,4-fulleropyrrolidine derivatives **60D** and **70D**. The ^{1}H, ^{13}C NMR and HSQC spectra for **60B-60D** and **70A-70D** are displayed in **APPENDIX II**.

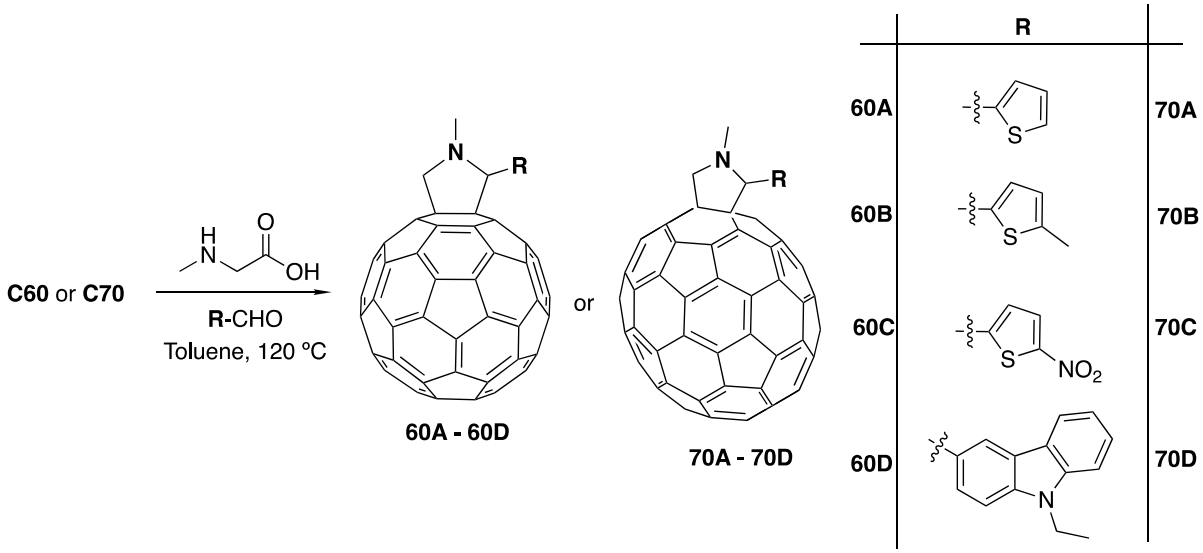

Figure 3. 1. Preparation method used in the synthesis of compounds 60A to 60D and 70A to 70D

60A: ^{1}H NMR (300 MHz, CS2 + Acetone-d6) δ 7.41 (d, J = 4.903 Hz, 2H), 7.06 (dd, J = 4.801, 3.819 Hz, 1H), 5.33 (s, 1H), 5.01 (d, J = 9.574 Hz, 1H), 4.32 (d, J = 9.534 Hz, 1H), 2.93 (s, 3H); ^{13}C NMR (126 MHz, Acetone-d6) δ 156.83, 154.67, 154.10, 153.91, 147.83, 147.56, 147.03, 146.87, 146.83, 146.76, 146.72, 146.65, 146.62, 146.48, 146.36, 146.15, 146.12, 145.92, 145.84, 145.82, 145.79, 145.68, 145.29, 145.24, 144.95, 143.70, 143.55, 143.25, 143.15, 142.85, 142.82, 142.75, 142.70, 142.63, 142.61, 142.60, 142.50, 142.43, 142.24, 142.18, 141.32, 140.73, 140.70, 140.45, 140.14, 137.62, 137.24, 136.55, 136.30, 128.60, 127.47, 127.24, 79.52, 77.77, 70.35, 69.34, 40.57. (Figures 3.1, 3.2 and 3.3)

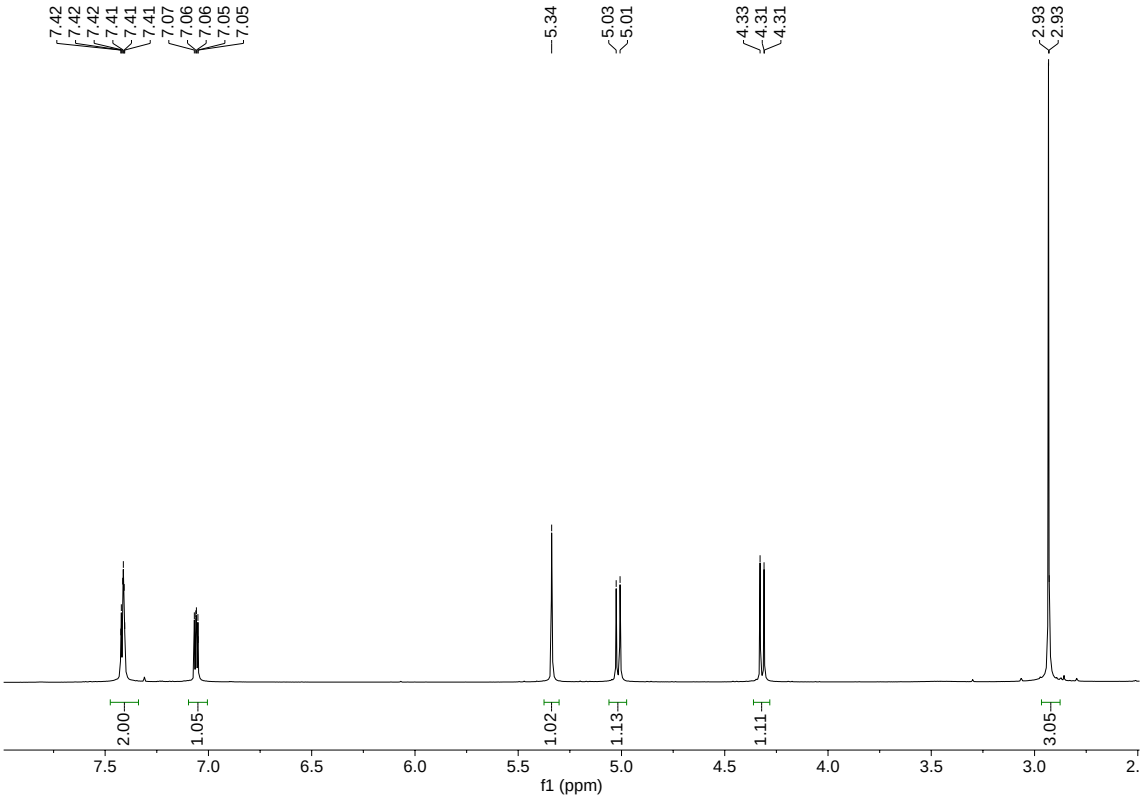

Figure 3. 2. ^{1}H NMR spectrum of compound **60A** in a mixture of CS2 and acetone-d6.

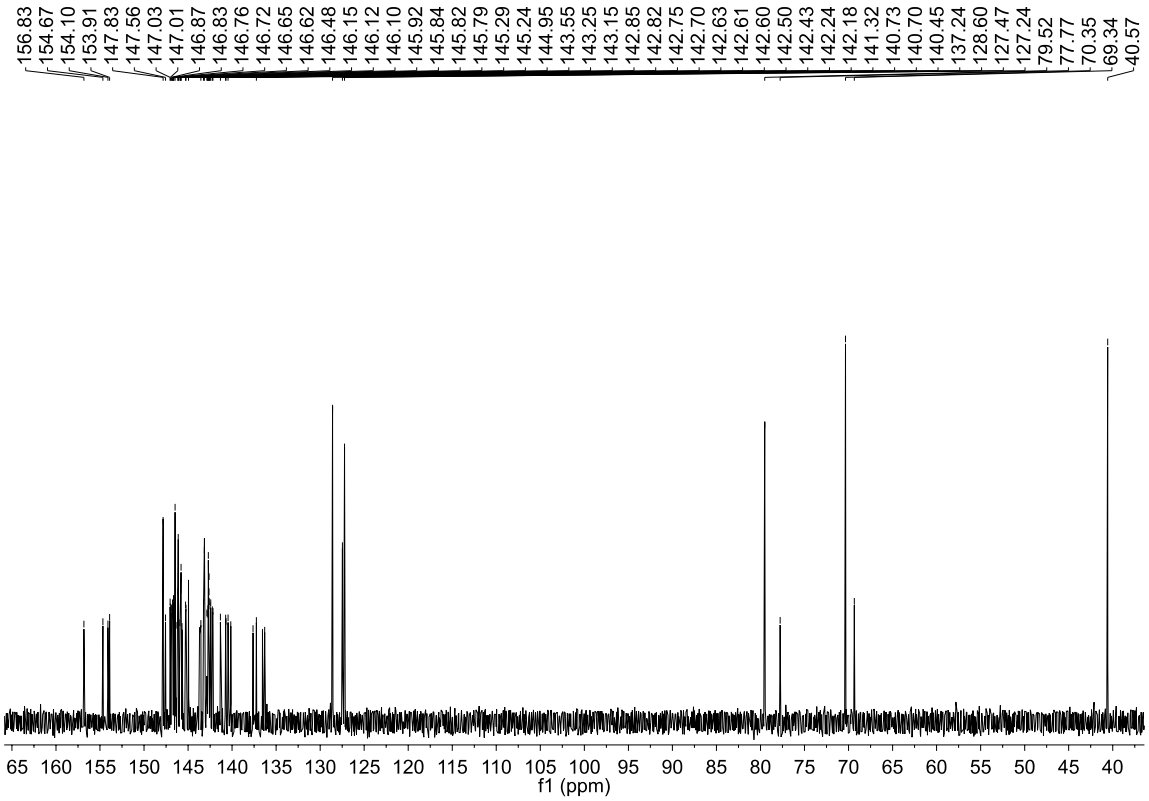

Figure 3. 3. ^{13}C NMR spectrum of compound **60A** in a mixture of CS_2 and acetone-d6.

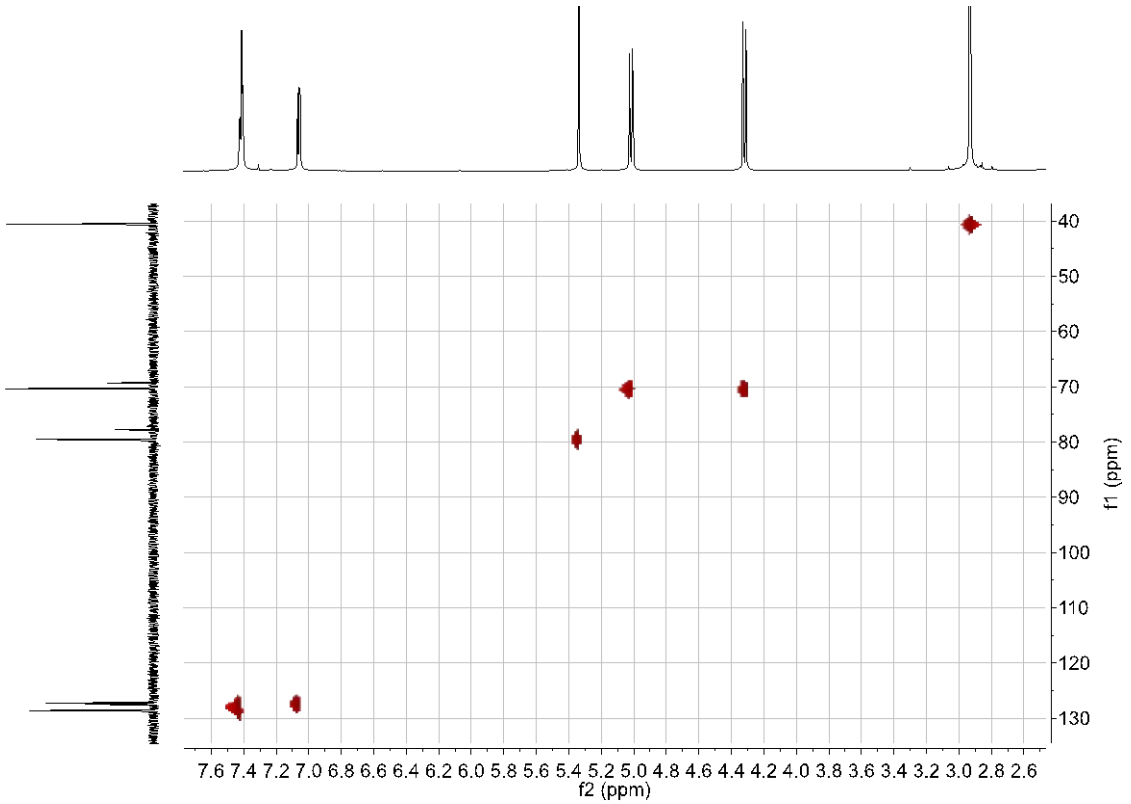

Figure 3. 4. HSQC spectrum of compound **60A** in a mixture of CS_2 and acetone-d6.

3.2.4 Cyclic Voltammetry

Autolat PGSTAT302N potentiostat was used in electrochemical experiments. Voltammograms were recorded using a three-electrode cell arrangement; a polished glassy-carbon (GC) pin (3 mm in diameter) served as a working electrode, a platinum wire as a counter electrode, and the reference electrode was acetonitrile Ag|Ag^+. Acetonitrile solution of $AgNO_3$ (0.01 M) with addition of 0.1 M of Bu4NPF6 was used in the compartment of the reference electrode. The fullerenes (ca. 0.6 mg/mL) were dissolved in a solvent mixture of 4:1 (by volume) chlorobenzene:acetonitrile with addition of 0.1 M Bu_4NPF_6 as a supporting electrolyte. Before measurements, the solutions were deaerated by purging high purity Argon during 7 minutes. Cyclic voltammograms were recorded at a potential scan rate of 100 mV/s. During the measurement the Argon flow was kept above the solution in the cell. All electrode potentials were quoted with respect to equilibrium potential ($E_{1/2}$) of Fc+/Fc redox couple in the same solvent mixture. The LUMO and HOMO energy levels were estimated from the onset potential of the reduction (E_{Red}^{on}) and oxidation (E_{Ox}^{on}) respectively.

3.2.5 Ab initio DFT calculations

Density Functional Theory calculations at the PBEh-3c level were performed to compute all molecular structures [45]. The electronic structure energies reported were computed at the PBE-def2-TZVP level which has been found to show better accuracy than hybrid functionals for these systems [46-48]. For C_{70} systems all isomers and diestereoisomers, α1, α2, β1and β2, were explicitly computed. All calculations were performed with the ORCA 4.2 program [49].

3.2.6 Absorption Spectroscopy

UV-Vis absorption spectroscopy was used, in a first stage, to characterize the optical properties of the pure fullerenes in o-dichlorobenzene solution. Attempts to measure the UV-Vis spectra of spin-coated thin films of the pure fullerenes on quartz windows were also made but without success due to the difficulty in preparing homogeneous thin films.

UV-Vis absorption spectroscopy was later used to evaluate the effect of fullerenes in the light absorption of the different blends, which is one of the first steps to charge generation. Absorption spectra (UV-Vis) were obtained on a Shimadzu UV-2501PC spectrophotometer, in the 350–800 nm range in solid-state film deposited in quartz substrates.

3.2.7 Device fabrication

OPV devices were made with a standard structure ITO/PEDOT:PSS/Active layer/Ca/Al. The active layers were all spin-coated from a o-dichlorobenzene solution with the polymer PffBT4T-2OD and the several fullerene derivatives shown in Figure 1, having concentrations of 4 $mg{\cdot}ml^{-1}$ and 4.8 $mg{\cdot}ml^{-1}$ respectively (1:1.2 ratio). Other PffBT4T-2OD:fullerene mass ratios were tested initially (1:3 and 3:1) but they produced lower device performances. Previous works with BHJs based on PffBT4T-2OD have typically used a solvent mixture of chlorobenzene:o-dichlorobenzene (1:1) to dissolve the polymer. However, in the present work it proved more appropriate to use a pure o-dichlorobenzene solvent (which has a stronger solubilizing power) due to the relatively high M_w of the polymer that makes it harder to dissolve. Some initial tests have shown, similarly to previous reports on fulleropyrrolidine based OPVs [39], no benefits on the use of additives and therefore no additives were used. The active layers were spin coated from pre-heated solutions (120 °C) at a spin speed of 800 rpm onto the PEDOT:PSS/glass substrate that was pre-heated to 120 °C. The active layer was spin-cast in a nitrogen filled glove box. The films were then left inside the glove box for 1 hour to dry. The cathode evaporation was then made sequentially composed by 5 nm Calcium (Ca) and 100 nm. Aluminium (Al) on top of the active layer under a vacuum < 2×10^{-6} mbar to form the top electrode contact.

3.2.8 Device performance characterization

Photovoltaic properties of the devices were determined using a Newport 92251A-1000 AM 1.5 solar simulator which was calibrated using an NREL standard silicon solar cell to ensure an irradiance level of 1000 W/m^2. An aperture mask was utilised to limit the light-exposed area of the device to 2.6 mm^2.

3.2.9 Morphological characterization using Atomic Force Microscopy (AFM)

Atomic Force Microscopy (AFM) in tapping mode was used to image the surface morphology of the PffBT4T-2OD:fullerene thin films. AFM experiments were performed using a Molecular Imaging PicoLE AFM. The measurements were performed in contact mode and several scans were imaged in flattened mode data to remove the background slope. The scan size of topographic AFM images presented in all experiments is 5x5 μm.

3.3 Results and Discussion

Several C_{60} and C_{70} fullerene compounds were prepared following the well-known Prato methodology where, the appropriate azomethine ylide precursors are generated using N-methyl glycine (sarcosine) and the corresponding aldehyde, in this case tiophene and carbazole moieties (Figure 3.25). These precursors react readily with C_{60} and C_{70} providing fullereopyrrolidines containing substituted tiophene and carbazole units moieties (Figure 3.25). Herein, this was achieved by a controlled cycloaddition reaction in which a pyrrolidine ring is fused with a 6,6 ring junction of both C_{60} or C_{70}.

Compounds **60A** to **60D** were synthesized by a 1,3-dipolar cycloaddition of the corresponding thiophene and carbazole aldehydes and C_{60}, with *N*-methylglycine in toluene under reflux. After purification by column chromatography on silica gel compounds **60A** to **60D** were obtained in around 40% yield. **70A** to **70D** were prepared in the same manner replacing C_{60} with C_{70}. The final structures were confirmed by ^{1}H NMR spectroscopy assignments by 2D-H experiments.

It is possible to note that, the solubility of the resulting C_{70} derivatives was improved when compared with the solubility of the substituted C_{60}. In fact, in all compounds comprised by C_{60} these were only possible to dissolve when CS_2 was used. On the other hand, most of the modified C_{70} were soluble or partially soluble in deuterated chloroform (C_{70} bearing the carbazole unit showed to be a little less soluble). The ^{1}H NMR spectra of the C_{60} derivatives are quite simple and shows the characteristic features of a *N*-methyl[60]fulleropyrrolidine mono-adducts. The ^{1}H NMR spectra of the C_{70} derivatives showed four singlets and four sets of doblets ($J \approx 9.5$ Hz) for the pyrrolidine protons as a characteristic feature of four distinct C_{70} isomeric products. Unlike C_{60}, in which all carbon atoms and double bonds are initially equivalent, the lower symmetry of C_{70} gives rise to an array of different reactivity's. Integration of spectra based on the pyrrolidine protons allowed us to estimate the fractions of each isomer (Table 3.1).

Table 3. 1. Estimation in percentage of the fraction of isomers present in C70 derivatives. * NMR is too complex to make a correct estimation

	1α	**2α**	**1β**	**2β**
70A	30	20	25	24
70B	30	27	25	17
70C	47	18	20	18
70D	*	*	*	*

The cyclic voltammograms of the eight synthesized fulleropyrrolidine acceptors, as well as the voltammograms of the corresponding $PC_{61}BM$ and $PC_{71}BM$ references are shown in Figure 3.26(a). The corresponding HOMO/LUMO levels determined from these voltammograms are shown in Table 3.2 in

and represented graphically in Figure 3.26(b). Also represented in Figure 3.26(b) are the HOMO/LUMO levels of PffBT4T-2OD as taken from the literature [10]. The HOMO/LUMO levels that we have determined for $PC_{61}BM$ and $PC_{71}BM$ are in very good agreement with literature [50, 51] which attests the reliability of our measurements for the fulleropyrrolidine acceptors. The fullerenes **60A**, **60B**, **70A** and **70B** have slightly higher LUMO levels than the standards $PC_{71}BM$ and in theory this should favour higher V_{oc} and PCE values assuming that all other factors remain unchanged.

(a)

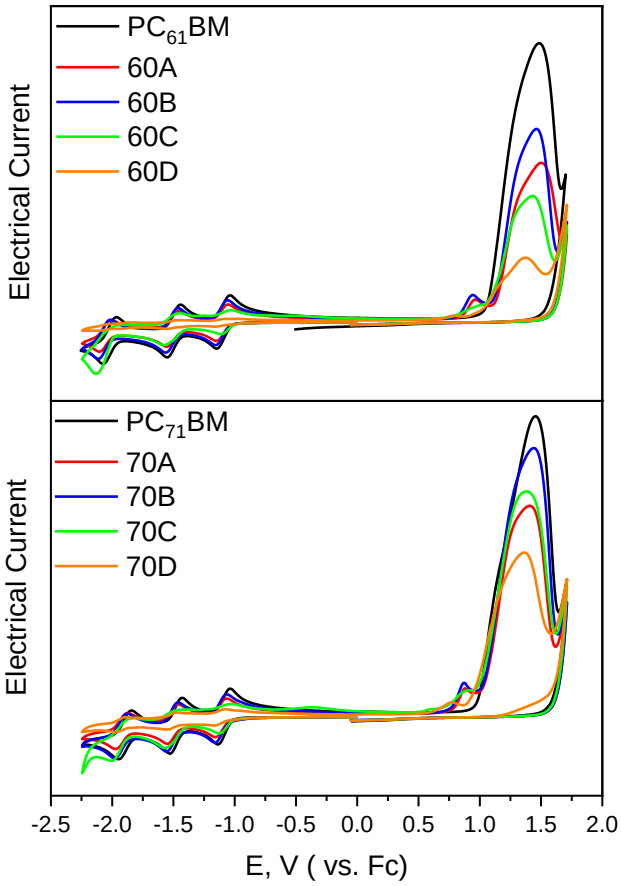

(b)

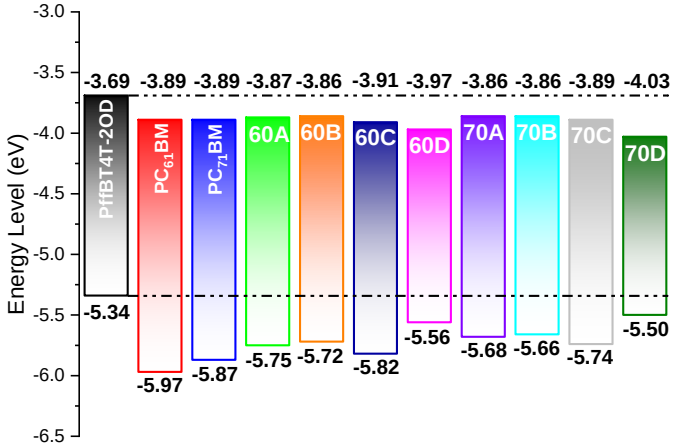

Figure 3. 5. (a) Cyclic Voltammetry curves for all different materials. The Electrical Current scale is arbitrary shifted in order to show all curves. (b) Scheme of HOMO and LUMO levels for all materials as calculated from cyclic voltammetry. The HOMO and LUMO levels for PffBT4T-2OD as indicated in are also shown.

Table 3. 2. HOMO and LUMO levels for all materials as calculated from cyclic voltammetry. The potential onsets used for the calculations are also indicated.

Material	E_{ox}^{onset} (V)	HOMO (eV)	E_{red}^{onset} (V)	LUMO (eV)
PffBT4T-2OD	-	-5.34	-	-3.69
$PC_{61}BM$	1.07	-5.97	-1.01	-3.89
$PC_{71}BM$	0.97	-5.87	-1.01	-3.89
60A	0.85	-5.75	-1.03	-3.87
60B	0.82	-5.72	-1.04	-3.86
60C	0.92	-5.82	-0.99	-3.91
60D	0.66	-5.56	-0.93	-3.97
70A	0.78	-5.68	-1.04	-3.86
70B	0.76	-5.66	-1.04	-3.86
70C	0.84	-5.74	-1.01	-3.89
70D	0.60	-5.50	-0.87	-4.03

The DFT computed HOMO and LUMO energies show a reasonable agreement with the voltammetry measured values, Table 3.3 . The LUMO energies show the best agreement, with differences up to 0.17 and 0.28 eV for **70C** and **70D** respectively. For C_{70}, α1 and α2 diastereoisomers generally yield very similar frontier orbital energies with the exception of α1-**70D** and α2-**70D** HOMOs which differ by 0.08 eV. Also, the β1 and β2 HOMO and LUMO energies are very similar. Remarkably, when α and β C_{70} isomers are systematically compared, HOMOs show lower energies, while LUMOs show higher energies. Thus, all α isomers have larger HOMO-LUMO gaps than β isomers. Figure 3.27 shows the electron density for both frontier orbitals for all molecules. The HOMO orbitals are localized on the carbazole

moiety for **60D** and **70D** structures. In all the other cases, the HOMO electron sit predominantly on the fullerene part, although for some systems, namely: **60A**, α-**70A**, α-**70B**, and β2-**70B**, some density is also found on the functional groups. Interestingly, the LUMO orbitals, associated with the capacity of these molecules to act as electron acceptors, reside on the fullerene for all structures.

Table 3. 3. Experimental and computed HOMO and LUMO energies at the PBE-def2-TZVP/PBEh-3c level. All values in eV.

	HOMO					LUMO				
	Exp.	α1	α2	β1	β2	Exp.	α1	α2	β1	β2
C_{60}		-5.80					-4.10			
C_{70}		-5.80					-4.03			
$PC_{61}BM$	-5.97	-5.47				-3.89	-3.94			
$PC_{71}BM$	-5.87	-5.52		-5.44		-3.89	-3.85		-3.87	
60A	-5.75	-5.40				-3.87	-3.90			
60B	-5.72	-5.36				-3.86	-3.88			
60C	-5.82	-5.60				-3.91	-4.06			
60D	-5.56	-5.09				-3.97	-3.84			
70A	-5.68	-5.47	-5.47	-5.40	-5.38	-3.86	-3.79	-3.79	-3.84	-3.83
70B	-5.66	-5.43	-5.42	-5.37	-5.35	-3.86	-3.77	-3.77	-3.82	-3.83
70C	-5.74	-5.69	-5.69	-5.61	-5.60	-3.89	-4.01	-4.00	-4.06	-4.04
70D	-5.50	-5.06	-5.05	-5.04	-5.12	-4.03	-3.76	-3.75	-3.80	-3.79

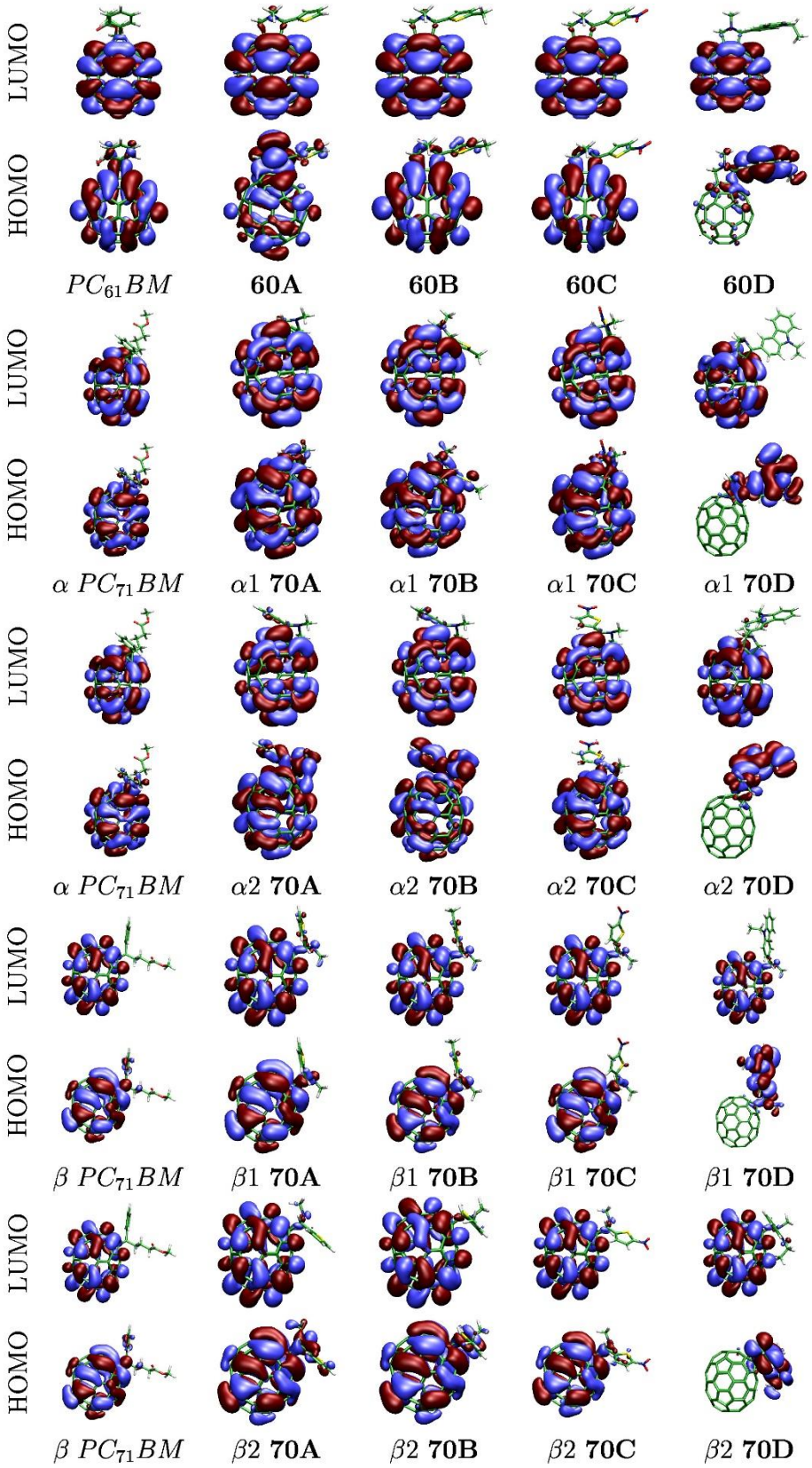

Figure 3. 6. Frontier orbitals of pristine and functionalized C_{60} and C_{70} molecules.

The UV-Vis absorption spectra recorded between 300 and 800 nm for the four C_{60} derivatives and the four C_{70} derivatives in 1,2-dichlorobenzene are shown in Figure 3.28. As expected, the C_{70} derivatives have a broader photo-absorption profile in the visible region. The absorption bands of the C_{60} derivatives are similar and the same happens with the absorption bands of the C_{70} derivatives. In consistency with the literature [40, 43, 44], the C_{60} derivatives display a large peak at ~330 nm, a small peak at ~430 nm and a very weak absorption peak ~700 nm.

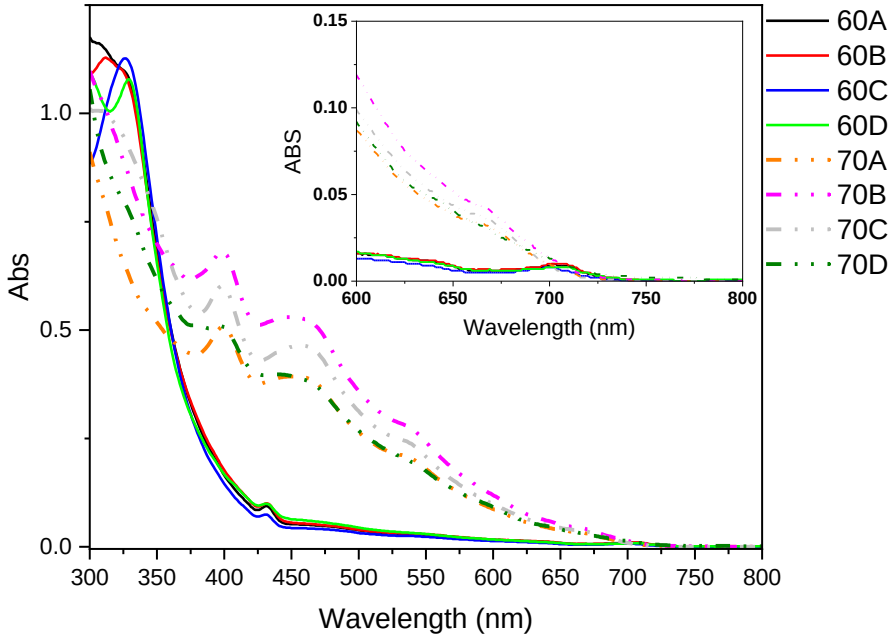

Figure 3. 7. UV-Vis absorption spectra of the pure fullerenes in 1,2-dichlorobenzene

The current density-voltage (J-V) curves of devices with the standard architecture ITO/PEDOT:PSS/BHJ/Ca/Al, as shown in Figure 3.29(a), and processed with the eight different fulleropyrrolidines, as well as a $PC_{71}BM$-based reference device, are shown in Figure 3.29(b). The corresponding figures of merit are represented in Figure 3.29(c) and in Table 3.4. As it is evident from Figure 3.29(b), all the fulleropyrrolidines originated devices with photovoltaic performances considerably lower than reference devices based on $PC_{71}BM$. All the J-V curves of devices with fulleropyrrolidine acceptors show a more or less pronounced influence of a space charge limited current (SCLC), and interestingly devices based on 70A display a characteristic S-shaped similar to S-shaped J–V curves that have been previously reported in fulleropyrrolidine-based OPVs [40].

(a)

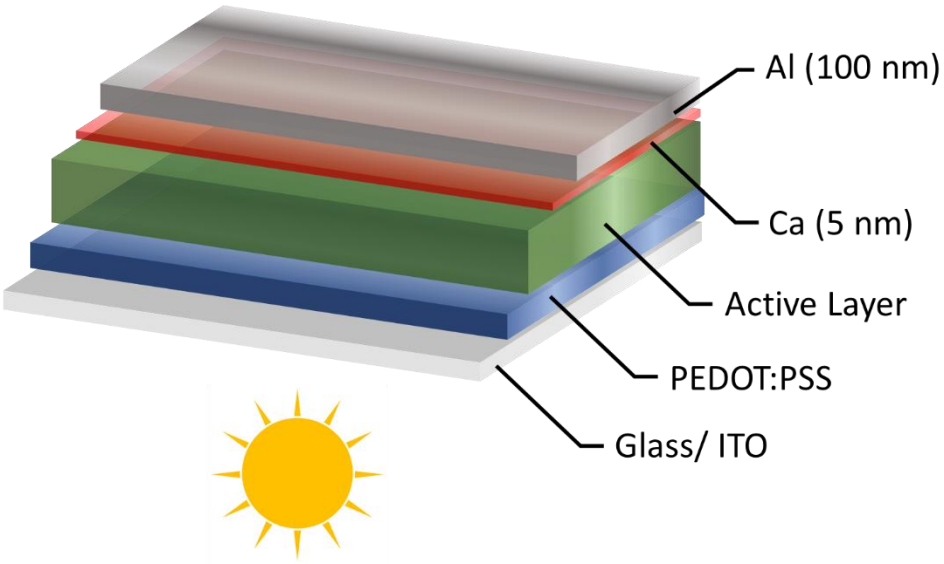
Al (100 nm)
Ca (5 nm)
Active Layer
PEDOT:PSS
Glass/ ITO

(b)

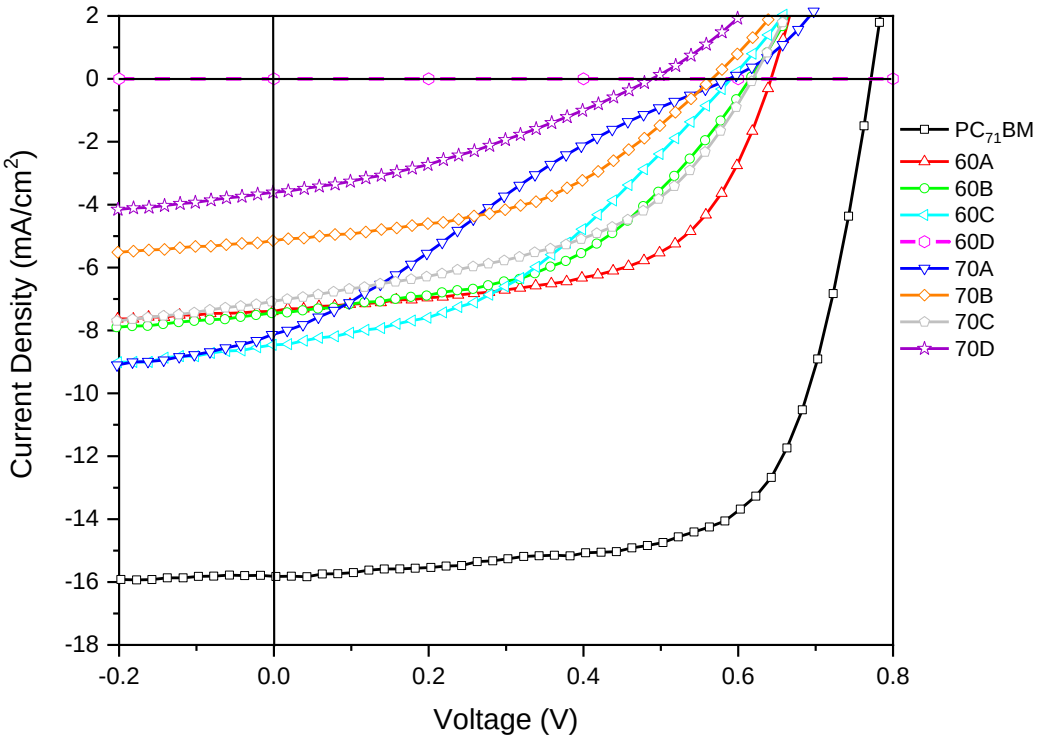
Current Density (mA/cm^2)
Voltage (V)
2
0
-2
-4
-6
-8
-10
-12
-14
-16
-18
-0.2
0.0
0.2
0.4
0.6
0.8
PC$_{71}$BM
60A
60B
60C
60D
70A
70B
70C
70D

(c)

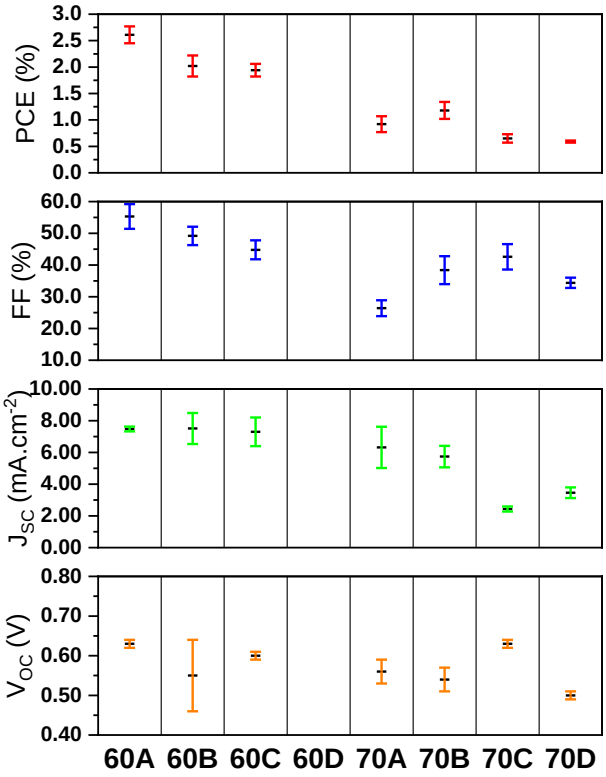

Figure 3. 8. (a) A schematic of the standard device structure used in the fabrication of devices; (b) Representative electrical current density – applied voltage (J-V) curves for PffBT4T-2OD based devices with each particular type of fullerene species 60A-60D and 70A-70D; (c) Overall device metrics for PffBT4T-2OD based devices using the different fullerenes 60A-60D and 70A-70D.

Table 3. 4. Device metrics showing the peak and (average) values for PCE for devices prepared using different fullerene derivatives.

PffBT4T-2OD	PCE (%)	V_{oc} (V)	FF (%)	J_{sc} (mA/cm²)
$PC_{71}BM$	8.41 (8.19±0.24)	0.72 (0.74±0.02)	71.2 (69.8±1.8)	16.41 (15.87±0.40)
60A	2.78 (2.61±0.16)	0.64 (0.63±0.01)	58.7 (55.3±3.9)	7.36 (7.48±0.15)
60B	2.20 (2.02±0.20)	0.62 (0.55±0.09)	47.9 (49.2±2.9)	7.46 (7.51±0.98)
60C	2.04 (1.94±0.12)	0.59 (0.60±0.01)	40.7 (44.8±3.0)	8.46 (7.30±0.90)
60D	0	0	0	0
70A	1.15 (0.92±0.15)	0.59 (0.56±0.03)	24.2 (26.4±2.5)	8.08 (6.32±1.30)
70B	1.33 (1.18±0.16)	0.57 (0.54±0.03)	45.9 (38.4±4.4)	5.14 (5.74±0.68)
70C	0.75 (0.65±0.08)	0.62 (0.63±0.01)	47.5 (42.6±4.0)	2.52 (2.43±0.16)
70D	0.60 (0.59±0.02)	0.49 (0.50±0.01)	34.2 (34.4±1.6)	3.61 (3.46±0.34)

Among the fulleropyrrolidine-based devices, the best efficiencies are achieved by devices with the C_{60} derivatives **60A** (2.78%) **60B** (2,20%) and **60C** (2.04 %). These results show that a higher efficiency is obtained when the thiophene moiety does not contain any substituent in the remaining alpha position and the efficiency tends to decrease when this position is substituted with electron withdrawing substituents. It is also evident from Figure 3.29(c) and Table 3.4 that, in general, the C_{60} derivatives originate higher performing devices than the C_{70} derivatives, even though the latter have broader light absorption in the visible region. The only exception occurs in compounds 60D and 70D, where 60D originates no efficiency and 70D originates an efficiency of 0.60%. However, this exception is most likely associated with the solubility differences observed between 60D (less soluble) and 70D (more soluble) as the use of derivatives with a higher solubility tends to facilitate the process of thin film formation and dispersion in the BHJ, increasing therefore the efficiency of the devices. The lower performance that we generally observe in our C_{70}-based devices, compared to C_{60}-based devices, is probably due to the structural and energetic disorder introduced in these systems by the presence of several C_{70}-fulleropyrrolidine isomers, as our DFT calculations show that different isomers of C_{70}-fulleropyrrolidine have systematically different electronic properties. For example, according to Umeyama et al. [52], in the particular case of the $PC_{71}BM$ mixture of isomers, the β1-isomer present in the mixture of four isomers (α1, α2, β1 and β2) does not contribute to the efficiency of the mixture.

Figure 3.30 shows the UV-Vis spectra of the blends and pure polymer, normalized based on the intensity of their 0-1 transition peak at ~700 nm. As expected, the BHJs with C_{70}-fulleropyrrolidines exhibit a stronger light absorption in the range 400–700 nm than the BHJs with C_{70}-fulleropyrrolidines.

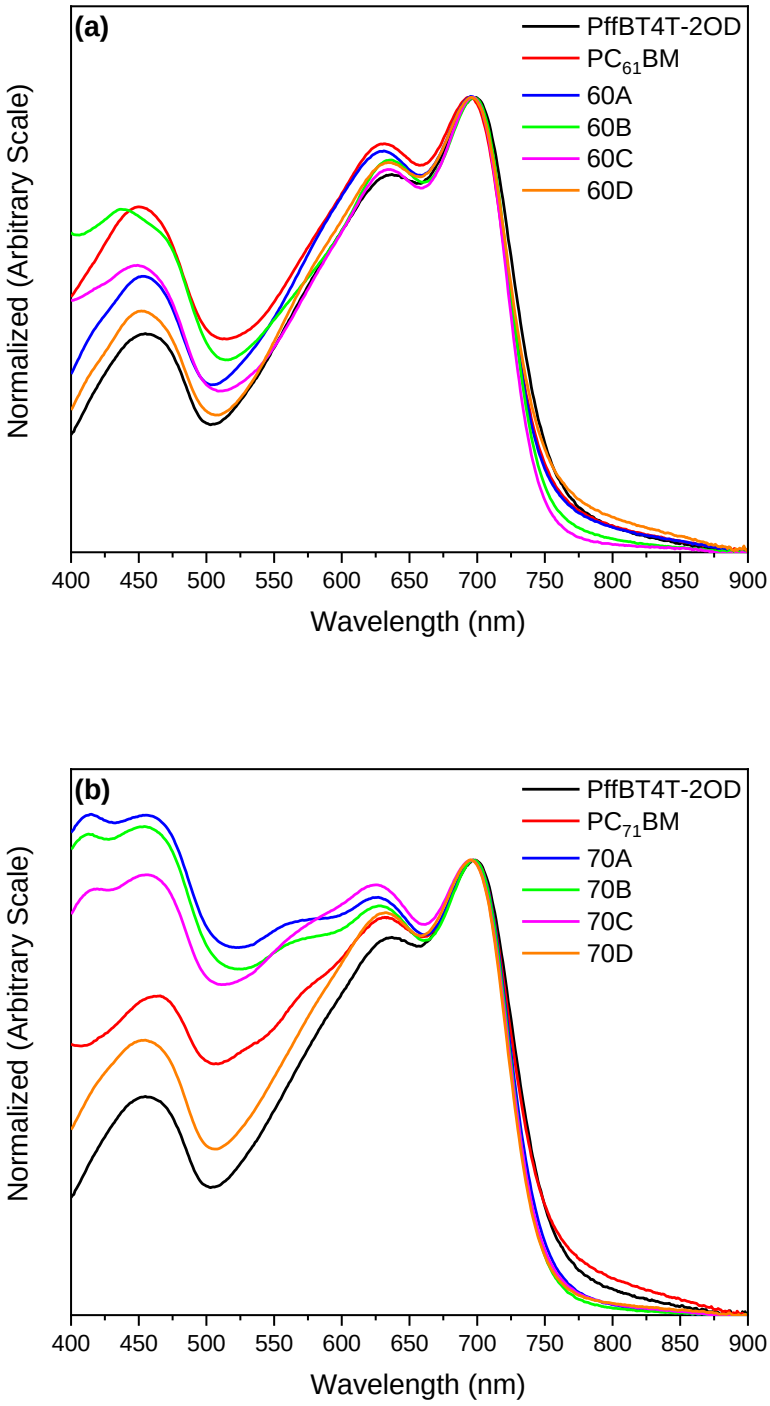

Figure 3. 9. UV-Vis absorption spectra of a pristine PffBT4T-2OD film and of PffBT4T-2OD:fullerene blend films with: a) C_{60} based fullerenes and b) C_{70} based fullerenes. All spectra are normalized based on the intensity of the polymer characteristic 0-1 transition peak at ~700 nm.

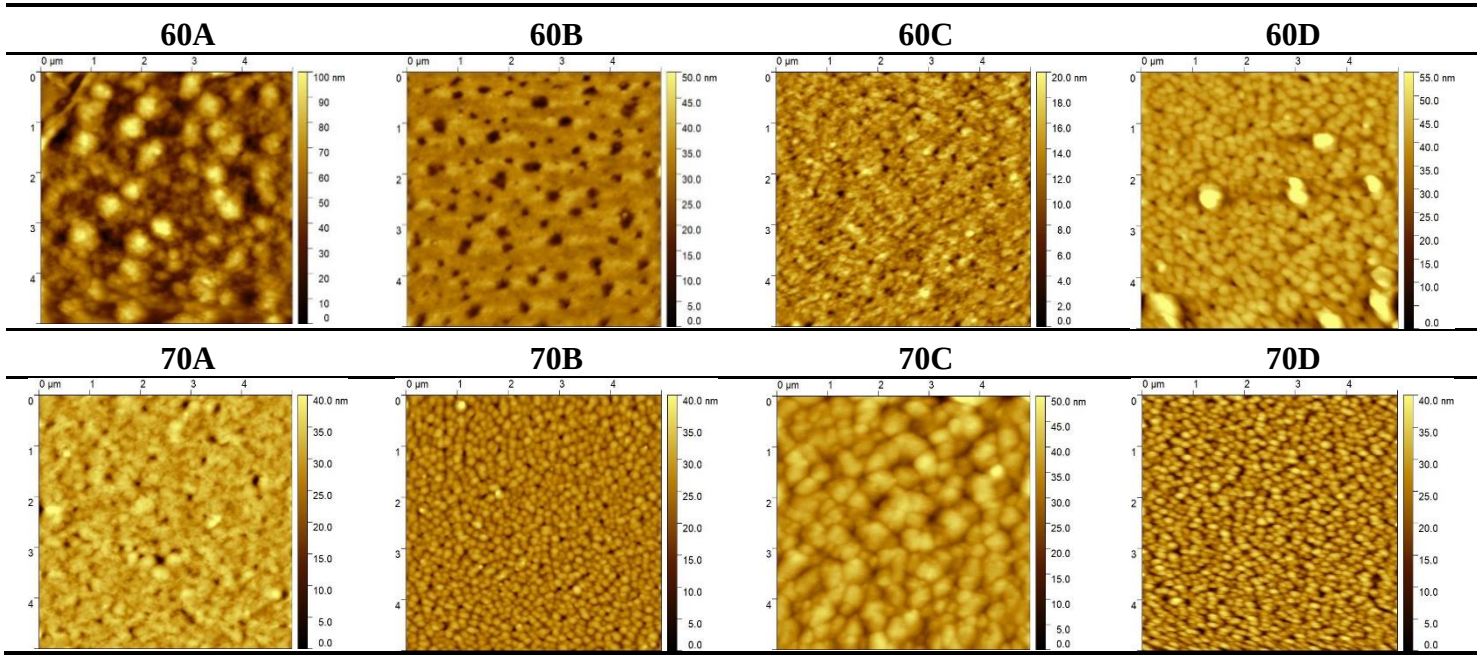

Figure 3. 10. AFM morphology images of PffBT4T-2OD based bulk-heterojunction films with the different fullerene

AFM in tapping mode was used to study the surface of the different BHJ films with the goal of elucidating some possible correlation between the surface morphology and the efficiency of the devices, and some representative images are shown in Figure 3.31. However, no clear correlation between surface morphology and efficiency can be established. For example, although film 60A looks rougher than film 60C, apparently indicating a much coarser phase segregation, devices 60A have a better performance than devices 60C. As mentioned in the previous chapter this is not surprising, as AFM only probes the surface morphology which can be very different from the underlying bulk morphology.

3.4 Conclusions

In summary, a facile approach for the chemical modification of fullerenes that can be extended to thiophene and carbazole based moieties has been demonstrated. These are significantly interesting since some of the most common donor polymers used in OPVs are constituted by several of these basic units. Furthermore, the results here presented confirm the critical dependence of the device performance on the chemical structures of the fulleropyrrolidine derivatives.

References

[1] O. Inganas, Organic Photovoltaics over Three Decades, Adv. Mater., 30 (2018).
[2] J.S. Yu, Y.F. Zheng, J. Huang, Towards High Performance Organic Photovoltaic Cells: A Review of Recent Development in Organic Photovoltaics, Polymers, 6 (2014) 2473-2509.
[3] R. Sondergaard, M. Hosel, D. Angmo, T.T. Larsen-Olsen, F.C. Krebs, Roll-to-roll fabrication of polymer solar cells, Materials Today, 15 (2012) 36-49.
[4] Z. Xiao, X. Jia, L.M. Ding, Ternary organic solar cells offer 14% power conversion efficiency, Sci. Bull., 62 (2017) 1562-1564.
[5] S.S. Li, L. Ye, W.C. Zhao, H.P. Yan, B. Yang, D.L. Liu, W.N. Li, H. Ade, J.H. Hou, A Wide Band Gap Polymer with a Deep Highest Occupied Molecular Orbital Level Enables 14.2% Efficiency in Polymer Solar Cells, J. Am. Chem. Soc., 140 (2018) 7159-7167.
[6] Y. Cui, H.F. Yao, J.Q. Zhang, T. Zhang, Y.M. Wang, L. Hong, K.H. Xian, B.W. Xu, S.Q. Zhang, J. Peng, Z.X. Wei, F. Gao, J.H. Hou, Over 16% efficiency organic photovoltaic cells enabled by a chlorinated acceptor with increased open-circuit voltages, Nature Communications, 10 (2019) 8.
[7] L.X. Meng, Y.M. Zhang, X.J. Wan, C.X. Li, X. Zhang, Y.B. Wang, X. Ke, Z. Xiao, L.M. Ding, R.X. Xia, H.L. Yip, Y. Cao, Y.S. Chen, Organic and solution-processed tandem solar cells with 17.3% efficiency, Science, 361 (2018) 1094-+.
[8] S.Q. Zhang, L. Ye, W.C. Zhao, D.L. Liu, H.F. Yao, J.H. Hou, Side Chain Selection for Designing Highly Efficient Photovoltaic Polymers with 2D-Conjugated Structure, Macromolecules, 47 (2014) 4653-4659.
[9] W. Ma, G.F. Yang, K. Jiang, J.H. Carpenter, Y. Wu, X.Y. Meng, T. McAfee, J.B. Zhao, C.H. Zhu, C. Wang, H. Ade, H. Yan, Influence of Processing Parameters and Molecular Weight on the Morphology and Properties of High-Performance PffBT4T-2OD:PC71BM Organic Solar Cells, Advanced Energy Materials, 5 (2015) 9.
[10] Y. Liu, J. Zhao, Z. Li, C. Mu, W. Ma, H. Hu, K. Jiang, H. Lin, H. Ade, H. Yan, Aggregation and morphology control enables multiple cases of high-efficiency polymer solar cells, Nature Communications, 5 (2014) 5293.
[11] Y. Zhang, A.J. Parnell, F. Pontecchiani, J.F.K. Cooper, R.L. Thompson, R.A.L. Jones, S.M. King, D.G. Lidzey, G. Bernardo, Understanding and controlling morphology evolution via DIO plasticization in PffBT4T-2OD/PC71BM devices, Scientific Reports, 7 (2017) 44269.
[12] Y.W. Zhang, A.J. Parnell, O. Blaszczyk, A.J. Musser, I.D.W. Samuel, D.G. Lidzey, G. Bernardo, Effect of fullerene acceptor on the performance of solar cells based on PffBT4T-2OD, Physical Chemistry Chemical Physics, 20 (2018) 19023-19029.
[13] W. Zhang, R. Hu, X.K. Zeng, X.J. Su, Z.F. Chen, X.S. Zou, J. Peng, C.Y. Zhang, A. Yartsev, Effect of Post-Thermal Annealing on the Performance and Charge Photogeneration Dynamics of PffBT4T-2OD/PC71BM Solar Cells, Polymers, 11 (2019).
[14] Z.Z. Bi, H.B. Naveed, Y.M. Mao, H.P. Yan, W. Ma, Importance of Nucleation during Morphology Evolution of the Blade-Cast PffBT4T-2OD-Based Organic Solar Cells, Macromolecules, 51 (2018) 6682-6691.
[15] L.P. Duan, H.M. Yi, Z.M. Wang, Y. Zhang, A.A.Z. Haque, B.R. Sang, R. Deng, A. Uddin, Semitransparent organic solar cells based on PffBT4T-2OD with a thick active layer and near neutral colour perception for window applications, Sustainable Energy & Fuels, 3 (2019) 2456-2463.
[16] R. Ganesamoorthy, G. Sathiyan, P. Sakthivel, Review: Fullerene based acceptors for efficient bulk heterojunction organic solar cell applications, Solar Energy Materials and Solar Cells, 161 (2017) 102-148.

[17] H. Gaspar, F. Figueira, L. Pereira, A. Mendes, C.J. Viana, G. Bernardo, Recent Developments in the Optimization of the Bulk Heterojunction Morphology of Polymer: Fullerene Solar Cells, Materials, 11 (2018).
[18] C.H. Zhang, A. Mumyatov, S. Langner, J.D. Perea, T. Kassar, J. Min, L.L. Ke, H.W. Chen, K.L. Gerasimov, D.V. Anokhin, D.A. Ivanov, T. Ameri, A. Osvet, D.K. Susarova, T. Unruh, N. Li, P. Troshin, C.J. Brabec, Overcoming the Thermal Instability of Efficient Polymer Solar Cells by Employing Novel Fullerene-Based Acceptors, Adv. Energy Mater., 7 (2017).
[19] C. Zhang, S. Langner, A.V. Mumyatov, D.V. Anokhin, J. Min, J.D. Perea, K.L. Gerasimov, A. Osvet, D.A. Ivanov, P. Troshin, N. Li, C.J. Brabec, Understanding the correlation and balance between the miscibility and optoelectronic properties of polymer–fullerene solar cells, Journal of Materials Chemistry A, 5 (2017) 17570-17579.
[20] D. Srivani, A. Gupta, S.V. Bhosale, K. Ohkubo, R.S. Bhosale, S. Fukuzumi, A. Bilic, L.A. Jones, S.V. Bhosale, A Triphenylamine-Naphthalenediimide-Fullerene Triad: Synthesis, Photoinduced Charge Separation and Solution-Processable Bulk Heterojunction Solar Cells, Asian Journal of Organic Chemistry, 7 (2018) 220-226.
[21] D. Landerer, C. Sprau, D. Baumann, P. Pingel, T. Leonhard, D. Zimmermann, C.L. Chochos, H. Kruger, S. Janietz, A. Colsmann, Thermal Stabilization of the Bulk-Heterojunction Morphology in Polymer:Fullerene Solar Cells Using a Bisazide Cross-Linker, Solar Rrl, 3 (2019).
[22] W. Wang, R. Sun, J. Guo, J. Guo, J. Min, An Oligothiophene-Fullerene Molecule with a Balanced Donor-Acceptor Backbone for High-Performance Single-Component Organic Solar Cells, Angewandte Chemie-International Edition, 58 (2019) 14556-14561.
[23] N.S. Sariciftci, L. Smilowitz, A.J. Heeger, F. Wudl, Photoinduced electron-transfer from a conducting polymer to Buckminsterfullerene, Science, 258 (1992) 1474-1476.
[24] J.C. Hummelen, B.W. Knight, F. Lepeq, F. Wudl, J. Yao, C.L. Wilkins, PREPARATION AND CHARACTERIZATION OF FULLEROID AND METHANOFULLERENE DERIVATIVES, J. Org. Chem., 60 (1995) 532-538.
[25] G. Yu, J. Gao, J.C. Hummelen, F. Wudl, A.J. Heeger, Polymer photovoltaic cells - Enhanced efficiencies via a network of internal donor-acceptor heterojunctions, Science, 270 (1995) 1789-1791.
[26] M.M. Wienk, J.M. Kroon, W.J.H. Verhees, J. Knol, J.C. Hummelen, P.A. van Hal, R.A.J. Janssen, Efficient methano 70 fullerene/MDMO-PPV bulk heterojunction photovoltaic cells, Angewandte Chemie-International Edition, 42 (2003) 3371-3375.
[27] M. Williams, N.R. Tummala, S.G. Aziz, C. Risko, J.L. Bredas, Influence of Molecular Shape on Solid-State Packing in Disordered PC61BM and PC71BM Fullerenes, Journal of Physical Chemistry Letters, 5 (2014) 3427-3433.
[28] F.J. Zhang, Z.L. Zhuo, J. Zhang, X. Wang, X.W. Xu, Z.X. Wang, Y.S. Xin, J. Wang, W.H. Tang, Z. Xu, Y.S. Wang, Influence of PC60BM or PC70BM as electron acceptor on the performance of polymer solar cells, Solar Energy Materials and Solar Cells, 97 (2012) 71-77.
[29] C.-Z. Li, H.-L. Yip, A.K.Y. Jen, Functional fullerenes for organic photovoltaics, Journal of Materials Chemistry, 22 (2012) 4161-4177.
[30] D. Mi, J.H. Kim, H.U. Kim, F. Xu, D.H. Hwang, Fullerene Derivatives as Electron Acceptors for Organic Photovoltaic Cells, Journal of Nanoscience and Nanotechnology, 14 (2014) 1064-1084.
[31] S. Kitaura, K. Kurotobi, M. Sato, Y. Takano, T. Umeyama, H. Imahori, Effects of dihydronaphthyl-based 60 fullerene bisadduct regioisomers on polymer solar cell performance, Chemical Communications, 48 (2012) 8550-8552.
[32] Y. He, H.-Y. Chen, J. Hou, Y. Li, Indene–C60 Bisadduct: A New Acceptor for High-Performance Polymer Solar Cells, J. Am. Chem. Soc., 132 (2010) 1377-1382.

[33] L.L. Deng, J. Feng, L.C. Sun, S. Wang, S.L. Xie, S.Y. Xie, R.B. Huang, L.S. Zheng, Functionalized dihydronaphthyl-C-60 derivatives as acceptors for efficient polymer solar cells with tunable photovoltaic properties, Sol. Energy Mater. Sol. Cells, 104 (2012) 113-120.
[34] X.Y. Meng, W.Q. Zhang, Z.A. Tan, C. Du, C.H. Li, Z.S. Bo, Y.F. Li, X.L. Yang, M.M. Zhen, F. Jiang, J.P. Zheng, T.S. Wang, L. Jiang, C.Y. Shu, C.R. Wang, Dihydronaphthyl-based 60 fullerene bisadducts for efficient and stable polymer solar cells, Chemical Communications, 48 (2012) 425-427.
[35] J.K. Lee, K. Fujida, T. Tsutsui, M.R. Kim, Synthesis and photovoltaic properties of soluble fulleropyrrolidine derivatives for organic solar cells, Sol. Energy Mater. Sol. Cells, 91 (2007) 892-896.
[36] K. Matsumoto, K. Hashimoto, M. Kamo, Y. Uetani, S. Hayase, M. Kawatsura, T. Itoh, Design of fulleropyrrolidine derivatives as an acceptor molecule in a thin layer organic solar cell, J. Mater. Chem., 20 (2010) 9226-9230.
[37] D. Mi, H.U. Kim, J.H. Kim, F. Xu, S.H. Jin, D.H. Hwang, Synthesis of a soluble fulleropyrrolidine derivative for use as an electron acceptor in bulk-heterojunction polymer solar cells, Synthetic Met, 162 (2012) 483-489.
[38] C. Saravanan, C.-L. Liu, Y.-M. Chang, J.-D. Lu, Y.-J. Hsieh, S.-P. Rwei, L. Wang, [60]Fulleropyrrolidines Bearing π-Conjugated Moiety for Polymer Solar Cells: Contribution of the Chromophoric Substituent on C60 to the Photocurrent, ACS Applied Materials & Interfaces, 4 (2012) 6133-6141.
[39] X.N. Zhang, L. Sun, W. Zheng, X.C. Bao, N. Wang, T. Wang, R.Q. Yang, The preparation and properties of bulk-heterojunction organic solar cells with indole-containing fulleropyrrolidine derivatives as acceptors, Tetrahedron, 69 (2013) 9544-9550.
[40] M. Karakawa, T. Nagai, K. Adachi, Y. Ie, Y. Aso, N-phenyl 60 fulleropyrrolidines: alternative acceptor materials to PC61BM for high performance organic photovoltaic cells, Journal of Materials Chemistry A, 2 (2014) 20889-20895.
[41] K.M. Kaunisto, N.K. Subbaiyan, K.C.C. Bikram, V.I. Chukharev, H.M. Hakola, T.K. Vuorinen, V.M. Manninen, N.V. Tkachenko, H.J. Lemmetyinen, F. D'Souza, The effect of thiophene substituents of fulleropyrrolidine acceptors on the performance of inverted organic solar cells, Synthetic Met, 195 (2014) 193-200.
[42] P. Pitliya, Y. Sun, J.C. Garza, C. Liu, X. Gong, A. Karim, D. Raghavan, Synthesis and characterization of novel fulleropyrrolidine in P3HT blended bulk heterojunction solar cells, Polymer, 55 (2014) 1769-1781.
[43] Y.L. Liang, Y.J. Hao, X.D. Liu, L. Feng, M.Z. Chen, Q.Q. Tang, N. Chen, M.L. Tang, B.B. Sun, Y. Zhou, B. Song, Efficiency enhancement from 60 fulleropyrrolidine-based polymer solar cells through N-substitution manipulation, Carbon, 92 (2015) 185-192.
[44] S. Yamane, J. Mizukado, T. Takahashi, Y. Suzuki, M. Sakurai, H. Hagihara, H. Suda, Fulleropyrrolidine Derivatives with Benzophenone Moiety as Electron Acceptors in Thermally Stable Organic Photovoltaic Devices, Chemistry Letters, 44 (2015) 527-529.
[45] S. Grimme, J.G. Brandenburg, C. Bannwarth, A. Hansen, Consistent structures and interactions by density functional theory with small atomic orbital basis sets, The Journal of Chemical Physics, 143 (2015) 054107.
[46] A. Karton, S.L. Waite, A.J. Page, Performance of DFT for C60 Isomerization Energies: A Noticeable Exception to Jacob's Ladder, The Journal of Physical Chemistry A, 123 (2019) 257-266.
[47] H. Wang, Y. He, Y. Li, H. Su, Photophysical and Electronic Properties of Five PCBM-like C60 Derivatives: Spectral and Quantum Chemical View, The Journal of Physical Chemistry A, 116 (2012) 255-262.
[48] T.A. Beu, J. Onoe, A. Hida, First-principles calculations of the electronic structure of one-dimensional ${\mathrm{C}}_{60}$ polymers, Physical Review B, 72 (2005) 155416.

[49] F. Neese, The ORCA program system, Wiley Interdisciplinary Reviews: Computational Molecular Science, 2 (2012) 73-78.
[50] L.Y. Lu, W. Chen, T. Xu, L.P. Yu, High-performance ternary blend polymer solar cells involving both energy transfer and hole relay processes, Nature Communications, 6 (2015).
[51] M.-A. Pan, T.-K. Lau, Y. Tang, Y.-C. Wu, T. Liu, K. Li, M.-C. Chen, X. Lu, W. Ma, C. Zhan, 16.7%-efficiency ternary blended organic photovoltaic cells with PCBM as the acceptor additive to increase the open-circuit voltage and phase purity, Journal of Materials Chemistry A, 7 (2019) 20713-20722.
[52] T. Umeyama, K. Igarashi, D. Sakamaki, S. Seki, H. Imahori, Unique cohesive nature of the β1-isomer of [70]PCBM fullerene on structures and photovoltaic performances of bulk heterojunction films with PffBT4T-2OD polymers, Chemical Communications, 54 (2018) 405-4

Chapter IV. Graded morphologies and the performance of PffBT4T-2OD:$PC_{71}BM$ devices using additive choice

Abstract

The impact of several additives (1-chloronaphthalene, methylnaphthalene, hexadecane, 1-phenyloctane and p-anysaldehyde) on the performance and morphology of poly[(5,6-difluoro-2,1,3-benzothiadiazol-4,7-diyl)-alt-(3,3‴-di(2-octyldodecyl)2,2′;5′,2″;5″,2‴-quaterthiophen-5,5‴-diyl)] (PffBT4T-2OD):[6,6]-phenyl-C71-butyric acid methyl ester (PC71BM) based polymer solar cells are investigated. Some additives are shown to improve the power conversion efficiency (PCE), others decrease PCE by ~30% and others completely eliminate any power conversion efficiency. Grazing Incidence Wide Angle X-ray Scattering (GIWAXS) reveals a clear stepwise variation in the crystallinity of the systems when changing the additive between the two extreme-situations of maximum PCE (1-chloronaphthalene) and PCE null (hexadecane). Small Angle Neutron Scattering (SANS) reveals that the morphology of devices with PCE ~ 0% is composed of large domains with correlation lengths ~ 30 nm, i.e. much larger than the typical exciton diffusion length in organic semiconductors.

4.1 Introduction

The work reported in this chapter is in preparation for article submission.

Organic photovoltaics (OPVs), in comparison with other photovoltaic technologies currently available in the market, are able to be manufactured over large areas, on lightweight plastic substrates with high flexibility, using high-throughput roll-to-roll (R2R) compatible processing technologies [1]. The efficiency of single junction OPV cells has been increasing steadily in the last 10–15 years, increasing from 5% in 2005 to above 16% in 2019 [2] and tandem OPV cells have reached an efficiency > 17% [3]. Criteria such as efficiency, lifetime and cost, will need to be satisfied for the successful large scale commercialization of OPVs, but considering the steady progress that has been happening in the field, the future of the technology looks very promising, particularly for small energy production in portable technologies and wearables, when others kind of photovoltaics (PV) cannot be easily incorporated.

The small band gap polymer donor poly[(5,6-difluoro-2,1,3-benzothiadiazol-4,7-diyl)-alt-(3,3‴-di(2-octyldodecyl)2,2′;5′,2″;5″,2‴-quaterthiophen-5,5‴-diyl)] (PffBT4T-2OD) has attracted attention due to its potential to produce high performing OPV devices [4-18]. PffBT4T-2OD, also known as PCE11, exhibits relatively high hole mobility under space charge conditions – SCLC – (over 1.5–3.0 × 10^{-2} $cm^2V^{-1}s^{-1}$ [4]) due to its high crystallinity. These properties, together with its tendency to form relatively pure polymer domains when blended with fullerenes, allow it to perform well in an OPV device, when used in relatively thick BHJ layers (~300 nm), it has excellent light absorption. PffBT4T-2OD when in solution also exhibits a peculiarly strong temperature dependent aggregation behaviour, forming a gel at room temperature. Consequently, PffBT4T-2OD based devices need to be cast from warm solutions (>60 °C), which then aggregate or crystallize during cooling and film forming processes. Further improvements can naturally be made, if a high degree of molecular conformation is achieved in the active layer film formation, that results in electrical transport improvement.

The processing conditions used in the preparation of a bulk-heterojunction (BHJ) layer play a crucial role in nano-morphology formation, which is directly linked to resultant device energy efficiency. The use of additives [19-21] has been the standard processing methodology used to optimize the morphology and increase device performance in OPV devices based on small band gap copolymers such as PffBT4T-2OD. Additives can provide fine control of the BHJ morphology by strongly influencing the film formation process during solution casting.

Recent studies have shown that additives act primarily during film drying [10] and not in solution [22, 23]. Zhang *et al.* [10] studied the effect of the additive 1,8-diiodooctane (DIO) on the performance and BHJ morphology of PffBT4T-2OD:$PC_{71}BM$ based devices, using a polymer with M_w = 117,800 $g.mol^{-1}$. The additive was shown to increase by ~20 % the PCE of the OPV devices, from 7.2% to 9.0%, due to a coarsening of the phase domains from an initial characteristic length scale of ~9–10 nm to a final value of ~12–13 nm. This coarsening process is assisted by thermal annealing and the slow evaporation of DIO, which acts as a plasticizer to promote molecular mobility and coarsening. DIO was also shown to affect the orientation and crystallinity of the BHJ. The dominant orientation for the blends without additive is a face-on lamellar structure. Annealing this blend for 5 minutes improves the out-of-plane ordering as revealed by well-defined peaks for the face-on lamellar packing at 0.29 $Å^{-1}$ along with higher orders at 0.59 $Å^{-1}$ and 0.88 $Å^{-1}$. The sample processed with DIO, exhibits a much more isotropic orientation of the polymer crystallites, with Debye-Scherrer like rings instead of the strong out-of-plane orientation dominance seen without DIO.

Zhao *et al.*[6] studied the impact of the additives DIO, 1,8-octanedithiol (ODT), diphenylether (DPE) and 1-chloronaphthalene (CN), on the performance of PffBT4T-2OD:$PC_{71}BM$ based devices. The best devices were those processed using CN and displayed an average PCE of 10.01 % compared with 7.89 % for reference devices processed without additive. DIO and DPE additives both improved the device performance with average PCE of 8.82 % and 9.10 % respectively. By contrast ODT was shown to have a negative effect on efficiency, producing devices with average PCE of 7.62 %. GIWAXS revealed that DIO and CN affect the molecular orientation of the BHJ films in different directions. CN, which dissolves both PffBT4T-2OD and $PC_{71}BM$, leads to enhanced crystallinity of PffBT4T-2OD in the (100) direction corresponding to the alkyl stacking peak, located at a q_z value of 0.29 $Å^{-1}$. By contrast DIO, which dissolves $PC_{71}BM$ but not the polymer, has more profound effect on the crystallization of PffBT4T-2OD in the π–π stacking direction (010). The effect of ODT and DPE on crystallinity was not addressed.

Despite these studies, most device optimization and choice of processing additive has been largely driven by empiricism, as such there is still a lack of fundamental understanding of the relationship between the processing additive used, the resultant BHJ morphology and the corresponding device efficiency. Nevertheless, a deep understanding of the impact of additives on the BHJ morphology and device performance of OPVs, should rely on understanding both the intended morphological improvement with favourable additives as well as the morphological degradation with unfavourable additives, however unwanted or unuseful the latter might be. This understanding is required to tailor the desired morphology and device performance properties. As is well known, the final efficiency of a PV depends primarily on several fundamental properties, from light absorption through to exciton formation and transport, and finally to free charge capture at the electrodes. The central stage involving exciton separation and electrical carrier transport plays a crucial role, critically dependent on the molecular conformation and morphology. Particularly, at donor-acceptor (D-A) interfaces, with the exciton separation/recombination probabilities and bulk free electrical carrier transport (besides the effect of the internal electrical field in both process), with the latter also dependent on the energy levels acting as carrier traps. All, these processes and steps depend on a favourable morphology.

In the present work we study the impact of five different processing additives (1-chloronaphthalene (CN), 1-methylnaphthalene (MN), hexadecane (HD), 1-phenyloctane (PO) and p-anisaldehyde (AN)), with different Hansen solubility parameters [24] and different boiling temperatures (between 242 °C and 287 °C), on the efficiency and BHJ morphology of devices based on PffBT4T-2OD:$PC_{71}BM$. Whilst some of these additives improve device performance we have deliberately chosen some additives that degrade

the efficiency and we develop the understanding of the interplay between morphology and device performance.

4.2 Experimental Section

4.2.1 Materials

The following materials were sourced from Ossila Ltd.: i) Poly(3,4-ethylenedioxy-thiophene):poly(styrene sulfonic acid) (PEDOT:PSS, Heraeus Clevios AI4083); ii) the polymer PffBT4T-2OD (M302) with M_n = 83,008 g.mol^{-1} and M_w = 172,033 g.mol^{-1} and iii) the fullerene $PC_{71}BM$ (M113), [6,6]-phenyl-C71 butyric acid methyl ester, with empirical formula $C_{82}H_{14}O_2$ and M_w = 1030.99 g mol^{-1}. The solvent and additives used were all high purity grade and purchased from Sigma-Aldrich, namely: *o*-dichlorobenzene (DCB), 1-chloronaphthalene (CN), methylnaphthalene (MN), p-anisaldehyde (AN), 1-phenyloctane (PO) and hexadecane (HD). All the materials and solvents were used as received without further purification. Figure 4.1 illustrates the molecular structures of the polymer, fullerene and additives used in the present work.

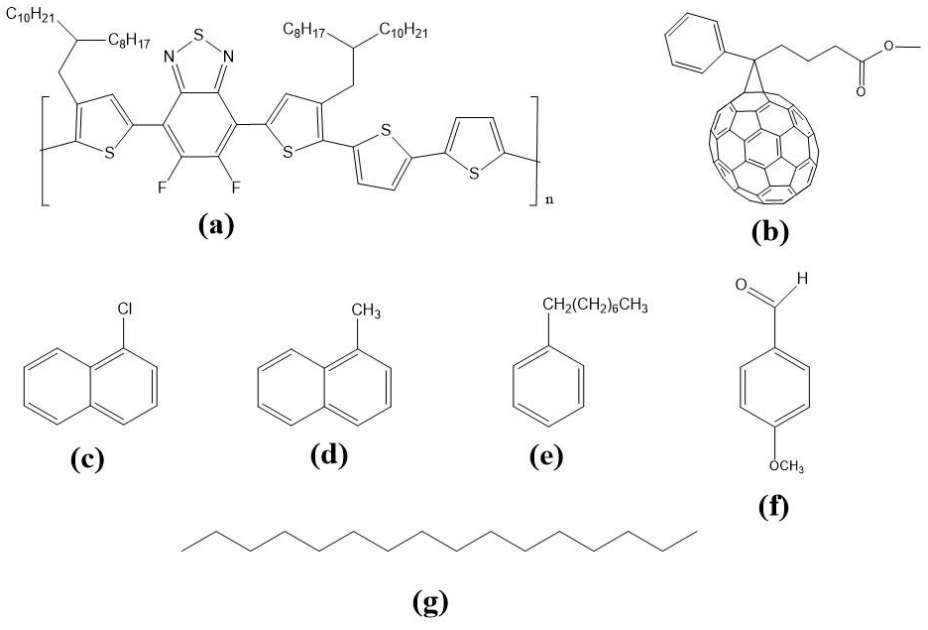

Figure 4. 1. Molecular structures of the polymer, fullerene and additives used in the present work: (a) PffBT4T-2OD; (b) $PC_{71}BM$; (c) 1-Chloronaphthalene; (d) 1-Methylnaphthalene; (e) 1-Phenyloctane; (f) *p*-Anisaldehyde; (g) Hexadecane.

4.2.2 Device Fabrication

The standard structure ITO/HTL/Active layer/Ca/Al was used for the OPV devices studied in this work. PEDOT:PSS was used as hole transport layer (HTL). The active layers were all spin-coated from a solution of *o*-dichlorobenzene with 3% of solvent additive (volume percentage), with the polymer PffBT4T-2OD and $PC_{71}BM$ having concentrations of 4 mg/mL^{-1} and 4.8 mg/mL^{-1} respectively (1:1.2 ratio). We note that, contrary to most of the previous works with PffBT4T-2OD which has used solvent mixtures of chlorobenzene:*o*-dichlorobenzene (1:1) to dissolve the polymer, in the present work due to the relatively high M_w of the polymer used, it proved necessary to use pure *o*-dichlorobenzene (which has a stronger solubilizing power than the standard chlorobenzene:*o*-dichlorobenzene mixture). The active layers were spin coated from pre-heated solutions (120 °C) at a spin speed of 800 rpm onto the PEDOT:PSS/ITO/glass substrate that was pre-heated to 120 °C. The active layer was spin-cast in a nitrogen filled glove box. The films were then left in the glove box for 2 hours to dry, after being thermally annealed at 100 °C for 5 minutes. As a reference, some BHJ films were prepared without additive and were not annealed. The cathode evaporation was then deposited sequentially, first 5 nm Calcium (Ca) and then 100 nm Aluminium (Al) on top of the active layer under a vacuum < 2×10^{-6} mbar to form the top electrode contact. Finally, the devices were encapsulated using UV-cured epoxy (E131, Ossila Ltd) and a glass slide.

4.2.3 Morphological characterization

Atomic Force Microscopy (AFM) was used to image the surface morphology of the PffBT4T-2OD:$PC_{71}BM$ BHJ thin films processed with different additives. AFM measurements were performed using a Molecular Imaging PicoLE AFM with a silicon cantilever/tip (Nanosensors, force constant 13 - 77 N/m and cantilever resonance frequency 5 – 25 kHz) at room temperature in air and with scan rate of 0.5 lines/s. The measurements were performed in contact mode and several scans were imaged in flattened mode data to remove the background slope. Topography images were recorded with a resolution of 512 × 512 pixels. The scan size of topographic AFM images presented in all experiments is 5x5 μm. All images were visualized in two and three dimensions, as well as root mean square (RMS) roughness measurements were performed using the software Gwyddion - version 2.53.

Grazing incidence wide-angle X-ray scattering (GIWAXS) was used to study the impact of the different additives on the crystalline structure of the BHJs. GIWAXS measurements were performed on a Xeuss 2.0 SAXS/WAXS laboratory beamline using a liquid Gallium MetalJet (Excillum) x-ray source (9.2 keV,1.34Å). The scattered X-rays were detected using a Pilatus3R 1M detector. Samples were prepared

on PEDOT coated Silicon substrates following identical processing to that used in the preparation of actual OPV devices.

Small Angle Neutron Scattering (SANS) was used to study the impact of the different additives on the phase morphology of the BHJs. SANS experiments were performed on the LOQ diffractometer at the ISIS Pulsed Neutron Source (Didcot, UK) and processed using Mantid for transmission and thickness. The SANS data (on an absolute scale) were then fitted to appropriate models using SasView software (Version 4.1.1). For sample preparation, blend films were spin-coated onto 0.5 mm thick quartz slides, pre-coated with PEDOT:PSS following the same procedure used in device fabrication. Therefore, the thickness of the SANS films is exactly the same as the thickness of the device films. Stacks of 16 individual blend films on quartz discs were then assembled in order to produce good signal to noise statistics for the SANS measurement.

4.2.4 Electrical characterization

The electrical current density – voltage (J-V) was acquired under AM1.5 Global conditions with a Newport 92251A-1000 AM 1.5 solar simulator which was calibrated using an NREL standard silicon solar cell to ensure an irradiance level of 1000 W/m^2. To limit the light-exposed area of the device to 2.6 mm^2, an aperture mask was utilized. The usual one diode equivalent electrical circuit was employed for the data simulation using a genetic algorithm as previously reported [25]. The full electrical characteristic parameters (besides the conventional figures of merit) that includes the generated photocurrent and the series / parallel resistances, can therefore, be used for characterization of the electrical carrier process resulting in the additive effect. Small signal analysis (impedance spectroscopy) was carried out using an Agilent 4294A RLC Meter in the frequency range 100 Hz - 5×10^6 Hz, with an ac level of 100 mV. The capacitance and loss (conductance / angular frequency) was used to determine the relaxation frequency (and the corresponding relaxation time) with further correlation with charge separation / recombination at the D-A interface.

4.3 Results and Discussion

Figure 4.2(a) and Table 4.1 present the current density-voltage (J-V) curves and characteristics of devices processed with different additives and a reference device without additives. Figure 2(b) shows the equivalent circuit used for the simulations and some example simulation curves are shown in Figures 4.2(c), 4.2(d) and 4.2(e) for devices with chloronaphthalene, p-anisaldehyde and 1-phenyloctane, respectively. The corresponding simulation parameters J_{ph}, R_s and R_p are also shown in Table 4.1. Taking into account the average values of PCE obtained (1st column, inside brackets in Table 4.1), it can be seen that compared to the reference device, the additive 1-chloronaphthalene improves the efficiency and the remaining four additives degrade it (methylnaphthalene, p-anisaldehyde, 1-phenyloctane and hexadecane). Devices prepared using the additive 1-chloronaphthalene exhibited the best overall device performance, yielding an average PCE of 8.44 %, and a V_{oc}, *FF* and J_{sc} of 0.75 V, 69.0 % and 14.15 $mA.cm^{-2}$ respectively. Among the additives that degrade the device performance, 1-phenyloctane and hexadecane are particularly detrimental: 1-phenyloctane reduces the average PCE to 0.55 % and hexadecane completely destroys any photovoltaic effect.

.

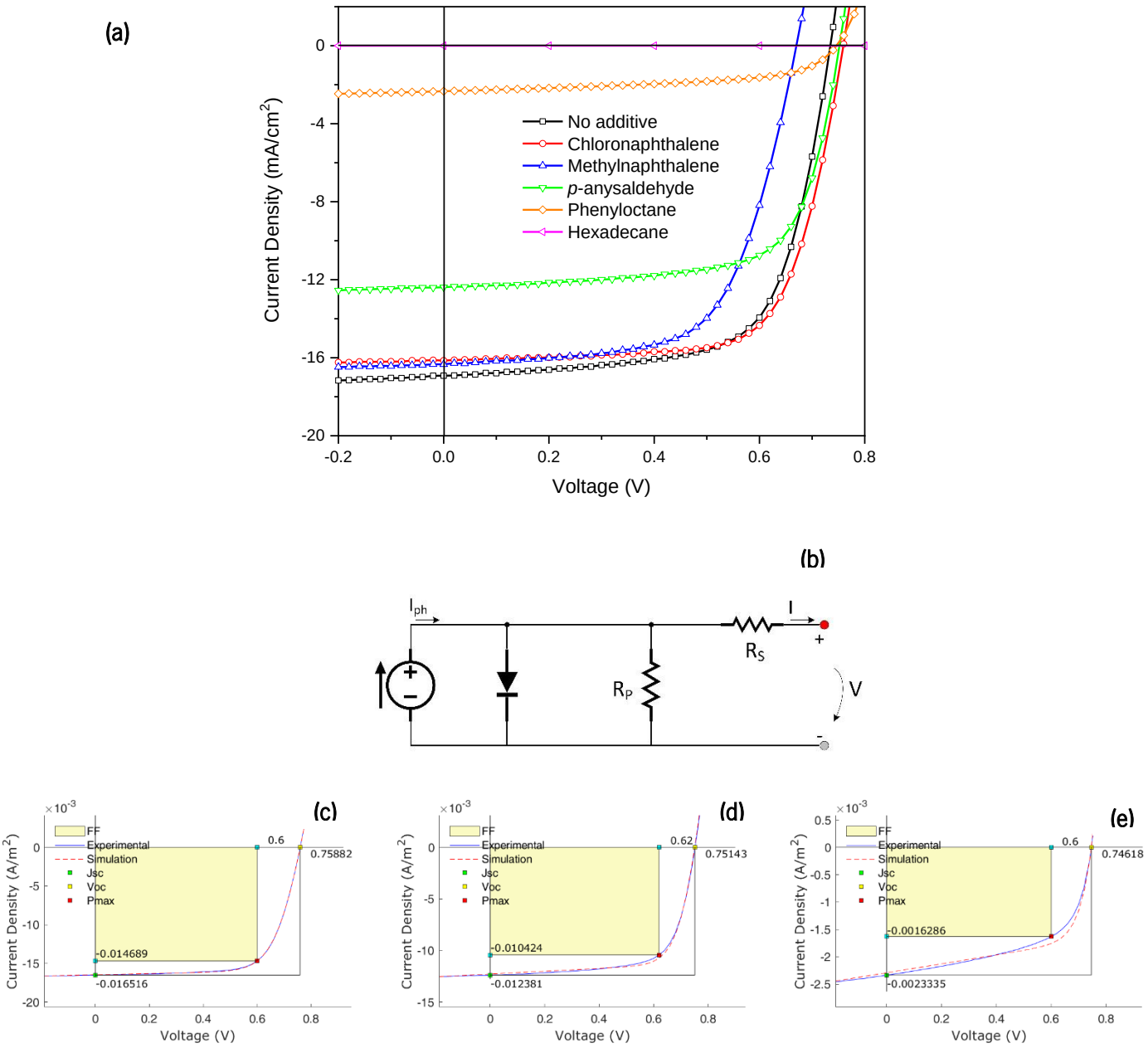

Figure 4. 2. (a) J-V curves of devices processed with different additives; (b) Equivalent circuit used; Simulations for (c) chloronaphthalene, (d) p-anisaldehyde and (e) phenyloctane.

Table 4. 1. Device metrics showing the peak and (average) values for PCE, Voc, FF and Jsc for devices prepared using different additives. Generated photocurrent (J_{ph}) and parallel (R_p) and series resistances (R_s) obtained by the equivalent circuit fit with experimental data.

PffBT4T-2OD/$PC_{71}BM$	PCE (%)	V_{oc} (V)	FF (%)	J_{sc} (mA/cm^2)	Simulation		
					J_{ph} (mA/cm^2)	R_s (Ω)	R_p (Ω)
No additive	8.40 (7.96±0.39)	0.73 (0.73±8.86E-05)	69.4 (69.0±2.27)	-14.50 (-13.71±1.16)	-17.41	159	3.78×10^4
1-Chloronaphthalene	8.75 (8.44±0.25)	0.76 (0.75±0.008)	70.2 (69.0±1.13)	-15.09 (-14.15±0.56)	-16.50	177	7.65×10^4
Methylnaphthalene	6.98 (6.63±0.19)	0.67 (0.67±0.004)	66.7 (65.8±1.11)	-13.97 (-13.09±0.50)	-16.74	217	5.00×10^4
p-Anisaldehyde	6.46 (5.89±0.53)	0.77 (0.76±0.007)	69.4 (64.5±4.36)	-12.38 (-11.97±0.37)	-12.31	146	4.83×10^4
1-phenyloctane	0.98 (0.55±0.32)	0.76 (0.75±0.008)	56.2 (45.2±8.48)	-1.63 (-0.98±0.06)	-2.29	239	6.70×10^4
Hexadecane	0	-	-	-			

The overall comparison of the J-V figures of merit reveals interesting points, all devices exhibit relatively high parallel resistance (this parameter can be interpreted physically, where higher values indicates lower loss by recombination) and, although a trend can be observed (higher R_p corresponds to high PCE) this is not the case (in particular) for OPVs employing 1-phenyloctane and hexadecane as additives. An interesting parameter is the photocurrent density (J_{ph}) as it reveals an estimate of the generated electrical current. The higher the difference to the J_{sc}, the higher probability of exciton loss. In our results, we observed a significant difference between J_{sc} and J_{ph} when the 1-phenyloctane additive is used (J_{sc} is near 0.7 of J_{ph}) when the typical value is about $J_{sc} \approx 0.8 \times J_{ph}$ (devices without additives, with methylnaphtalene and chloronaphtalene) and even higher ($J_{sc} \approx 0.97 \times J_{ph}$ when *p*-anisaldehyde was used as additive). Although not a perfect trend (and not directly related with R_p), it is worth mentioning that the best PCE is obtained in samples with a lower ratio of loss. All these results are essentially due to the different film nanostructure because of the different effect promoted by the different additives on the BHJ morphology. Therefore, we can conclude that the additives changes (and in some cases with a noticeable effect) the way that excitons are created / separated at the D-A interface and also changes the electrical charge transport process. Although some fluctuations, the R_s have no noticeable changes independently of the additive used and, considering the evaluated values deviations can be attributed to the usual differences in contact resistance.

In order to get more information regarding the exciton separation / recombination at D-A interfaces, some straightforward small signal analysis was performed. Several models are widely used for impedance spectroscopy of OPVs. When the devices are measured under dark conditions (as in our case), the data can be interpreted in terms of thickness and position of the layers forming the surface or interface of the device. This means that typically two different relaxation processes (besides the simplest charge accumulation / release at electrodes) can be eventually observed and analyzed in the time domain: slowest electrical carrier diffusion time and its lifetime. These times can be related with the time needed for carriers to diffuse out of the bulk layer in the direction of the electrodes and to the time of the recombination rate respectively [26].

Considered as the most representative situations, the capacitance and loss (conductance over frequency ω) were measured for a reference sample without additives and for samples with hexadecane and 1-phenyloctane (the two most detrimental additives) and with chloronaphtalene (the most favorable additive). The results are shown in Figure 4.3 for boot impedance spectra (a) and Nyquist plot (b). From the impedance spectra, it is clear that we have two relaxations, one at low frequency (< 1 KHz) and a

second at much high frequency (> 2 MHz). The low frequency range relaxation can usually be attributed to charge accumulation at the electrodes, the high frequency relaxation needs to be carefully analyzed. From the Nyquist plot (Figure 4.3b), it can be seen that the relaxation peak changes slightly depending on the additive employed. In a very simple way, we can determine the relaxation frequency (and therefore the relaxation time) for the different data. In our case, the relaxation time is near 0.50 μs, 0.53 μs, 0.59 μs and 0.68 μs for samples with chloronaphthalene, without additive, 1-phenyloctane and hexadecane respectively. As an immediate conclusion, as the relaxation time in high frequency region increases, we observe a decrease of the PCE mostly due to the decrease of the J_{sc} (regardless of the relationship with J_{ph}). Although in our data is not clear if the presence of a second relaxation time (that should be high in this kind of organic semiconductors), these relaxation times seem to be correlated to the diffusion time (less than 1 μs) in opposite to the expected slower relaxation times observed for recombination (a few μs). For now, an increase in the relaxation time in our samples, corresponds to a decrease of the efficiency that can be linked to electrical transport controlled by electrically active traps, reducing mobility and, and increasing the diffusion time, leading to a high probability of loss. Some degradation of the D-A interfaces can also be present (and we expect that) but it is not simple to quantify.

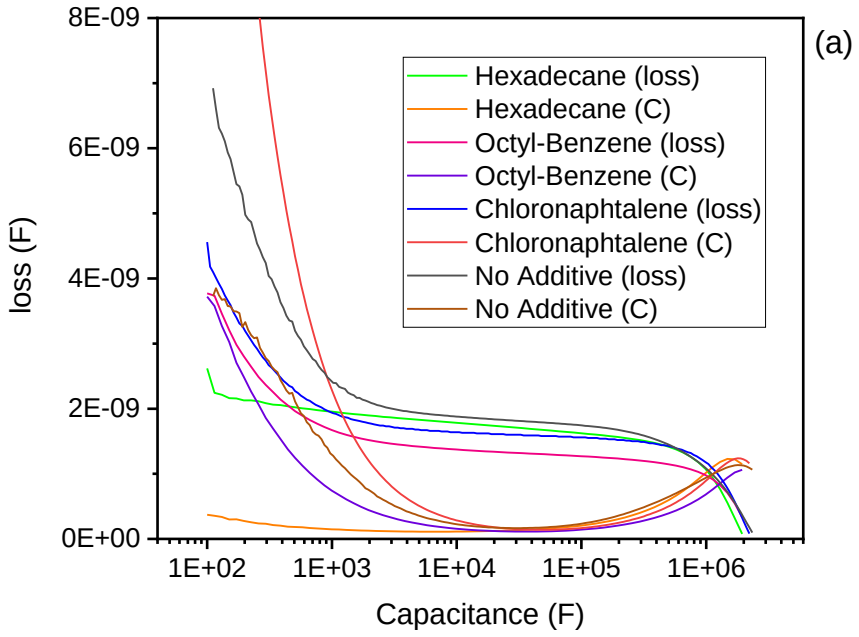

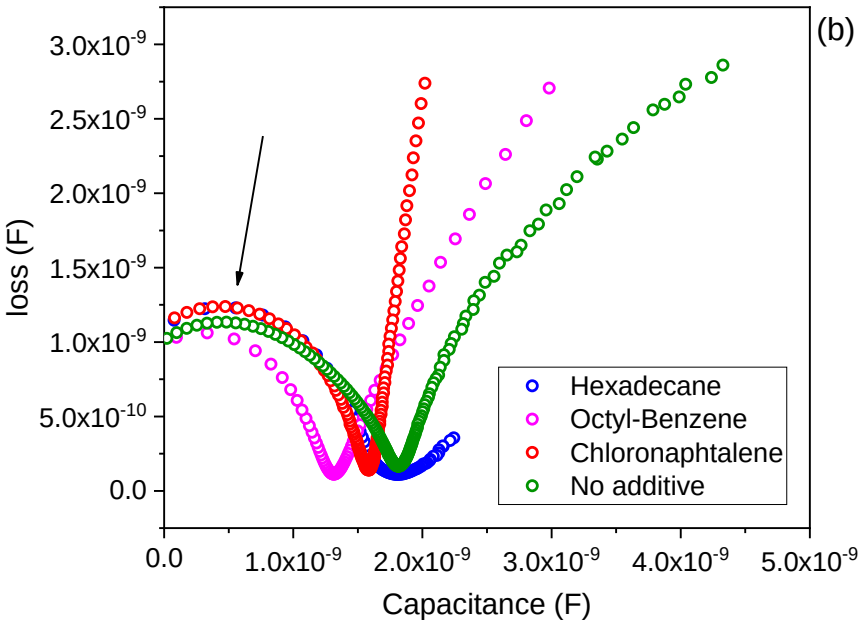

Figure 4. 3. Small signal data of four different devices. (a) Capacitance and loss and (b) Nyquist plot enhancing the region of high-frequency relaxation.

Grazing incidence wide-angle X-ray scattering (GIWAXS) reveals the molecular packing and crystalline structure of the thin BHJ films processed with different additives, the results are shown in Figure 4.4. The films exhibit a high degree of molecular order, as evidenced by strong lamellar (100) and (200) peaks at 0.29 $Å^{-1}$ and 0.58 $Å^{-1}$. More importantly, the (010) peak at q ~ 1.79 $Å^{-1}$, corresponding to π-π stacking, and clearly shows that this is very pronounced in the BHJ processed with the best additives and completely disappears in the BHJ processed with the most harmful additives (1-phenyloctane and hexadecane). We also observe a broad halo at q ~ 1.39 $Å^{-1}$ characteristic of $PC_{71}BM$ aggregation which remains almost unchanged in the different BHJs. These results show that the difference in performance of the devices largely derives from a rearrangement in the molecular packing of the polymer molecules.

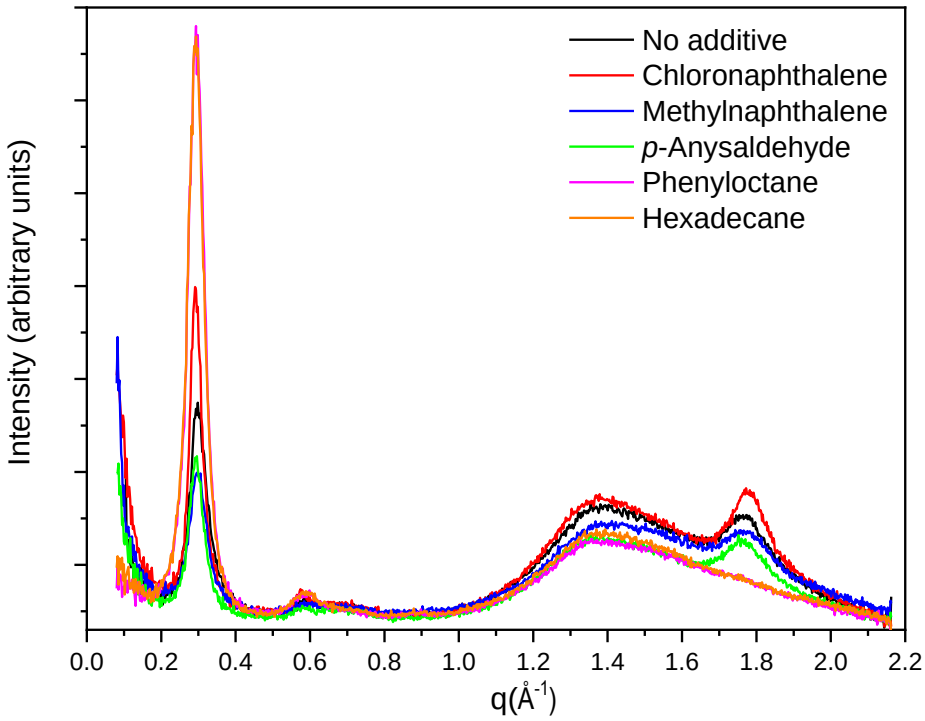

Figure 4. 4. GIWAXS data of the BHJs processed using different additives.

In an attempt to elucidate the impact of the different additives on the degree of phase segregation in the BHJ films processed with different additives, we have started by using atomic force microscopy (AFM) to study their surface morphologies. We present a selection of images in Figure 4.5. As it is evident, the interpretation of these figures is ambiguous and inconclusive. At this point it is worth noting that AFM only probes the surface morphology of the film and this may be very different from that of the underlying bulk material.

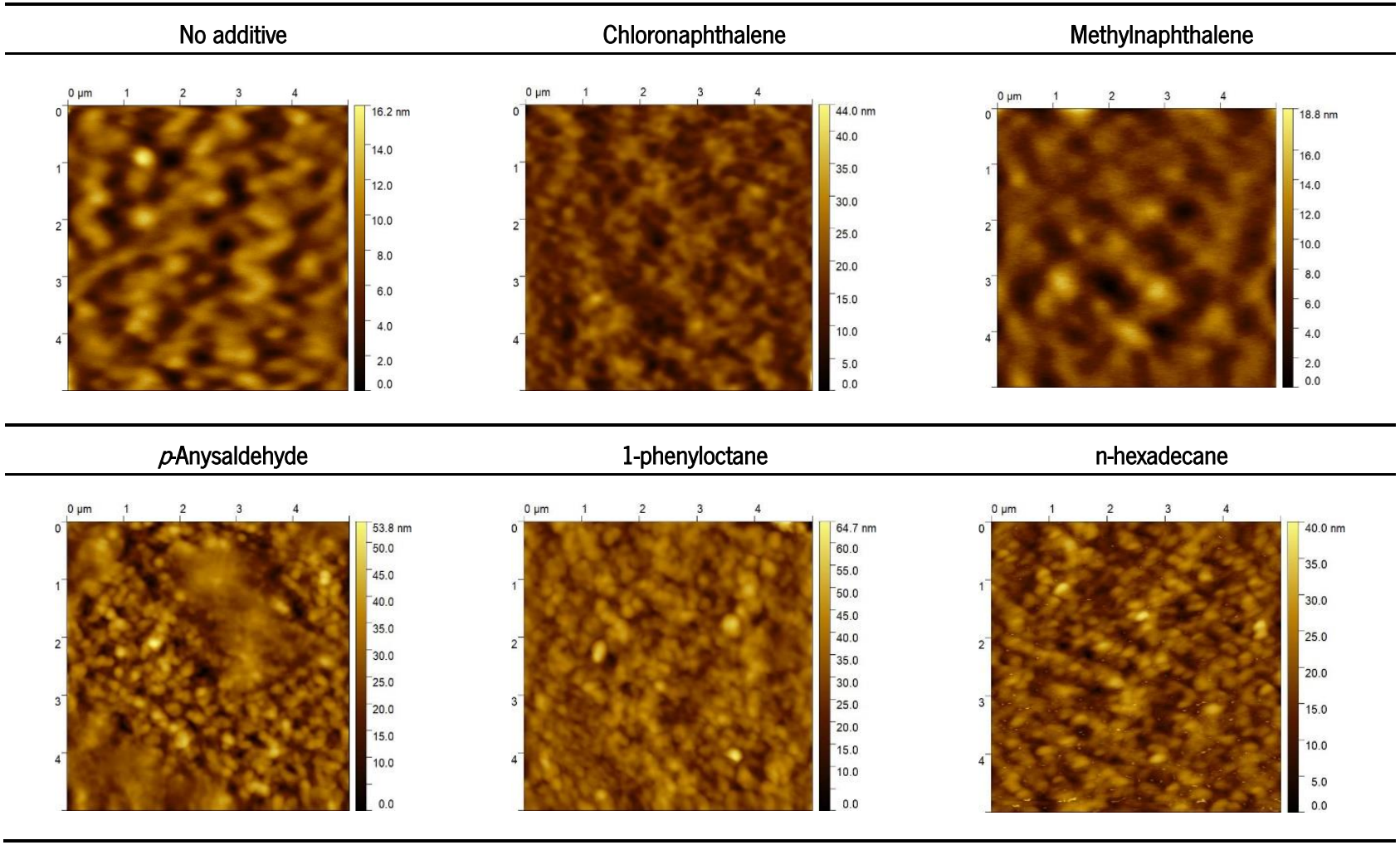

Figure 4. 5. AFM of the PffBT4T-2OD:$PC_{71}BM$ BHJs processed with different additives.

As a next step in the study of the effect of additives on the polymer:fullerene domain size in the bulk of the films, we have used SANS using the stacking method previously reported [10]. Compared to AFM, SANS has the advantage of being a bulk sampling technique that due to the intrinsically very different neutron scattering length densities (SLD) between hydrogenous polymers (such as PffBT4T-2OD) and fullerenes (such as $PC_{71}BM$), allows to obtain a high contrast between both phase regions, irrespective of these being crystalline or amorphous. In the SANS measurements we have focused on the two extreme cases of additive-modified BHJs, namely the BHJs processed with 1-chloronaphtahlene (highest efficiency) and with hexadecane (zero efficiency), as well as on a reference BHJ processed without additive. In Figure 4.6, we show the SANS spectra recorded from stacks of 16 PffBT4T-2OD:$PC_{71}BM$ films on quartz disks (corresponding to a total dry active layer thickness of ~3.2 μm), with intensity plotted versus scattering vector.

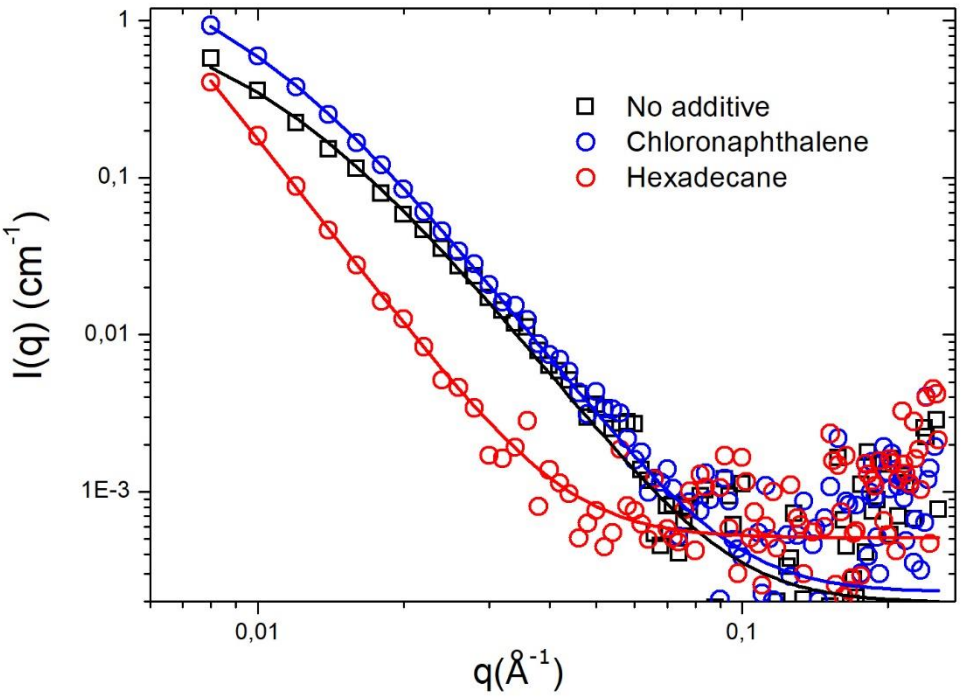

Figure 4. 6. SANS intensity (I) as a function of scattering vector (q) for PffBT4T-2OD:$PC_{71}BM$ BHJs processed with 1-chloronaphthalene (best morphology with the highest efficiency) and hexadecane (worst morphology with zero efficiency) and a reference BHJ processed without additives.

In SANS, the intensity is proportional to the number, size and contrast of the scattering entities in a sample, while the *q*-dependence of the intensity is related to their shape and local arrangement. Following the same procedure as described in previous work [10, 11], the data range from 0.008 Å^{-1} to 0.254 Å^{-1} (corresponding to the LOQ main detector) was fitted using the Debye-Bueche (DB) or Debye-Anderson-Brumberger (DAB) model. This model calculates the scattering from a randomly distributed, phase segregated system that is characterized by a single length scale - the correlation length, L – this is a measure of the average spacing between regions of two adjacent phases. This function has the form:

$$\frac{d\Sigma}{d\Omega}(\mathrm{q}) = \frac{c_{DB}L^3}{(1+(qL)^2)^2} + b \qquad (1)$$

where the scaling factor $C_{DB} = 8\pi(\Delta\rho)^2\phi_1\phi_2$ and $\Delta\rho$ is the neutron scattering length density difference between the phases having volume fractions of ϕ_1 and ϕ_2. The second term on the right hand side of the equation (b) is the background intensity that includes both instrumental and sample specific factors, i.e. the incoherent scattering intensity. As shown in Figure 5, the DAB model gives a good description of the data. The values obtained from the fitting for C_{DB} and L using equation 1 are given in Table 4.2.

Table 4. 2. Scaling factors (CDB) and correlation lengths (L) obtained by fitting the experimental data using the Debye-Anderson-Brumberger (DAB) model in the interval q = 0.008–0.254 Å^{-1}.

Additive	Scaling factor C_{DB}	Length (nm)	(χ^2/Npts)
No additive	1.4008×10^{-6}	9.4	1.94
Chloronaphthalene	1.993×10^{-6}	11.1	1.07
Hexadecane	0.5134×10^{-6}	31.2	0.67

Also shown are the corresponding values of the normalized χ^2 that confirm the quality of the fits. As shown in Table 4.2, a BHJ processed without additive has a correlation length of 9.4 nm and the BHJ of the best performing devices, processed with 1-chloronaphthalene, has a correlation length of 11.1 nm. This small coarsening of the phase domains upon the addition of good additives is in good agreement with previous reports [10]. A BHJ processed with hexadecane (a non-solvent for both the polymer and the fullerene) has a much coarser phase segregation with a correlation length of 31 nm, i.e. much larger than the typical exciton diffusion length in organic semiconductors. Therefore, in BHJ processed with hexadecane, all the generated excitons will most likely suffer recombination before they can reach a D:A interface.

As a last part of this study, we investigate the correlation between the morphological and efficiency changes caused by the different additives and their chemical affinity to the polymer and fullerene as expressed by their corresponding Hansen Solubility Parameters (HSP) [24]. The HSP of the materials, solvents and additives used in this work are shown in Table 4.3, and these empirical parameters can be used to predict the ability of one solvent or additive to dissolve a solute (either polymer or fullerene). The solubility properties of each solid (polymer or fullerene) and liquid (solvent or additive) can be characterized by their corresponding HSP, which is a vector in a 3-D orthogonal space with dimensions δ_D (dispersion), δ_P (polar) and δ_H (hydrogen bonding). The radius of interaction (R_a) for two substances 1 and 2 with HSP_1 (δ_{D1}, δ_{P1}, δ_{H1}) and HSP_2 (δ_{D2}, δ_{P2}, δ_{H2}) is defined as the distance between their coordinates in the HSP space (Equation 2) with a pre-factor of 4 for the dispersive component.

$$Ra = \sqrt{4\,(\delta_{D1} - \delta_{D2})^2 + (\delta_{P1} - \delta_{P2})^2 + (\delta_{H1} - \delta_{H2})^2} \qquad (2)$$

Table 4. 3. Hansen solubility parameters of the materials, solvents and additives used in this work. To the authors knowledge, no Hansen solubility parameters for p-anisaldehyde have been published in the literature and therefore we indicate the corresponding values for its isomer o-anisaldehyde. We can safely assume that they are very similar. (a) Ref. [27]; (b) Ref. [28]; (c) Ref. [24]; (d) Ref. [29]

	δ_D $MPa^{1/2}$	δ_P $MPa^{1/2}$	δ_H $MPa^{1/2}$	b.p. (°C)
PffBT4T-2OD [a]	18.56	4.07	2.31	——
$PC_{71}BM$ [b]	20.2	5.4	4.5	——
o-dichlorobenzene [c]	19.2	6.3	3.3	180
1-Chloronaphthalene [c]	19.9	4.9	2.5	263
1-Methylnaphthalene [c]	20.6	0.8	4.7	242
p-Anisaldehyde	——	——	——	248
o-Anisaldehyde [c]	19.4	11.9	8.3	238
Hexadecane [c]	16.3	0	0	287
Phenyl octane [d]	16.7	5.4	0	262

The Hansen solubility parameters of PffBT4T-2OD, $PC_{71}BM$ and of the solvent o-dichlorobenzene and the additives is shown in Table 4.3 and represented graphically in the HSP space in Figure 4.7. It can be seen clearly that additives with HSP closer to the HSP of PffBT4T-2OD and $PC_{71}BM$, namely 1-chloronaphthalene and 1-methylnaphthalene, produce better devices than additives with HSP more distant from the HSP of PffBT4T-2OD and $PC_{71}BM$.

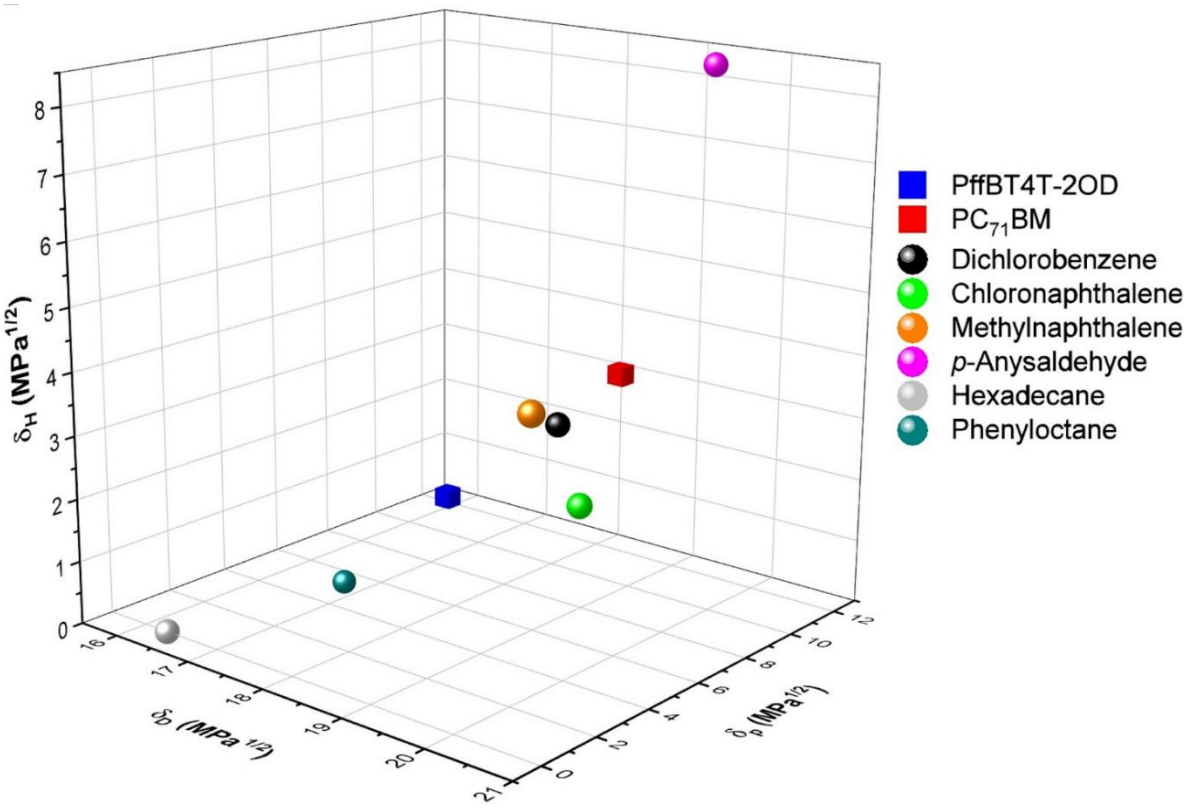

Figure 4. 7. Hansen solubility parameters of polymer, fullerene, solvent and additives used in this study.

4.4 Conclusions

A general theory that can explain the effect of additives on the morphology and efficiency of OPV devices should be able to explain not only the reason for the morphological and efficiency improvement upon the addition of some favorable additives but also the reason for the morphological and efficiency degradation upon the addition of unfavorable additives. In this work we tested the impact of several additives with different solubility parameters and boiling points on the morphology and efficiency of bulk-heterojunction solar cells based on the system PffBT4T-2OD:PC71BM. Our results demonstrate the intimate relationship between the efficiency and the morphology of the devices: i) the best devices (PCE=8.75%), prepared using an additive (chloronaphthalene) with HSP nearby the HSP of the polymer and fullerene, exhibit a morphology characterized by a correlation length of ~11 nm and a high degree of polymer π-π stacking and ii) the worst devices (PCE=0%), prepared using an additive (hexadecane) with HSP far away from the HSP of the polymer and fullerene, exhibit a morphology characterized by a correlation length of ~30 nm, i.e. much higher than the exciton diffusion length, and no polymer π-π stacking.

References

[1] H. Gaspar, F. Figueira, L. Pereira, A. Mendes, J.C. Viana, G. Bernardo, Recent Developments in the Optimization of the Bulk Heterojunction Morphology of Polymer: Fullerene Solar Cells, Materials, 11 (2018) 36.
[2] Y. Cui, H. Yao, J. Zhang, T. Zhang, Y. Wang, L. Hong, K. Xian, B. Xu, S. Zhang, J. Peng, Z. Wei, F. Gao, J. Hou, Over 16% efficiency organic photovoltaic cells enabled by a chlorinated acceptor with increased open-circuit voltages, Nat. Commun., 10 (2019) 2515.
[3] L. Meng, Y. Zhang, X. Wan, C. Li, X. Zhang, Y. Wang, X. Ke, Z. Xiao, L. Ding, R. Xia, H.-L. Yip, Y. Cao, Y. Chen, Organic and solution-processed tandem solar cells with 17.3% efficiency, Science, (2018).
[4] Y.H. Liu, J.B. Zhao, Z.K. Li, C. Mu, W. Ma, H.W. Hu, K. Jiang, H.R. Lin, H. Ade, H. Yan, Aggregation and morphology control enables multiple cases of high-efficiency polymer solar cells, Nature Communications, 5 (2014) 8.
[5] W. Ma, G.F. Yang, K. Jiang, J.H. Carpenter, Y. Wu, X.Y. Meng, T. McAfee, J.B. Zhao, C.H. Zhu, C. Wang, H. Ade, H. Yan, Influence of Processing Parameters and Molecular Weight on the Morphology and Properties of High-Performance PffBT4T-2OD:PC71BM Organic Solar Cells, Advanced Energy Materials, 5 (2015) 9.
[6] J. Zhao, S.L. Zhao, Z. Xu, B. Qiao, D. Huang, L. Zhao, Y. Li, Y.Q. Zhu, P. Wang, Revealing the Effect of Additives with Different Solubility on the Morphology and the Donor Crystalline Structures of Organic Solar Cells, Acs Applied Materials & Interfaces, 8 (2016) 18231-18237.
[7] X. Zhang, D. Zheng, S. Xing, H. Wang, J. Huang, J. Yu, Precisely control the morphology and crystallization of temperature-dependent aggregation bulk heterojunction by using co-solvent system for optimized light intensity distribution and its effect on thick active layer polymer solar cells, Solar Energy, 147 (2017) 106-112.
[8] G. Pirotte, S. Agarkar, B. Xu, J. Zhang, L. Lutsen, D. Vanderzande, H. Yan, P. Pollet, J.R. Reynolds, W. Maes, S.R. Marder, Molecular weight tuning of low bandgap polymers by continuous flow chemistry: increasing the applicability of PffBT4T for organic photovoltaics, Journal of Materials Chemistry A, 5 (2017) 18166-18175.
[9] J.D. Perea, S. Langner, M. Salvador, B. Sanchez-Lengeling, N. Li, C. Zhang, G. Jarvas, J. Kontos, A. Dallos, A. Aspuru-Guzik, C.J. Brabec, Introducing a New Potential Figure of Merit for Evaluating Microstructure Stability in Photovoltaic Polymer-Fullerene Blends, The Journal of Physical Chemistry C, 121 (2017) 18153-18161.
[10] Y.W. Zhang, A.J. Parnell, F. Pontecchiani, J.F.K. Cooper, R.L. Thompson, R.A.L. Jones, S.M. King, D.G. Lidzey, G. Bernardo, Understanding and controlling morphology evolution via DIO plasticization in PffBT4T-2OD/PC71BM devices, Sci Rep, 7 (2017) 12.
[11] Y. Zhang, A.J. Parnell, O. Blaszczyk, A.J. Musser, I.D.W. Samuel, D.G. Lidzey, G. Bernardo, Effect of fullerene acceptor on the performance of solar cells based on PffBT4T-2OD, Physical Chemistry Chemical Physics, 20 (2018) 19023-19029.
[12] Z.Z. Bi, H.B. Naveed, Y.M. Mao, H.P. Yan, W. Ma, Importance of Nucleation during Morphology Evolution of the Blade-Cast PffBT4T-2OD-Based Organic Solar Cells, Macromolecules, 51 (2018) 6682-6691.
[13] W. Li, J.L. Cai, F.L. Cai, Y. Yan, H.N. Yi, R.S. Gurney, D. Liu, A. Iraqi, T. Wang, Achieving over 11% power conversion efficiency in PffBT4T-2OD-based ternary polymer solar cells with enhanced open-circuit-voltage and suppressed charge recombination, Nano Energy, 44 (2018) 155-163.
[14] R. Sharma, V. Gupta, H. Lee, K. Borse, R. Datt, C. Sharma, M. Kumar, S. Yoo, D. Gupta, Charge carrier dynamics in PffBT4T-2OD: PCBM organic solar cells, Org. Electron., 62 (2018) 441-447.

[15] T. Umeyama, K. Igarashi, D. Sakamaki, S. Seki, H. Imahori, Unique cohesive nature of the beta(1)-isomer of 70 PCBM fullerene on structures and photovoltaic performances of bulk heterojunction films with PffBT4T-2OD polymers, Chemical Communications, 54 (2018) 405-408.
[16] A. Weu, T.R. Hopper, V. Lami, J.A. Kress, A.A. Bakulin, Y. Vaynzof, Field-Assisted Exciton Dissociation in Highly Efficient PffBT4T-2OD:Fullerene Organic Solar Cells, Chemistry of Materials, 30 (2018) 2660-2667.
[17] C. Xu, M. Wright, N.K. Elumalai, M.A. Mahmud, D. Wang, V.R. Goncales, M.B. Upama, F. Haque, J.J. Gooding, A. Uddin, Realizing 11.3% efficiency in PffBT4T-2OD fullerene organic solar cells via superior charge extraction at interfaces, Applied Physics a-Materials Science & Processing, 124 (2018).
[18] Y.F. Dong, H. Cha, J.B. Zhang, E. Pastor, P.S. Tuladhar, I. McCulloch, J.R. Durrant, A.A. Bakulin, The binding energy and dynamics of charge-transfer states in organic photovoltaics with low driving force for charge separation, Journal of Chemical Physics, 150 (2019).
[19] H.C. Liao, C.C. Ho, C.Y. Chang, M.H. Jao, S.B. Darling, W.F. Su, Additives for morphology control in high-efficiency organic solar cells, Materials Today, 16 (2013) 326-336.
[20] C. McDowell, M. Abdelsamie, M.F. Toney, G.C. Bazan, Solvent Additives: Key Morphology-Directing Agents for Solution-Processed Organic Solar Cells, Advanced Materials, 30 (2018) 30.
[21] F. Machui, P. Maisch, I. Burgues-Ceballos, S. Langner, J. Krantz, T. Ameri, C.J. Brabec, Classification of Additives for Organic Photovoltaic Devices, ChemPhysChem, 16 (2015) 1275-1280.
[22] G. Bernardo, A.L. Washington, Y.W. Zhang, S.M. King, D.T.W. Toolan, M.P. Weir, A.D.F. Dunbar, J.R. Howse, R. Dattani, J.P.A. Fairclough, A.J. Parnell, Does 1,8-diiodooctane affect the aggregation state of PC71 BM in solution?, R. Soc. Open Sci., 5 (2018) 11.
[23] G. Bernardo, A.L. Washington, Y. Zhang, S.M. King, D.T.W. Toolan, M.P. Weir, A.D.F. Dunbar, J.R. Howse, R. Dattani, J.P.A. Fairclough, A.J. Parnell, Data from: Does 1,8-Diiodooctane affect the aggregation state of PC71BM in solution?, Dryad Digital Repository, (2018).
[24] C.M. Hansen, Hansen Solubility Parameters - A User's Handbook, Second Edition ed., CRC Press - Taylor & Francis Group, Boca Raton, 2007.
[25] A.J. Trindade, L. Pereira, Bulk Heterojunction Organic Solar Cell Area-Dependent Parameter Fluctuation, International Journal of Photoenergy, (2017).
[26] G. Garcia-Belmonte, A. Munar, E.M. Barea, J. Bisquert, I. Ugarte, R. Pacios, Charge carrier mobility and lifetime of organic bulk heterojunctions analyzed by impedance spectroscopy, Org. Electron., 9 (2008) 847-851.
[27] C. Zhang, S. Langner, A.V. Mumyatov, D.V. Anokhin, J. Min, J.D. Perea, K.L. Gerasimov, A. Osvet, D.A. Ivanov, P. Troshin, N. Li, C.J. Brabec, Understanding the correlation and balance between the miscibility and optoelectronic properties of polymer–fullerene solar cells, Journal of Materials Chemistry A, 5 (2017) 17570-17579.
[28] B. Walker, A. Tamayo, D.T. Duong, X.D. Dang, C. Kim, J. Granstrom, T.Q. Nguyen, A Systematic Approach to Solvent Selection Based on Cohesive Energy Densities in a Molecular Bulk Heterojunction System, Adv. Energy Mater., 1 (2011) 221-229.
[29] A.F.M. Barton, CRC Handbook of Solubility Parameters and Other Cohesion Parameters, Second ed.1991.

Chapter V. Conclusions and Future work

In the first part of this thesis (Chapter II and Chapter III) sixteen novel C_{60} and C_{70} N-methyl-fulleropyrrolidine derivatives (8 with C_{60} and 8 with C_{70}) were synthesized by the well-known Prato reaction. Chapter II focused in eight phenyl-substituted acceptors (4 with C_{60} and 4 with C_{70}) and chapter III focused in eight acceptors containing thiophene- and carbazole-based pendant groups (4 with C_{60} and 4 with C_{70}).

^{1}H and ^{13}C solution NMR as well as HSQC technique were utilized for the structural characterization of all the synthetized fullerene derivatives. These characterizations showed that, due to the lower symmetry of the C_{70} molecule its functionalization yielded a mixture of four regioisomers ($\alpha1$, $\alpha2$, $\beta1$, $\beta2$). Once synthesized, the sixteen methyl-fulleropyrrolidine derivatives were characterized electrochemically and optically. Their HOMO-LUMO levels were determined experimentally by cyclic voltammetry, from the onset oxidation and reduction potentials respectively. The experimentally determined HOMO/LUMO levels show that several of the synthesized fullerene acceptors have more favourable (higher) LUMO levels than the standard fullerenes $PC_{61}BM$ and $PC_{71}BM$. *Ab initio* DFT calculations of the HOMO/LUMO levels of all the fulleropyrrolidine derivatives were performed and showed a reasonably good agreement with the experimentally determined values. UV-Vis absorption spectroscopy was used to characterize the optical properties of the pure fullerenes in solution. As expected, the C_{70} derivatives have a broader light absorption in the visible range than the C_{60} derivatives.

In order to test the performance of these new materials as acceptors in OPVs, devices were made and tested, using as donor the low bandgap polymer PffBT4T-2OD. The photovoltaic properties of the devices were determined using a solar simulator at room temperature. For both groups of N-methyl-fulleropyrrolidine derivatives, it was observed that all the novel fullerenes originated PffBT4T-2OD-based devices with poorer performances than reference devices (PffBT4T-2OD: $PC_{71}BM$), even though several of the novel fullerene acceptors have more favourable (higher) LUMO levels than the standard $PC_{71}BM$. The surface morphology of all the thin BHJ films was imaged by AFM in tapping mode, and their light absorption properties was evaluated using UV-Vis absorption spectroscopy. However, it was not possible to correlate unambiguously the surface morphologies and absorption properties of the BHJs with the efficiency of the corresponding devices. Even though, the C_{70} derivatives and their BHJ films exhibited broader light absorption in the visible range than the corresponding C_{60} derivatives and C_{60}-based BHJs, the device performance of C_{70}-based devices was in general lower than the corresponding performance of C_{60}-based devices. Through DFT calculations it was possible to determine that the 4 different regioisomers ($\alpha1$, $\alpha2$, $\beta1$, $\beta2$) of C_{70}-derivatives have different HOMO/LUMO levels. This structural and

energetic disorder introduced by the mixture of regioisomers and the presence in a relatively high amount of the β1-isomer is pointed as a likely reason for the lower general performance of devices based on C_{70} derivatives. Indeed, energetic disorder, especially at D:A interface, tends to degrade the V_{OC}, and introduces intrinsic defects responsible for increasing the exciton loss by recombination and for the low J_{SC}. Furthermore, it was possible to observed that the high amounts of β1-isomer are enough to interact negatively in the film blends decreasing this way their overall efficiency when compared with C_{60} derivatives (even if it is not possible to make any straightforward correlation between the quantity of β1-isomer and the values of efficiency observed for each C_{70} derivative). Overall, these results provide new knowledge on the effect of the fullerene functionalization on the efficiency of BHJ solar cells.

In Chapter IV, a different strategy was followed with the goals of improving the efficiency of OPV devices and also gaining a better understanding of the relationship between morphology and efficiency in BHJs. Instead of testing different electron acceptors, this chapter focused on the standard acceptor $PC_{71}BM$ blended with the now popular low bandgap polymer PffBT4T-2OD. The strategy consisted in forcing morphological changes in the BHJ films through the use of different additives, possessing different Hansen solubility parameters and different boiling points, and on measuring the photovoltaic performance of the resulting devices. Detailed electrical and morphological characterizations were carried out to elucidate the effect of different additives on the active layer of OPVs. Surface morphology of the thin films with the different additives was imaged by AFM in contact mode. GIWAXS and SANS were used to study the impact of the different additives on the crystalline structure and phase morphology of the BHJs, respectively. Impedance spectroscopy (range 100 Hz - 5×10^6 Hz) was carried out to determine the relaxation frequency with further correlation with charge separation / recombination at the donor-acceptor interface. The photovoltaic properties of the devices were determined using a solar simulator at room temperature. The results obtained demonstrated clearly the intimate relationship that exists between the type of additive used, the nano-morphology of the devices and their efficiency: the best devices exhibited a morphology characterized by a high degree of polymer π-π stacking and a correlation length (average distance between adjacent domains) of ~11 nm, i.e. well within the typical exciton diffusion length in organic semiconductors; by contrast, the worst devices exhibited a morphology characterized by the absence of polymer π-π stacking and a correlation length of ~30 nm, i.e. much larger than the typical exciton diffusion length. By impedance spectroscopy, a direct relationship with relaxation time and efficiency could be obtained, showing how additives modify the electrical properties and assures at D:A phase a suitable modification in the exciton separation charge (CT states) and the loss by recombination. All these results, show a complete characterization of the effect of additives in the

OPV performance, purely related with morphological assessments with further influence in the OPV figures of merit.

With all the work done, several aspects are of major importance. Effectively, morphology is one of the most important key issues for the OPV success. In addition, the current work opened new possibilities for improvements. As interesting points for future work, the possibility of new fullerene acceptors with improved molecular morphology, either by new film forming conditions or by the incorporation of chemical additives, should be considered. Although novel non-fullerene acceptors are now being extensively investigated, the main results of all work behind this thesis show that fullerenes can be easily synthetized and, particularly interesting, easily controlled for a good active film formation. Moreover, the additives use, are far from a closed work. The results herein obtained, show that there is a large amount of degrees of freedom to improve the effect of additives in the morphology towards OPV improvement. Having this in mind, a different strategy can be adopted in the future by testing the solubility of the several N-methyl-fulleropyrrolidine derivatives groups with different chemical additives and compare the results with the standard $PC_{61}BM$ and $PC_{71}BM$ acceptors. Additionally, these new approaches studied in this work can be, with a high degree of probability, useful even for non-fullerene acceptors. In this way, new interesting research routes for thin film OPVs will be opened

Appendix I

60b: ^{1}H NMR (300 MHz, CS_2 + Acetone-d6): δ 7.69 (d, *J* = 8.1 Hz, 2H), 6.92 (m, 2H), 5.00 (d, *J* = 9.3 Hz, 1H), 4.92 (s, 1H), 4.30 (d, *J* = 9.3 Hz, 1H), 3.81 (s, 3H), 2.82 (s, 3H); ^{13}C NMR (126 MHz, Acetone-*d*$_6$): δ 157.00, 154.08, 154.05, 147.78, 147.36, 147.10, 146.82, 146.76, 146.73, 146.69, 146.63, 146.60, 146.44, 146.32, 146.12, 146.08, 146.04, 145.89, 145.81, 145.74, 145.69, 145.65, 145.25, 145.18, 144.93, 143.66, 143.54, 143.20, 143.13, 143.10, 143.08, 142.84, 142.71, 142.65, 142.58, 142.48, 142.32, 142.23, 140.73, 140.68, 139.99, 137.50, 137.42, 137.14, 136.48, 136.36, 129.38, 129.11, 83.98, 77.76, 70.44, 69.58, 40.33. (Figures 2.4, 2.5 and 2.6)

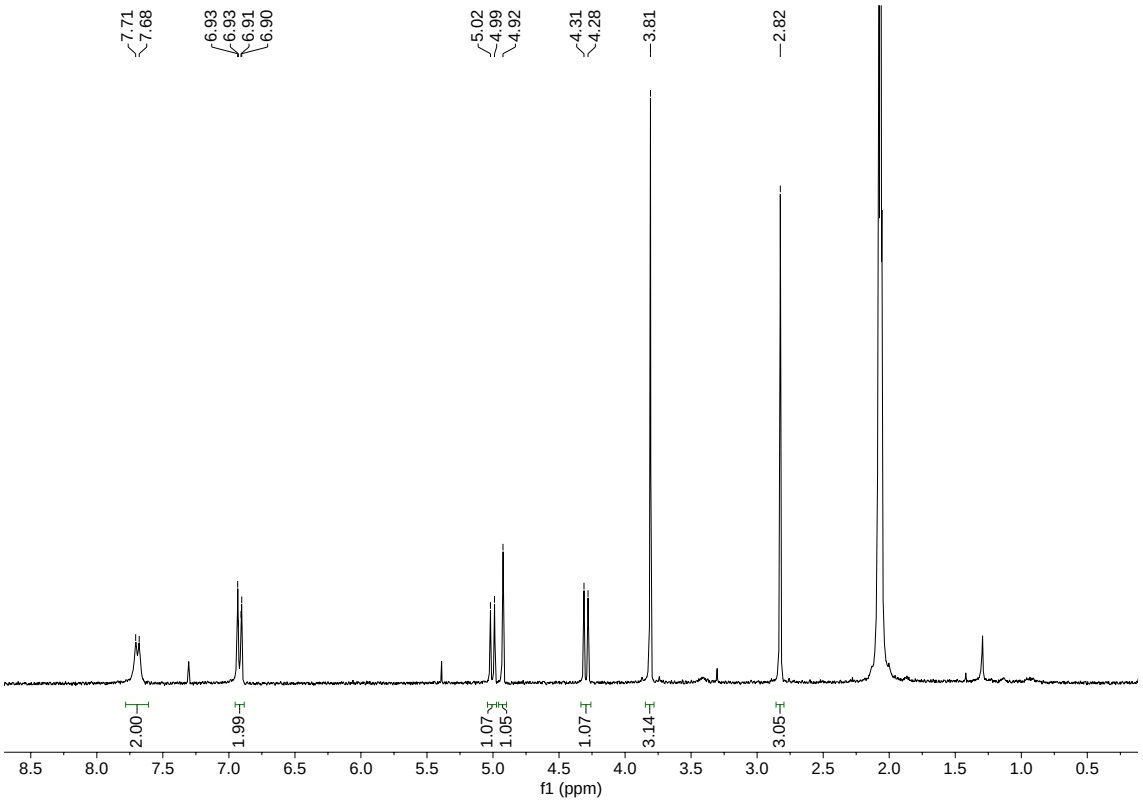

Figure 2. 12. ^{1}H NMR spectra of compound **60b** in a mixture of CS_2 and acetone-d6.

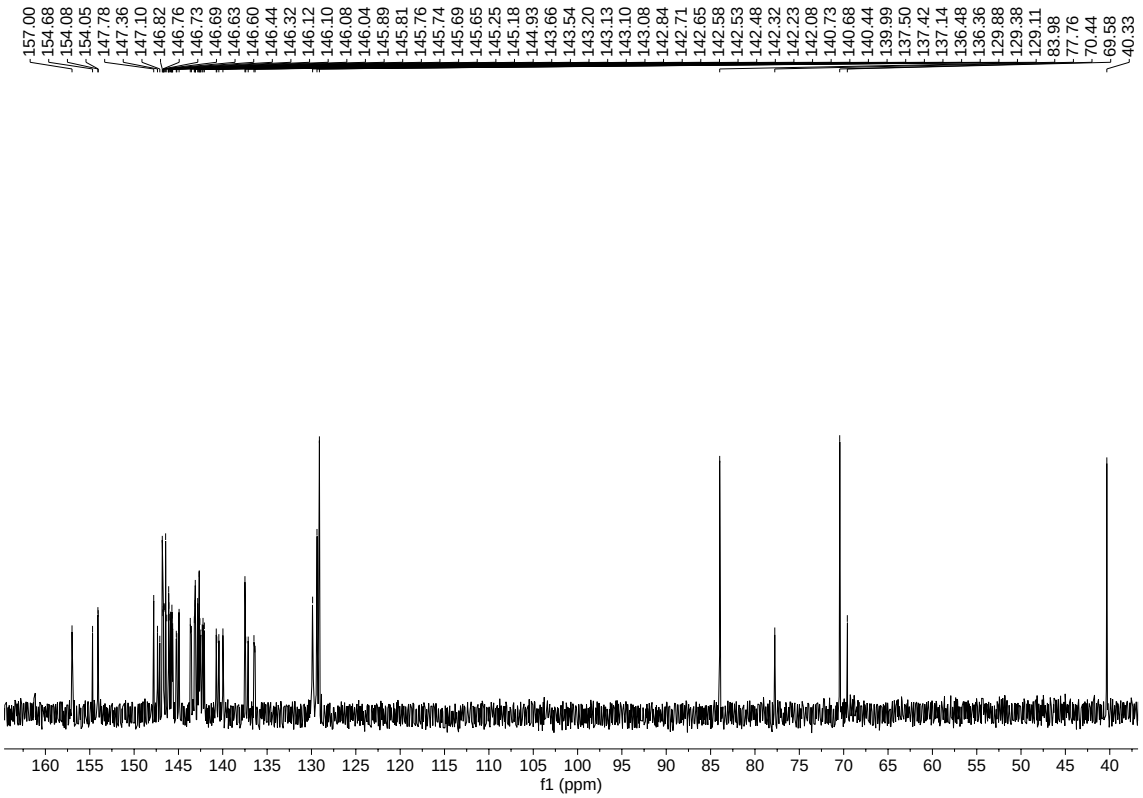

Figure 2. 13. ^{13}C NMR spectra of compound **60b** in a mixture of CS_2 and acetone-d6.

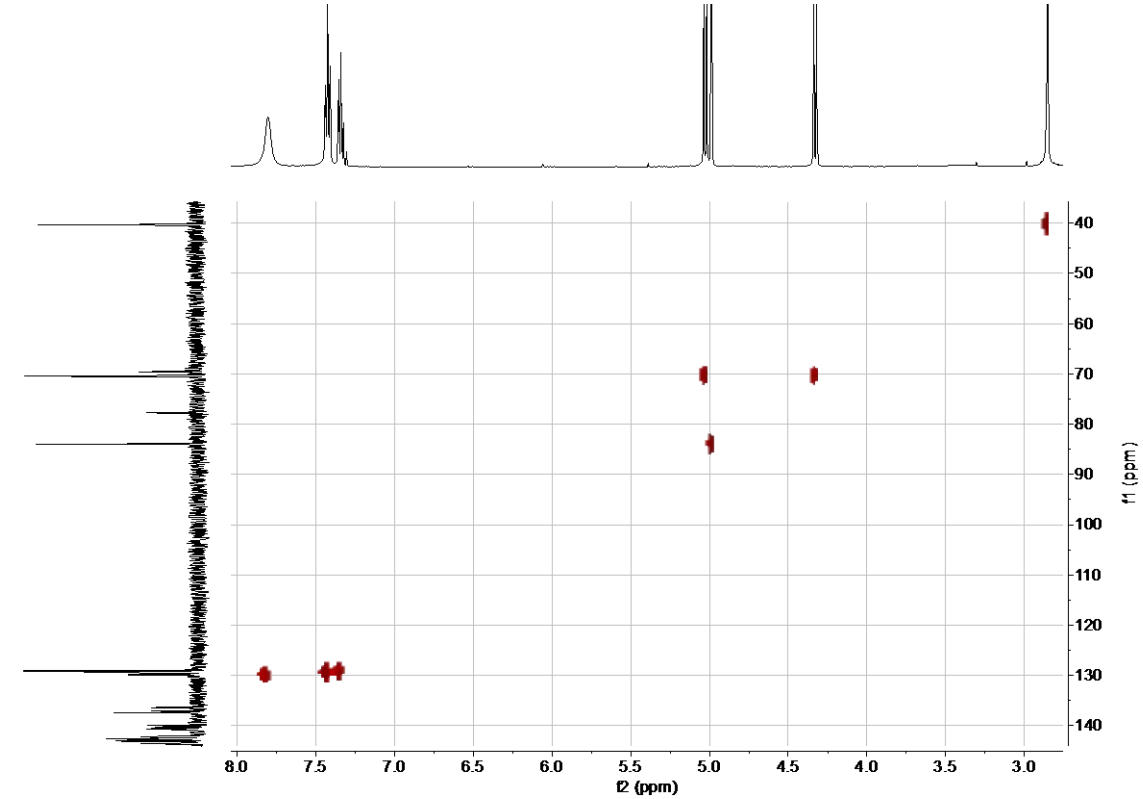

Figure 2. 14. HSQC spectra of compound **60b** in a mixture of CS_2 and acetone-d6.

60c: ^{1}H NMR (300 MHz, CS_2 + Acetone-d6): δ 7.70 (d, *J* = 8.104 Hz, 2H), 6.93 (d, *J* = 8.90 Hz, 2H), 5.01 (d, *J* = 9.3 Hz, 1H), 4.93 (s, 1H), 4.30 (d, *J* = 9.3 Hz, 1H), 3.81 (s, 3H), 2.83 (s, 3H); ^{13}C NMR (126 MHz, CS_2 + Acetone-d6): δ 165.72, 156.56, 154.30, 153.47, 153.22, 147.72, 147.00, 146.88, 146.76, 146.70, 146.66, 146.57, 146.38, 146.32, 146.19, 146.05, 145.95, 145.91, 145.84, 145.76, 145.68, 145.61, 145.17, 145.07, 144.86, 143.60, 143.48, 143.15, 143.07, 143.05, 143.01, 142.74, 142.63, 142.58, 142.54, 142.51, 142.49, 142.44, 142.33, 142.27, 142.16, 142.03, 140.69, 140.42, 139.96, 136.96, 136.51, 136.21, 130.95, 130.50, 83.42, 77.42, 70.39, 69.50, 52.09, 40.32. (Figures 2.7, 2.8 and 2.9)

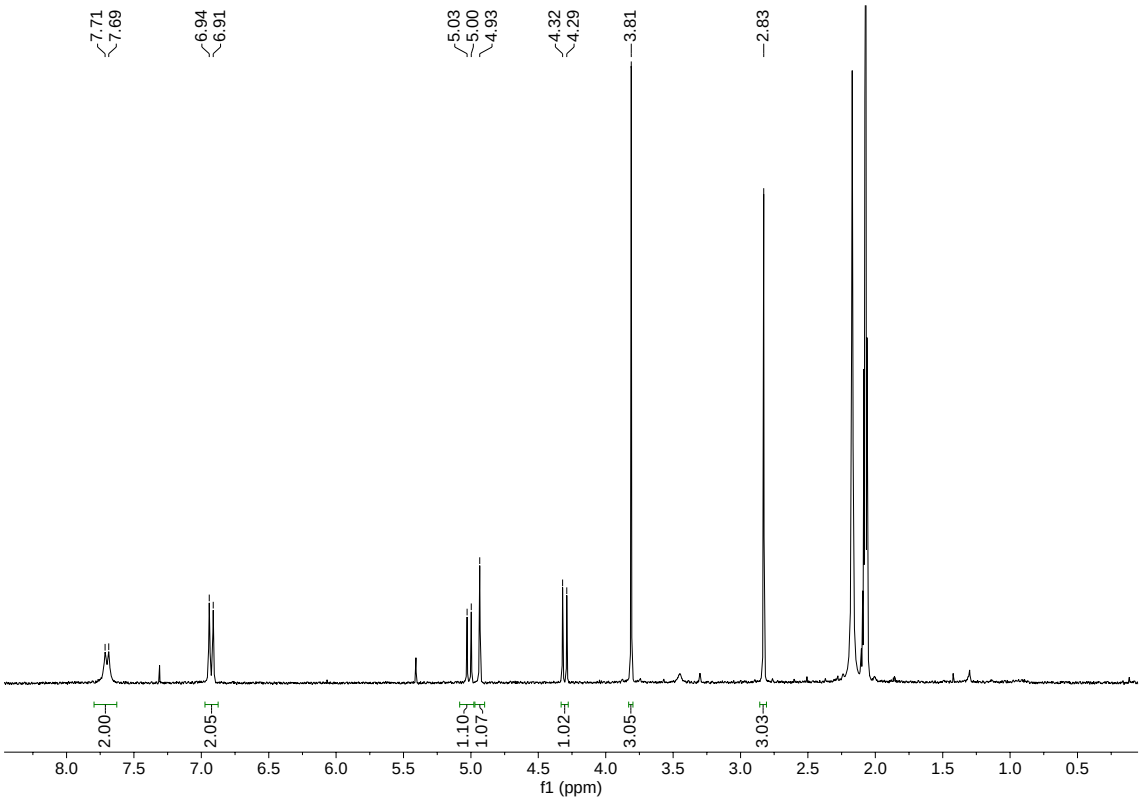

Figure 2. 15. ^{1}H NMR spectra of compound 60c in a mixture of CS_2 and acetone-d6.

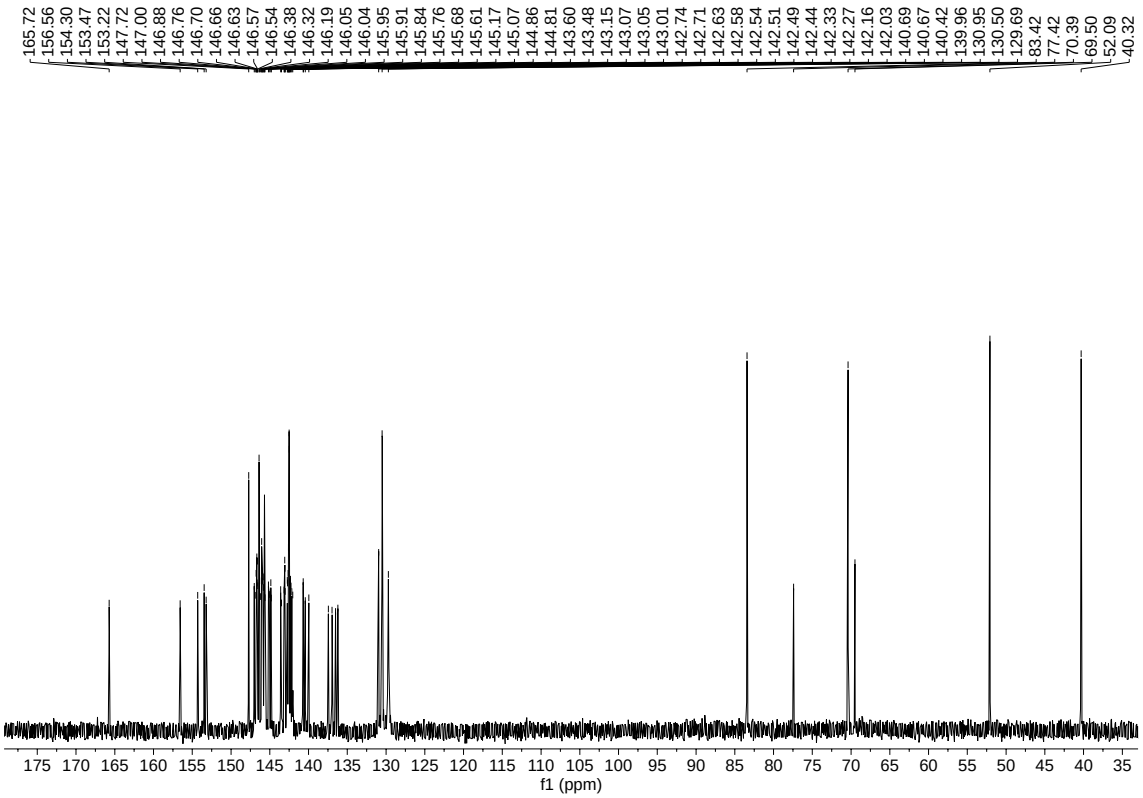

Figure 2. 16. ^{13}C NMR spectra of compound **60c** in a mixture of CS_2 and acetone-d6.

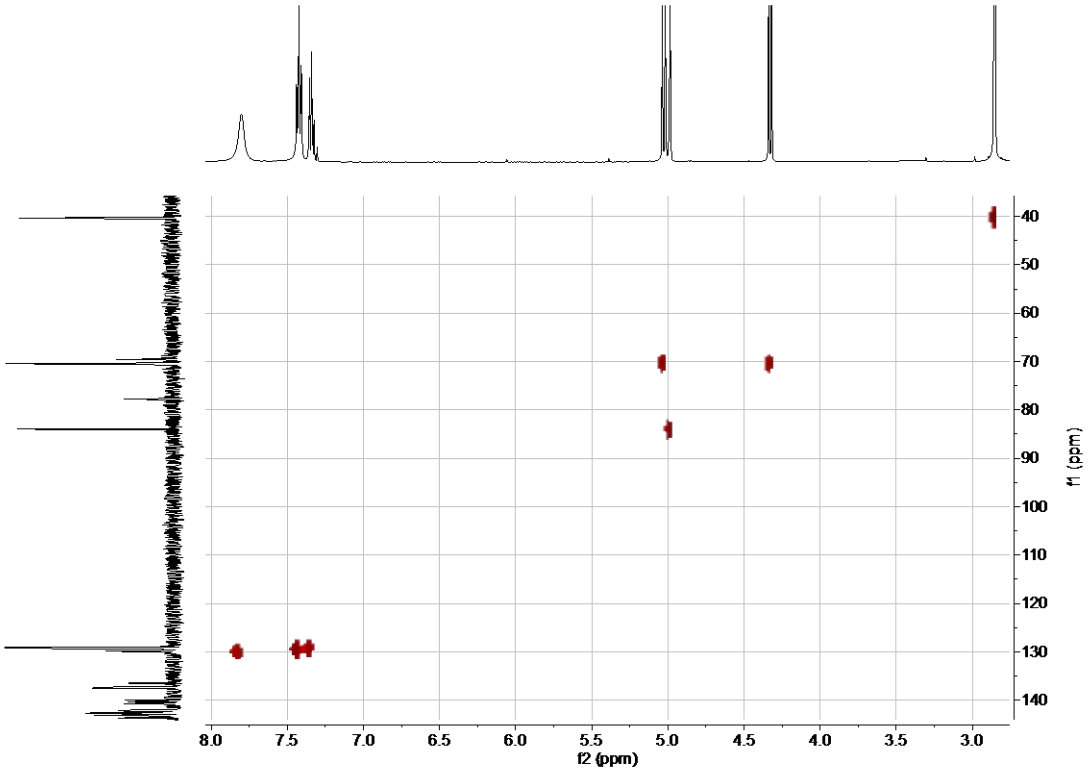

Figure 2. 17. HSQC spectra of compound **60c** in a mixture of CS_2 and acetone-d6.

70a: ^{1}H NMR (500 MHz, CS_2+Acetone-d_6): δ 7.95 – 7.05 (m, 5H), 5.50 – 4.29 (m, 1H), 4.30 – 3.92 (m, 1H), 3.71 – 3.27 (m, 1H), 2.61 – 2.43 (m, 3H); ^{13}C NMR (126 MHz, CS_2 + Acetone-d_6): δ 159.43, 159.06, 158.72, 156.94, 156.61, 156.25, 155.48, 155.41, 153.94, 153.21, 153.12, 152.13, 151.93, 151.90, 151.87, 151.82, 151.75, 151.63, 151.49, 151.32, 151.24, 151.16, 151.07, 150.93, 150.70, 150.55, 150.35, 150.20, 150.16, 150.08, 149.98, 149.92, 149.87, 149.79, 149.69, 149.64, 149.55, 149.50, 149.45, 149.37, 149.26, 149.10, 148.78, 148.45, 148.22, 148.00, 147.94, 147.87, 147.71, 147.51, 147.34, 147.24, 147.10, 147.00, 146.77, 146.69, 146.67, 146.28, 146.19, 146.17, 146.09, 146.04, 145.77, 145.40, 145.29, 145.12, 144.33, 143.96, 143.90, 143.69, 143.62, 143.58, 143.52, 143.34, 143.29, 143.15, 142.81, 142.28, 142.20, 141.58, 141.38, 141.26, 141.13, 140.73, 140.67, 138.30, 138.23, 138.17, 137.87, 137.43, 136.99, 134.28, 134.07, 134.00, 133.47, 132.78, 132.52, 132.47, 131.96, 131.69, 131.65, 130.94, 130.18, 129.60, 129.25, 129.18, 129.08, 129.01, 128.98, 128.82, 127.26, 127.08, 83.72, 83.41, 82.77, 80.61, 71.34, 70.59, 70.38, 69.10, 68.55, 67.08, 66.63, 62.56, 60.81, 59.22, 58.84, 39.79, 39.77, 39.74, 39.70. (Figures 2.10, 2.11 and 2.12)

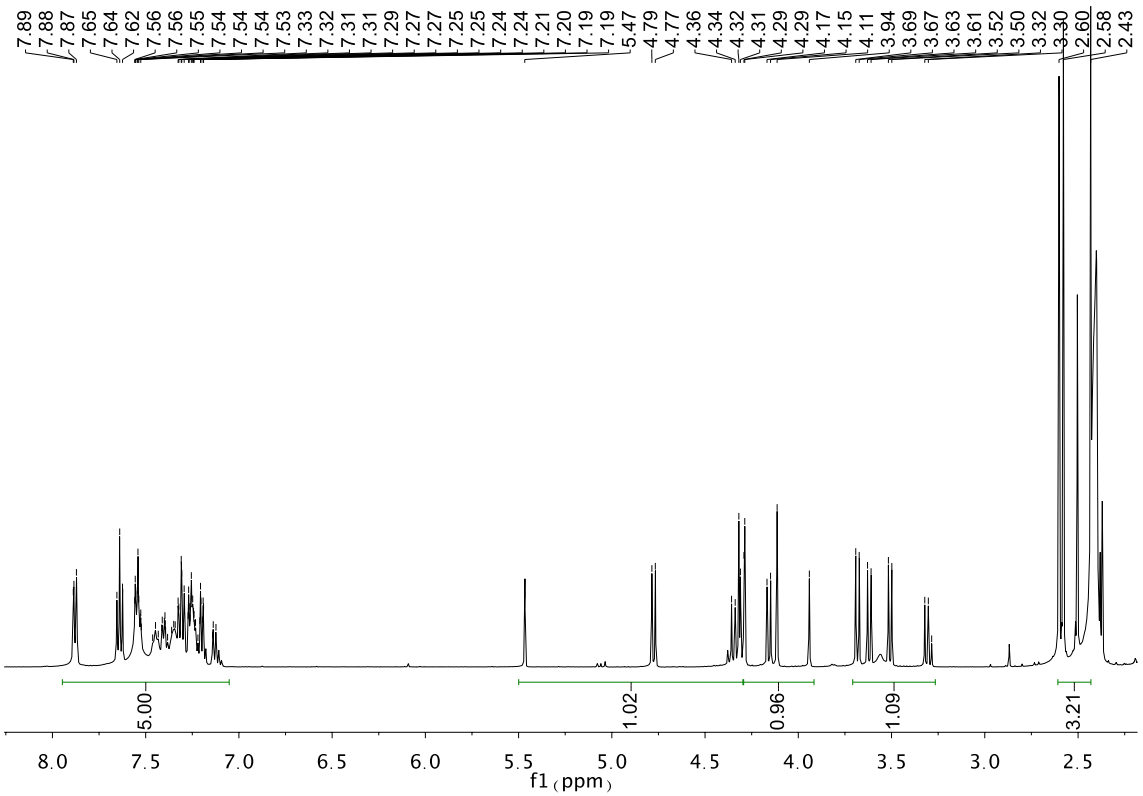

Figure 2. 18. ^{1}H NMR spectra of compound **70a** in a mixture of CS_2 and acetone-d6.

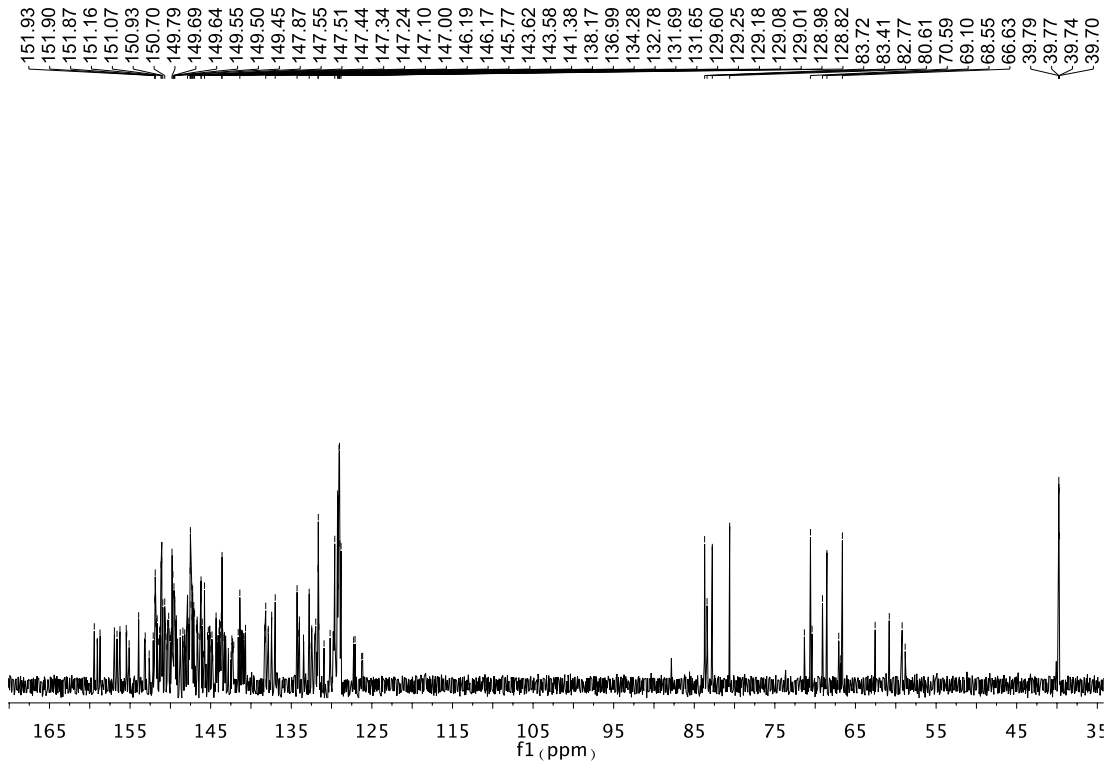

Figure 2. 19. ^{13}C NMR spectra of compound **70a** in a mixture of CS_2 and acetone-d6.

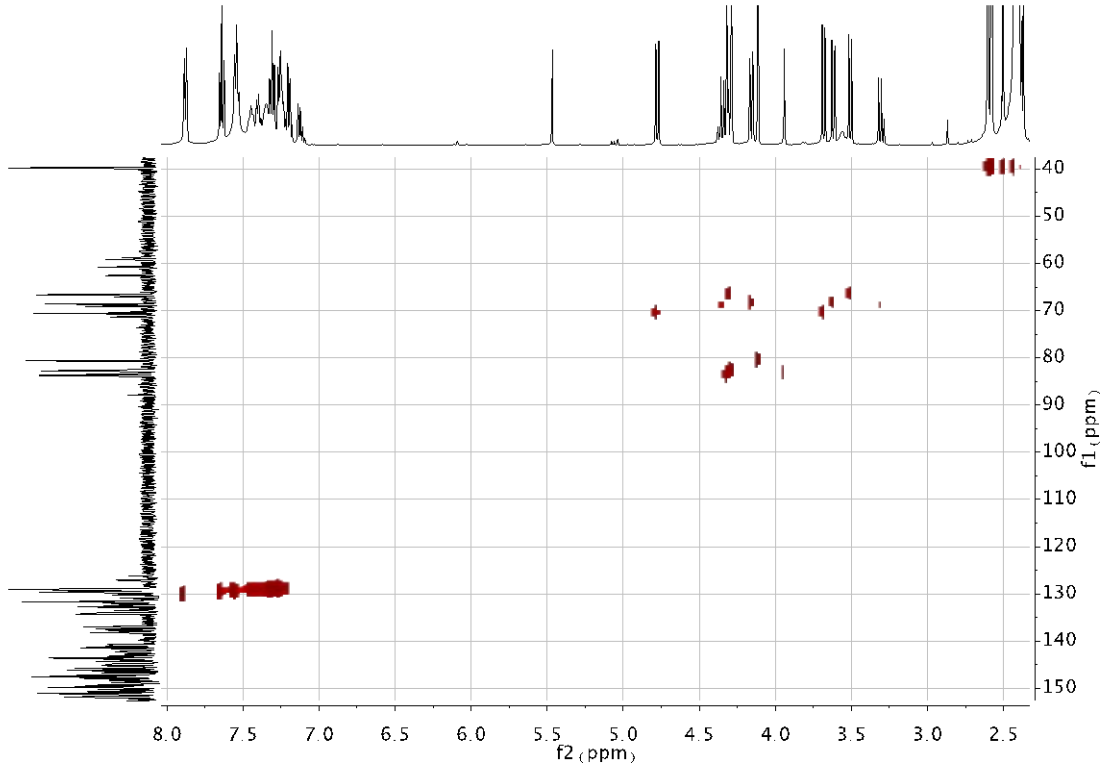

Figure 2. 20. HSQC spectra of compound **70a** in a mixture of CS_2 and acetone-d6.

70b: ^{1}H NMR (500 MHz, CS_2 + Acetone-d_6): δ 8.47 – 7.12 (m, 4H), 4.81 – 4.31 (m, 1H), 4.32 – 4.08 (m, 1H), 4.00 – 3.78 (m, 3H), 3.72 – 3.26 (m, 1H), 2.66 – 2.41 (m, 3H); ^{13}C NMR (126 MHz, Acetone-d6): δ 165.81, 165.69, 165.52, 165.49, 159.18, 158.77, 158.18, 156.75, 156.38, 155.53, 155.24, 155.12, 155.00, 153.74, 153.72, 152.82, 152.70, 152.38, 152.07, 151.85, 151.80, 151.77, 151.73, 151.67, 151.64, 151.56, 151.50, 151.45, 151.28, 151.18, 151.10, 151.08, 151.01, 150.98, 150.95, 150.86, 150.78, 150.64, 150.49, 150.46, 150.31, 150.29, 150.26, 150.19, 150.13, 150.10, 150.08, 150.02, 149.95, 149.82, 149.72, 149.65, 149.63, 149.62, 149.60, 149.52, 149.47, 149.44, 149.41, 149.37, 149.33, 149.30, 149.26, 149.20, 149.17, 149.09, 149.03, 148.74, 148.68, 148.43, 148.41, 148.38, 148.33, 148.17, 148.06, 147.93, 147.85, 147.81, 147.79, 147.73, 147.60, 147.55, 147.51, 147.48, 147.43, 147.41, 147.38, 147.30, 147.27, 147.22, 147.18, 147.14, 147.05, 147.01, 146.95, 146.92, 146.88, 146.84, 146.81, 146.69, 146.64, 146.60, 146.58, 146.56, 146.54, 146.31, 146.22, 146.18, 146.16, 146.08, 145.93, 145.79, 145.75, 145.74, 145.72, 145.71, 145.33, 144.99, 144.95, 144.73, 144.64, 144.33, 144.31, 143.92, 143.89, 143.82, 143.80, 143.68, 143.66, 143.65, 143.59, 143.58, 143.45, 143.29, 143.26, 143.23, 143.22, 143.14, 143.13, 142.42, 142.38, 142.04, 141.96, 141.49, 141.41, 141.31, 141.10, 141.03, 140.97, 140.86, 140.71, 140.65, 140.53, 138.43, 138.08, 137.91, 137.73, 134.23, 134.21, 134.15, 134.00, 133.90, 133.36, 132.71, 132.69, 132.46, 132.40, 132.04, 132.02, 131.95, 131.88, 131.69, 131.62, 131.58, 131.49, 131.10, 130.92, 130.83, 130.75, 130.64, 130.35, 130.22, 130.14, 130.00, 129.58, 127.13, 127.06, 126.02, 83.23, 82.85, 82.24, 80.09, 71.07, 70.53, 70.17, 69.05, 68.52, 66.90, 66.68, 66.59, 62.52, 60.79, 59.19, 58.83, 52.19, 52.11, 52.04, 52.00, 39.80, 39.79, 39.76, 39.72. (Figures 2.13, 2.14 and 2.15)

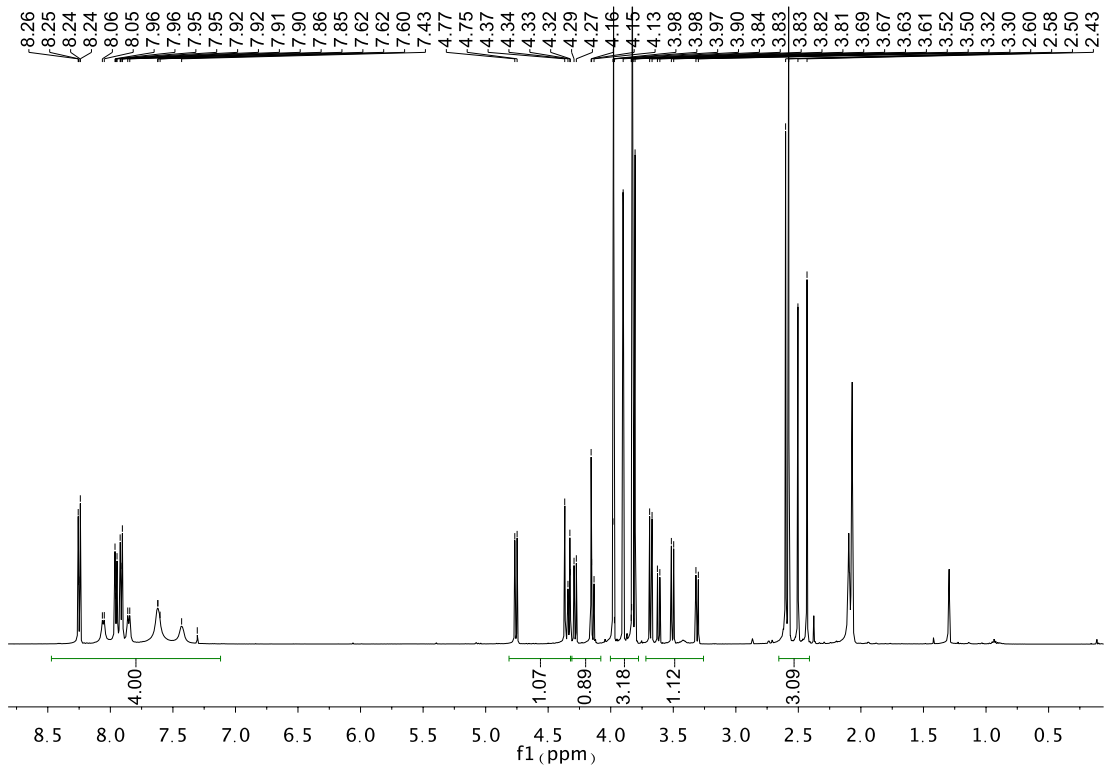

Figure 2. 21. ^{1}H NMR spectra of compound **70b** in a mixture of CS_2 and acetone-d6.

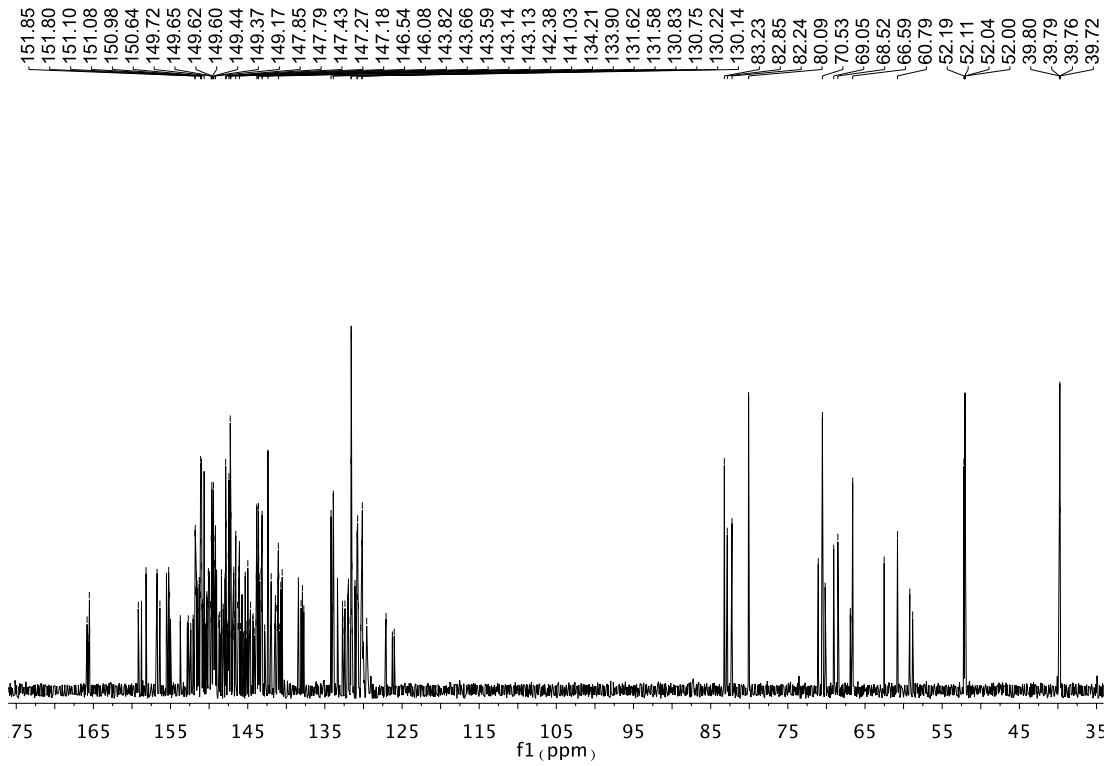

Figure 2. 22. ^{13}C NMR spectra of compound **70b** in a mixture of CS_2 and acetone-d6.

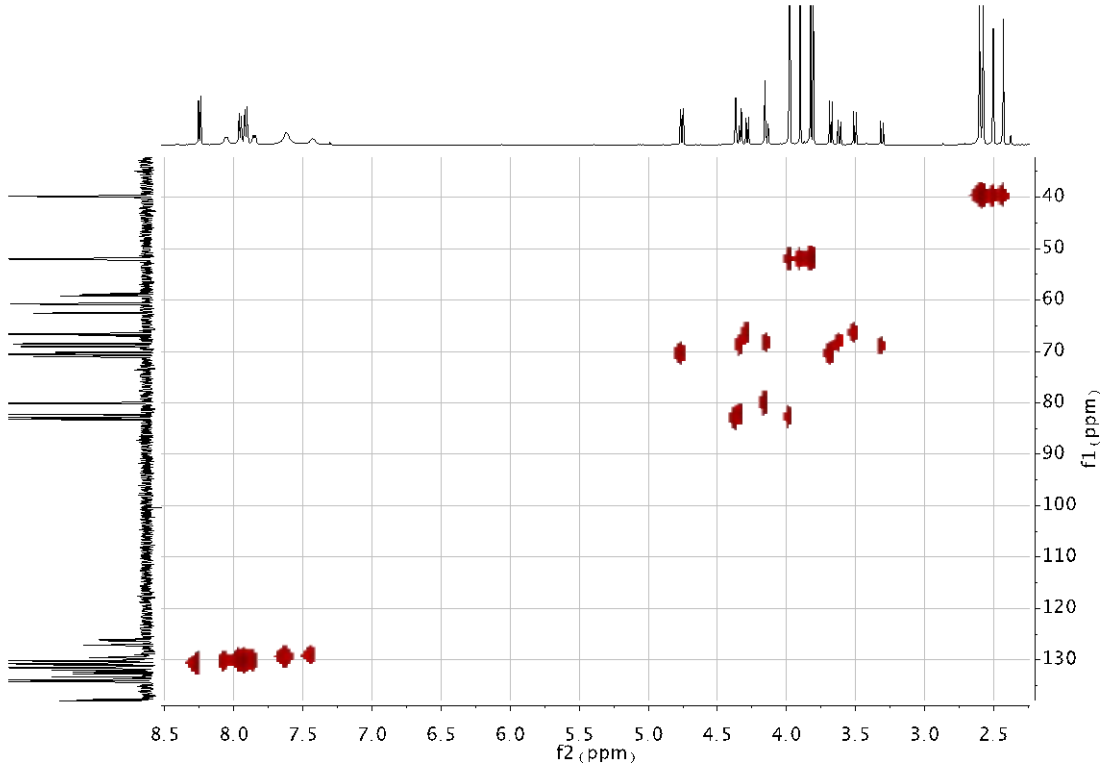

Figure 2. 23. HSQC spectra of compound **70b** in a mixture of CS_2 and acetone-d6.

70c: ^{1}H NMR (500 MHz, CS_2 + Acetone-d_6): δ 7.78 – 6.64 (m, 4H), 4.78 – 4.22 (m, 1H), 4.23 – 3.99 (m, 1H), 3.99 – 3.69 (m, 3H), 3.65 – 3.17 (m, 1H), 2.60 – 2.35 (m, 3H); ^{13}C NMR (126 MHz, CS_2 + Acetone-d6): δ 160.41, 160.24, 160.11, 159.95, 159.60, 159.28, 159.07, 157.08, 156.71, 156.65, 155.78, 155.53, 154.10, 154.07, 153.55, 153.31, 152.75, 152.19, 152.01, 151.95, 151.93, 151.84, 151.81, 151.78, 151.66, 151.56, 151.37, 151.26, 151.18, 151.15, 151.03, 150.78, 150.76, 150.54, 150.43, 150.37, 150.31, 150.23, 150.15, 150.08, 149.92, 149.90, 149.86, 149.80, 149.75, 149.63, 149.60, 149.57, 149.53, 149.50, 149.43, 149.33, 149.24, 149.18, 148.82, 148.78, 148.55, 148.51, 148.44, 148.21, 148.07, 148.03, 148.00, 147.95, 147.83, 147.79, 147.68, 147.64, 147.60, 147.58, 147.54, 147.44, 147.38, 147.35, 147.31, 147.22, 147.16, 147.10, 147.07, 146.86, 146.79, 146.76, 146.69, 146.62, 146.38, 146.34, 146.29, 146.26, 146.21, 146.15, 145.83, 145.68, 145.65, 145.47, 145.17, 144.91, 144.78, 144.38, 144.03, 143.96, 143.94, 143.88, 143.82, 143.74, 143.70, 143.66, 143.58, 143.42, 143.33, 143.21, 143.18, 143.09, 142.53, 142.42, 142.20, 141.67, 141.47, 141.44, 141.38, 141.23, 141.06, 141.00, 140.82, 140.78, 138.35, 138.31, 137.98, 137.83, 134.35, 134.14, 134.06, 133.66, 132.85, 132.53, 132.16, 132.14, 132.05, 131.93, 131.73, 131.68, 131.63, 131.26, 130.92, 130.00, 129.26, 128.83, 128.80, 126.30, 126.25, 114.99, 114.46, 87.54, 83.31, 83.05, 82.42,

80.22, 73.64, 71.61, 70.65, 70.56, 69.04, 68.50, 67.01, 66.59, 62.56, 60.81, 59.22, 58.82, 55.47, 55.36, 55.26, 55.22, 40.07, 39.76, 39.72, 39.69, 39.66. (Figures 2.16, 2.17 and 2.18)

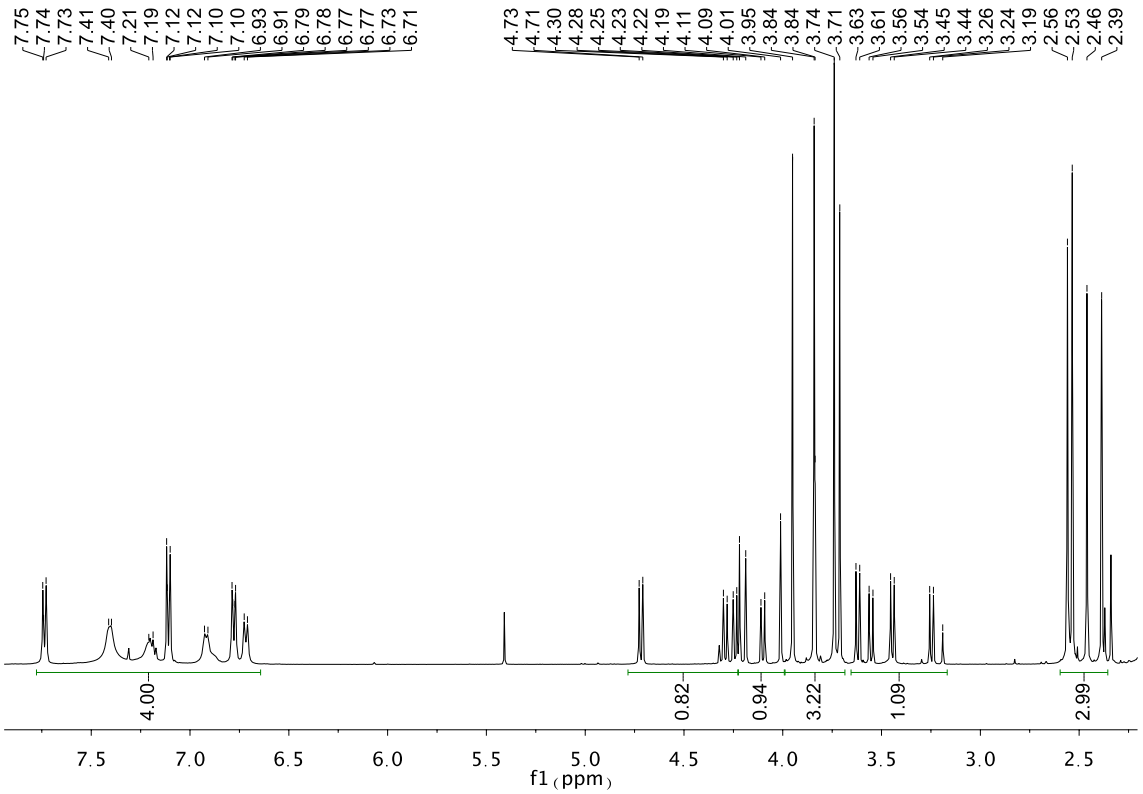

Figure 2. 24. ^{1}H NMR spectra of compound **70c** in a mixture of CS_2 and acetone-d6.

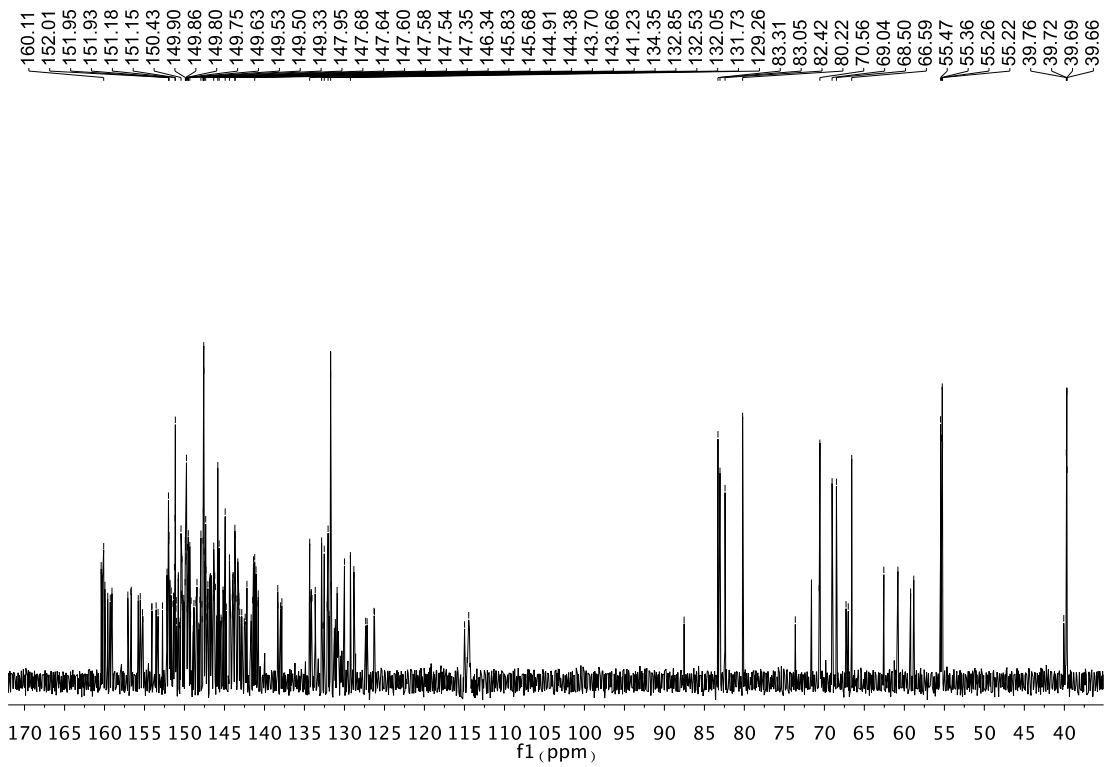

Figure 2. 25. ^{13}C NMR spectra of compound **70c** in a mixture of CS_2 and acetone-d6.

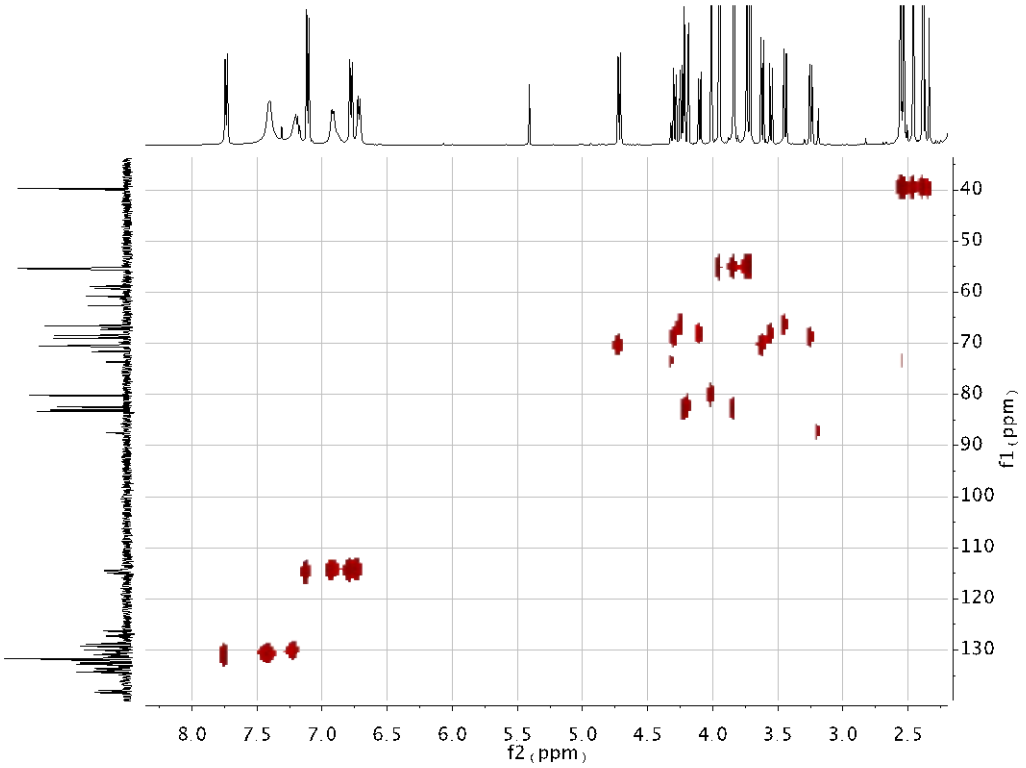

Figure 2. 26. HSQC spectra of compound **70c** in a mixture of CS_2 and acetone-d6.

60d: ^{1}H NMR (300 MHz, CS_2 + Chloroform-d): δ 5.48 (s, 1H), 5.02 (d, *J* = 9.39 Hz, 1H), 4.23 (dd, *J* = 9.46, 3.109 Hz, 1H), 2.89 (d, *J* = 2.439 Hz, 3H); ^{13}C NMR (126 MHz, CS_2 + Chloroform-d): δ 156.69, 154.29, 153.24, 152.14, 148.01, 147.97, 147.01, 146.98, 146.90, 146.87, 146.77, 146.75, 146.64, 146.47, 146.40, 146.33, 146.29, 146.23, 146.20, 146.14, 146.03, 145.94, 145.88, 145.43, 145.17, 143.78, 143.72, 143.38, 143.29, 143.27, 142.96, 142.88, 142.79, 142.67, 142.63, 142.58, 142.39, 142.33, 140.92, 140.81, 140.27, 137.25, 136.71, 136.33, 76.50, 75.22, 70.20, 70.01, 54.87, 40.23. (Figures 2.19, 2.20 and 2.21)

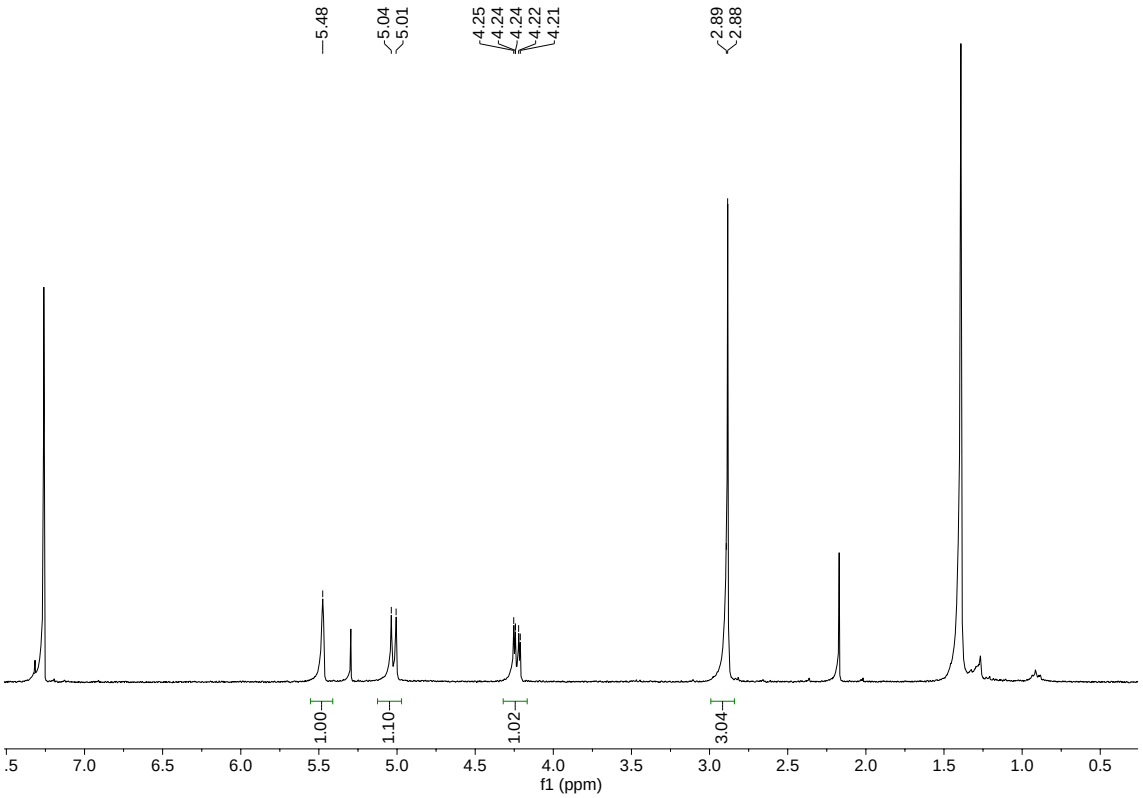

Figure 2. 27. ^{1}H NMR spectra of compound **60d** in a mixture of CS_2 and acetone-d6.

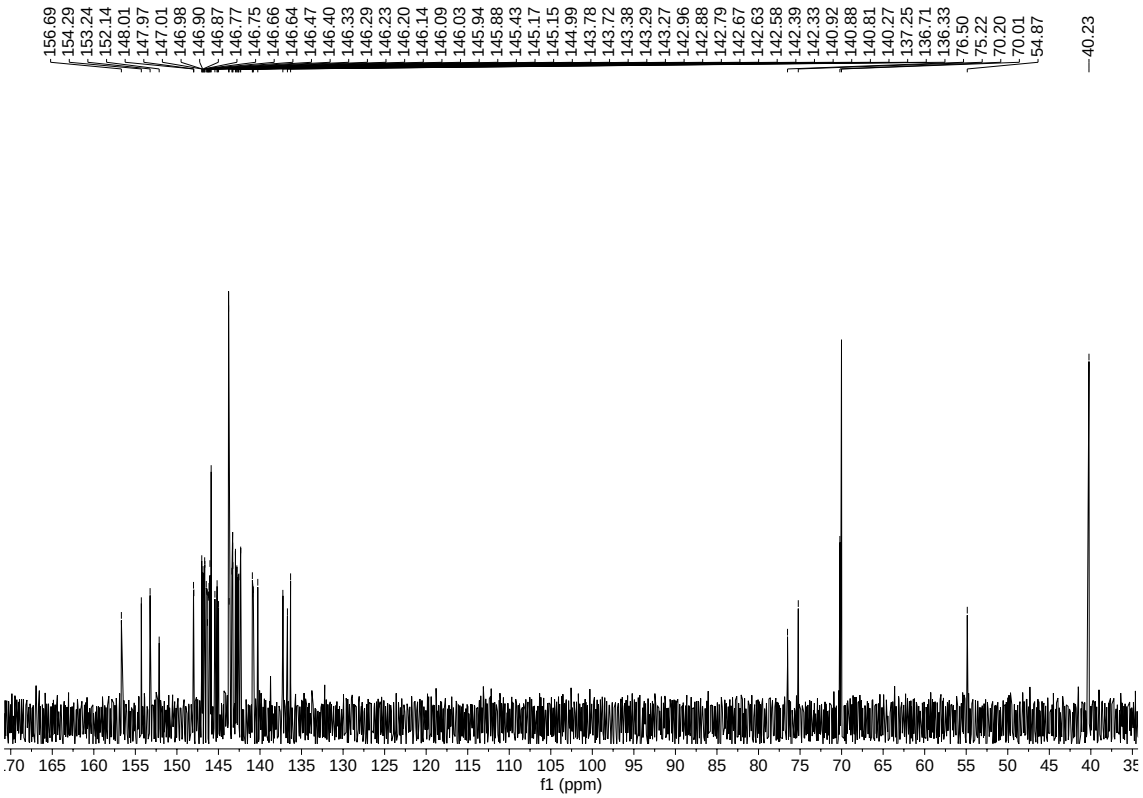

Figure 2. 28. ^{13}C NMR spectra of compound **60d** in a mixture of CS_2 and acetone-d6.

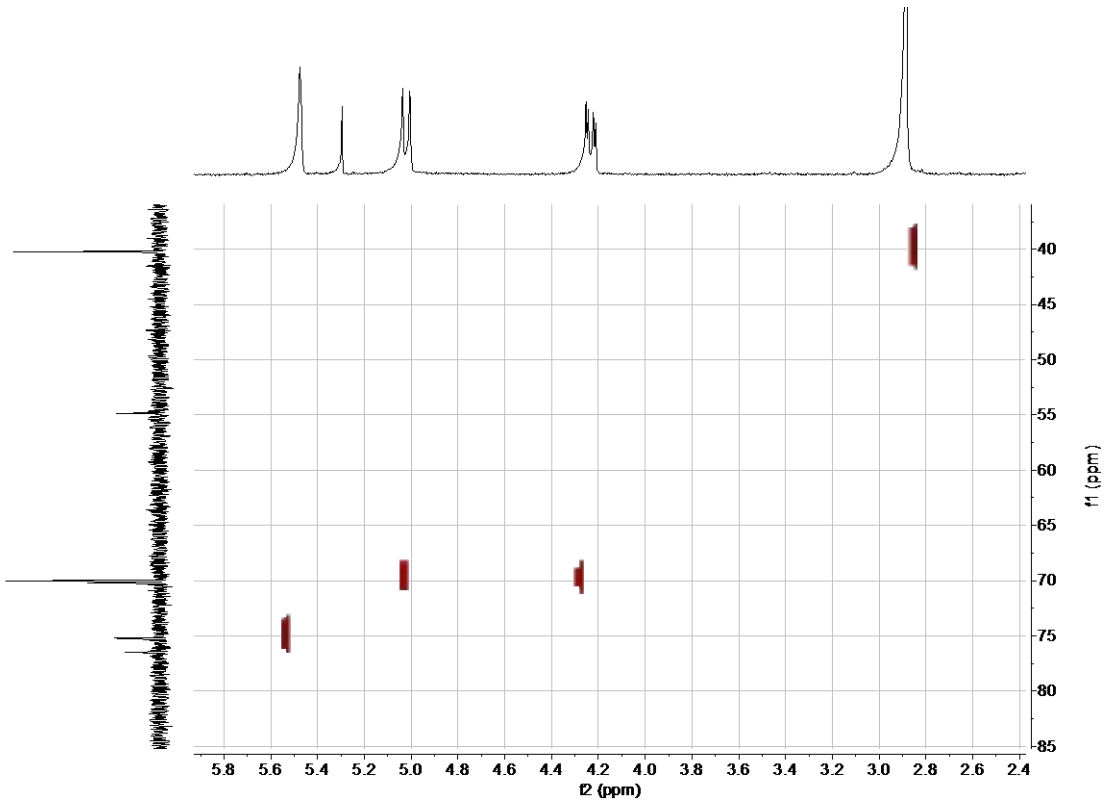

Figure 2. 29. HSQC spectra of compound **60d** in a mixture of CS_2 and acetone-d6.

70d: ^{1}H NMR (500 MHz, Chloroform-*d*): δ 4.79 – 4.48 (m, 1H), 4.38 – 3.67 (m, 1H), 3.58 – 3.09 (m, 1H), 2.65 – 2.38 (m, 3H); ^{13}C NMR (126 MHz, Chloroform-*d*): δ 158.58, 158.24, 157.32, 156.32, 155.23, 155.20, 154.91, 154.81, 153.54, 153.23, 153.12, 152.24, 151.88, 151.63, 151.53, 151.51, 151.49, 151.32, 151.21, 151.16, 151.00, 150.94, 150.86, 150.83, 150.76, 150.44, 150.39, 150.03, 149.98, 149.68, 149.62, 149.57, 149.50, 149.48, 149.47, 149.34, 149.27, 149.17, 148.93, 148.79, 148.41, 148.20, 147.75, 147.58, 147.53, 147.50, 147.45, 147.35, 147.27, 147.21, 147.18, 147.15, 147.10, 147.00, 146.85, 146.80, 146.75, 146.67, 146.37, 146.32, 146.25, 146.13, 146.09, 145.94, 145.90, 145.80, 145.54, 145.37, 145.05, 144.84, 144.58, 144.51, 144.10, 143.61, 143.53, 143.44, 143.39, 143.21, 143.05, 143.00, 142.97, 142.88, 142.14, 141.69, 141.01, 140.69, 140.56, 140.37, 140.31, 140.14, 140.03, 139.29, 137.61, 137.45, 137.21, 134.02, 133.82, 133.76, 133.71, 133.36, 132.25, 132.15, 131.77, 131.60, 131.42, 131.34, 74.88, 71.71, 69.83, 69.64, 68.88, 68.60, 67.99, 65.89, 65.75, 65.55, 62.53, 60.88, 58.80, 39.82. (Figures 2.22, 2.23 and 2.24)

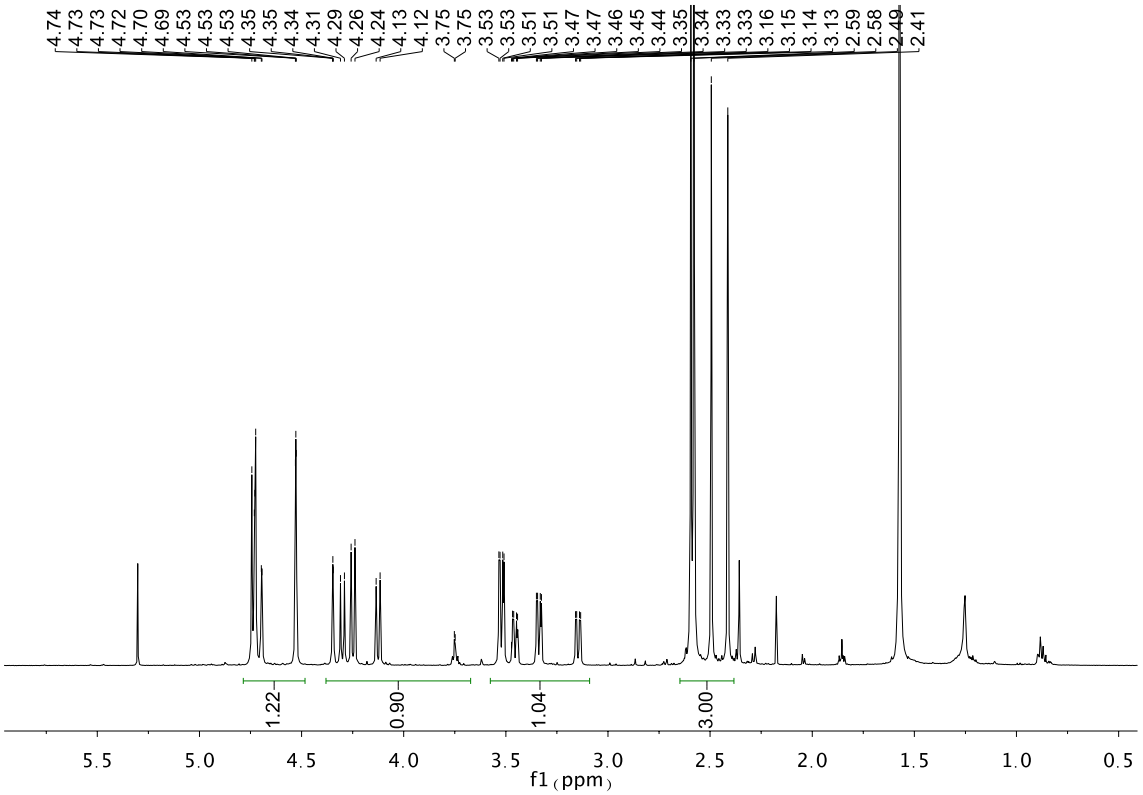

Figure 2. 30. ^{1}H NMR spectra of compound **70d** in a mixture of CS_2 and acetone-d6.

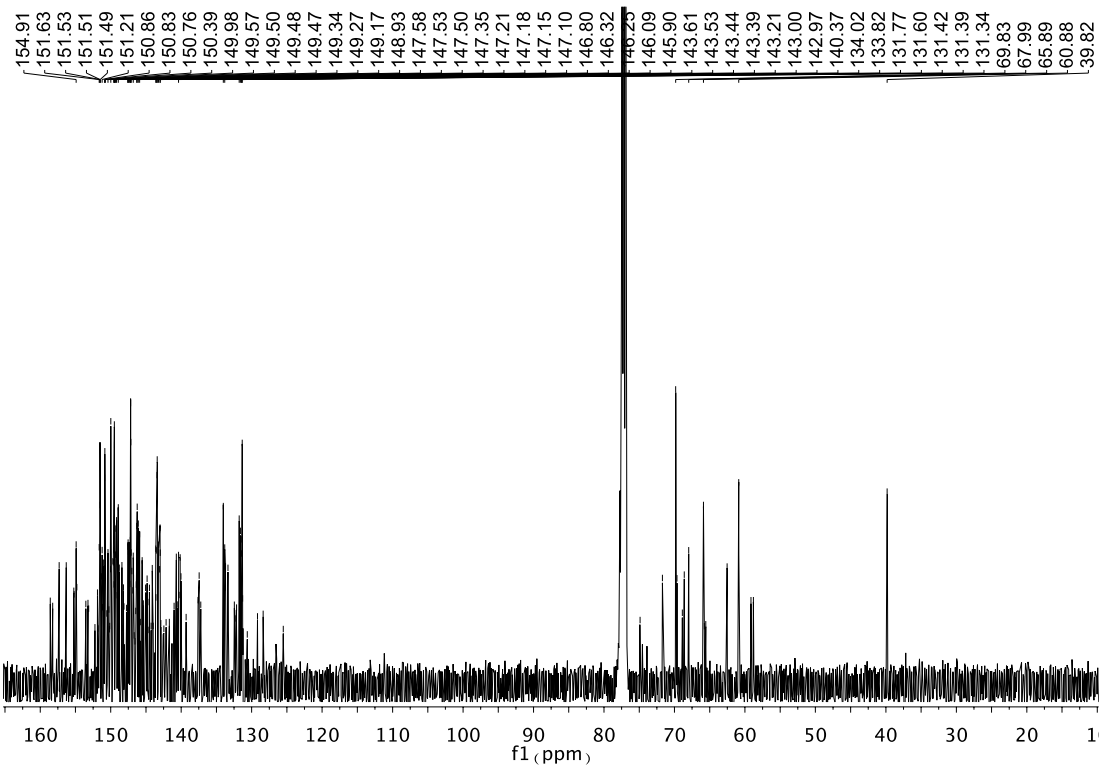

Figure 2. 31. ^{13}C NMR spectra of compound **70d** in a mixture of CS_2 and acetone-d6.

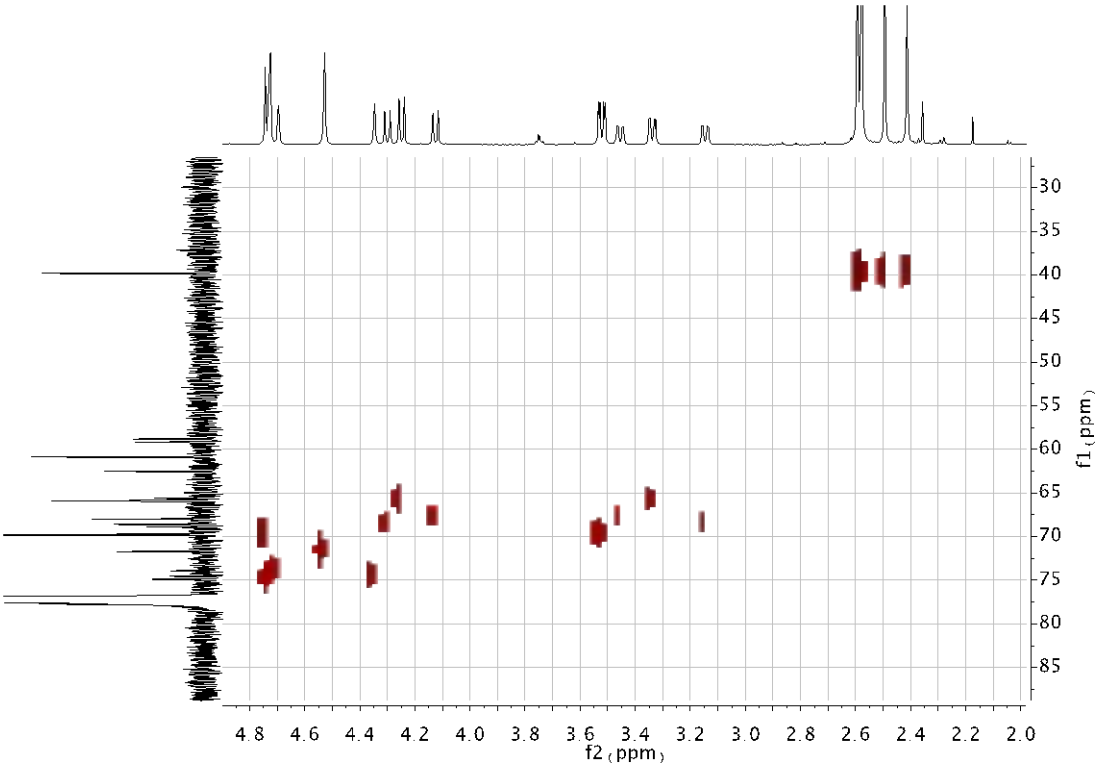

Figure 2. 32. HSQC spectra of compound **70d** in a mixture of CS_2 and acetone-d6.

Appendix II

60B: ^{1}H NMR (500 MHz, CS2 + Acetone-d6) δ 7.22 (d, J = 3.5 Hz, 1H), 6.80 – 6.63 (m, 1H), 5.27 (s, 1H), 5.02 (d, J = 9.5 Hz, 1H), 4.31 (d, J = 9.6 Hz, 1H), 2.93 (s, 3H), 2.55 (s, 3H); ^{13}C NMR (126 MHz, CS2 + Acetone-d6) δ 156.86, 154.73, 154.24, 154.08, 147.80, 147.61, 147.21, 147.02, 146.85, 146.80, 146.73, 146.69, 146.62, 146.59, 146.45, 146.36, 146.11, 146.09, 145.89, 145.84, 145.78, 145.66, 145.26, 145.23, 144.92, 143.67, 143.52, 143.22, 143.14, 143.12, 142.83, 142.79, 142.73, 142.69, 142.60, 142.52, 142.44, 142.23, 142.18, 141.52, 140.69, 140.45, 140.20, 138.77, 137.60, 137.25, 136.44, 136.27, 128.75, 125.55, 79.84, 77.72, 70.24, 69.31, 40.54. (Figures 3.4, 3.5 and 3.6)

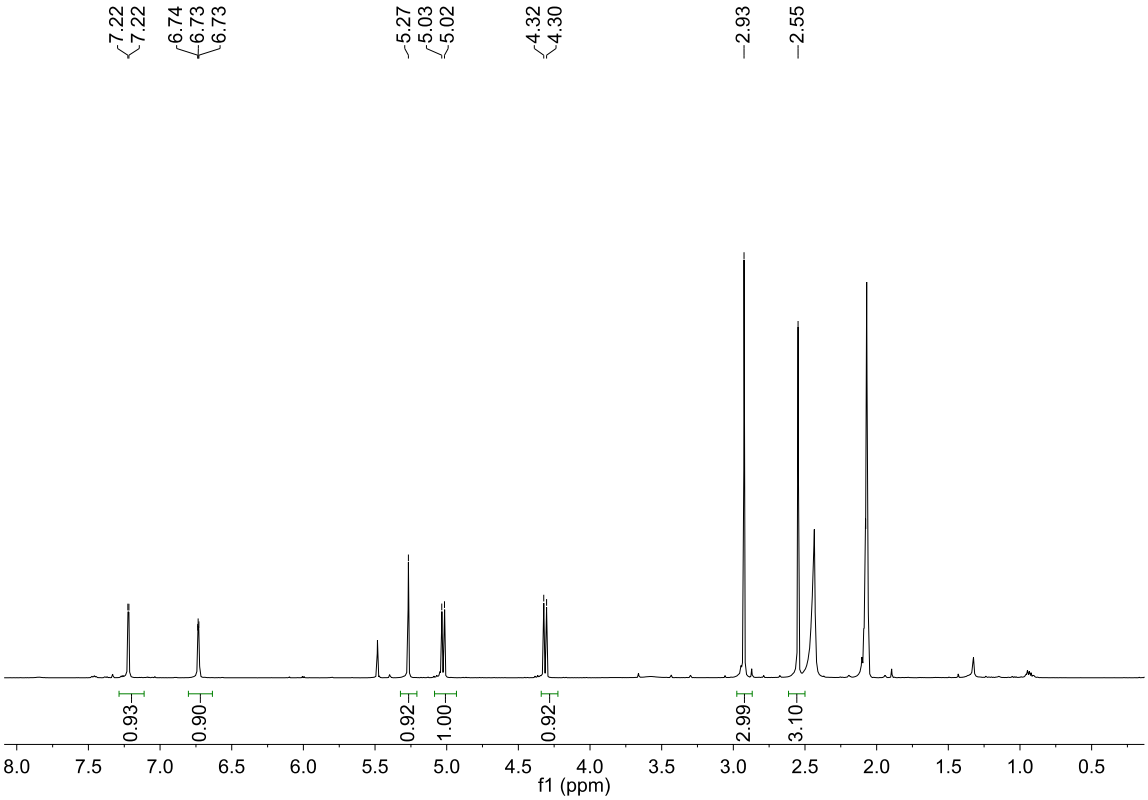

Figure 3. 11. ^{1}H NMR spectrum of compound **60B** in a mixture of CS_2 and acetone-d6.

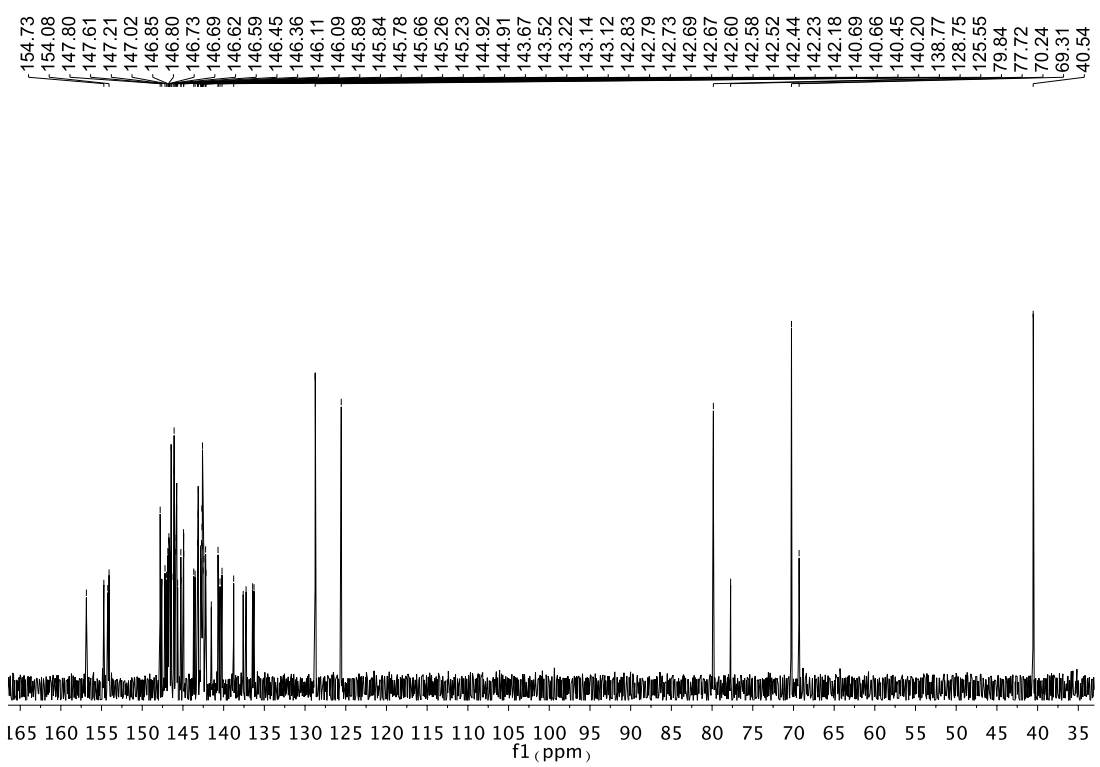

Figure 3. 12. ^{13}C NMR spectrum of compound **60B** in a mixture of CS_2 and acetone-d6

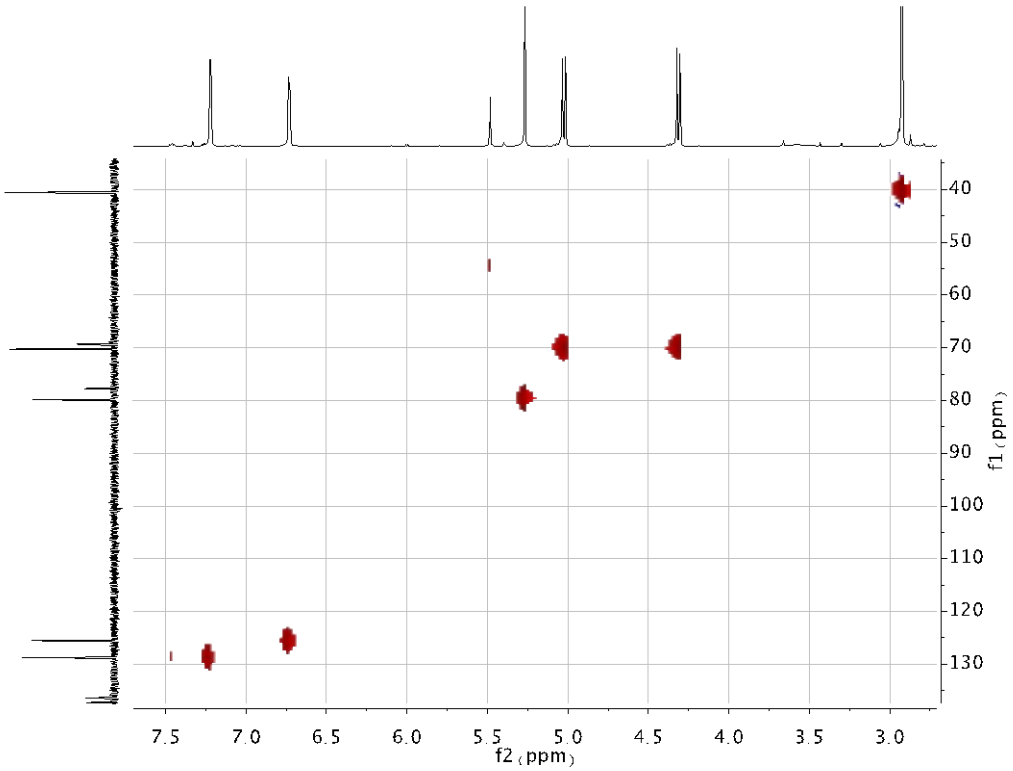

Figure 3. 13. HSQC spectrum of compound **60B** in a mixture of CS_2 and acetone-d6.

60C: ^{1}H NMR (300 MHz, CS2 + Acetone-d6) δ 7.84 (dd, J = 4.3, 1.2 Hz, 1H), 7.43 (dd, J = 4.3, 1.1 Hz, 1H), 5.35 (d, J = 2.3 Hz, 1H), 5.05 (d, J = 9.8 Hz, 1H), 4.37 (dd, J = 9.8, 1.0 Hz, 1H), 3.01 (d, J = 1.0 Hz, 3H); ^{13}C NMR (75 MHz, Acetone-d6) δ 150.53, 146.99, 143.28, 129.61, 128.88, 128.88, 128.29, 125.97, 117.32, 109.61, 79.11, 70.38, 40.67. (Figures 3.7, 3.8 and 3.9)

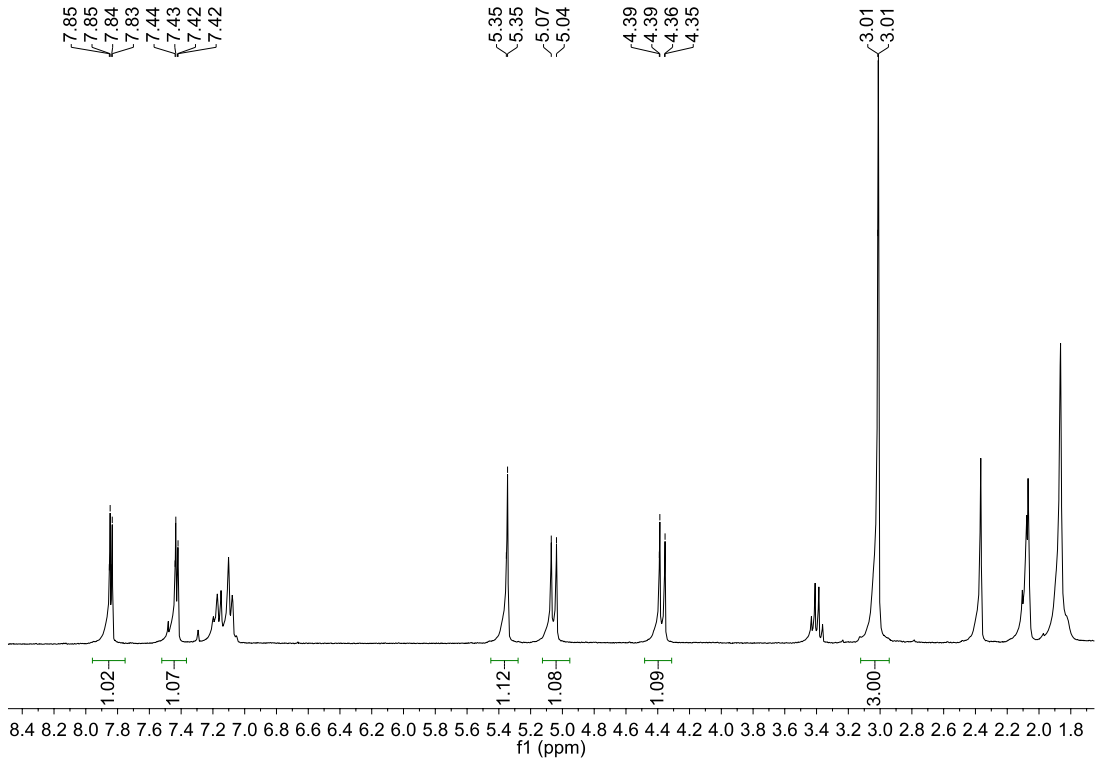

Figure 3. 14. ^{1}H NMR spectrum of compound **60C** in a mixture of CS_2 and acetone-d6.

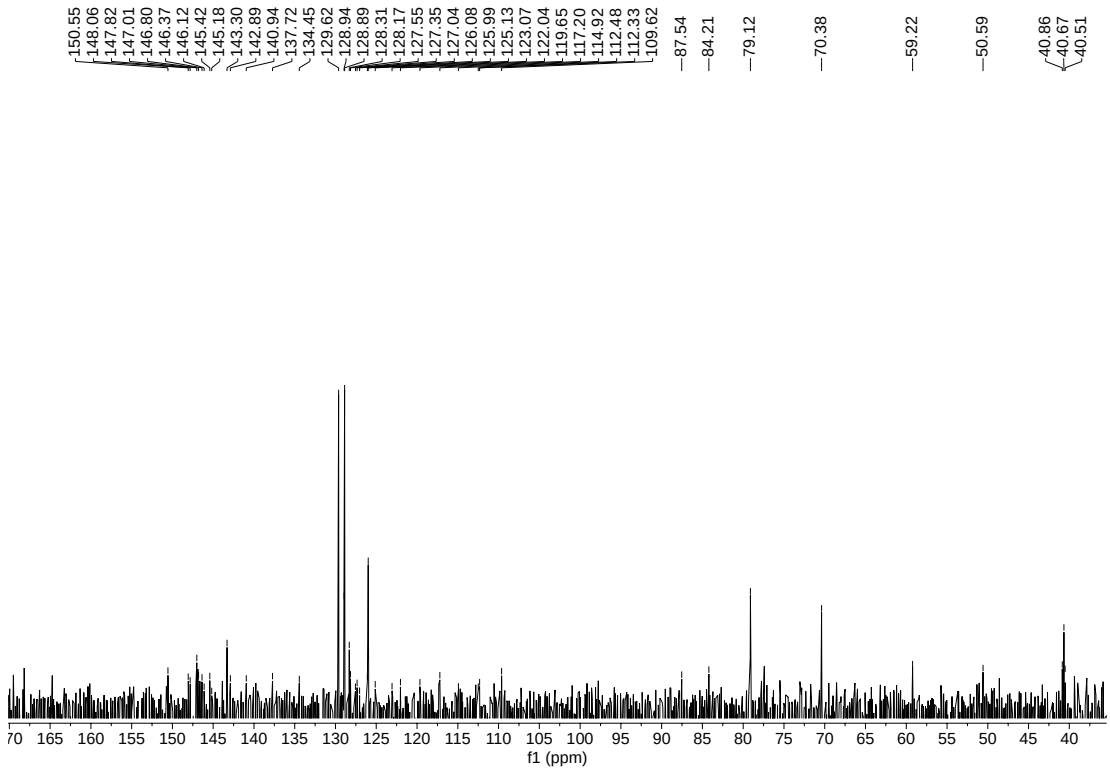

Figure 3. 15. ^{13}C NMR spectrum of compound **60C** in a mixture of CS_2 and acetone-d6.

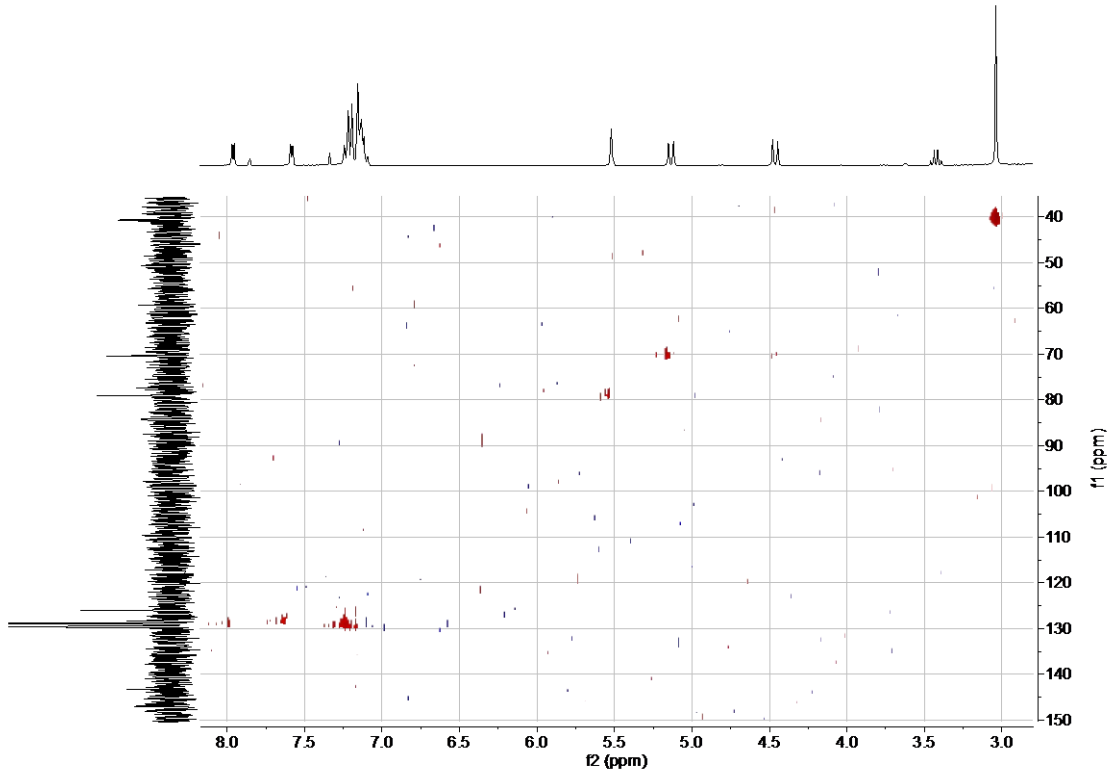

Figure 3. 16. HSQC spectrum of compound **60C** in a mixture of CS_2 and acetone-d6.

60D: ^{1}H NMR (300 MHz, CS2 + Chloroform) δ 7.47 – 7.26 (m, 3H), 7.19 – 7.03 (m, 3H), 5.20 – 4.91 (m, 2H), 4.44 – 4.24 (m, 3H), 2.83 (s, 3H), 1.46 (t, J = 7.1 Hz, 3H). (Figures 3.10, 3.11 and 3.12)

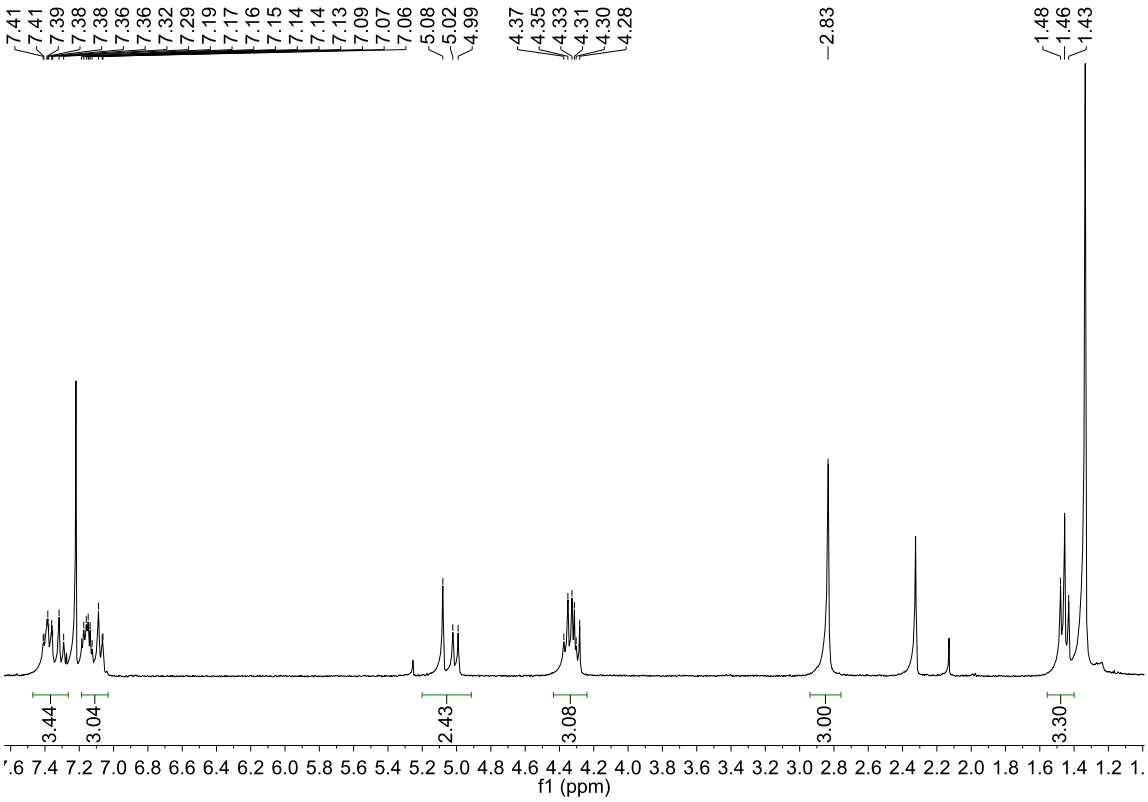

Figure 3. 17. ^{1}H NMR spectrum of compound **60D** in a mixture of CS_2 and chloroform-d.

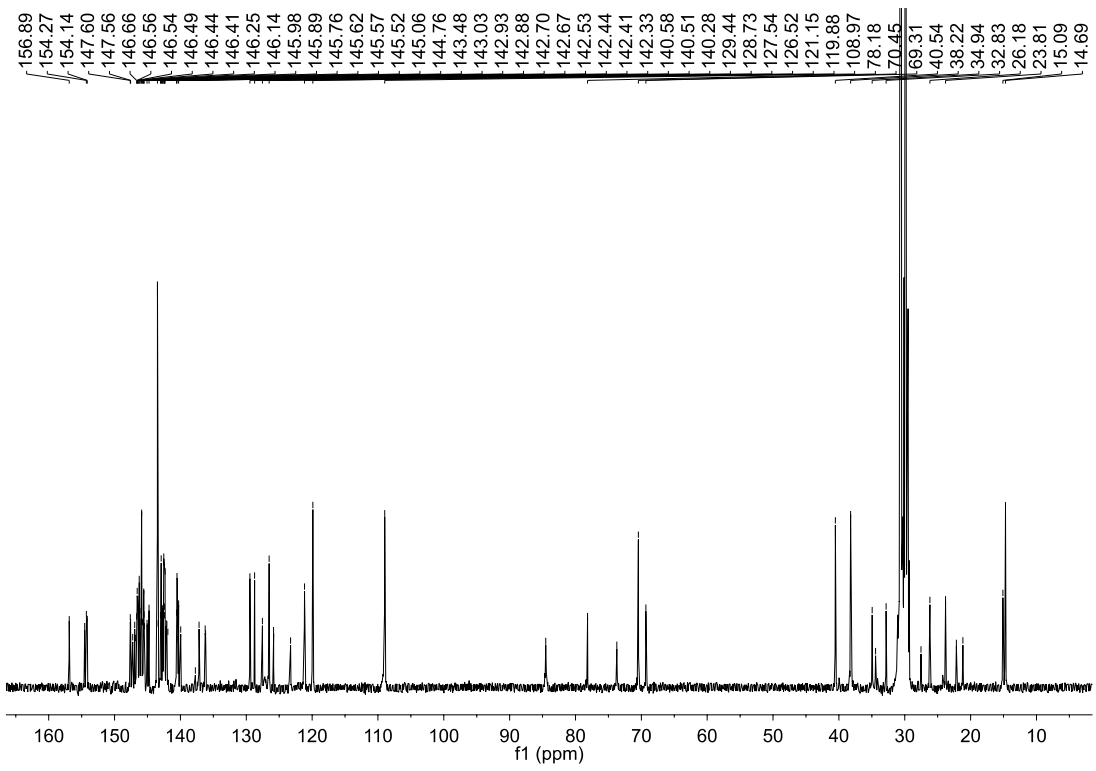

Figure 3. 18. ^{13}C NMR spectrum of compound **60D** in a mixture of CS_2 and chloroform-d.

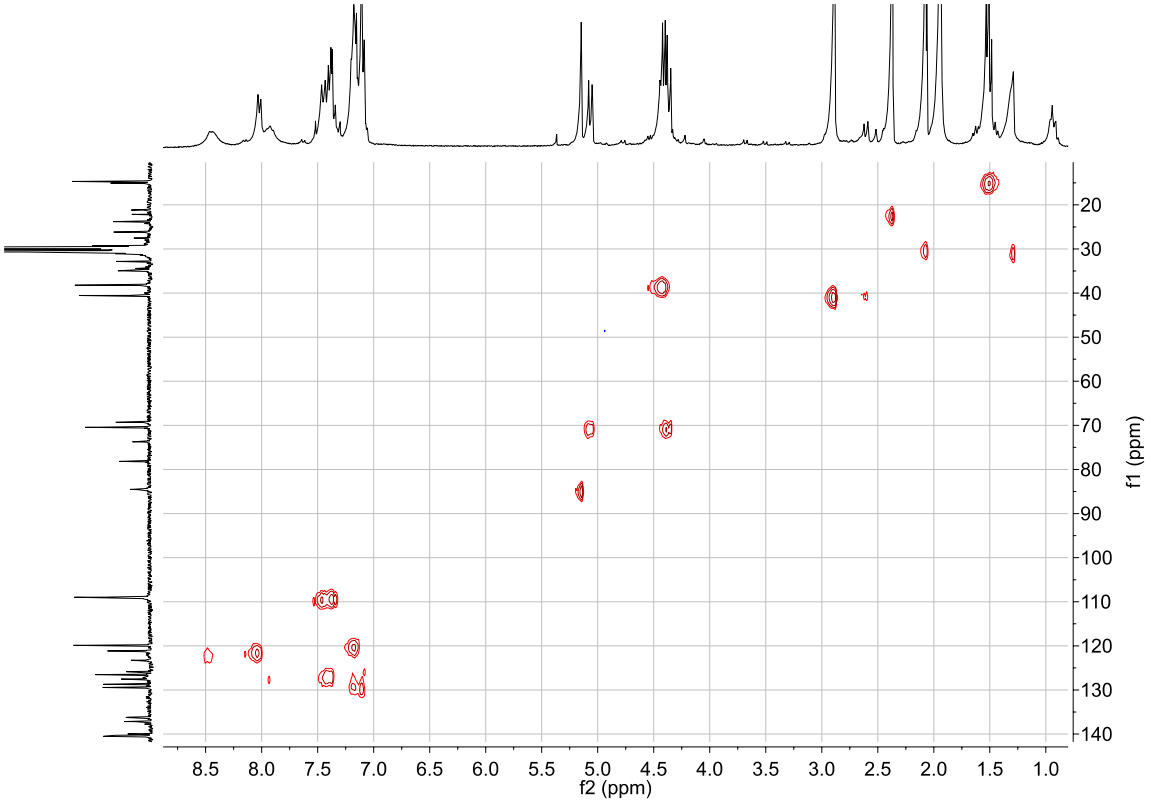

Figure 3. 19. HSQC spectrum of compound **60D** in a mixture of CS_2 and chloroform-d.

70A: ^{1}H NMR (300 MHz, Chloroform-d) δ 7.8 – 7.3 (m, 2H), 7.2 – 6.8 (m, 3H), 4.8 – 4.1 (m, 3H), 3.7 – 2.9 (m, 3H), 2.8 – 2.4 (m, 3H); ^{13}C NMR (126 MHz, Chloroform-d) δ 151.83, 151.37, 151.05, 150.77, 150.66, 150.34, 149.84, 149.41, 149.34, 149.09, 147.47, 147.42, 147.11, 147.06, 146.94, 146.18, 145.91, 145.44, 145.28, 143.33, 142.92, 140.48, 137.31, 133.86, 132.37, 131.66, 131.34, 131.25, 39.82, 34.15, 31.96, 26.75, 25.36, 22.73, 21.35, 14.16. (Figures 3.13, 3.14 and 3.15)

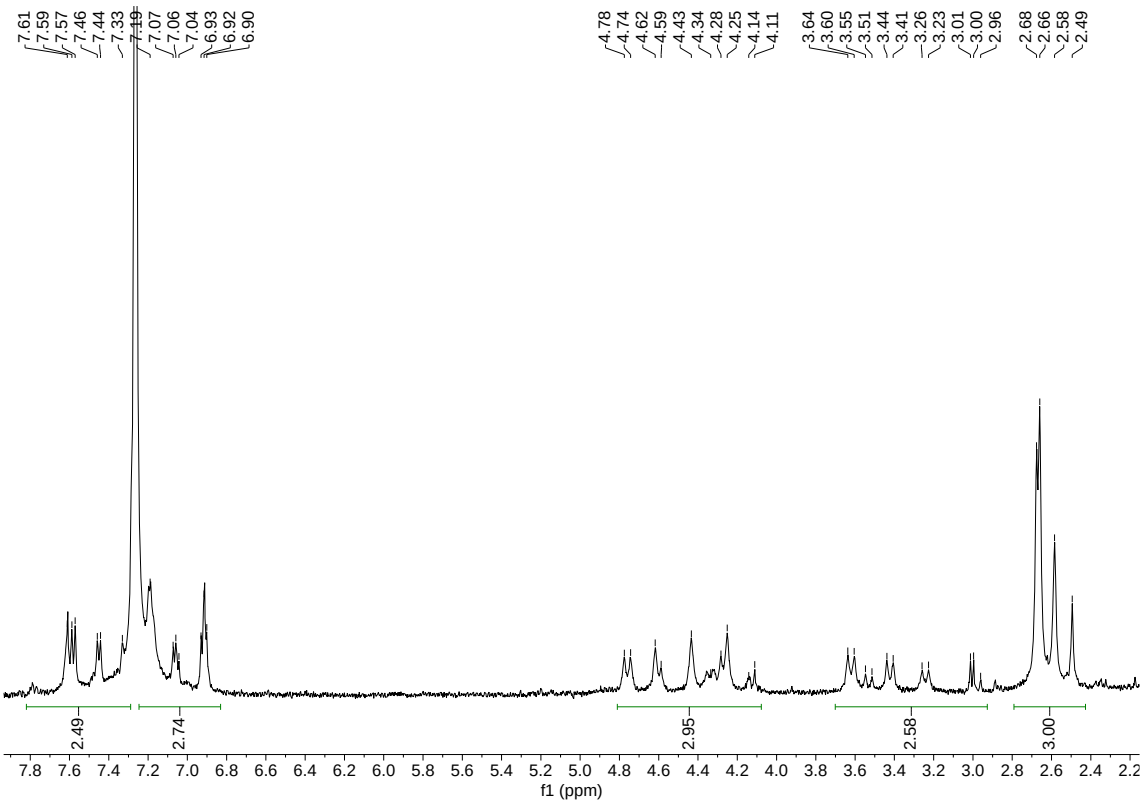

Figure 3. 20. [1]H NMR spectrum of compound **70A** in Choroform-d.

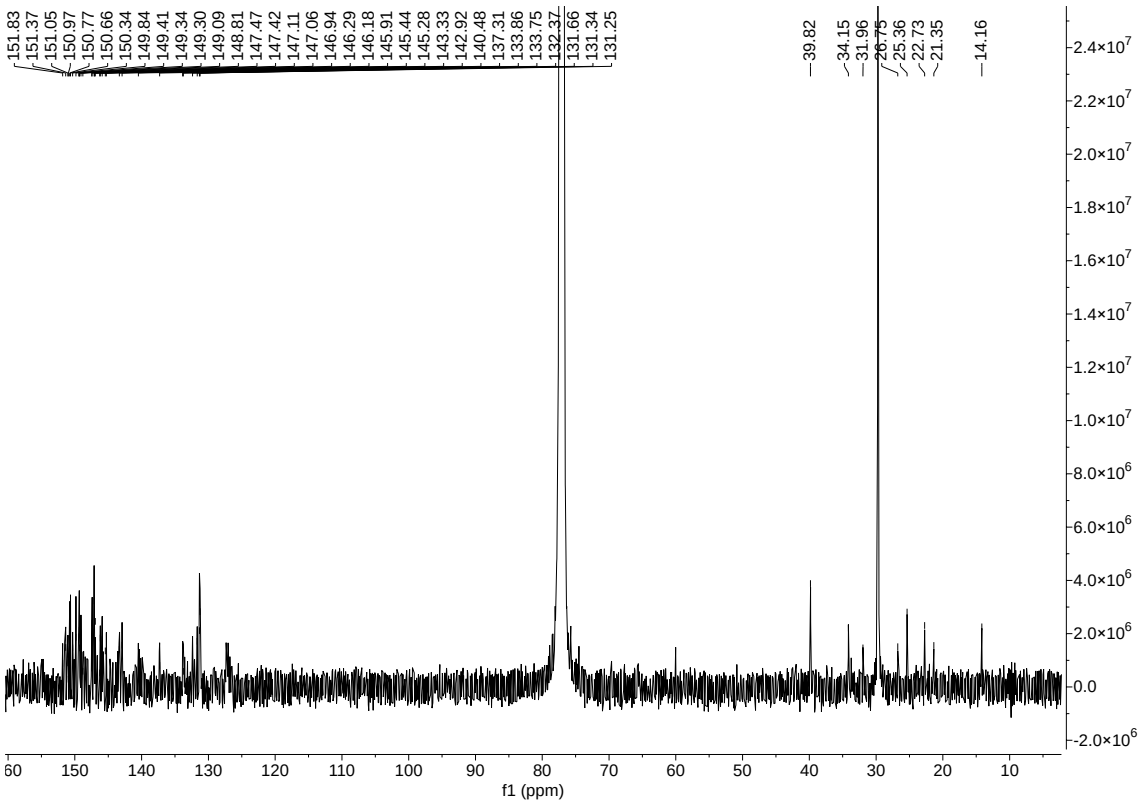

Figure 3. 21. [13]C NMR spectrum of compound **70A** in Choroform-d.

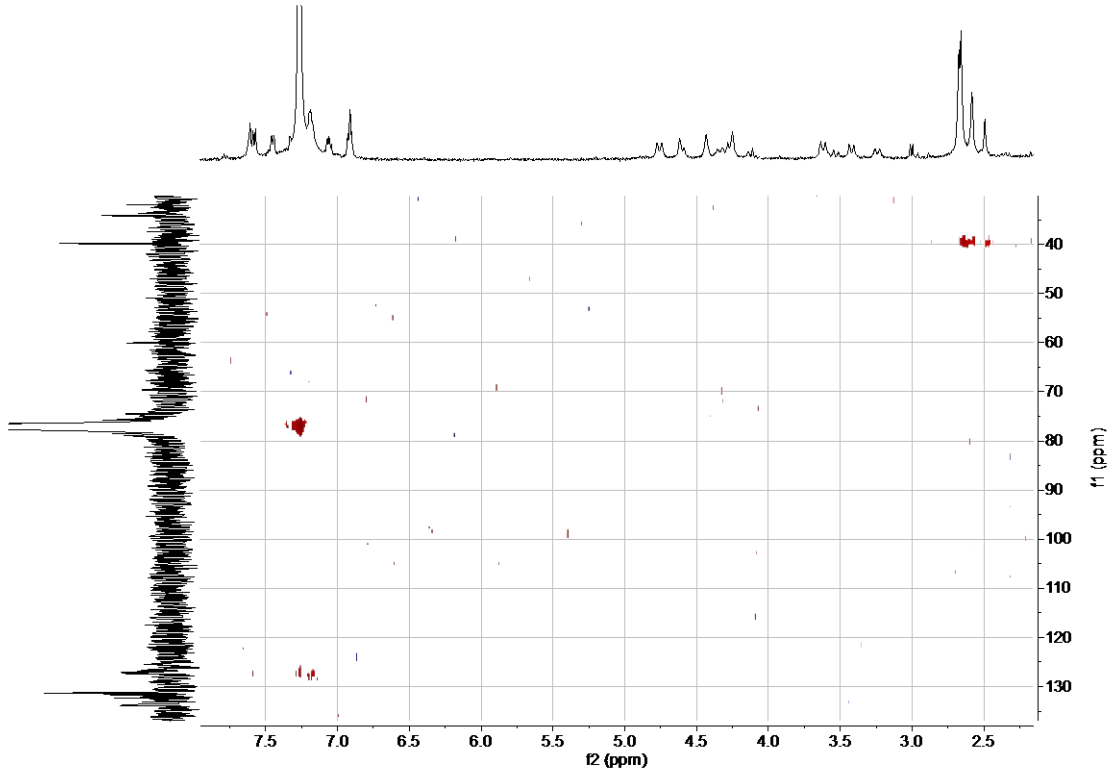

Figure 3. 22. HSQC spectrum of compound **70A** in Choroform-d.

70B: ^{1}H NMR (300 MHz, Chloroform-d) δ 7.02 – 6.42 (m, 1H), 4.82 – 3.97 (m, 2H), 3.79 – 3.03 (m, 1H), 2.75 – 2.24 (m, 6H); ^{13}C NMR (75 MHz, Chloroform-d) δ 165.39, 163.79, 160.74, 160.72, 159.36, 158.10, 156.70, 155.19, 151.75, 150.64, 149.30, 149.28, 146.95, 146.92, 144.62, 143.28, 143.21, 138.35, 137.33, 135.35, 133.84, 131.22, 130.11, 128.23, 126.90, 125.69, 124.42, 64.12, 60.09, 39.76, 29.72, 28.04, 15.81, 15.55. (Figures 3.16, 3.17 and 3.18)

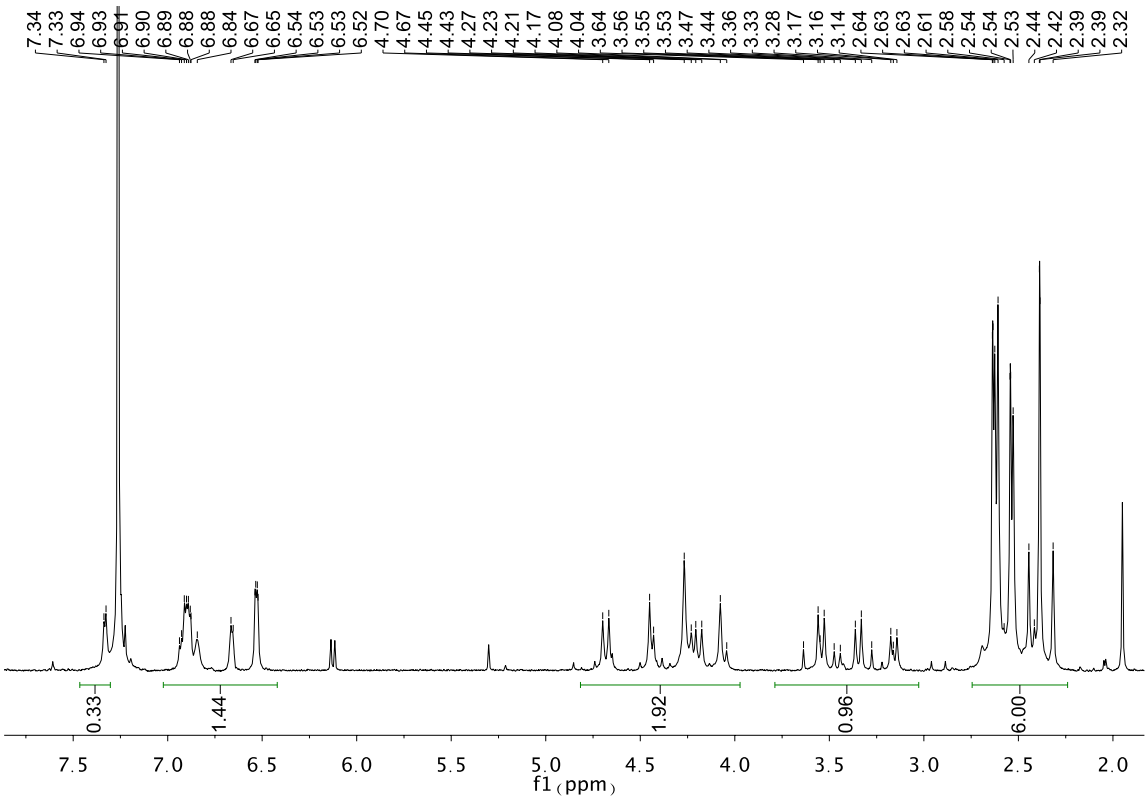

Figure 3. 23. ^{1}H NMR spectrum of compound **70B** in chloroform-d.

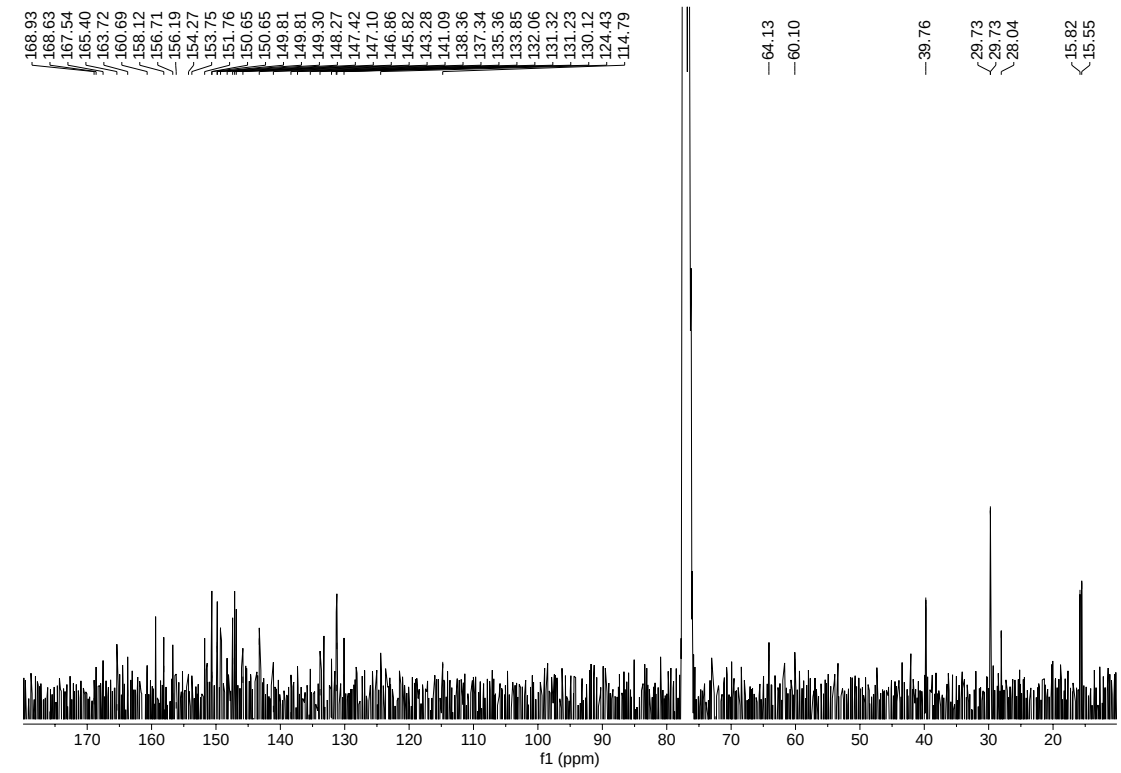

Figure 3. 24. ^{13}C NMR spectrum of compound **70B** in chloroform-d.

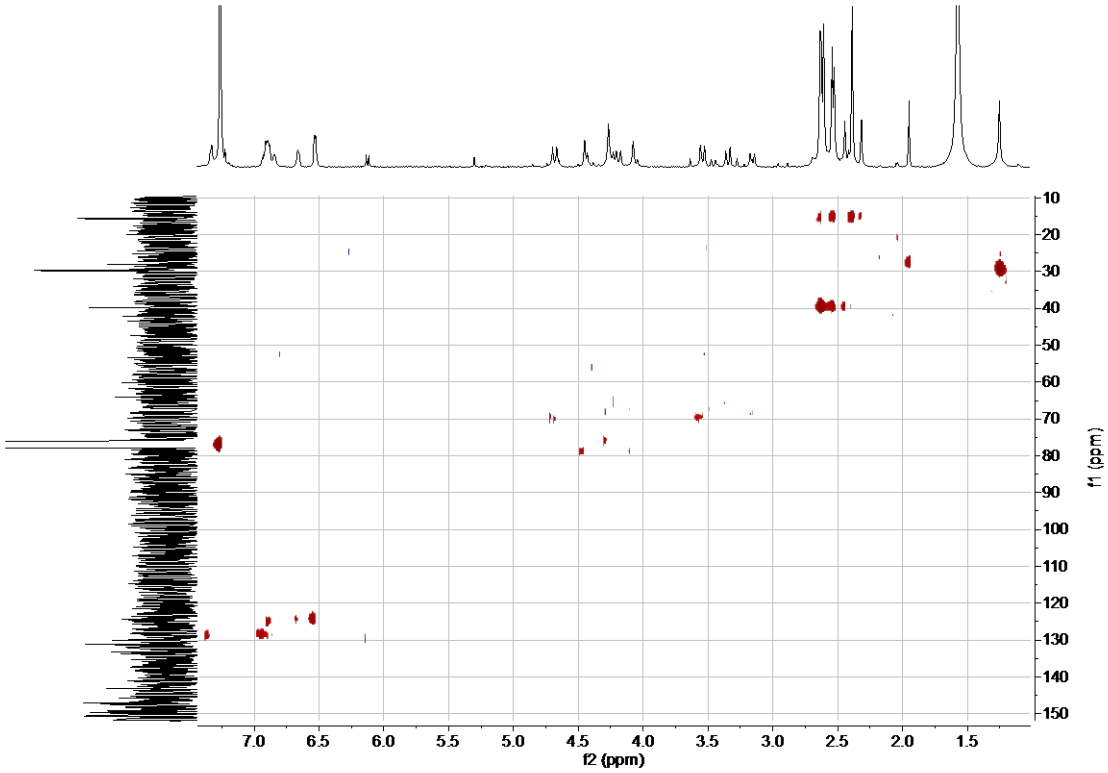

Figure 3. 25. HSQC spectrum of compound **70B** in chloroform-d.

70C: ^{1}H NMR (500 MHz, Chloroform-d) δ 8.19 – 7.42 (m, 1H), 7.19 – 6.99 (m, 1H), 4.83 – 4.41 (m, 1H), 4.34 – 3.99 (m, 1H), 3.67 – 3.14 (m, 1H), 2.73 – 2.43 (m, 3H); ^{13}C NMR (126 MHz, Chloroform-d) δ 157.01, 156.20, 154.26, 151.64, 151.48, 151.27, 150.86, 150.79, 150.74, 150.01, 149.92, 149.43, 149.27, 149.14, 148.97, 148.78, 148.06, 147.56, 147.21, 147.07, 146.09, 145.96, 143.58, 143.48, 143.39, 143.06, 140.63, 133.99, 133.70, 133.31, 131.81, 131.64, 131.36, 128.66, 127.94, 127.56, 127.32, 127.10, 126.79, 75.71, 70.60, 70.32, 68.93, 66.28, 61.90, 60.29, 53.59, 40.04. (Figures 3.19, 320 and 3.21)

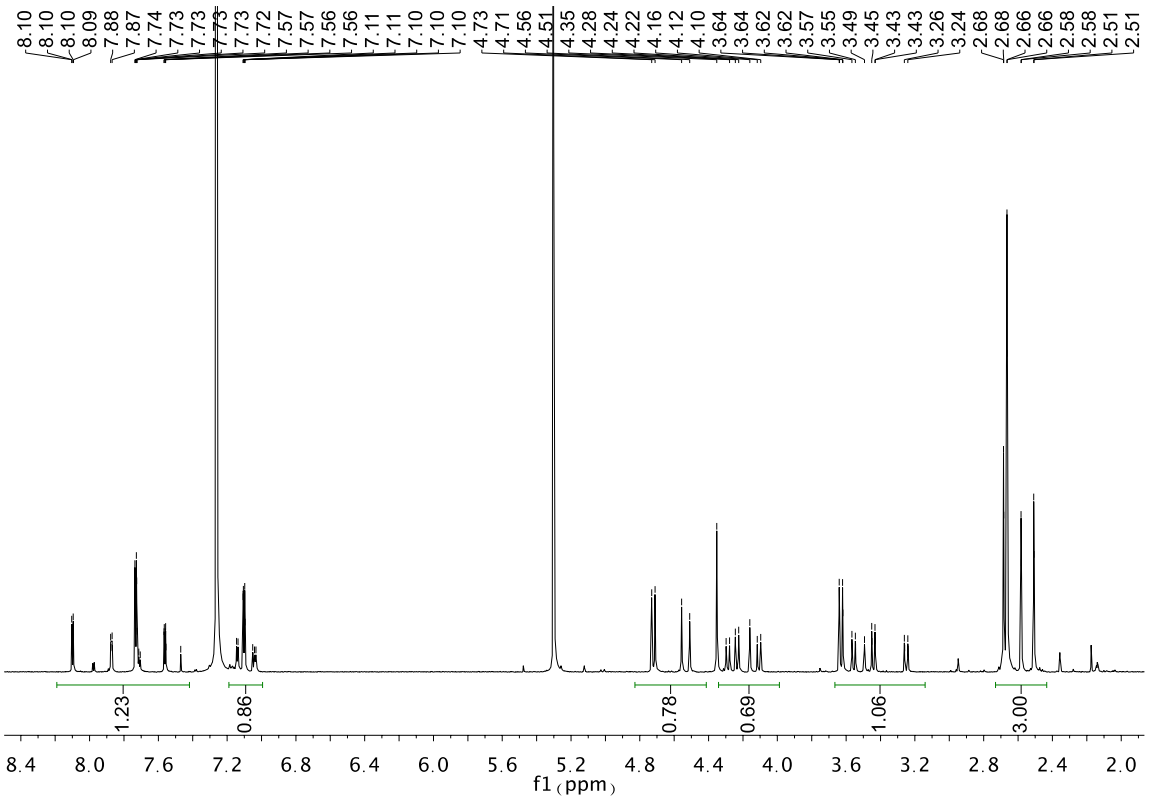

Figure 3. 26. ^{1}H NMR spectrum of compound **70C** in a mixture of CS_2 and chloroform-d.

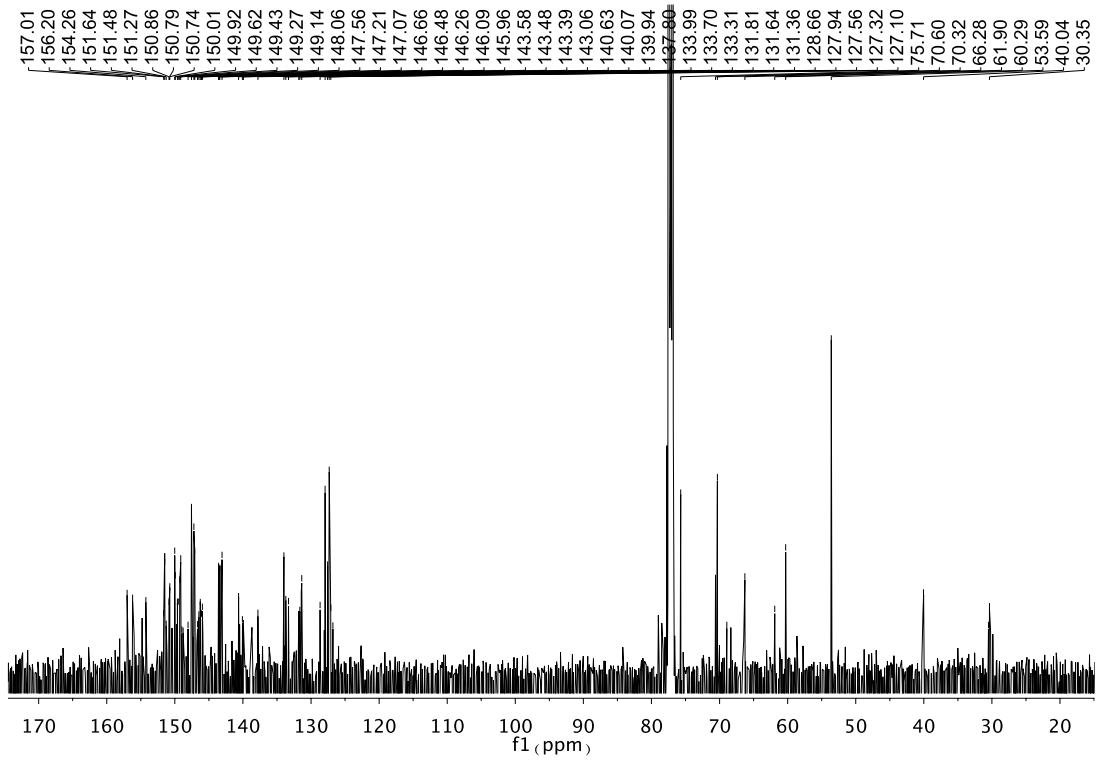

Figure 3. 27. ^{13}C NMR spectrum of compound **70C** in a mixture of CS_2 and chloroform-d.

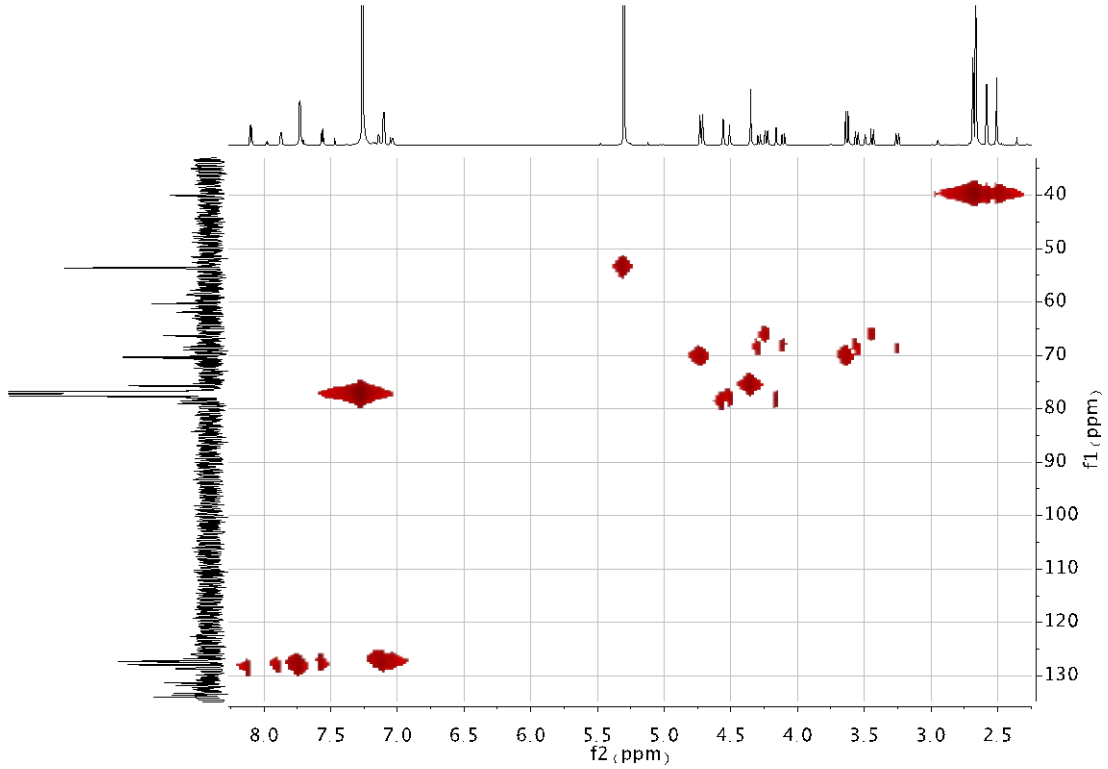

Figure 3. 28. HSQC spectrum of compound **70C** in a mixture of CS_2 and chloroform-d.

70D: ^{1}H NMR (500 MHz, CS2 + Acetone-d6) δ 8.72 – 6.98 (m, 7H), 4.71 – 4.18 (m, 2H), 3.61 (dd, J = 35.4, 7.7 Hz, 1H), 2.56 (d, J = 11.3 Hz, 6H), 1.50 – 1.09 (m, 5H), 1.03 – 0.78 (m, 3H); ^{13}C NMR (126 MHz, CS2 + Acetone-d6) δ 151.64, 151.54, 151.49, 151.44, 151.30, 151.28, 151.20, 151.16, 151.09, 150.87, 150.84, 150.75, 150.71, 150.65, 150.60, 150.54, 150.48, 150.34, 150.31, 150.14, 149.99, 149.94, 149.90, 149.85, 149.81, 149.70, 149.57, 149.51, 149.47, 149.45, 149.36, 149.30, 149.27, 149.21, 149.16, 149.09, 149.07, 149.01, 148.94, 148.84, 148.75, 148.68, 148.47, 148.37, 148.23, 148.09, 148.05, 148.00, 147.96, 147.75, 147.60, 147.56, 147.47, 147.41, 147.33, 147.20, 147.15, 147.09, 147.07, 146.97, 146.90, 146.87, 146.86, 146.81, 146.67, 146.62, 146.57, 146.38, 146.35, 146.23, 146.12, 145.92, 145.79, 145.75, 145.73, 145.68, 145.52, 145.32, 145.19, 145.00, 144.94, 144.86, 144.72, 144.65, 144.42, 144.20, 143.91, 143.85, 143.71, 143.58, 143.50, 143.41, 143.35, 143.27, 143.22, 143.18, 143.12, 142.92, 142.86, 142.67, 142.40, 142.21, 141.92, 141.80, 141.69, 141.22, 140.98, 140.92, 140.78, 140.55, 140.42, 140.36, 140.18, 140.01, 139.88, 139.74, 137.98, 137.84, 137.58, 137.30, 133.89, 133.65, 133.58, 133.14, 132.79, 132.36, 132.29, 132.11, 132.04, 131.73, 131.69, 131.58, 131.48, 131.30, 131.25, 131.20, 131.13, 130.82, 130.64,

129.12, 128.40, 128.03, 127.28, 126.95, 126.84, 126.74, 126.32, 126.18, 125.82, 123.11, 122.78, 120.95, 120.70, 120.66, 119.62, 119.52, 119.48, 119.44, 108.89, 108.79, 108.74, 108.70, 84.00, 83.15, 80.97, 73.36, 71.56, 70.59, 70.32, 69.72, 68.77, 68.24, 67.18, 66.86, 66.36, 62.12, 60.39, 58.81, 58.42, 39.97, 39.64, 39.59, 39.56, 38.02, 37.92, 37.82, 37.78, 29.61, 29.46, 29.30. (Figures 3.22, 3.23 and 3.24)

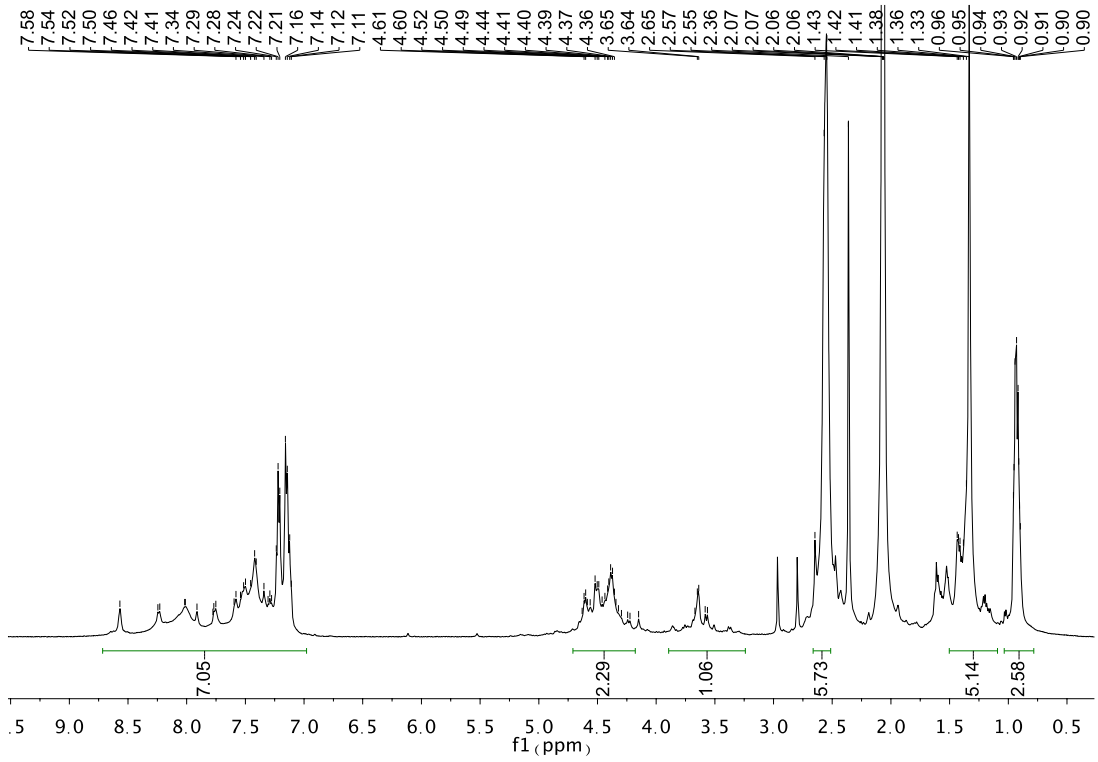

Figure 3. 29. ^{1}H NMR spectrum of compound **70D** in a mixture of CS_2 and acetone-d6.

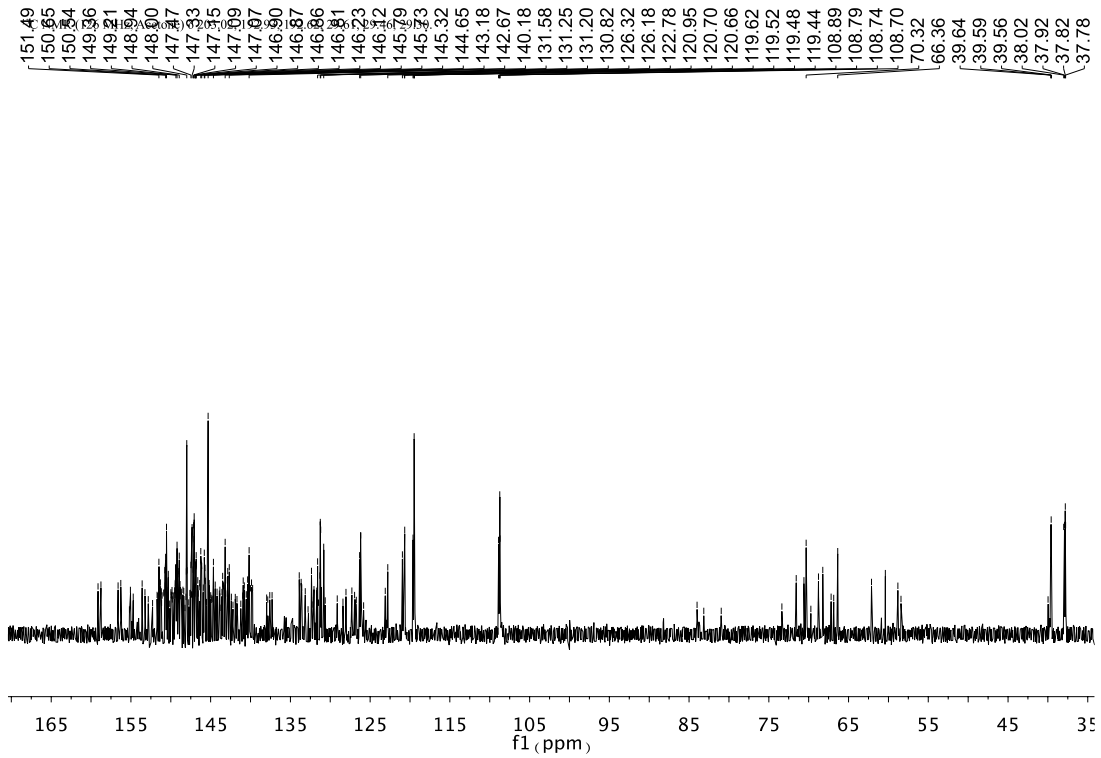

Figure 3. 30. ^{13}C NMR spectrum of compound **70D** in a mixture of CS_2 and acetone-d6.

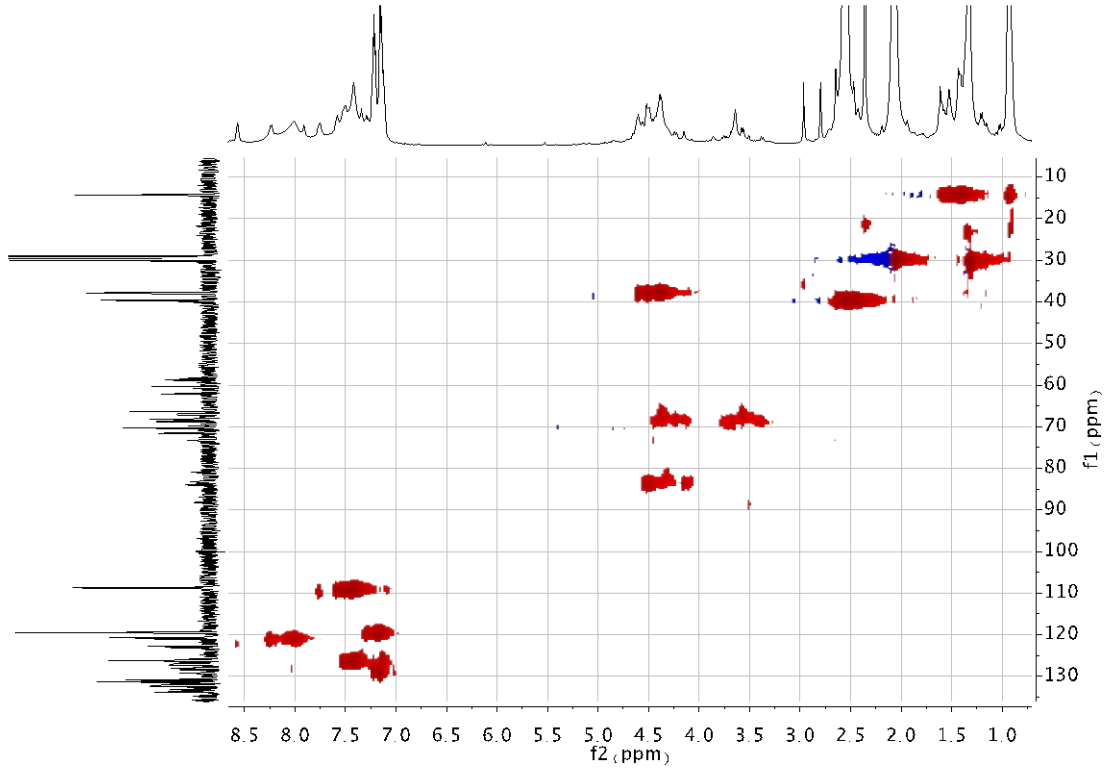

Figure 3. 31. HSQC spectrum of compound **70D** in a mixture of CS_2 and acetone-d6.